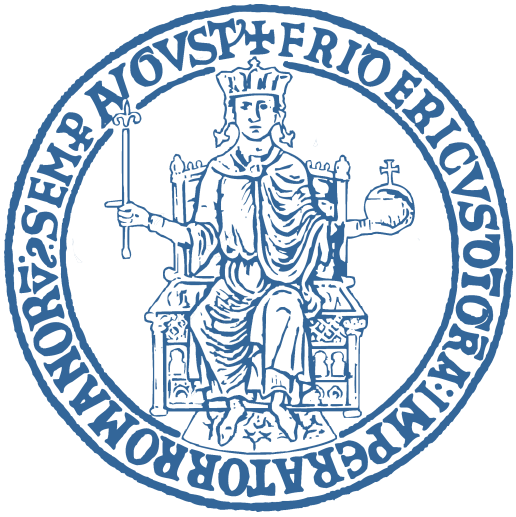
Università degli Studi di Napoli Federico II



DOTTORATO DI RICERCA IN FISICA

Ciclo XXXVIII

Coordinatore: prof. Vincenzo Canale

Search for Electromagnetic Counterparts of Gravitational Waves from Binary Neutron Star mergers and Core-Collapse Supernovae

Settore Scientifico Disciplinare FIS/05

Candidate:
Ines Francesca Giudice
Matricola:
DR996879

Tutor:
Dott.ssa Maria Teresa Botticella
Dott. Luca Izzo
Prof. Rosario De Rosa

A.A. 2024/2025

Contents

Introduction **1**

I Gravitational Waves and Electromagnetic Counterpart **5**

1 Physics and Sources of Gravitational Waves **7**
1.1 Einstein Field Equation 9
1.2 Energy of Gravitational Waves 11
1.3 Types and Sources of Gravitational Waves 14
1.4 Core-Collapse Supernovae 17
1.5 Isolated Neutron Stars 20
1.6 Binary Neutron Star Mergers 24

2 Detection of Gravitational Waves **27**
2.1 Second Generation interferometers 27
2.1.1 LIGO, VIRGO, KAGRA 28
2.1.2 Observing Runs 30
2.2 Third Generation interferometers 31
2.2.1 Einstein Telescope 34
2.2.2 Cosmic Explorer 36
2.2.3 Lunar Gravitational Wave Antenna 38
2.2.4 LISA 39

3 Electromagnetic Counterparts **41**
3.1 Electromagnetic counterparts of Binary Neutron Stars 42
3.2 GW170817 46
3.3 Search for Electromagnetic counterpart during O4 48

II Search for electromagnetic counterparts of Binary Neutron Star mergers **53**

4 Potential Binary Neutron Star merger events from the Fermi GBM Burst Catalog **55**
4.1 Clustering procedure 56
4.1.1 Pre-processing data phase 56
4.1.2 Dimensionality reduction 57
4.1.3 K-Means algorithm 60
4.2 GRB sample 61
4.3 Cluster number selection 62

4.4 Clustering results and merger-associated GRB Sample 64
4.5 Host galaxy association procedure 69
4.6 Conclusions 71

5 Modeling kilonova and sGRB afterglow emission 73
5.1 The Vera Rubin Observatory and the Legacy Survey of Space and Time . . 74
5.2 Simulation framework 75
5.3 Results 76
5.4 Case study: 2025ulz 80
5.5 Conclusions 84

III Perspectives for Detection of Gravitational Waves from Core-Collapse Supernovae 85

6 Prediction for the Einstein Telescope within the Milky Way 87
6.1 CCSN progenitor simulation in the Milky Way 87
6.2 CCSN rate 89
6.3 CCSN Waveforms 92
6.4 GWFISH 94
6.5 Results 96
6.6 Conclusions 100

7 Core-Collapse Supernova rate within the Local Universe 101
7.1 Rate of CCSNe 101
7.2 Current measurements 103
7.2.1 Direct measurements 104
7.2.2 Indirect measurements 105
7.3 Discussion 108

8 Conclusions 111

A Core-Collapse Supernova Sample within 10 Mpc 115

B GRB Clustered Sample 117
B.1 Parameter distributions 120

C Kilonova and afterglow emission modeled for E_{iso}=10^{50} 121

D Kilonova and afterglow emission modeled for an event GW170817-like 127

Introduction

The direct detection of gravitational waves (GWs) by the Advanced LIGO interferometer in 2015 marked a revolutionary milestone in modern astronomy [Abbott et al., 2016a,b]. For the first time, the Universe could be observed through a messenger different from electromagnetic (EM) emission or neutrinos, providing unprecedented access to the coalescence of compact binary objects. GWs, predicted by Einstein in 1916 [Einstein, 1916, 1918, Schwarzschild, 1916] as solutions to the linearized Einstein field equations, carry direct information from the innermost regions and merger dynamics of compact binaries, offering an observational channel that is complementary to and more penetrating than traditional EM observations. This new messenger has expanded the landscape of multimessenger astronomy (MMA). Long before the advent of GW detectors, the field was inaugurated by the nearly simultaneous detection of neutrinos and EM radiation from SN1987A [Hirata et al., 1987, Haines et al., 1988], which provided the first direct insight into the core-collapse mechanism of a massive star (e.g. constraining the neutrino mass or proving the release of gravitational binding energy through neutrinos). For decades, however, multimessenger observations were limited to combinations of electromagnetic signals and neutrinos, leaving the gravitational sector unexplored. Achieving a joint GW-neutrino-EM observation then would provide a novel view of the complex physical processes governing astrophysical phenomena, such as the core-collapse supernovae (CCSNe).

Nearly a decade after the first detection, GW astronomy has become a rapidly expanding field. The possibility that compact binaries merge within a Hubble time was first demonstrated through the September 14 2015 observation, which showed that GW emission would gradually shrink the orbit of binary compact objects, leading to coalescence over cosmological timescales [Peters, 1964, Abbott et al., 2016a]. These predictions laid the foundation for the subsequent search for GW signals from binary mergers. Since 2015 the LIGO-Virgo-KAGRA Collaboration has identified tens of compact binary mergers, primarily involving black holes. In particular, the third observing run (O3) led to a substantial increase in the number of detected events and to the release of a GW sources catalog [Abbott et al., 2021], providing valuable insights into the population properties of these objects. These analyses have provided key constraints on compact objects star mass distributions, spins and formation channels. The fourth observing run (O4), which ended in 2025, further extended this census. While events involving binary black hole (BBH) generally lack a clear EM counterpart, and are expected to be largely EM silent, some models suggest that rare BBHe mergers occurring in dense gaseous environments (e.g., AGN disks) could produce EM emission. In contrast, mergers involving neutron stars (NSs), as well as CCSNe, are suitable multimessenger sources, emitting signals across the EM spectrum, neutrinos and GWs. The association of GW170817 with the short gamma-ray burst (sGRB) GRB 170817A [Goldstein et al., 2017] and the kilonova (KN) AT 2017gfo [Coulter et al., 2017] demonstrated the new potential of multimessenger observations. This

event triggered a significant worldwide observational campaign, with observation spanning over the entire EM spectrum, from gamma rays and X-rays to optical and radio. The combination of these observations enabled the reconstruction of the merger dynamics, jet structure and r-process nucleosynthesis, reshaping our understanding of NS mergers and setting the benchmark for future multimessenger studies.

However, despite the success of GW170817, no other GW event with a certain EM counterpart have been confirmed to date, due to current GW detector sensitivities and sky localization capabilities, as well as the challenges in identifying rapidly fading transients such as KNe in wide-field searches. As a result, alternative strategies for discovering KNe, independent of a GW trigger, are becoming increasingly valuable. This motivates the first part of the PhD research presented in this dissertation, which focuses on the development of data-driven and simulation methods to identify EM counterparts of currently detectable GW sources, the binary neutron stars coalescence, even in the absence of a contemporaneous GW detection. To this end, I developed a clustering-based analysis of the Fermi GBM burst catalog to isolate GRBs with properties consistent with known KN-associated GRB events. This is complemented by a galaxy association pipeline designed to enhance the feasibility and efficiency of follow-up observations once promising GRB candidates are identified. In parallel, the simulation of KN and GRB afterglow light curves under realistic observational conditions provides a second, complementary tool for future searches. These simulations explore the impact of viewing angle, burst energetics and ambient density on the observed emission, with the idea to generate a library of templates optimized for upcoming wide-field surveys. In particular, the Vera Rubin Observatory [Bianco et al., 2021], with its significant depth and cadence, is expected to play a pivotal role in transient astronomy over the next decade. The methodologies developed in this dissertation thus offer the foundation of a framework for maximizing the likelihood of KN discovery.

While these efforts address the challenges of the current GW detection era, the next generation of detectors will significantly broaden observational horizons and open the door to GW sources that are currently inaccessible. Among these detectors, the Einstein Telescope (ET) is the European ground-based observatory, designed as a single underground facility in order to mitigate seismic noise and enhance sensitivity at low frequencies [Punturo et al., 2010]. Two main configurations are currently under study: a triangular layout of three nested 10 km interferometers, and the 2L configuration with interferometer arms of 15 km [Branchesi et al., 2023]. With an expected improvement in strain sensitivity of about an order of magnitude over current detectors [Branchesi et al., 2023, Abac et al., 2025], ET will expand the range of detectable frequencies, allowing for the observation of isolated NS signals or the pre-merging phase of binary coalescence. Most notably, ET will have the sensitivity required to detect GWs from CCSNe across the Milky Way and potentially beyond, thereby offering a unique opportunity to probe the violent, rapidly evolving dynamics of stellar collapse.

The second part of this dissertation is focused on evaluating the scientific potential of 3rd generation GW detectors. First, I investigate the capabilities of ET for detecting GW signals from CCSNe within the Milky Way by employing the GWFish [Dupletsa et al., 2023] simulation framework, adapted to CCSN waveforms, together with a realistic Galactic CCSN progenitor population obtained with `TRILEGAL` [Girardi et al., 2005]. This analysis yields detection horizons, expected signal-to-noise ratios and event rate estimates that are essential for planning future multimessenger campaigns. Then the study is extended to

extragalactic distances through an estimate of the CCSN rate in the local Universe. This analysis provides a first input for the development of future strategies and improvements in order to push the ET capabilities beyond our Galaxy.

The thesis is organized as follows:

- Chapter 1 introduces the theoretical background of GWs, from the derivation of the linearized Einstein equations to the physical mechanisms that generate GW emission. It also reviews the main astrophysical sources relevant to this work, including compact binary coalescences and CCSNe.
- Chapter 2 provides a comprehensive overview of current and future GW detectors. After discussing the present LIGO-Virgo–KAGRA network and its key observational achievements, it explores 3rd generation instruments such as the Einstein Telescope and Cosmic Explorer, as well as upcoming space-based missions.
- Chapter 3 reviews the diversity of EM counterparts associated with compact binary mergers. Particular attention is given to sGRBs and KNe, including the case of GW170817 and the most promising events identified during the fourth observational run of the LIGO-Virgo-KAGRA Collaboration.
- Chapter 4 describes the data-driven methodology for identifying potential KN-associated GRBs within the Fermi GBM catalog. Using unsupervised clustering and a galaxy-association pipeline, the analysis isolates events that may represent EM counterparts of binary neutron star mergers.
- Chapter 5 presents simulations of KN and GRB afterglow light curves under realistic observational scenarios. The generated templates incorporate LSST cadence constraints to mock realistic optical observations.
- Chapter 6 examines the potential of the ET for detecting CCSN GWs in the Milky Way. The analysis employs the GWFish framework modified for CCSN waveforms, together with progenitor populations derived from TRILEGAL.
- Chapter 7 extends the analysis to extragalactic distances by estimating the CCSN rate in the local Universe. This result provides key input for forecasting the scientific potential of 3rd generation GW detectors and for developing future multimessenger observing strategies.
- Chapter 8 summarise our results and present our conclusions.

List of pubblications

- **I. F. Giudice** et al. "Identifying potential binary neutron star merger events from the Fermi GBM Gamma-Ray Burst Catalog." Astronomy & Astrophysics 701 (2025): A83. [Giudice et al., 2025]
- Abac, A., ...,**I.F. Giudice**, ...et al. "The science of the Einstein telescope." arXiv preprint arXiv:2503.12263 (2025) [Abac et al., 2025]
- Ajith, Parameswaran, ...,**I.F. Giudice**, ...et al. "The Lunar Gravitational-wave Antenna: mission studies and science case." Journal of Cosmology and Astroparticle Physics 2025.01 (2025): 108. [Parameswaran et al., 2025]

Part I

Gravitational Waves and Electromagnetic Counterpart

Chapter 1

Physics and Sources of Gravitational Waves

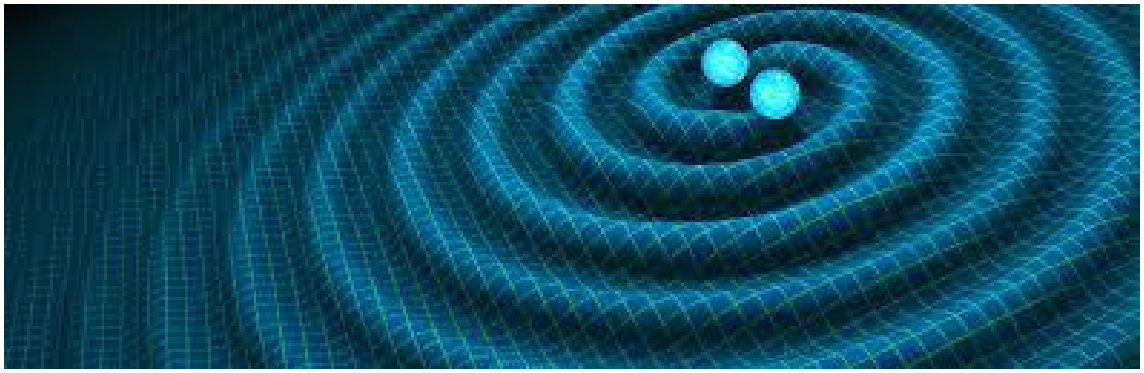


Figure 1.1: Artistic representation of gravitational waves from a binary neutron stars merger. Credit: Caltech / JPL, R. Hurt.

GWs are perturbations of the spacetime curvature that propagate at the speed of light. Intuitively, they can be thought of as "ripples" in the gravitational field generated by cataclysmic events such as compact-object mergers or core-collapse supernovae. These waves propagate as transverse distortions with two independent polarizations, h_+ and $h_\times$, each causing alternating stretching and compressing effects on both spacetime and matter. GWs carry critical information about their sources and the events that produced them, opening a new window into the cosmos and enabling us to study phenomena that were previously undetectable through traditional EM observations.

The existence of GWs was first postulated in the beginning ot the 1900 [Einstein, 1916, 1918, Schwarzschild, 1916], but it was not until a century later that they were confirmed through direct experimental observation. The first indirect evidence emerged in 1974, when Russell Hulse and Joseph Taylor observed a binary pulsar system, PSR 1913+16 [Hulse and Taylor, 1975]. By tracking the stars radio emissions and observing fluctuations in their orbital period, they identified a gradual decrease in this parameter, indicating the stars were spiraling closer together at a rate consistent with General Relativity (GR) predictions. With the following decades of advancement in experimental techniques, the field of observational GW astronomy achieved a significant breakthrough on 14 September 2015. During the inaugural GW Observing Run, the Advanced Laser Interferometer Gravitational-Wave Observatory directly detected the final inspiral signal and coalescence

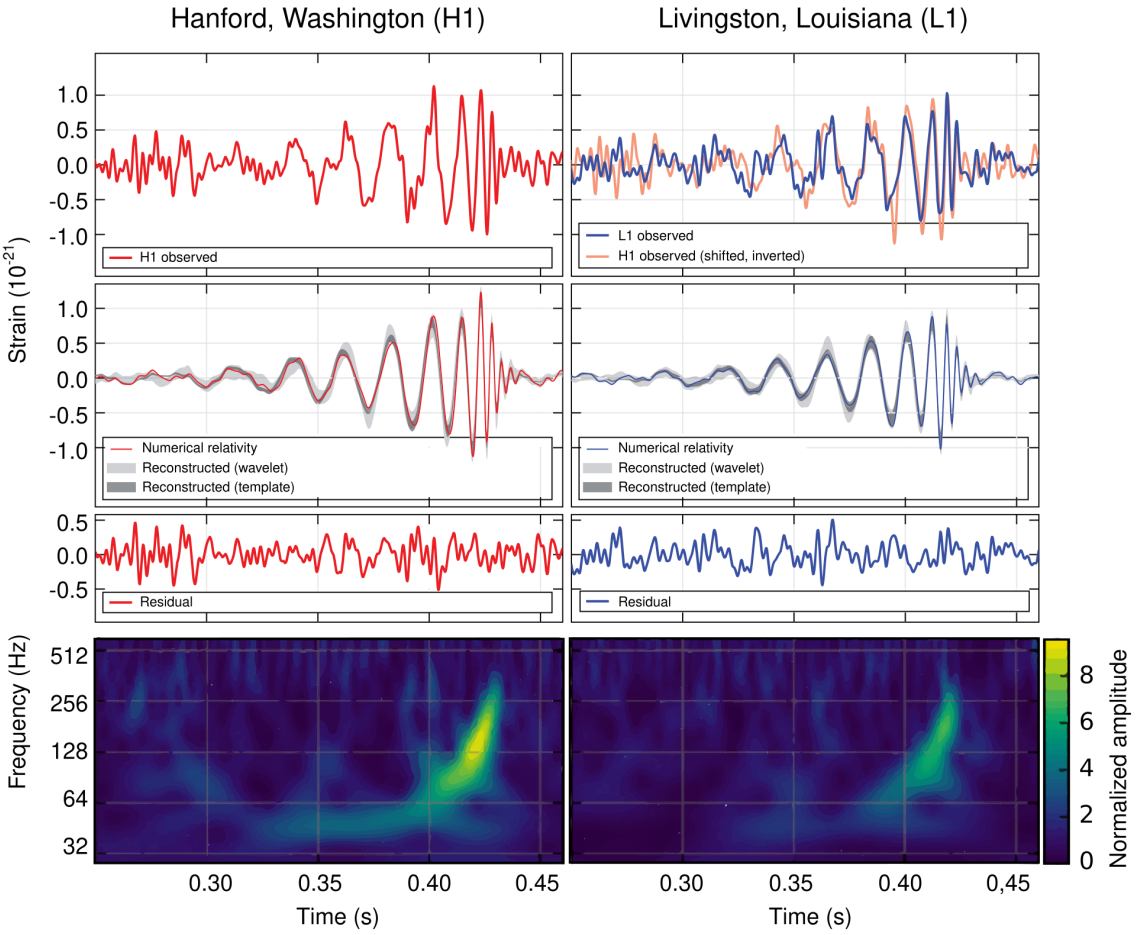


Figure 1.2: First observed GW signal by LIGO. [Abbott et al., 2016b,a]

of two compact objects (Figure 1.2). Analysis of the signal's amplitude and frequency evolution allowed the inference of the component masses, each approximately 30 $M_\odot$. Based on these masses, above the maximum theoretical mass of NS, the components were identified as black holes (BHs). This observation confirmed that compact object binaries can merge within a Hubble time, producing detectable GW signals [Peters, 1964]. The extraction of GW signals from detector data now relies on sophisticated techniques such as matched filtering. In this approach, the measured strain is compared against theoretical waveform templates based on GR, allowing for the identification of signals that would otherwise be buried in instrumental noise.

This Chapter introduces the theoretical background of GWs, from their derivation to the characterization of their observable properties. Section 1.1 outlines the formulation of GR in the weak-field approximation and the derivation of the linearized Einstein equations. Section 1.2 discusses the energy carried by GW waves and the quadrupole formula governing their emission. Finally, Section 1.3 addresses the characterization of GW signals, introducing their sources, described in further details in Sections 1.4, 1.5, 1.6.

1.1 Einstein Field Equation

GR is the modern theoretical formulation that describes the gravitational interactions on macroscopical scales. In the limit of weak field and low velocities, GR reproduces Newtonian gravity, thereby ensuring consistency with classical mechanics. A fundamental distinction between Newton's instantaneous action-at-a-distance model and Einstein's formulation is that, in the latter, gravitational effects propagate at a finite speed, namely the speed of light. The dynamics of the GR is described by the metric tensor $g_{\alpha\beta}$, a 2-rank tensor with ten components, which we wil assume in the weak field approximation for simplicity

$$g_{\mu\nu} = \eta_{\alpha\beta} + h_{\alpha\beta} \tag{1.1.1}$$

where $\eta_{\alpha\beta} = diagonal(-1, 1, 1, 1)$ is the Minkowski metric[1] and $h_{\alpha\beta}$ is a small perturbation ($|h_{\alpha\beta}| << 1$). To connect the metric to spacetime curvature, we introduce the affine connection, or Christoffel symbols, which describe how vectors change under parallel transport in curved spacetime

$$\Gamma^{\sigma}_{\alpha\beta} = \frac{1}{2} g^{\sigma\mu}(g_{\mu\alpha,\beta} + g_{\mu\beta,\alpha} - g_{\alpha\beta,\mu}). \tag{1.1.2}$$

In the weak-field approximation, by introducing Eq. 1.1.1 and neglecting higher-order terms, this simplifies to

$$\Gamma^{\mu}_{\alpha\beta} = \frac{1}{2}\eta^{\mu\nu}(\partial_\beta h_{\nu\alpha} + \partial_\alpha h_{\nu\beta} - \partial_\nu h_{\alpha\beta}) = \frac{1}{2}(\partial_\beta h^{\mu}_{\alpha} + \partial_\alpha h^{\mu}_{\beta} - \partial^\mu h_{\alpha\beta}). \tag{1.1.3}$$

From the Christoffel symbols we can build the curvature elements. First, the *Ricci tensor* $R_{\mu\nu} = g^{\alpha\beta}R_{\alpha\beta\mu\nu}$, which is given by the contraction of the Riemann tensor and defines the degree of curvature of the manifold

$$R_{\mu\nu} = \partial_\alpha \Gamma^{\alpha}_{\mu\nu} - \partial_\nu \Gamma^{\alpha}_{\mu\alpha} = \frac{1}{2}(\partial_\alpha\partial_\nu h^{\alpha}_{\mu} + \partial_\alpha\partial_\mu h^{\alpha}_{\nu} - \partial_\alpha\partial^\alpha h_{\mu\nu} - \partial_\mu\partial_\nu h), \tag{1.1.4}$$

where $h = h^{\alpha}_{\alpha} = \eta_{\alpha\beta}h^{\alpha\beta}$ is the trace of the perturbation. Then, the *Ricci scalar*, a futrher contraction of the Ricci tensor, is given by

$$R = R^{\mu}_{\mu} = \partial_\alpha\partial_\beta h^{\alpha\beta} - \partial^{\alpha}_{\alpha} h. \tag{1.1.5}$$

With these quantities defined, the Einstein Field Equation can be introduced. This equation relates the geometry of spacetime, represented by curvature tensors, to the matter-energy content described by the stress-energy tensor $T_{\mu\nu}$

$$G_{\mu\nu} = R_{\mu\nu} - \frac{1}{2}Rg_{\mu\nu} = \frac{8\pi T_{\mu\nu}}{c^4}, \tag{1.1.6}$$

In the weak-field limit, substituting the linearized expressions of the Christoffel symbols, Ricci tensor and scalar into the Einstein tensor, and introducing the trace-reversed perturbation

$$\overline{h}_{\alpha\beta} = h_{\alpha\beta} - \frac{1}{2}\eta_{\alpha\beta}h, \tag{1.1.7}$$

the Einstein Field Equation reduces to its linearized form:

$$G_{\mu\nu} = -\frac{1}{2}(\partial_\alpha\partial^\alpha\overline{h}_{\mu\nu} + \eta_{\mu\nu}\partial^\alpha\partial^\beta\overline{h}_{\alpha\beta} - \partial_\nu\partial^\alpha\overline{h}_{\mu\alpha} - \partial_\mu\partial^\alpha\overline{h}_{\nu\alpha}) = \frac{8\pi T_{\mu\nu}}{c^4} \tag{1.1.8}$$

[1]The Minkowski metric describes a flat space-time and it's defined as $ds^2 = dt^2 - dx^2 - dy^2 - dz^2$

The last step is imposing the *Lorentz gauge condition* $\partial^\alpha \overline{h}_{\alpha\beta} = 0$, which plays a role analogous to the Lorentz gauge in electromagnetism ($\partial_\mu A^\mu = 0$). It does not represent a physical constraint but rather a choice of coordinate system (a *gauge choice*) that simplifies the linearized Einstein equations, filtering out unphysical degrees of freedom associated with coordinate transformation. Once this condition is applied, the mixed-derivative terms vanish and the Einstein field equations in the weak-field limit take the form of a wave equation

$$\Box \overline{h}_{\mu\nu} = \frac{-16\pi T_{\mu\nu}}{c^4}, \tag{1.1.9}$$

which shows that the perturbations propagate as waves at the speed of light.

Plane wave solution and TT gauge

To find the simplest solution of the Einstein equations describing GWs we start by assuming a plane-wave form for the metric perturbation. We introduce the ansatz

$$\overline{h}^{\alpha\beta} = \mathrm{Re}\left(A^{\alpha\beta} e^{ik_\mu x^\mu}\right), \tag{1.1.10}$$

where x^μ are the spacetime coordinates, k_μ is the wave vector and $A^{\alpha\beta}$ is a symmetric amplitude (or polarization) tensor with ten independent components.
Substituting this ansatz into the linearized vacuum field equations and applying the Lorenz gauge condition $\partial_\beta \overline{h}^{\alpha\beta} = 0$ leads to the dispersion relation $k_\mu k^\mu = 0$, showing that GWs propagate at the speed of light. The Lorenz condition imposes four constraints on $A^{\alpha\beta}$, reducing the number of independent components from ten to six. Further gauge freedom can then be used to eliminate four additional components, leaving only two physical degrees of freedom. These correspond to the two independent polarization states of the GW.
To make this explicit, let us consider a plane GW propagating in the z-direction. In this case, the perturbation tensor in the transverse–traceless (TT) gauge can be written as

$$h^{TT}_{\mu\nu}(t,z) = \begin{pmatrix} 0 & 0 & 0 & 0 \\ 0 & h_+(t-z) & h_\times(t-z) & 0 \\ 0 & h_\times(t-z) & -h_+(t-z) & 0 \\ 0 & 0 & 0 & 0 \end{pmatrix}. \tag{1.1.11}$$

This representation makes it clear that the perturbation is purely spatial, transverse to the direction of propagation and traceless.
For a monochromatic wave of angular frequency ω, the two polarization components can be expressed as

$$h_+(t,z) = \mathrm{Re}\left(A_+ e^{i\omega(t-z)}\right), \qquad h_\times(t,z) = \mathrm{Re}\left(A_\times e^{i\omega(t-z)}\right), \tag{1.1.12}$$

where A_+ and $A_\times$ are the complex amplitudes of the two polarization modes.
The two polarization states do not correspond to different types of GWs but to two independent oscillatory modes of spacetime. Each produces a characteristic tidal deformation; for example, in the case of a ring of freely falling test particles, the h_+ mode causes alternating stretching and compression along orthogonal axes, while the $h_\times$ mode produces the same effect rotated by 45° (see Figure 1.3). The combination of these polarizations defines the dimensionless *GW strain* h, which quantifies the relative change in distance between freely falling test masses induced by the passing wave. Typical astrophysical sources produce strains in the range

$$h \sim 10^{-26} - 10^{-21}, \tag{1.1.13}$$

depending on the source mass, geometry, and distance from the observer.

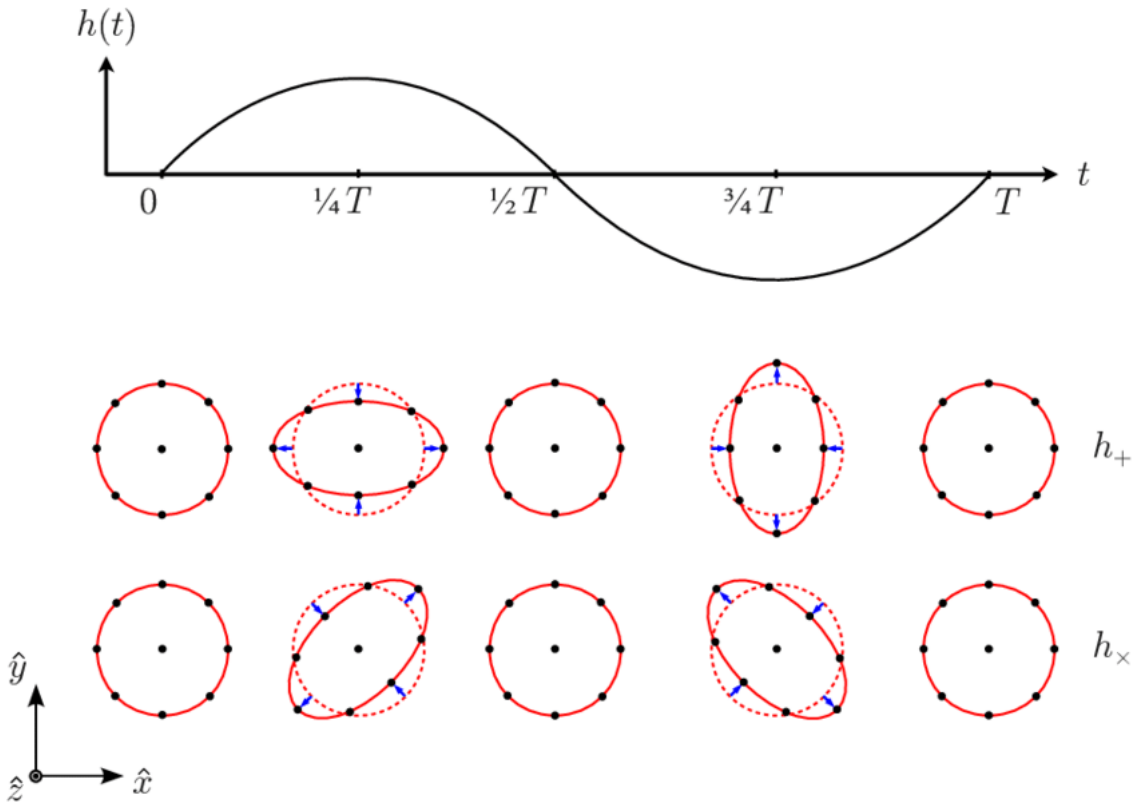


Figure 1.3: Schematic representation of the effect of the two polarization states, h_+ and $h_\times$, on a ring of test particles.

1.2 Energy of Gravitational Waves

GWs transport both energy and momentum, as can be seen from the motion they induce in matter. To describe this within the weak-field approximation, we expand the Einstein tensor order by order in the metric perturbation:

$$G^{[0]}_{\mu\nu} = G_{\mu\nu}[\eta] = 0^2, \qquad G^{[1]}_{\mu\nu} = G_{\mu\nu}[h]. \tag{1.2.1}$$

The covariant conservation law $\nabla_\mu T^{\mu\nu} = 0$ then suggests that the matter stress–energy tensor $T_{\mu\nu}$ is no longer conserved by itself once perturbations are included. This motivates the introduction of a gravitational *pseudo-tensor* $t_{\mu\nu}$, which effectively accounts for the energy and momentum carried by the gravitational field. At first order the Einstein equation becomes

$$G^{[1]}_{\mu\nu} = -\frac{8\pi G}{c^4}\left(T_{\mu\nu} + t_{\mu\nu}\right), \tag{1.2.2}$$

while at second order

$$G^{[2]}_{\mu\nu} = \frac{8\pi G}{c^4}\, t_{\mu\nu}, \tag{1.2.3}$$

showing that the effective stress–energy of the gravitational field arises from terms quadratic in the perturbation. Although $t_{\mu\nu}$ is not a true tensor and depends on the gauge choice, its physical interpretation becomes meaningful once we average over spacetime regions that

[2]It vanishes as $\eta_{\mu\nu}$ satisfies the Einstein equation in the vacuum

are large compared to the wavelength of the GW but small compared to the curvature scale of the background.
This procedure leads to the Isaacson stress–energy tensor:

$$t_{\mu\nu} = \frac{c^4}{8\pi G}\langle G^{[2]}_{\mu\nu}\rangle = \frac{c^4}{32\pi G}\langle(\partial_\mu h^{TT}_{ij})(\partial_\nu h^{ij}_{TT})\rangle. \tag{1.2.4}$$

For a purely time-dependent GW, the averaged energy density is

$$t^{00} = \frac{c^2}{16\pi G}\langle \dot{h}_+^2 + \dot{h}_\times^2\rangle, \tag{1.2.5}$$

while the associated energy flux is

$$t^{0i} = -\frac{c^2}{32\pi G}\langle \dot{h}^{TT}_{jk}\,\partial^i h^{jk}_{TT}\rangle. \tag{1.2.6}$$

The total GW energy contained in a spatial volume V is

$$E_{\rm GW} = \int_V d^3x\, t^{00}, \tag{1.2.7}$$

and the rate of energy loss (luminosity) is

$$\frac{dE_{\rm GW}}{dt} = -L_{\rm GW} = -\int_V d^3x\,\partial_t t^{00}. \tag{1.2.8}$$

In summary, at first order GWs behave as free radiation, while at quadratic order they reveal their physical content as carriers of energy and momentum, described effectively by the Isaacson tensor.

The Quadrupole Moment

The quadrupole formula describes how the energy flux can be expressed in terms of the time variation of the source's quadrupole moment. To derive it, we again adopt the TT gauge and introduce the projection operator $\Lambda_{ij,kl}$, which extracts the transverse–traceless components of a tensor

$$\overline{h}^{TT}_{ij} = \Lambda_{ij,kl}\,\overline{h}_{kl}. \tag{1.2.9}$$

Applying this to the retarded solution of the linearized Einstein equation, we obtain

$$\overline{h}^{TT}_{ij}(t,\mathbf{x}) = \frac{4G}{c^2}\Lambda_{ij,kl}\int \frac{d^3\mathbf{x}'}{|\mathbf{x}-\mathbf{x}'|}\,T_{kl}\left(t-\frac{|\mathbf{x}-\mathbf{x}'|}{c},\mathbf{x}'\right). \tag{1.2.10}$$

Through a perturbative expansion, the leading-order contribution becomes

$$\overline{h}^{TT}_{ij} = \frac{4G}{c^2}\Lambda_{ij,kl}\left(\frac{1}{2}\ddot{M}^{kl} + \mathcal{O}\big(\tfrac{1}{c}\big)\right), \tag{1.2.11}$$

where

$$M^{kl}(t) = \int d^3x\, T^{00}(t,\mathbf{x})\,x^k x^l \tag{1.2.12}$$

is the mass quadrupole moment of the source. This result shows that the dominant radiative degrees of freedom are encoded in the second time derivative $\ddot{M}^{kl}$. Assuming again a wave propagating along the z direction, the projection operator yields

$$\Lambda_{ij,kl}\,\ddot{M}^{kl} = \begin{pmatrix} \frac{1}{2}(\ddot{M}_{11}-\ddot{M}_{22}) & \ddot{M}_{12} & 0 \\ \ddot{M}_{12} & -\frac{1}{2}(\ddot{M}_{11}-\ddot{M}_{22}) & 0 \\ 0 & 0 & 0 \end{pmatrix}. \tag{1.2.13}$$

Comparing with the standard TT form of the perturbation, the two physical polarizations are

$$h_+ = h_{11}^{TT} = \frac{G}{rc^4}\,(\ddot{M}_{11} - \ddot{M}_{22}), \qquad h_\times = h_{12}^{TT} = \frac{2G}{rc^4}\,\ddot{M}_{12}. \tag{1.2.14}$$

It is convenient now to decompose the quadrupole tensor as

$$M^{kl} = \left(M^{kl} - \frac{1}{3}\delta^{kl}M_{ii}\right) + \frac{1}{3}\delta^{kl}M_{ii}. \tag{1.2.15}$$

The trace term does not contribute after TT projection[3], so only the traceless quadrupole moment

$$Q_{ij} = \int d^3x\,\rho(t,\mathbf{x})\left(x^i x^j - \tfrac{1}{3}r^2\delta^{ij}\right) \tag{1.2.16}$$

remains. The perturbation can thus be written compactly as

$$h_{ij}^{TT}(t,r) = \frac{2G}{rc^4}\,\ddot{Q}_{ij}^{TT}\left(t - \tfrac{r}{c}\right). \tag{1.2.17}$$

The total GW luminosity is obtained from the energy flux:

$$\frac{dE_{\rm GW}}{dt} = \frac{c^3 r^2}{16\pi G}\int d\Omega\,\langle \dot{h}_+^2 + \dot{h}_\times^2\rangle. \tag{1.2.18}$$

After performing the angular integration, we obtain the *quadrupole formula*, sometimes called the master equation of gravitational radiation:

$$\frac{dE_{\rm GW}}{dt} = \frac{G}{5c^5}\,\langle \dddot{Q}_{ij}\,\dddot{Q}_{ij}\rangle \equiv -L_{\rm GW}. \tag{1.2.19}$$

This relation shows that only a time-varying quadrupole moment can generate gravitational signals.

Connection with the inertia tensor

The quadrupole moment can be related to the inertia tensor I^{ij} of the source:

$$Q_{ij} = \int d^3x\,\rho(t,\mathbf{x})\left(x^i x^j - \tfrac{1}{3}r^2\delta^{ij}\right) = -\left(I^{ij} - \tfrac{1}{3}\delta^{ij}I_{kk}\right). \tag{1.2.20}$$

This relation makes explicit the dependence of gravitational radiation on the distribution of mass within the system. In particular, only sources with time-dependent asymmetries in their inertia tensor can emit GWs. As an example we can consider a homogeneous ellipsoid of semiaxes (a,b,c) and total mass M. In the non-rotating case, the inertia tensor is diagonal:

$$I_{ij} = M\begin{pmatrix} b^2+c^2 & 0 & 0 \\ 0 & c^2+a^2 & 0 \\ 0 & 0 & a^2+b^2 \end{pmatrix}. \tag{1.2.21}$$

Introducing rotation about the z-axis with angular velocity ω, the coordinates transform as $x_i = R_{ij}x'_j$ with

$$R_{ij}(\phi) = \begin{pmatrix} \cos\phi & -\sin\phi & 0 \\ \sin\phi & \cos\phi & 0 \\ 0 & 0 & 1 \end{pmatrix}, \qquad \phi = \omega t. \tag{1.2.22}$$

[3]This follows because $\Lambda_{ij,kl}\,\delta^{kl} = 0$.

In the rotating frame the quadrupole tensor acquires off-diagonal terms oscillating at frequency 2ω. The TT-projected quadrupole becomes

$$Q_{ij}(t) = \frac{I_2 - I_1}{2} \begin{pmatrix} \cos 2\phi & \sin 2\phi & 0 \\ \sin 2\phi & -\cos 2\phi & 0 \\ 0 & 0 & 0 \end{pmatrix} + \text{const.} \tag{1.2.23}$$

The example illustrates that GW emission does not require a permanent or intrinsic asymmetry of the source. Instead, the necessary condition is the presence of a time-varying mass quadrupole moment. Systems whose mass distribution evolves in time, such as binary systems in orbital motion, rotating NSs with non-axisymmetric deformations, or CCSNe, naturally satisfy this condition and emit gravitational radiation. Conversely, systems with exact spherical symmetry or with a quadrupole moment that is constant in time do not produce GWs.

1.3 Types and Sources of Gravitational Waves

GWs can exhibit distinct characteristics depending on their astrophysical origin and the physical processes responsible for their generation. They can be broadly classify into three categories: *transient*, *continuous* and *stochastic* signals. Each type occupies a different region in frequency space and requires specific data-analysis techniques and detector configurations for their identification.

Transient Signals and Their Sources

Transient signals are short-lived events, lasting from a few milliseconds to several minutes, and are associated with highly dynamic and energetic processes. They are produced when massive objects undergo rapid changes in their quadrupole moment, such as during the coalescence of compact binary systems or the collapse of a massive star.
Among these, compact binary coalescences are the only transient GW sources detected so far. These occur when two compact objects, NSs or BHs, lose orbital energy and angular momentum, causing the binary separation to decrease until merger. The GW signal from such systems typically exhibits three distinct phases:

- **Inspiral:** a chirp-like increase in frequency and amplitude as the orbit decays;
- **Merger:** a short, highly nonlinear phase dominated by strong-field relativistic effects;
- **Post merger or ringdown:** an exponentially damped oscillation as the remnant settles into equilibrium (a Kerr BH or a massive NS).

Transient signals dominate the sensitivity band of current ground-based detectors, spanning roughly 10 Hz to several kHz. The detection of such events, particularly BNS, neutron star-black hole (NSBH) and BBH mergers, has enabled precision tests of GR and measurements of cosmic distances through GW standard sirens. Figure 1.4 illustrates typical waveforms associated with these mergers.
In addition to compact binaries, other transient sources include CCSNe, which generate broadband GW burst signals, with frequencies typically spanning from a few tens of Hz up to the kHz range, reflecting the complex and rapidly evolving dynamics of the collapse and explosion. Although their signals are harder to predict than binary coalescences, their detection would yield valuable insight into the physics of stellar death, proto-neutron star (PNS) formation and neutrino-driven convection.

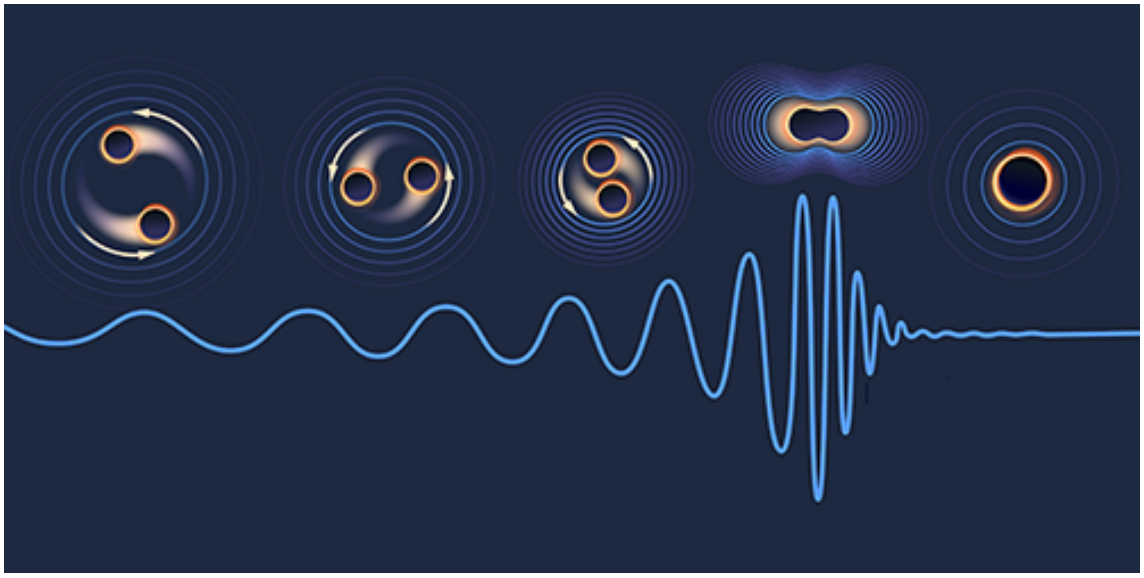


Figure 1.4: Typical GW signal from a BBH merger. Credit: Lucy Reading-Ikkanda.

Continuous Signals

Continuous GW signals are long-lived, nearly monochromatic emissions, typically originating from isolated, rapidly rotating NSs with non-axisymmetric deformations. Such deformations may result from crustal mountains, strong internal magnetic fields, or oscillation modes (e.g., r-modes) that slightly break rotational symmetry. These signals evolve slowly and persist over months or years, allowing coherent integration methods to enhance sensitivity. Their characteristic amplitudes are, however, several orders of magnitude lower than those of transient signals, making them a primary target for next-generation detectors and space-based observatories.

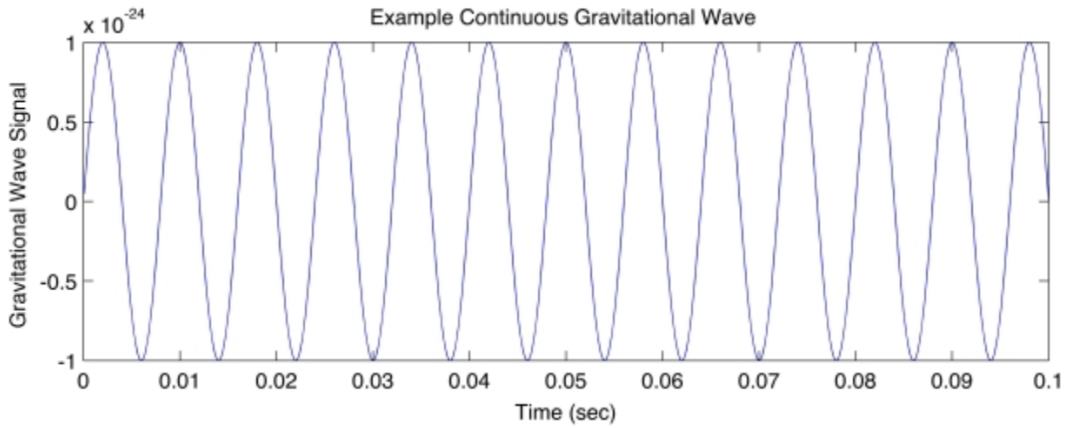


Figure 1.5: Simulated continuous gravitational wave signal. Image credit: A. Stuver/LIGO Collaboration.

Stochastic Background

A stochastic GW background arises from the incoherent superposition of numerous unresolved sources, both astrophysical and cosmological. Astrophysical contributions may

include the cumulative signal from distant compact binary mergers and CCSNe, while cosmological components could originate from inflationary fluctuations, cosmic strings, or early Universe phase transitions. The background manifests as a random, noise-like signal characterized statistically by its energy density spectrum $\Omega_{\mathrm{GW}}(f)$. Detection efforts rely on cross-correlating data from independent detectors to distinguish this background from instrumental noise.

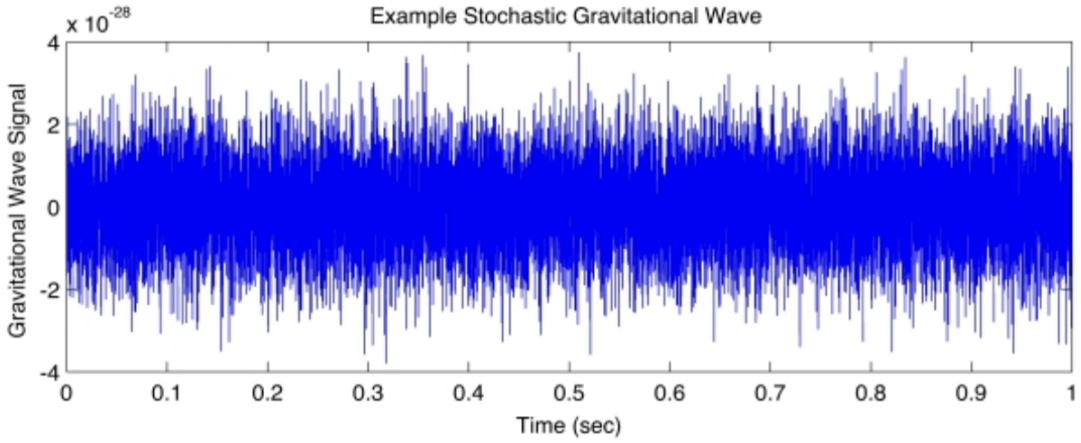


Figure 1.6: Simulated stochastic gravitational wave signal. Image credit: A. Stuver/LIGO Collaboration.

Astrophysical Sources of Gravitational Waves

Since GWs are emitted whenever mass-energy distributions undergo an accelerated non-spherical motion, a wide range of astrophysical systems can serve as GW sources. Each class of sources carries unique information about high-energy astrophysics, nuclear physics and fundamental gravity. In the context of MMA, particular attention is toward events capable of producing both strong GW and EM emissions. The discovery of GW170817 [Abbott et al., 2017] marked a milestone: for the first time, a GW detection was accompanied by EM counterparts across the spectrum, linking BNS mergers to sGRBs and KNe.
As this dissertation focuses on the EM counterparts of GW signals, the primary astrophysical sources of interest are the following three systems:

- **Core-collapse supernovae:** violent stellar explosions of massive stars ($M \gtrsim 8\,M_{\odot}$) producing highly non-axisymmetric mass motions. Their GW emission is broadband, stochastic and model-dependent, but offers a direct probe of the explosion mechanism and PNS dynamics [Kotake et al., 2012, Wang and Wheeler, 2008].
- **Isolated neutron stars:** rotating and asymmetric NSs that emit continuous, nearly periodic GWs at twice their spin frequency. These signals are ideal for constraining NS structure, internal magnetic fields and crustal properties [Haskell and Schwenzer, 2022].
- **Binary neutron star mergers:** the most precisely modeled GW sources, characterized by a predictable inspiral waveform followed by a short, high-frequency merger and post-merger phase. Their detection provides constraints on the NS equation of state and serves as a key probe of relativistic dynamics and nucleosynthesis [Abbott et al., 2017, Dietrich et al., 2021].

Such systems will be described in detail in the following Sections.

1.4 Core-Collapse Supernovae

CCSNe are among the most energetic astrophysical events in the Universe, releasing $\sim 10^{51}$erg in kinetic energy and electromagnetic radiation. They mark the violent deaths of massive stars ($M \geq 8\,M_{\odot}$) and drive the synthesis and distribution of heavy elements that shape galactic evolution. Yet, despite their astrophysical importance, our understanding of the explosion mechanism remains incomplete, as most available information derives solely from EM observations.

Following silicon burning, the stellar core consists primarily of iron-group nuclei supported by electron degeneracy pressure. Electron captures and photodisintegration progressively reduce pressure support and internal energy, lowering the effective Chandrasekhar mass and triggering gravitational collapse [Kotake and Kuroda, 2017, Abdikamalov et al., 2022]. During collapse, the inner core contracts nearly homologously, while the outer core accretes supersonically. When the central density approaches nuclear saturation ($\rho \sim 10^{14}\,\mathrm{g\,cm^{-3}}$), the nuclear equation of state stiffens, halting the inner core and launching an outward-propagating shock at the sonic point. As it traverses the infalling material, the shock rapidly loses energy to photodisintegration and neutrino emission and stalls at a radius of order 100–200 km, forming a standing accretion shock [Vartanyan et al., 2023, Abac et al., 2025].

For a successful explosion, the standard scenario assumes a stalled shock must be revived through neutrino heating. Electron-flavor neutrinos ν_e and antineutrinos $\bar{\nu}_e$ emitted from the hot PNS deposit energy in the gain region behind the shock, with an approximate local heating rate $\dot{q}_\nu \sim L_{\nu_e}\langle E^2_{\nu_e}\rangle$ where L_{ν_e} is the electron-neutrino luminosity, $\langle E^2_{\nu_e}\rangle$ its energy. Whether heating unbinds the accreting mantle depends critically on the competition between the heating and advection timescales [Janka, 2017, Abdikamalov et al., 2022].

Multi-dimensional effects, such as neutrino-driven convection and the Standing Accretion Shock Instability (SASI), enhance energy deposition and increase the time matter spends in the gain region, supporting shock expansion. The SASI is a global oscillation of the stalled shock that arises from a feedback cycle between advected perturbations (entropy and vorticity) and acoustic waves [Blondin et al., 2003, Foglizzo et al., 2015]. This instability can drive large scale sloshing or spiral motions of the shock, producing strong asymmetries in 2D and 3D simulations [Kotake and Kuroda, 2017, Vartanyan et al., 2023]. In progenitors with rapid rotation and strong magnetic fields, magnetic winding and instabilities can instead drive collimated outflows or jets, resulting in highly energetic and anisotropic explosions with distinct multimessenger signatures [Abdikamalov et al., 2022, Abac et al., 2025].

While these mechanisms govern the central engine, their first observable manifestation is the shock breakout, defined as the moment at which the optical depth of the material ahead of the shock drops below $\tau \sim c/v_{\mathrm{shock}}$, allowing the radiation that was previously trapped behind the shock front to escape [Waxman and Katz, 2017, Falk, 1978, Epstein, 1981]. This produces an intense flash of UV/X-ray radiation followed by cooling emission in optical and UV bands [Patat et al., 2017]. As the ejecta expand and cool, the emission transitions into a plateau phase lasting up to ~ 100 days, powered by radioactive decay. These EM signals reveal key properties of the progenitor and its environment but provide limited insight into the core-collapse dynamics.

To probe the inner engine directly, we must move beyond EM observations. Neutrinos, first detected from SN 1987A, offered glimpses of the collapse process, but GWs are the most

promising probe. Since gravitational signals can escape from deep within the collapsing core, they carry information about PNS oscillations and explosion asymmetries that photons cannot convey. As GWs arise from the second time derivative of the mass quadrupole moment, the asymmetric mass motions inherent translate directly into gravitational radiation, hence a purely spherical collapse produces no signal. However, observations of asymmetric ejecta, nucleosynthetic element distributions and pulsar natal kicks indicate that CCSNe are inherently aspherical [Wang and Wheeler, 2008, Kotake et al., 2012]. Looking ahead, next-generation detectors such as the ET and Cosmic Explorer (CE) will offer unprecedented sensitivity to these signals, potentially detecting CCSNe throughout the local universe [Maggiore et al., 2020]. Combined with future neutrino and EM observatories, they will usher in a new era of multimessenger astronomy, revealing the physical mechanisms behind stellar collapse.

Properties of Gravitational Waves from Core Collapse Supernovae

To derive the physical properites of the gravitational signal from a CCSN, we can use the quadrupole approximation introduced in Section 1.2. The strain introduced by GW propagation is

$$h_{ij}^{TT} = \frac{2G}{rc^4}\ddot{Q}_{ij}^{TT}\left(t - \frac{r}{c}\right). \tag{1.4.1}$$

From this relation, the characteristic scale of GW luminosity can be expressed as

$$L_{\rm GW} \sim \frac{G}{c^5}\langle \dddot{Q}_{ij}\dddot{Q}^{ij}\rangle, \tag{1.4.2}$$

with a natural upper scale set by $c^5/G \simeq 3.6 \times 10^{59}$ erg s^{-1}. A corresponding strain estimate is [Kotake and Kuroda, 2017]:

$$|h| \simeq 10^{-21}\left(\frac{\epsilon}{0.1}\right)\left(\frac{10\ \text{kpc}}{r}\right)\left(\frac{M}{M_\odot}\right)\left(\frac{R_c}{10\ \text{km}}\right)^2\left(\frac{T_{\rm dyn}}{1\ \text{ms}}\right)^{-2}, \tag{1.4.3}$$

where ϵ defines the degree of *nonsphericity*, R_c is the inner core radius and $T_{\rm dyn}$ is the dynamical timescale of the bounce. The latter sets the characteristic frequency of the emitted GWs:

$$f_{\rm GW} \simeq \frac{1}{T_{\rm dyn}} \sim \mathcal{O}(10^1 - 10^3)\ \text{Hz}. \tag{1.4.4}$$

The gravitational signal from a CCSN is expected to last from a few hundred milliseconds up to $\sim$ 1 s for the main emission, with possible weaker contributions extending to tens of seconds. Its spectral content spans from a few Hz to several kHz, reflecting the interplay between core bounce, PNS oscillations, hydrodynamical instabilities and anisotropic neutrino emission. Simulations consistently show that the PNS dynamics may be responsible for most of the GW emission, reflecting both its oscillation modes and its coupling to large-scale hydrodynamical instabilities [Vartanyan et al., 2023]. The GW emission generally begins with a short-lived, high-frequency burst associated with the *core bounce*. When the central density exceeds nuclear saturation, the stiffening of the equation of state halts the homologous collapse of the inner core, producing a sudden bounce and launching a shock wave [Kotake and Kuroda, 2017]. This generates the so-called *prompt* or *ringdown* signal, typically peaking in the 100–1000 Hz range. Its amplitude depends sensitively on the ratio of rotational kinetic to gravitational binding energy $T/|W|$, with $\Delta h \sim 10^{-21}$–10^{-20} at 10 kpc for rapidly rotating progenitors. For slowly rotating cores, the bounce signal is weaker or absent, while rapid rotation leads to a deterministic axisymmetric

waveform dominated by the plus polarization. This prompt emission carries information about the compactness and stiffness of the core, as well as the dynamical timescale of the bounce.

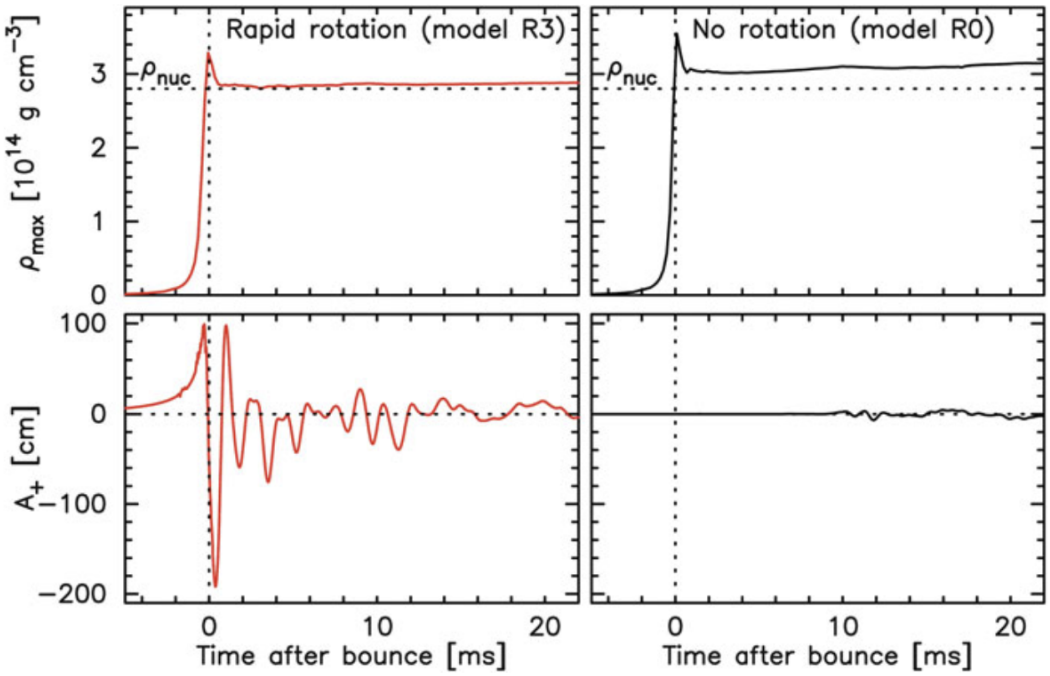


Figure 1.7: Simulations of GW signals from CCSNe with different progenitor rotations. Top panels show the central density evolution, while bottom panels display the corresponding GW waveforms. Left panels (red) correspond to rapidly rotating models, and right panels (black) to slowly rotating models. Adapted from Kotake & Kuroda (2017) [Kotake and Kuroda, 2017], based on Kuroda et al. (2014) [Kuroda et al., 2014].

Following this phase, the newly formed PNS becomes the dominant GW source. Oscillation modes of the PNS, in particular the fundamental f- and gravity g- modes, produce quasi-periodic features whose frequencies increase in time as the star contracts. Numerical simulations show a "ramp-up" track in spectrograms, starting at $\sim$ 100–500 Hz shortly after bounce and rising to $\sim$ 500–2500 Hz within $\sim$ 0.5–1 s [Vartanyan et al., 2023]. These oscillations encode the evolving mean density, compactness and surface gravity of the PNS. In rapidly rotating models, quasi-radial modes may also appear; their frequency tends toward zero as the PNS approaches BH collapse, providing a diagnostic of failed explosions. In non-rotating or slowly rotating progenitors, the shock typically stalls at $\sim$ 100–200 km and is destabilized by neutrino-driven convection and by the SASI. Its activity induces sloshing and spiral motions imprint low-frequency modulations in the GW signal at a few hundred Hz [Kotake and Kuroda, 2017, Abdikamalov et al., 2022]. These spikes despite being stochastic are related to the shock radius, offering an indirect diagnostic of the explosion geometry. Conversely, in rapidly rotating progenitors, the progenitors undergo centrifugal deformation which oblates the PNS. This configuration excites strong quadrupole oscillations (notably the $\ell = 2$ f-mode), generating a more deterministic bounce signal that can last up to $\sim$ 20 ms after bounce. At later times, rapid rotation can also trigger non-axisymmetric rotational instabilities, such as bar-mode and low-T/W instabilities, which sustain additional GW emission at 400–1000 Hz with amplitudes up to $\sim 10^{-21}$ at 10 kpc [Akiyama and Wheeler, 2006, Rampp et al., 1997].

These instabilities, though expected to occur only in a fraction of rapidly rotating CCSNe, provide distinctive GW signatures that are easier to characterize than the stochastic signals of non-rotating progenitors. Examples of these two regimes are shown in Figure 1.7, which compares simulations of slowly and rapidly rotating CCSNe.

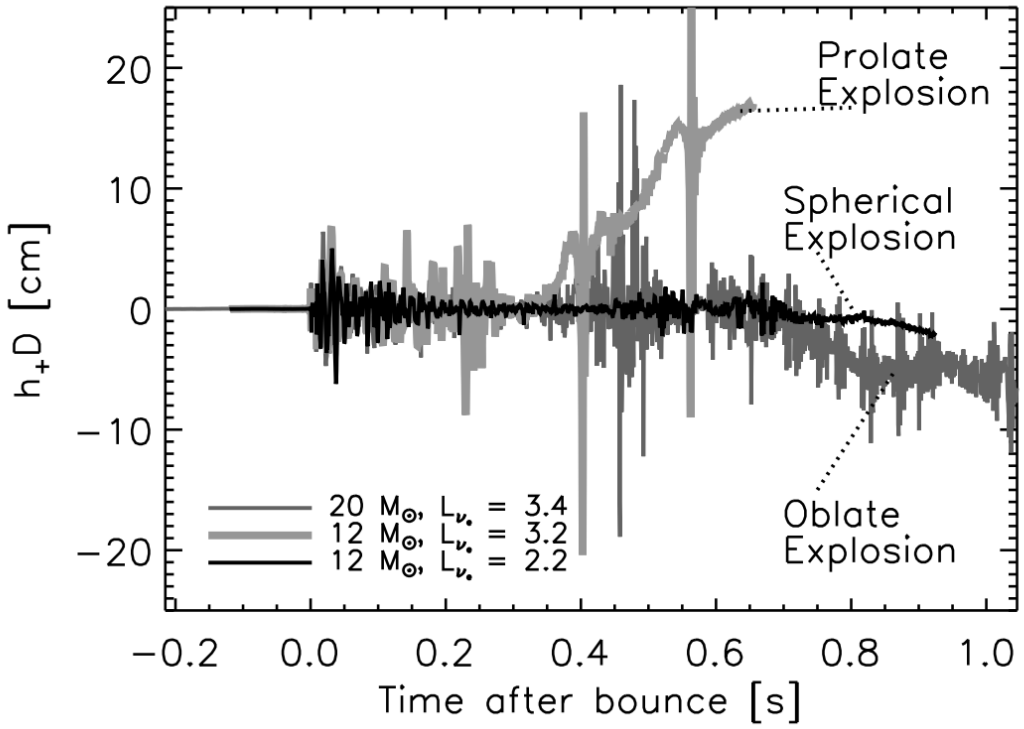


Figure 1.8: Simulated GW strains, comparing the signals obtained with different features combination from [Murphy et al., 2009].

An additional, though subdominant, contribution is expected to arise from anisotropic neutrino emission. As neutrinos carry away $\sim 10^{53}$ erg of binding energy, even small anisotropies in their flux produce a time-varying quadrupole moment. This results in a low-frequency ($\sim$ 1–10 Hz) GW *memory* component [Abac et al., 2025], which encodes the global asymmetries of the explosion. Shock anisotropies can contribute to the same memory channel. Although weaker than hydrodynamical contributions, these neutrino-driven GWs may become detectable for nearby Galactic CCSNe and would provide complementary information on the explosion geometry. The GW signal from CCSNe should be then a multi component object that reflects the interplay of core bounce, PNS oscillations, hydrodynamical instabilities, rotational effects and neutrino emission. Each of these channels carries complementary information about the nuclear equation of state, the role of rotation and the multi-dimensional dynamics of stellar explosions, making CCSNe uniquely valuable targets for multimessenger astrophysics.

1.5 Isolated Neutron Stars

NSs are one of the possible outcomes when a massive star undergoes the core collapse. With typical radii of $\sim$ 10–12 km and masses in the range 1.2–2.3 $M_\odot$, they contain matter at supra-nuclear densities, providing a unique environment to probe the physics of the

strong interaction. NSs are characterized by a gradual lose of rotational energy over time, resulting in a slow decrease in their spin frequency, a process known as *spin-down*. This loss of rotational energy can occur via EM radiation and, potentially, GW emission. For a rotating NS, the period $P = 1/\nu$, where ν is the spin frequency, can be expressed as a Taylor expansion around a reference time t_0

$$P(t) = P_0 + \dot{P}(t - t_0) + \frac{1}{2}\ddot{P}(t - t_0)^2 + \dots \tag{1.5.1}$$

The coefficients of this expansion, known as the *spin-down parameters*, are fundamental for characterizing NS evolution. From these parameters, in fact we can derive the so-called *braking index*

$$n = 2 - \frac{P\,\ddot{P}}{\dot{P}^2}, \tag{1.5.2}$$

which allows to quantify the energy loss over time. Moreover, the surface dipolar magnetic field strength is proportional to $\sqrt{P\dot{P}}$, linking the observed timing properties to the star's magnetic and rotational evolution [Abac et al., 2025].
These relations form the basis of the P–$\dot{P}$ *diagram*, a map of the observed NS population (see Figure 1.9). The main subpopulations of NSs include:

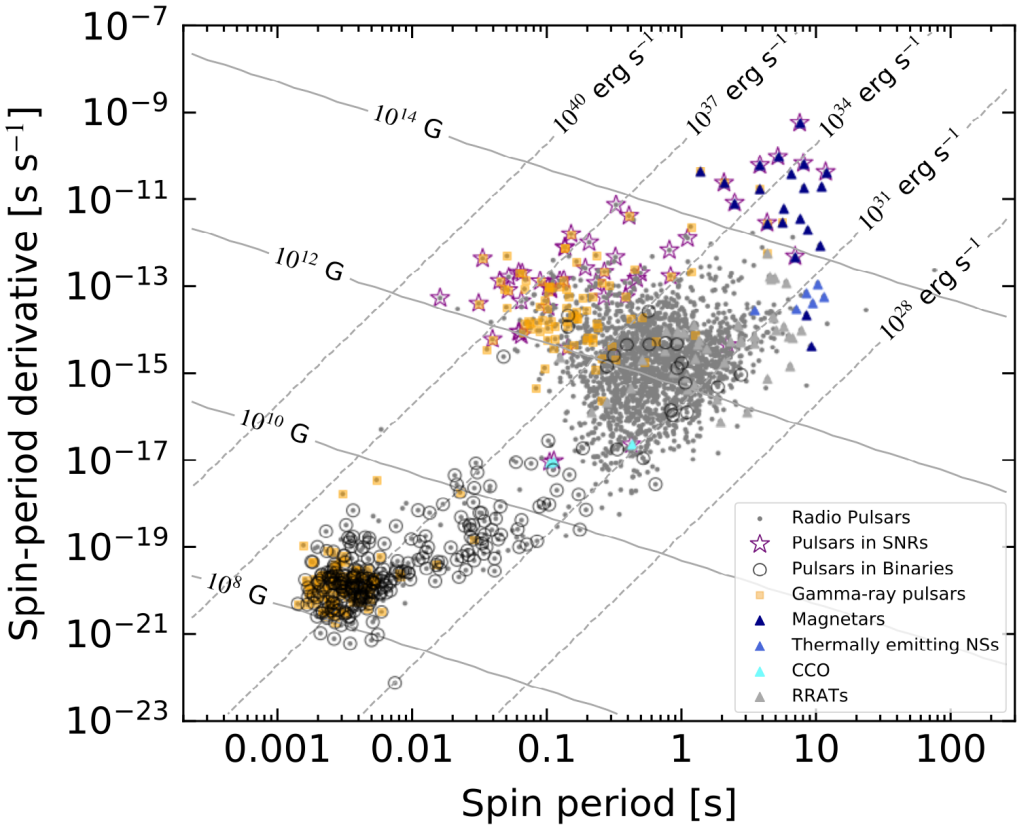


Figure 1.9: P–$\dot{P}$ diagram from [Abac et al., 2025].

- **Radio Pulsars:** rapidly rotating and highly magnetized NSs that emit periodic radio pulses due to beamed emission from their magnetic poles. Many also emit in the optical, X-ray and gamma-ray bands. They are the most numerous and well-studied NS population.

- **Low-Mass X-ray Binaries (LMXBs):** LMXBs are systems where a NS accretes matter from a low-mass stellar companion. The accretion process can spin up the NS to millisecond periods, leading to the formation of *recycled pulsars* or *millisecond pulsars* after accretion ceases.
- **Magnetars and X-ray Dim Isolated Neutron Stars (XDINs):** Magnetars are NSs powered primarily by their extremely strong magnetic fields ($B \sim 10^{14}$–10^{15} G), rather than rotational energy. They exhibit intense X-ray and GRBs. XDINs are a subcategory of thermally emitting magnetars with weaker activity and lower luminosities.
- **Pulsar Glitches:** Sudden, irregular increases in the rotation frequency observed in some pulsars. These events are interpreted as the transfer of angular momentum between the superfluid interior and the crust, providing valuable information about the star's internal structure and dynamics.

While EM observations have been the current primary tool for studying NSs, their rotational energy loss may also power continuous GW emission. Such signals, originating from non-axisymmetric deformations or internal oscillations, offer a complementary probe of the stellar interior, the equation of state of ultra-dense matter and the mechanisms driving the long term spin-down of NSs.

Physics of Gravitational Waves from Isolated Neutron Stars

Isolated NSs offer multiple channels for GW emission: persistent continuous waves from crustal or magnetic deformations, long-duration transient signatures from newborn magnetars and shorter signals associated with stellar oscillations or glitches. The details of these mechanisms depend on the star's internal structure, rotation rate, magnetic field and accretion history.
Asymmetries that produce GW signals can arise from various physical processes. A static deformation of the solid crust, often called a *mountain*, may produce a mass quadrupole moment that, as the star rotates, generates a continuous GW signal. The rigidity of the crust is a key factor in sustaining such deformations: the crust can support small but finite mountains on the stellar surface, in analogy with terrestrial mountains on Earth. However, because of the intense gravitational field, NS mountains are extremely small, with typical height estimates of the order of $\delta r \approx 1\,\mathrm{mm}$ [Haskell and Schwenzer, 2022]. The dimensionless strain amplitude from a deformed NS rotating about one of its principal axes can be expressed as

$$h_0 \simeq 10^{-25} \left(\frac{10\,\mathrm{kpc}}{d}\right) \left(\frac{\epsilon}{10^{-6}}\right) \left(\frac{I}{10^{45}\,\mathrm{g\,cm^2}}\right) \left(\frac{\nu}{500\,\mathrm{Hz}}\right)^2, \tag{1.5.3}$$

where ν is the GW frequency ($\nu = 2\nu_{\mathrm{spin}}$, where ν_{spin} is the stellar spin frequency), d is the distance to the source, ϵ the stellar ellipticity and I the moment of inertia about the rotation axis. Even within our Galaxy, such signals are expected to be faint, but their long coherence time allows the signal-to-noise ratio to build up through extended data integration.
In LMXBs, mass accretion onto the NS surface can also lead to highly asymmetric *accretion mountains*, producing time-varying quadrupole moments and continuous GW emission. Observations show that these stars rotate below their expected break-up limit, suggesting a balance between accretion-driven spin-up and GW-driven spin-down. In these systems,

light elements accreted from the companion are compressed to higher densities where they undergo reactions such as electron captures, releasing heat in a process known as *deep crustal heating* [Abac et al., 2025]. This localized heating modifies the temperature profile and mechanical properties of the crust, potentially enhancing its ability to sustain asymmetric deformations. Next-generation detectors such as the ET will be able to probe this regime and potentially confirm whether GW torques indeed regulate the spin evolution of LMXBs. Furthermore, accretion can modify the magnetic field structure, altering the interaction between disk and magnetospehere and influence the shape of the mountain.
Magnetars are also expected to be strong GW emitters. Their intense internal magnetic fields can induce a prolate deformation of the stellar structure, driving long-duration GW emission via the so called spin-flip mechanism. Depending on the magnetic configuration and ellipticity ($\epsilon \sim 10^{-4}$–10^{-3}), such signals could last from seconds to days and be detectable by ET up to distances of 5–10 Mpc [Abac et al., 2025].
Finally, stellar oscillation modes can be another strong GW emitters. Two classes of oscillations are mainly relevant. The fundamental f-mode, with frequencies in the kilohertz range, are global pulsation of the NS fluid that deform its shape and are sensitive to the average stellar density ($\nu_f \propto \sqrt{M/R^3}$). They can be excited by transient events such as pulsar glitches, producing short but energetic GW bursts. In contrast, the r-mode, a rotational instability driven by the Coriolis force, produces sustained continuous emission which can last over long timescales as the mode grows to nonlinear amplitudes. According to relativistic hydrodynamics, both f- and r- modes can become unstable to GW emission via the Friedman–Schutz mechanism. The instability strength increases with mode frequency, roughly proportional to the stellar rotation rate. R-modes are particularly interesting since, in the absence of dissipation, they are unstable at any frequency. Standard dissipation mechanisms such as Ekman layer friction are often insufficient to damp r-modes in millisecond pulsars, implying that such modes might be present in many astrophysical sources. In contrast, f-modes likely become unstable only near the Kepler frequency and thus are most relevant for newborn NSs.
The typical strain associated with an excited f-mode is

$$h_0 \sim 10^{-24} \left(\frac{\alpha}{10^{-6}}\right) \left(\frac{M}{1.4\,M_\odot}\right)^2 \left(\frac{R}{10\,\mathrm{km}}\right)^{-1} \left(\frac{d}{1\,\mathrm{kpc}}\right)^{-1}, \tag{1.5.4}$$

where α represents the mode amplitude. If the mode becomes unstable, α grows exponentially until nonlinear couplings and viscous effects saturate its amplitude at a finite value α_{sat}. Depending on this saturation mechanism, r-modes can produce continuous GWs for extended periods, potentially billions of years in millisecond pulsars, while f-modes are generally limited to newborn sources. The GW evolution typically follows three phases: an exponential growth, a plateau during saturation and a power-law decay as the source spins down and exits the instability region [Abac et al., 2025].
Transient deformations may also appear after pulsar glitches, when the sudden rearrangement of superfluid instabilities induces oscillations or *temporary crustal mountains*. These phenomena can lead to both short-lived and long-lived GW components, whose amplitudes ($h_0 \sim 10^{-26}$) and decay timescales reflect the post-glitch evolution of the star.
Although direct detection of continuous or transient GW signals from isolated NSs has not yet been achieved, current upper limits are approaching astrophysically interesting regions. The enhanced sensitivity of 3rd generation detectors such as ET will allow for systematic surveys of the Galactic NS population, probing spin-equilibrium scenarios in LMXBs, testing r-mode instability models, and potentially detecting post-glitch transients. Combined EM and GW observations will thus play a key role in unveiling the internal dynamics and composition of NSs in the coming decades.

1.6 Binary Neutron Star Mergers

BNSs can form through at least two main channels. In the *isolated binary evolution* scenario, two massive stars evolve in a binary system, each undergoing CCSN and leaving behind a NS. Depending on the details of mass transfer, common-envelope evolution and natal kicks imparted during the SN phase, a compact BNS system may survive and eventually merge within a Hubble time . This channel is supported by the observed Galactic population of BNSs, such as the Hulse–Taylor pulsar, and is considered the dominant formation mechanism. Alternatively, in dense stellar environments such as globular clusters and galactic nuclei, BNSs may form dynamically through *exchange interactions*, tidal capture, or multi-body scatterings [Baiotti, 2022]. While this dynamical channel is thought to contribute less to the overall rate, it could produce systems with higher eccentricities or unusual mass ratios. The timescale for coalescence is set by orbital energy loss through GW emission, as predicted by GR. Observational estimates from the LVK collaboration suggest a local BNS merger rate of $\mathcal{R} \sim 10$–$1700\ \mathrm{Gpc^{-3}\,yr^{-1}}$ based on GWTC-3 analyses [Abbott et al., 2021], while more recent studies constrain the local rate to $\mathcal{R} \sim 2.8$–$480\ \mathrm{Gpc^{-3}\,yr^{-1}}$ [Salafia, 2025], both consistent with rates inferred from Galactic BNS.
A newly formed BNS system possesses an open inspiral orbit, due to the emission of energy (e.g. GWs), leading the NSs to move around each other to eventually merge in a single object. During the inspiral phase, the orbital decay causes the stars to move closer while being tidally deformed by each other's gravity. These tidal effects increase the inspiral phase and leave characteristic features on the GW. As the outer layers of the stars come into contact, strong shear flows can develop at the interface, which are unstable to the formation of vortices through the Kelvin–Helmholtz mechanism. In simulations, this instability leads to rapid amplification of magnetic fields producing magnetar level field strengths that may influence the post-merger dynamics and jet launching mechanisms associated with sGRBs. Following the merger, the remnant may undergo a brief phase of decompression and violent oscillations before settling into a quasi-stable configuration. The remnant outcome depends on the total mass, mass ratio and the stiffness of the equation of state. Three main classes of remnants are possible: (i) a *stable neutron star* for sufficiently low total mass, (ii) a *supramassive neutron star* supported by uniform rotation, or (iii) a *hypermassive neutron star* supported by differential rotation and thermal pressure. For even higher total masses, a *prompt collapse* to a BH occurs.

Phases of a Binary Neutron Star Merger and Gravitational-Wave Emission

BNS produce strong GW signals and a broad range of possible multimessenger counterparts. In addition to GWs and EM emission, the merger remnant radiates neutrinos with luminosities up to $L_\nu \sim 10^{53}\,\mathrm{erg/s}$ and typical energies $\langle E_\nu \rangle \sim 10$–$20$ MeV [Rosswog et al., 2003]). While direct detection of such neutrinos from extragalactic BNS mergers is beyond current capabilities, their indirect effects on nucleosynthesis and GW emission are of great importance in the multimessenger context. Unlike the stochastic and broadband signals from CCSNe, the GWs produced by BNS mergers are highly deterministic during the inspiral and can be modeled with a good degree of accuracy using post-Newtonian expansions, effective-one-body formalisms and numerical relativity. This predictability enables the use of matched filtering techniques that extract faint signals buried in detector noise, allowing detections at cosmological distances and making BNS systems key *standard sirens* for cosmology.
The coalescence of two NSs proceeds through three principal stages: *inspiral*, *merger* and *post-merger* (see Figure 1.10), each of them leaving a distinct imprint on the GW wave-

form and encoding unique information about the binary's physical properties, relativistic dynamics and the nuclear equation of state of ultra-dense matter.

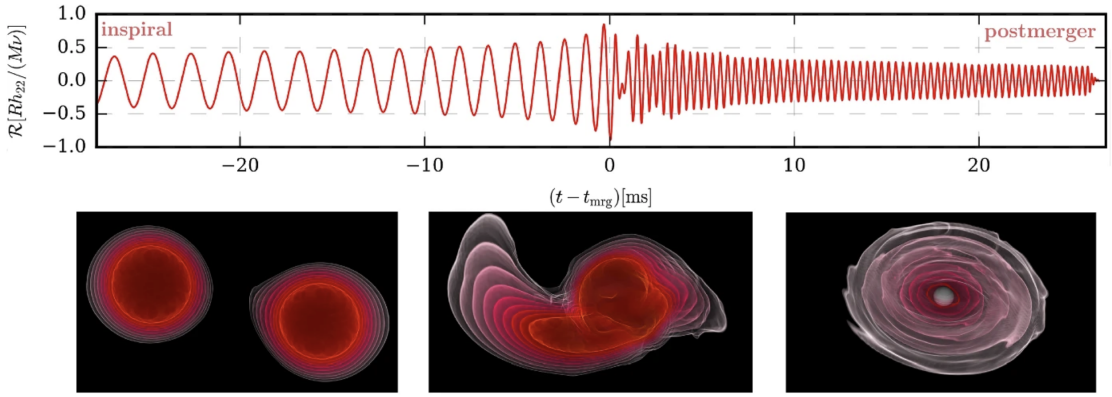


Figure 1.10: Simulated BNS merger showing the GW signal (top panel)and the matter (bottom panel) evolution. [Dietrich et al., 2021].

During the *inspiral* or *chirp phase*, the system orbit gradually shrinks due to energy and angular momentum loss through GW emission. The system emits a quasi-monochromatic signal whose frequency ω and amplitude increase over time in a characteristic *chirp*. The GW strain is

$$h(t) \approx \frac{4(G\mathcal{M})^{5/3}(\pi\omega)^{2/3}}{c^4 d}, \tag{1.6.1}$$

where $\mathcal{M} = (m_1 m_2)^{3/5}/(m_1+m_2)^{1/5}$ is the chirp mass and d is the luminosity distance to the source. At a fiducial distance of 100 Mpc, the characteristic strain reaches $h \sim 10^{-21}$. The frequency evolution follows

$$\frac{d\omega}{dt} = \frac{96}{5}\pi^{8/3}\left(\frac{G\mathcal{M}}{c^3}\right)^{5/3}\omega^{11/3}, \tag{1.6.2}$$

leading to a rapid *chirp* just before merger. The inspiral typically ranges through $\sim$ 10–1000 Hz. Then the *merger* phase emits GWs at frequencies of $\sim$ 1–4 kHz, often dominated by a single spectral peak $\omega_{\rm peak}$ that correlates tightly with the remnant radius and compactness. The total GW energy emitted reaches $E_{\rm GW} \sim 10^{53}$ erg ($\sim 0.01\, M_\odot c^2$). At this stage, strong-field and nonlinear hydrodynamic effects dominate, requiring full numerical-relativity simulations to capture the waveform accurately. Lastly, the system enters the *post-merger* or *ring-down* phase. If the remnant collapses rapidly into a BH, the GW signal transitions into a short-lived quasi-normal-mode characterized by a damped signal with frequency determined by the mass and spin of the newly formed BH. Alternatively, if a massive NS remnant survives, differential rotation and thermal pressure support the star against collapse, leading to strong non-axisymmetric oscillations that emit quasi-periodic GWs in the 2–4 kHz [Baiotti, 2022] range. These high-frequency components encode detailed information about the equation of state and angular-momentum transport processes in the remnant.
While current ground-based detectors are primarily sensitive to the inspiral phase (below $\sim$ 1 kHz), next-generation detectors such as ET and CE will open the high-frequency post-merger window, directly probing the NS equation of state and rotational instabilities.

Chapter 2

Detection of Gravitational Waves

GWs, ripples in the spacetime predicted by Einstein's GR, provide a unique window into the most energetic processes involving compact objects in the Universe. The direct detection of these waves has opened a new era in astronomy, allowing us to observe BHs and NSs through their gravitational signatures, rather than EM radiation alone.
This Chapter provides a comprehensive overview of the current and next-generation instruments designed to detect GWs. Section 2.1 outlines the LIGO-VIRGO-KAGRA network and their primary results during their observational runs (Section 2.1.2). Section 2.2 introduces the ongoing development of 3rd generation observatories, including the Einstein Telescope (Section 2.2.1) and Cosmic Explorer (Section 2.2.2) which promise substantial improvements in sensitivity and frequency coverage. These future detectors, together with planned space-based missions such as LISA (Section 2.2.4), will dramatically expand our understanding of the Universe.

2.1 Second Generation interferometers

Currently the detection of GWs relies on large scale laser interferometers, designed to measure changes in the relative distance between freely suspended test masses. The basic idea is that a passing GW induces a differential stretching and squeezing of space along orthogonal directions, which can be transformed into a measurable phase shift of a laser propagating in the two perpendicular arms of the interferometer.
The simpler configuration is a Michelson interferometer, in which a laser is split into two beams that travel along the interferometer arms and are reflected back by mirrors acting as test masses (see Figure 2.1). When recombined at the beam splitter, the two lasers interfere and their results is monitored by a photodiode. A GW reaching perpendicularly to the interferometer plane produces a relative change in the arm lengths, leading to a variation in the interference signal. The dimensionless strain measured by the detector is defined as

$$h(t) = \frac{\Delta L(t)}{L}, \tag{2.1.1}$$

where L is the arm length and $\Delta L(t)$ is variation induced by the wave. For detector arm lenghts of few kms, GWs generate fluctuations of about 10^{-18} m, corresponding to strains of $h \sim 10^{-21} - 10^{-22}$. To achieve the sensitivity required for such measurements, current interferometers go beyond the simple Michelson design. Each arm can be equipped with Fabry-Pérot resonant cavities, amplifying the phase shift produced by a GW. Additional techniques are used to maximize the GW impact inside the interferometers, such as power recycling cavities that reinject light otherwise lost at the beam splitter. The extreme

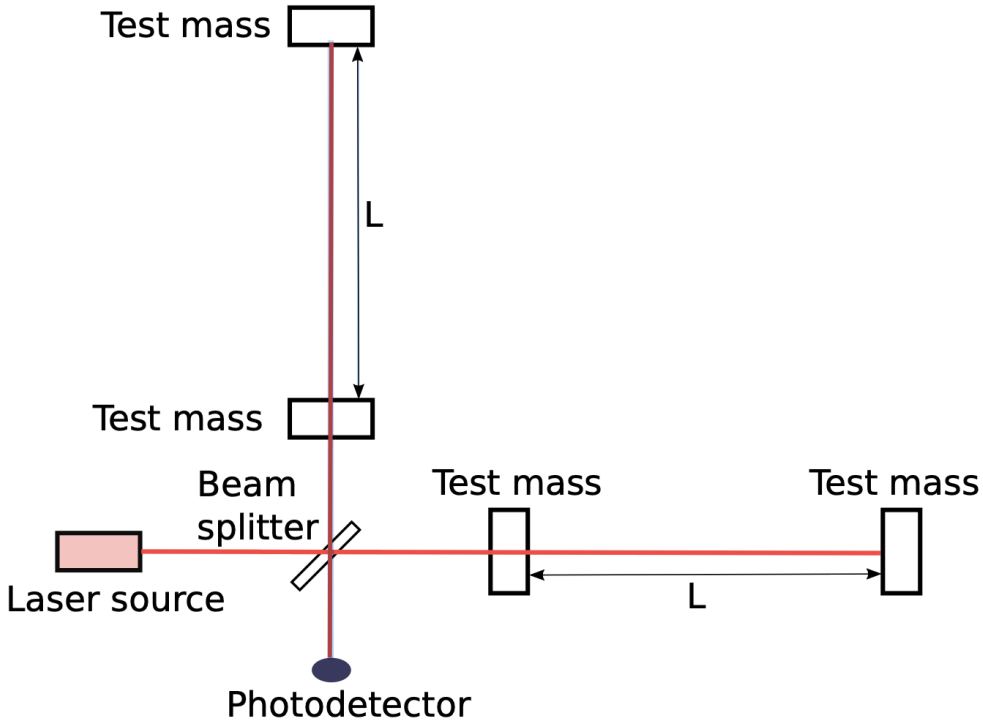


Figure 2.1: Schematic representation of an interferometer, where L is the lenght arm [Bishop, 2021].

precision of these kinds of detection necessitates the implementation of advanced techniques in interferometer designs. For example, to reduce the impact of effects like absorption and scattering, the optical elements are distributed inside vacuum-tubes. However, despite these advancements, ground-based interferometers remain subject to fundamental noise limitations. The main sources of noises are intrinsic to the detector: i) *thermal* noise, produced by the dissipation in mirror coatings and suspencions; ii) *seismic*, due to the coupling of the seismic waves with the mirror system; and iii) *Newtonian* noise, generated by the coupling of mirrors and density fluctuation in the environment. These noise sources limit the frequency range of current detector, with the thermal noise constraining the mid-frequency range to a few kHz and the other two noises dominant in the low frequency range.

2.1.1 LIGO, VIRGO, KAGRA

The current ground-based GW detector network includes four interferometers based on the Michelson configuration: Advanced Laser Interferometry Gravitational-Wave Observatory (Advanced LIGO) at Hanford and Livingston in the U.S. [Aasi et al., 2015], Advanced Virgo in Italy Acernese et al. [2014] and the Kamioka Gravitational Wave Detector (KAGRA) in Japan [Akutsu et al., 2021] (Figure 2.3).
The two LIGO detectors, situated in Hanford, Washington, and Livingston, Louisiana, share an identical design. Each interferometer consists of two orthogonal arms, 4 km in length, with suspended test-mass mirrors forming a Fabry–Pérot–Michelson interferometer equipped with power and signal recycling. The first configuration, called Initial LIGO, was

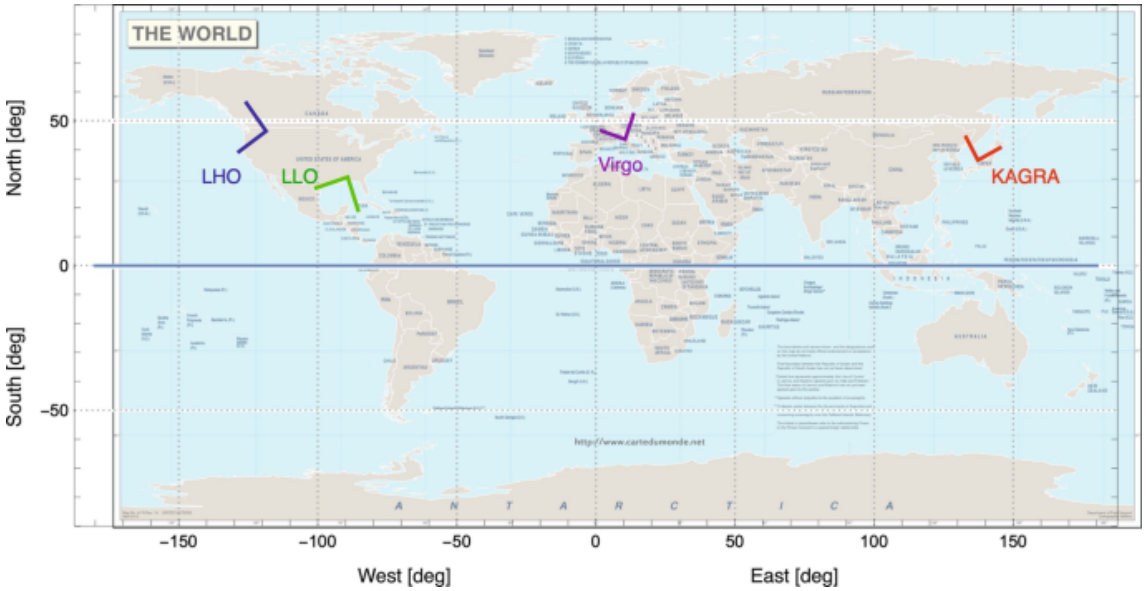


Figure 2.2: Location of the LVK network: LHO (LIGO Hanford Observatory), LLO (LIGO Livingston Observatory), Virgo and KAGRA.

built in 2002 and officially represented the first generation of laser interferometers GW detector. However, its sensitivity was not sufficient for regular astrophysical detections. To overcome its limitations, the project was upgraded to Advanced LIGO, achieving approximately a factor of ten improvement in strain sensitivity across a broad frequency band, with a lower frequency limit reduced from about 40 Hz to around 10 Hz [Aasi et al., 2015]. The detectors employ high-power stabilized lasers, pre-mode cleaners to ensure beam quality and Fabry–Pérot cavities to increase the effective optical path and enhance the interaction time of the laser light with passing GWs. Advanced seismic isolation systems and multi-stage pendulums minimize ground vibrations, while improved mirror coatings and thermal control reduce thermal noise. Additionally, squeezed-light injection is used to reduce quantum shot noise at high frequencies, further enhancing sensitivity.

The Virgo interferometer, located near Pisa (Italy) and inaugurated in 2003, features 3 km arms and similar Michelson–Fabry–Pérot design principles [Acernese et al., 2014]. Although its instantaneous sensitivity is generally lower than that of the LIGO detectors, Virgo plays a critical role in the network by improving the sky localization. Its location and arm orientation relative to the LIGO detectors allow the network to triangulate sources more accurately, constraining both their position on the sky and their distance. Virgo also implements sophisticated seismic isolation, superattenuators and advanced coatings and suspensions to mitigate thermal and seismic noise.

KAGRA, inaugurated in 2009 and situated underground in the Kamioka mine in Japan, introduces notable innovations. Its underground location significantly reduces seismic and anthropogenic noise, while cryogenic mirrors help to suppress thermal noise in the mid-frequency band [Akutsu et al., 2021]. With 3 km arms, KAGRA's current sensitivity is lower than that of LIGO or Virgo, but its inclusion in the network enhances sky coverage, baseline geometry and event localization.

Together, the LIGO-Virgo-KAGRA (LVK) network provides not only increased detection sensitivity but also improved astrophysical information. The strain response depends on the incident direction and polarization of each GW, so multiple detectors are essential for both detecting events robustly and accurately reconstructing their properties.

2.1.2 Observing Runs

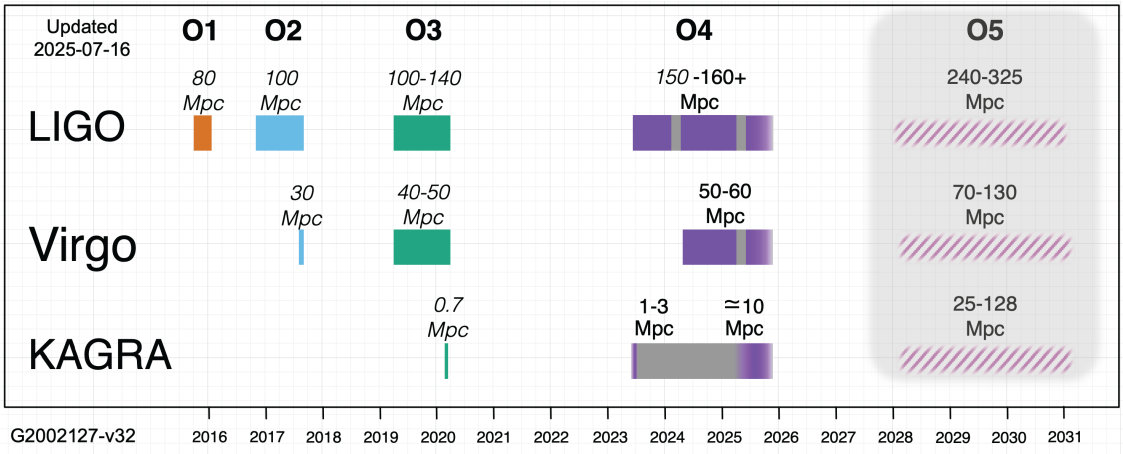


Figure 2.3: Observing Runs of the LIGO–Virgo–KAGRA Collaboration.

The operations of 2nd generation GW detectors began in September 2015 and initially involved only the two LIGO observatories. Figure 2.3 summarizes the observing runs of the LVK network. The first observing run, O1, lasted four months and was groundbreaking: on 14 September 2015, the network registered the first direct detection of GWs, GW150914, generated by the merger of two BHs with masses of approximately 30 and 36 $M_\odot$, located at a distance of about 400 Mpc [Abbott et al., 2016b,a]. This event not only confirmed the existence of GWs but also provided the first observational probe of BBHs.
The second run, O2, began in November 2016 for LIGO and in August 2017 for Virgo. The most notable outcome of O2 was the detection of the first GW signal from a BNS merger, GW170817, which inaugurated the era of MMA with its simultaneous EM counterpart detection. This event will be discussed in detail in Chapter 3.
The third observing run, O3, started on 1 April 2019 and was divided into two segments, O3a and O3b, separated by a commissioning break in October 2019. Compared to previous runs, O3 represented a major step forward in both sensitivity and duty cycle. During this run, the LIGO detectors reached a BNS range of approximately 110-130 Mpc, while Virgo reached about 50 Mpc. For BBHs, LIGO's sensitivity extended to roughly 990-1200 Mpc, with Virgo reaching approximately 500 Mpc. The improved network sensitivity resulted in the most prolific GW observing period to date, detecting a consistent number of confirmed signals.
The main outcome of this phase was the release of the second Gravitational-Wave Transient Catalog (GWTC-2), which reported 46 BBH mergers, two BNS events, and two additional compact binaries of uncertain classification [Abbott et al., 2021]. Subsequent extensions, GWTC-2.1 [Abbott et al., 2024] and GWTC-3 [Abbott et al., 2023], added several other events detected up to March 2020, bringing the total number of confidently observed GW signals to nearly ninety (Figure 2.4).
Population analyses based on these catalogs have refined estimates of BBH and BNS merger rates and revealed a rich and diverse population of compact objects. In particular, O3 data enabled to put constraints on BH mass and spin distributions and suggested the possible existence of a mass gap between NSs and BHs. Moreover, several unusual sources were identified, such as GW190814, a merger between a 23 $M_\odot$ BH and a 2.6 $M_\odot$ compact object of uncertain nature, and GW190521, a merger producing an intermediate mass BH of about 142 $M_\odot$ [Abbott et al., 2020]. These discoveries had remarkable implications for

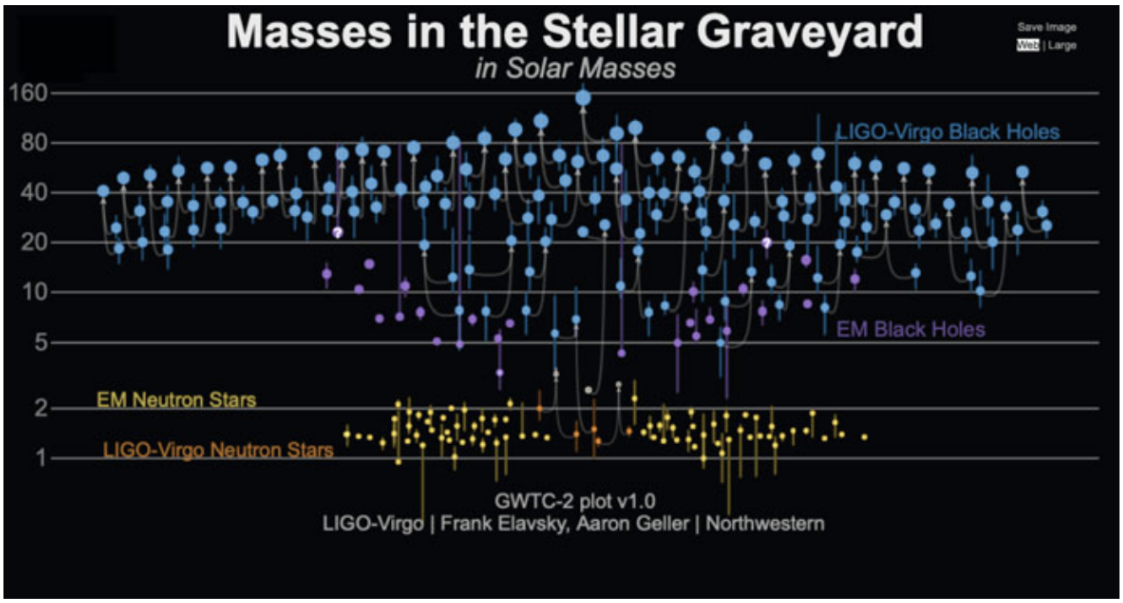


Figure 2.4: Results from the GWTC-2 Catalog. Credit: LIGO–Virgo Collaboration / Frank Elavsky, Aaron Geller / Northwestern University.

binary formation channels and the astrophysical environments hosting compact binaries. The O3 run concluded in March 2020, before a major series of upgrades leading to the ongoingrun.
Following a four-year break, largely attributable to the global COVID-19 pandemic, the fourth observing run O4 of the LVK Collaboration began on May 2023. During the initial phase of O4, referred to as O4a, only the LIGO detectors were operational, while Virgo underwent upgrades aimed at enhancing its sensitivity, particularly in the low-frequency range. These upgrades were part of a broader effort to improve the overall sensitivity and reach of the network, which included technical improvements to LIGO and KAGRA. The second phase of the run, designated O4b, began on April 10, 2024. During O4b, Virgo resumed operations alongside LIGO and KAGRA, enabling a three-detector network. This configuration significantly enhances the ability to localize GW events and improves sensitivity, particularly for low-frequency signals. In mid-August 2025, KAGRA experienced a failure of its main laser, temporarily taking the detector offline. At the end of the run, in November 2025, O4 has yielded several confirmed GW events, the majority of which are BBH mergers. This highlights the continued predominance of BBHs as observed in GWTC-2, though the addition of Virgo and KAGRA to the network is expected to improve the detection of lower-mass systems, such as BNS and NSBH mergers, which are anticipated up to redshifts of $z \sim 0.2$(Figure 2.5).

2.2 Third Generation interferometers

The 2nd generation of GW detectors has achieved remarkable results by identifying the first direct detection of a GW signal, proving the compact binary coalescences and allowing for the first statistical studies of BH populations.However, the current instruments remain limited by their structural design and intrinsic noise sources, which constraint their sensitivity and our ability to deep investigate the still open questions about our Universe.

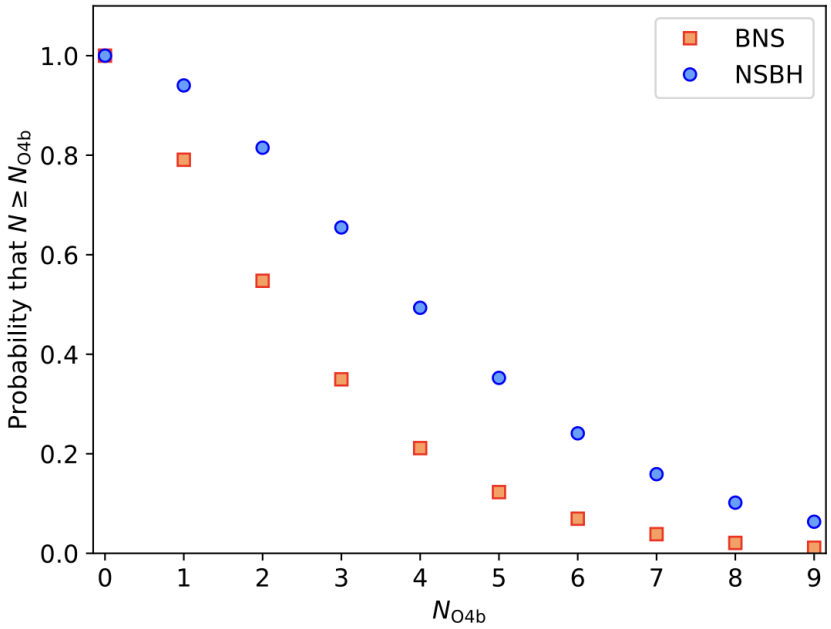


Figure 2.5: Probability of the detection of BNS and NSBH mergers in O4b. The red squares corresponds to BNS events, the blue dots to NSBH. From the plot the probability to detect at least one BNS event is almost 73%, while the probability for one NSBH detection is $\sim 94\%$ [lig, 2026].

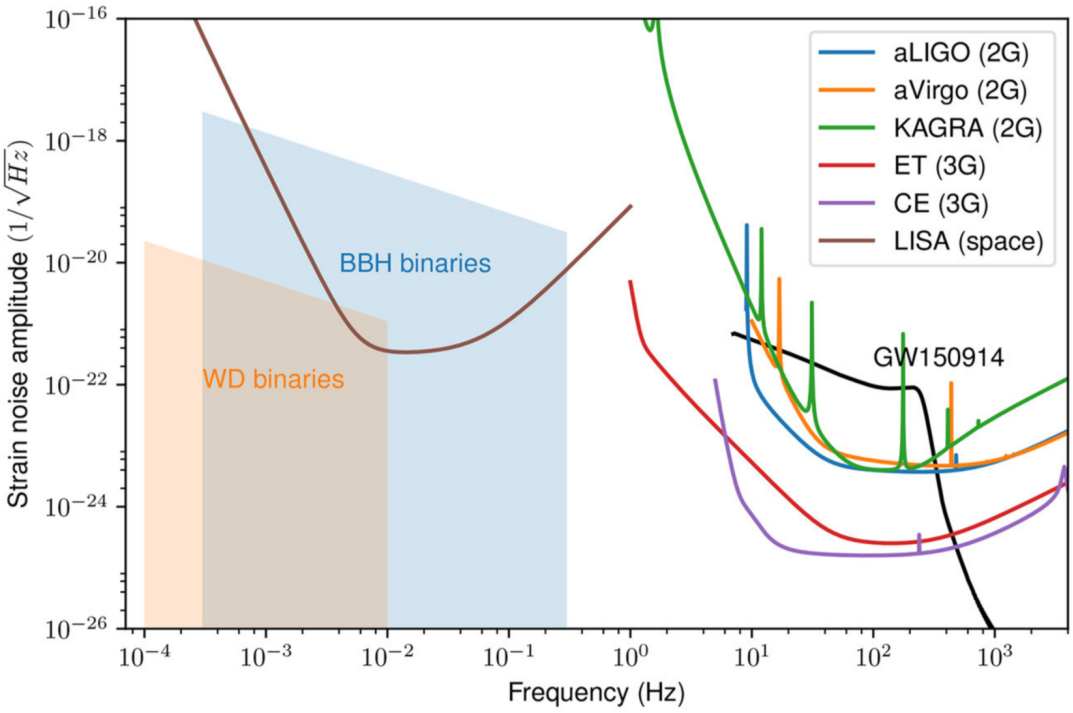


Figure 2.6: Comparison between strain sensitivities of the current and under development GW detectors [Abac et al., 2025].

To overcome these limitations, the so-called third generation is under development, with the first operational runs expected for the late 2030s. The main objective of these facilities is to achieve an increase in strain sensitivity (Figure 2.6), primarily through the extension of interferometer arm lengths to approximately 10–15 km. Because GWs induce minute perturbations that alternately stretch and compress spacetime, a longer baseline enhances the measurable spatial variation without introducing additional physical noise to the test masses. This improvement will dramatically expand the accessible volume of the Universe for GW observations, enabling detections of compact binary mergers up to redshifts of z $\sim$ 100 (see Figure 2.7).

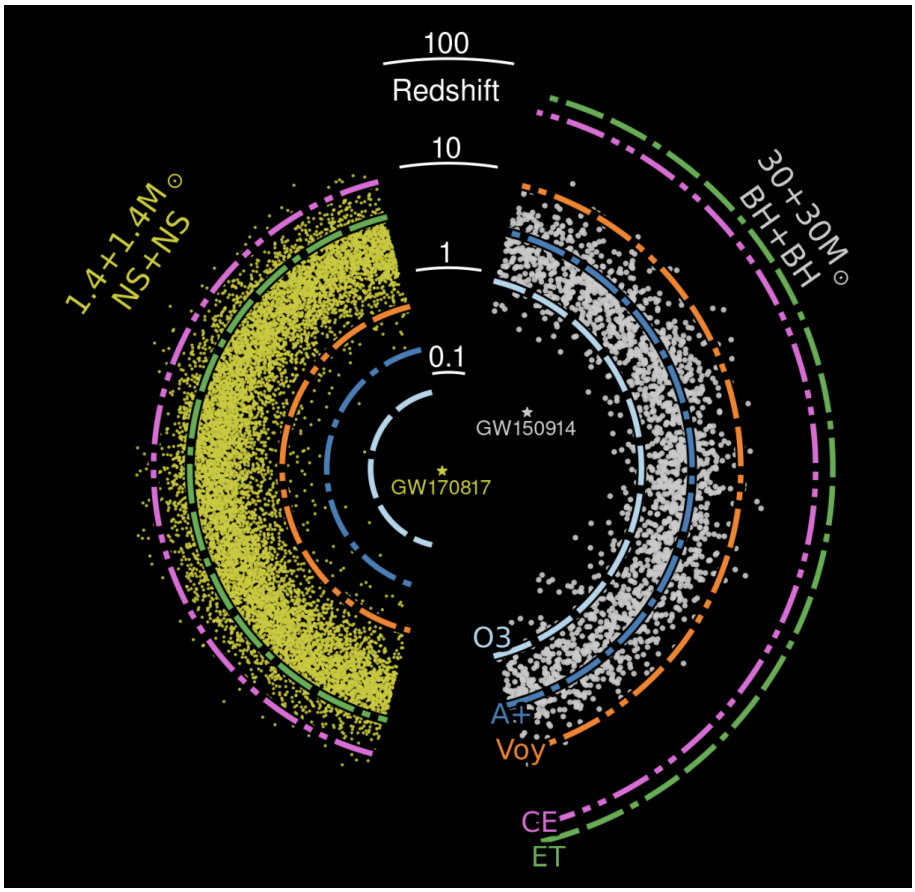


Figure 2.7: Horizon of current and future detectors: Advanced LIGO (A+), LIGO Voyager (Voy), ET and CE. The yellow and white dots represent simulated populations of BNS and BBH mergers, respectively [Evans et al., 2021].

Another innovation aims at extending the sensitivity toward lower frequenciy regime, that will allow the detection of earlier inspiral phases of compact binaries, as well as more massive systems, thereby broadening the astrophysical reach of GW astronomy. In this range, the main noise contributions arise from seismic motion, Newtonian fluctuations, thermal noise, and quantum shot noise (Figure 2.8). By cooling the interferometer mirrors to temperatures close to absolute zero, the contribution of thermal fluctuations in the substrate and coatings can be significantly reduced. Combined with enhanced seismic isolation systems or underground design and next-generation optical coatings, this approach is expected to extend the accessible frequency band down to a few hertz.
These concepts underpin the design of the two major observatories currently in development: Cosmic Explorer (CE) in the United States and the Einstein Telescope (ET) in Europe.

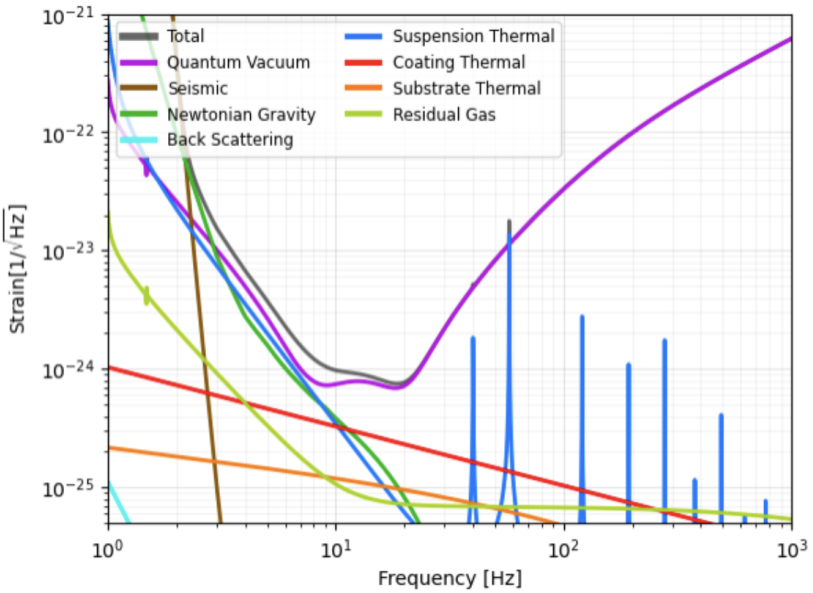


Figure 2.8: Strain noise budget of the low-frequency Einstein Telescope detector, corresponding to a single interferometer with an agle of 90 degrees [Einstein Telescope Collaboration, 2025].

Both are large-scale international collaborations that adopt complementary design strategies and site configurations to optimize sky coverage and source localization accuracy. This new network will be also complemented by space-based GW detectors, such as the Laser Interferometer Space Antenna (LISA), that will expand the observational window to frequency bands currently inaccessible from the ground. As a result, we will be able to detect signals from the inspiral and pre-merger phases of compact binary coalescences with unprecedented detail. Furthermore, the improved sensitivity will allow the observation of fainter or more exotic sources, such as the CCSNe and isolated NSs introduced in the previous Chapter, and a stochastic GW background.

2.2.1 Einstein Telescope

ET is the European collaboration that will improve GW detection and our understanding of cosmic evolution [Punturo et al., 2010]. These advances are enabled by a significant improvement in strain sensitivity and by an extension of the accessible frequency band toward lower frequencies. This enhanced low-frequency sensitivity will allow ET to observe compact binary inspirals much earlier than current detectors, resulting in longer signals in band, improved parameter estimation, and the possibility of early-warning alerts for BNS mergers.
Extensive analyses are currently carried out to test the scientific capabilities of the detector. Population studies of compact objects indicate that ET will be able to detect about 10^5 BBH mergers and about 10^4–10^5 BNS mergers per year with high signal-to-noise ratio, enabling the use of these sources as *standard sirens* to measure cosmological distances [Abac et al., 2025]. Moreover, the lower frequency sensitivity achieved by ET, by an order of magnitude over the current detectors, will push forward the ability to detect signals currently too faint, like the one emitted from CCSNe. Further discussion on the ET capabilities for CCSN GW detection will be addressed in Chapter 6 and Chapter 7.

The main technological advancement that differentiates ET from other projects is the decision to build the observatory underground, at a depth of approximately 200–300 meters, in order to strongly reduce the impact of seismic noise on the measured signals [Abac et al., 2025]. Since the project is still under development, two main detector configurations are currently under investigation (Figure 2.9).

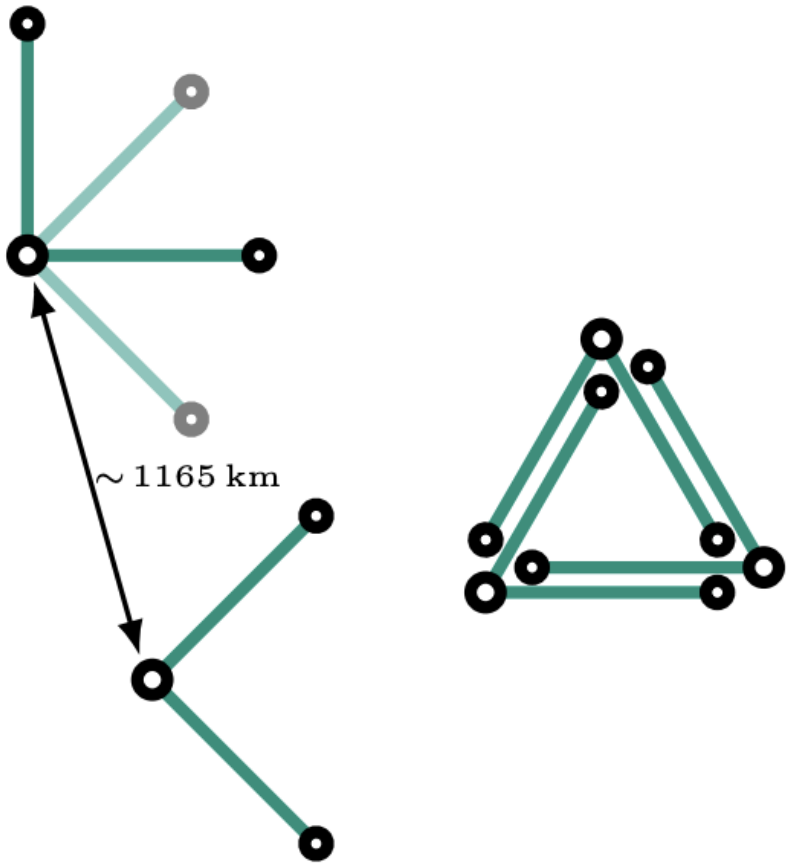


Figure 2.9: The two proposed configurations for the ET: on the left, two L-shaped detectors (parallel or rotated by $\pi/4$), and on the right the *xylophone* or triangular configuration [Branchesi et al., 2023].

The *xylophone*, or *triangular*, configuration (Δ) consists of three underground detectors arranged in pairwise-shared tunnels, each 10 km long and with opening angles of 60 degrees. This configuration aims to increase redundancy, namely the ability to reconstruct the GW polarizations, and provides a more isotropic response without null directions, unlike a single L-shaped detector. In the triangular geometry, the strain data from the three interferometers can be linearly combined to construct a *null stream*, in which the GW signal cancels out by construction while instrumental noise contributions remain. The null stream therefore provides a powerful tool to identify and characterize instrumental artifacts, since any residual signal in this channel must be of non-astrophysical origin. In addition, it enables consistency tests among the detectors, improving the robustness of GW signal validation in the presence of correlated noise.
Moreover, the Δ configuration involves two coupled interferometers for each detector: one

optimized for high frequencies, operating with high laser power, and one optimized for low frequencies, operating at cryogenic temperatures with reduced laser power [Abac et al., 2025].
On the other hand, the *2L* configuration with different orientations resembles the already adapted strategy for GW detection. In this case, the relative orientation of the detectors is still under discussion.By positioning the arms with an angle of $\pi/4$ the angular localization can be increased, enhancing the capabilities to better pinpoint the position of a source and determine its distance. The parallel arms configuration instead allows for the detection of the stochastic background, improving also the detection range for binary coalescences [Abac et al., 2025].
Recent comparative studies between these configurations have highlighted that, regardless of the chosen geometry, ET overcomes by an order of magnitude the capabilities of current 2nd generation GW detectors, accessing physical sources currently under our detection capability (see Figure 2.10 [Branchesi et al., 2023]). However, while both the 10 km Δ and the 15 km 2L configurations provide excellent scientific potential, notable differences emerge. The 15 km 2L layout with arms oriented at $\pi/4$ shows superior performance in most field of interest, particularly in the reconstruction of luminosity distance and the parameter estimate for binary coalescences. Moreover, the Δ, while being the only configuration sensible to stochastic backgrounds, may suffer more for seismic, Newtonian and magnetic noise at low frequencies. An additional advantage of the 15 km 2L at $\pi/4$ comes from the possibility to proceed in a staged implementation [Branchesi et al., 2023]. Even operating initially with only the high-frequency interferometer, this configuration would already yield valuable scientific results, while the full potential would be achieved once both the high-frequency and cryogenic low-frequency instruments are operational.
Finally, the ET Collaboration is currently investigating the feasibility of three potential sites for the observatory. The candidate locations are: (i) the *Sos Enattos* area in Sardinia, Italy; (ii) the *Euregio Meuse–Rhine* region spanning Belgium, Germany, and the Netherlands; and (iii) the *Lusatia* region in Saxony, Germany.

2.2.2 Cosmic Explorer

CE is a U.S. proposed ground-based interferometric observatory designed to significantly extend the reach of GW astronomy. The detector is expected to achieve a strain sensitivity approximately an order of magnitude over the current observatories, extending the low-frequency sensitivity down to $\sim 5\,\mathrm{Hz}$ [Evans et al., 2021]. This improvement will allow earlier detection of inspiral phases and provide tens of minutes of advance warning for BNS coalescences. The increased redshift reach and sensitivity of CE will enable the detection of GW signals from the earliest epochs of star formation, providing unique insights into the physics of ultra-dense matter and the nuclear equation of state. Operating as part of a global third-generation detector network together with ET, CE will provide complementary sky coverage and substantially improved source localization. This network will enable precision measurements of cosmological parameters through GW standard sirens, offer constraints on the expansion history of the Universe and test the limits of GR under extreme conditions. From a technological perspective, CE consists of two L-shaped interferometric facilities with arm lengths of approximately 40 km and 20 km, following the Advanced LIGO configuration of a dual-recycled Fabry–Pérot Michelson interferometer, but with a dramatic increase in length [Evans et al., 2021]. Achieving the target sensitivity will require major advancements in seismic isolation, thermal noise mitigation, and vacuum infrastructure. The facility will employ two ultra-high-vacuum beam tubes built on geologically stable and flat terrain to minimize environmental and

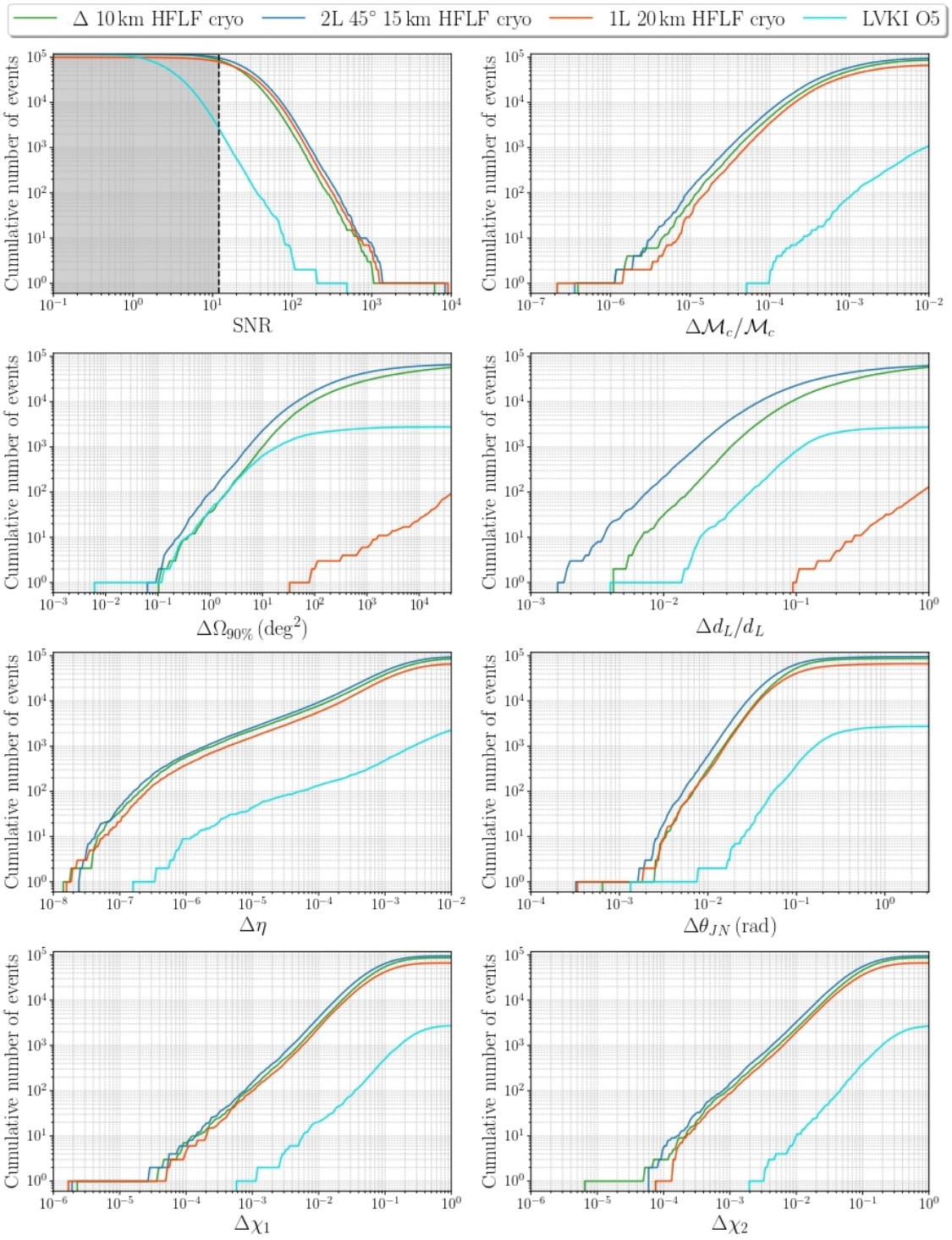


Figure 2.10: Performance comparison between different proposed ET configurations and the LVK detector network [Branchesi et al., 2023].

seismic disturbances. Advanced test-mass suspensions, improved mirror coatings, and cryogenic technologies are also under investigation to suppress noise sources and enhance low-frequency performance.

2.2.3 Lunar Gravitational Wave Antenna

The Lunar Gravitational-Wave Antenna (LGWA) is a proposed mission concept that aims to overcome many of the limitations of ground-based GW observatories by using the Moon as a planetary scale antenna. The basic idea is to deploy an array of ultra-sensitive inertial sensors on the lunar surface and measure the time fluctuations of the Moon induced by passing gravitational signals (Figure 2.11).



Figure 2.11: Star-shaped array of four LGWA stations, each equipped with cryogenic inertial sensors. The array is planned for deployment within a permanently shadowed region inside a crater near the lunar pole. A laser power-beaming system is depicted as a potential energy source for the observatory. Credit: LGWA Collaboration.

On Earth, terrestrial interferometers are limited in the low frequency regime by seismic noise and by fluctuating gravitational forces from moving masses (Newtonian noise), which prevent sensitive measurements of long-wavelength signals. LGWA can exploit the extremely low lunar seismic background and the stable environment in permanently shadowed lunar regions to operate highly sensitive inertial sensors at cryogenic temperatures [Parameswaran et al., 2025]. The baseline concept envisions a network of several stations (for example, four) arranged in a star-shaped array, each equipped with ultra-sensitive inertial sensors that monitor the Moon's normal modes and wide-band vibrations. GWs in the deci-Hertz range induce correlated displacements of the lunar surface that can be extracted from the relative signals of the array, allowing LGWA to access the frequency band roughly spanning 1 mHz to 1 Hz (Figure 2.11). This observatory will complement both terrestrial and space detectors by enabling new astrophysical investigations, such as the studies of intermediate mass and stellar mass BH populations, while also observing compact double white-dwarf binaries, which are potential progenitors of Type Ia SN, and measurements of the Hubble constant via multimessenger observations. Additionally, LGWA aims also at improve our understanding of the Moon's interior structure, its seismic and geophysical environment by analyzing how the satellite responds to an external signal [Parameswaran et al., 2025].

2.2.4 LISA

LISA is a planned European mission led by ESA, with participation from NASA, aiming to launch the first space-based GW observatory [Amaro-Seoane et al., 2017, Danzmann et al., 1996]. The mission will open the path to detecting GW signals with wavelengths too long to be observed by the current LVK network. The idea is to deploy an interferometric antenna directly in space, avoiding seismic noise, with arms long enough to be sensitive to these low-frequency signals.
The detector will consist of three spacecraft forming an equilateral triangle with sides of 2.5 million km. This configuration will orbit the Sun in an Earth-like orbit at a distance of 1 AU from the Sun and approximately 50 million km from Earth. The operating principle is similar to that of terrestrial interferometers: laser interferometry will measure the small variations in the distances between the test masses caused by passing GW, allowing LISA to determine their amplitude, strain and polarization.

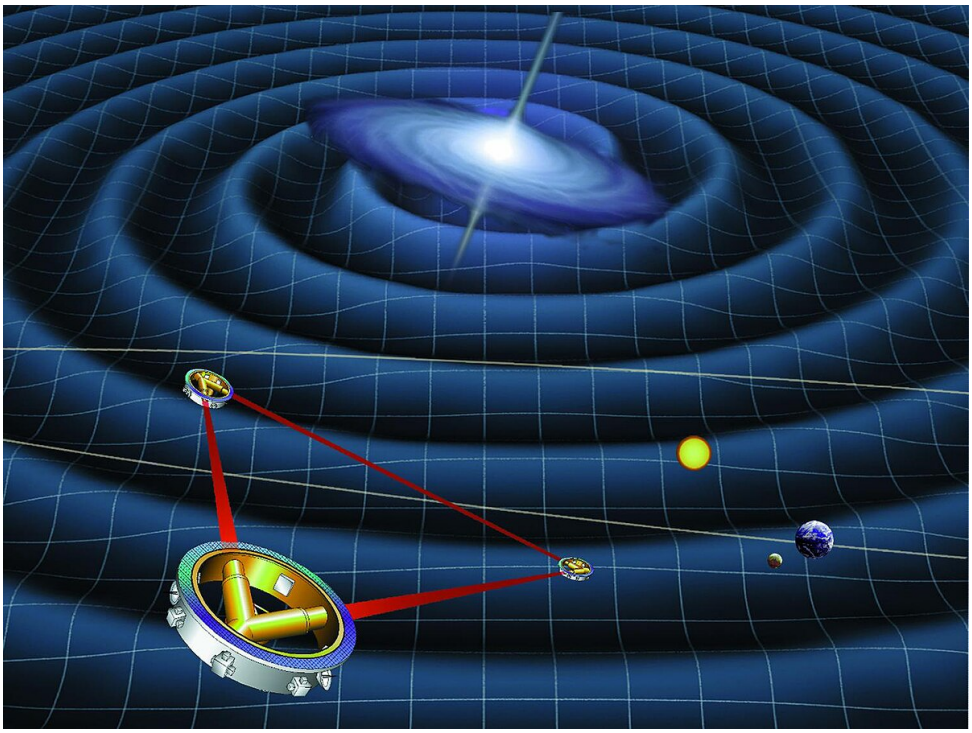


Figure 2.12: Artistic representation of LISA spacecraft. Credit: ESA.

LISA will operate in a frequency band completely complementary to ground-based detectors, from about 0.1 mHz to 0.1 Hz, enabling the observation of sources inaccessible from Earth. For example, LISA is expected to observe millions of compact stellar binaries in our Galaxy, such as white dwarf pairs. A large fraction of these Galactic binaries will be individually resolved, allowing precise determination of orbital periods, chirp masses, and distances, offering insights into binary evolution channels, including common envelope evolution and TypeIa supernova progenitors. Beyond the Galactic population, LISA will detect the inspirals and mergers of massive BBHs. These events will provide detailed information on masses, spins and luminosity distances, enabling studies of BH evolution and strong-field GR across cosmic time.
Together, these compact binary sources will allow LISA to probe astrophysical processes such as binary formation and evolution, stellar-remnant demographics, and galactic structure, as well as to contribute to cosmology through standard sirens and potentially stochastic

GW backgrounds.

Chapter 3

Electromagnetic Counterparts

In the last decade, MMA has experienced rapid growth, particularly with the advent of the GW+EM observational channel. MMA investigates astrophysical sources by combining information carried by different messengers: photons, neutrinos, cosmic rays and GWs (Figure 3.3). Each messenger can probe distinct physical processes and is generated from different evolutionary stages of the source, hence carrying unique and complementary information. When analyzed together, these signals enable a more complete reconstruction of the underlying phenomenon.

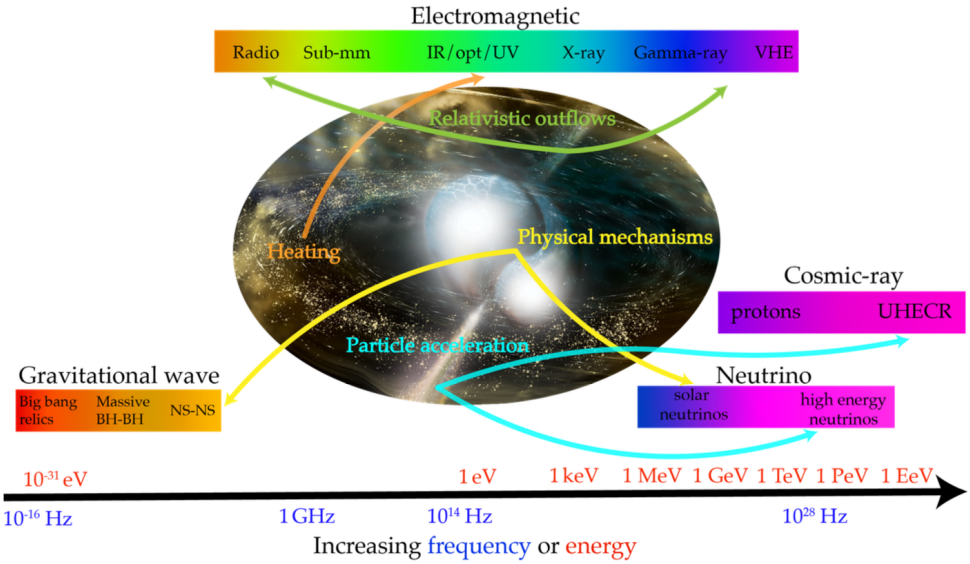


Figure 3.1: Schematic view of the different messengers that can be detected from a single event. The case presented here is a BNS coalescence [Abac et al., 2025].

The first milestone in MMA was the detection of high-energy neutrinos from the SN 1987A explosion in the Large Magellanic Cloud. A burst of 24 neutrinos was detected within a time window of $\sim$ 13 seconds by Kamiokande-II [Hirata et al., 1987], IMB [Haines et al., 1988] and Baksan [Alekseev et al., 1987], several hours before the first optical signal was observed. These detections provided direct insight into the physics of the collapsing core, confirming key predictions of core–collapse mechanism: the release of $\sim$ 99% of the gravitational binding energy in the form of neutrinos and typical neutrino energies of 10-30 MeV. Moreover, from the arrival time distribution it was possible to constraint the neutrino

mass to $m_\nu \lesssim 20\,\mathrm{eV}$. SN 1987A hence offered the first direct probe of a SN engine and demonstrated the power of neutrinos as unique diagnostics of the explosion mechanism.
Neutrinos and GWs, in fact, can probe the innermost regions of collapsing objects, providing an unaltered view of the physical conditions deep within the source at the moment of emission. EM observations alone cannot access such regions, but they are essential for localizing the source, identifying its host galaxy and characterizing the environment. For this reason, the simultaneous detection of EM, neutrino and GW signals allows a significantly more robust understanding of the source parameters and of the central engine behind the event.
A second important step in MMA occurred with the first direct detection of a GW, GW150914, by the LIGO-Virgo Collaboration, produced by the coalescence of a BBH system [Abbott et al., 2016b,a]. This moment marked the birth of GW astronomy and highlighted the potential of GWs to reveal sources inaccessible with EM surveys. To date, all confirmed GW detections originate from the coalescence of compact stellar remnants. However, theoretical models predict a broader diversity of GW sources. All these systems are associated with the final stages of massive-star evolution, as only catastrophic and strongly asymmetric processes generate detectable GW emission. Isolated NSs and CCSNe, as discussed in Chapter 1, are therefore expected to become key targets for MMA as detector sensitivity improves.
Finally, another case worth mentioning was the detection of the high-energy neutrino IceCube-170922A in 2017, with an energy of ~ 290 TeV and consistent with the flaring blazar TXS 0506+056 [Collaboration et al., 2018]. This event triggered an extensive follow-up campaign across the EM spectrum, involving Fermi-LAT, MAGIC and several radio, optical and X-ray facilities. This was the first high-confidence identification of an extra-Galactic neutrino source candidate and provided direct evidence that blazar jets can accelerate hadrons to ultrahigh energies.
In this Chapter, we review the GW events to date that have enabled or suggested the possibility of multimessenger investigations, and we discuss their expected EM counterparts. Section 3.1 outlines the main features of the EM counterparts associated with compact binary mergers, namely short GRBs and KNe. Then, Section 3.2 discusses the landmark GW170817 event and Section 3.3 summarizes the GW detections involving neutron stars during the LVK observing runs.

3.1 Electromagnetic counterparts of Binary Neutron Stars

An *EM counterpart* is generally defined as an EM signal that is spatially and temporally consistent with a GW event and physically compatible with theoretical emission models. Establishing such associations is often challenging, primarily because GW sky-localization regions can span tens to hundreds of square degrees. This necessitates large and well coordinated follow-up campaigns and the development of sophisticated selection strategies to identify real counterparts among numerous unrelated transients.
Joint EM/GW analyses can provide powerful probes of NS physics and relativistic astrophysics, enabling constraints on the NS equation of state, studies of GRB jet structure and investigations of r-process nucleosynthesis. The next generation of observatories will significantly expand the potential of MMA. For example, 3rd GW detectors will increase the detection horizon by more than an order of magnitude. Their improved sensitivity is expected to yield thousands of electromagnetically bright GW events per year, allowing population studies and a precise characterization of compact object formation and evolution [Branchesi et al., 2023]. For instance, simulations for ET indicate that the detector will

observe the early inspiral phase of compact mergers well in advance of coalescence, enabling early-warning alerts and rapid EM follow-up [Abac et al., 2025]. This will be complemented by improved sky localization: for BNS mergers, ET is expected to localize tens of events within ~ 100 deg^2 several minutes before merger [Abac et al., 2025].
The landmark GW170817 event, that we will discuss in more detail in Section 3.2, firmly established the connection between BNS mergers, sGRBs and KN. Moreover, even before direct GW detection, several cases, such as GRB 130603B, had already suggested a link between these phenomena. In this Section, we briefly discuss these two key classes of EM counterparts: GRBs and KNe.

Gamma-Ray Bursts

GRBs are one of the most extreme explosions in the universe, produced by catastrophic astrophysical events that produce collimated outflows of ultra-relativistic matter [Rees and Mészáros, 1992]. The initial emission, known as the *prompt emission*, lasts from a fraction of a second to several minutes and originates from internal dissipation within the relativistic jet, such as internal shocks [Rees and Mészáros, 1994] or magnetic reconnection [Drenkhahn, 2002]. It is typically characterized by the isotropic-equivalent energy

$$E_{\rm iso} = 4\pi d_L^2 \, \frac{f}{1+z}, \tag{3.1.1}$$

where f is the observed fluence, z the redshift and d_L the luminosity distance [Bloom et al., 2001].
Following the prompt phase, GRBs produce a long-lasting *afterglow* as the jet decelerates in the surrounding medium and emits synchrotron radiation observable from X-rays to radio frequencies [Mészáros and Rees, 1997, Sari et al., 1999]. The collimated nature of GRB jets is revealed through steep temporal breaks in their afterglow light curves. For a jet expanding in a homogeneous medium, the opening angle θ_j may be estimated as [Sari et al., 1999, Frail et al., 2001]

$$\theta_j \simeq 0.076 \left(\frac{t_j}{1\ \text{day}}\right)^{3/8} \left(\frac{1+z}{2}\right)^{-3/8} \left(\frac{n}{0.1\ \text{cm}^{-3}}\right)^{1/8} \left(\frac{E_{\rm iso}}{10^{52}\ \text{erg}}\right)^{-1/8}, \tag{3.1.2}$$

and the corresponding true, beaming-corrected gamma-ray energy is

$$E_\gamma = E_{\rm iso}(1-\cos\theta_j) \approx \frac{1}{2} E_{\rm iso}\, \theta_j^2. \tag{3.1.3}$$

GRBs have traditionally been divided into two classes based on their prompt-emission duration, quantified through the T_{90} interval: *long GRBs* ($T_{90} > 2$ s) and *short GRBs* ($T_{90} < 2$ s). Long GRBs are generally associated with the core collapse of rapidly rotating massive stars and are often accompanied by energetic broad-lined Type Ic SNe [Woosley and Heger, 2006]. However, some long GRBs, such as GRB 060614, 060505, 111005A, and 191019A, were observed without an associated bright SNe, suggesting that prompt duration alone is not always a reliable indicator of progenitor type. In contrast, sGRBs are linked to mergers of compact objects, such as BNS or NSBH systems [Eichler et al., 1989], which are also sources of the currently observed GWs [Kobayashi and Mészáros, 2003]. These mergers release jet energies of order $E_{\rm jet} \sim 10^{49}$–10^{51} erg [Fong and Berger, 2013]. As already stated before, this link between sGRBs and mergers was confirmed by the detection of GW170817 [Abbott et al., 2017, Goldstein et al., 2017, Savchenko et al., 2017], probing that at least a fraction of sGRBs originates from BNS mergers and firmly established compact

object coalescences as major sites of heavy-element production. Recently the traditional long/short dichotomy has been challenged. Two long-duration GRBs, GRB 211211A and GRB 230307A, displayed KN-like emission instead of the expected SN signatures, suggesting a compact-merger origin despite their long prompt durations [Rastinejad et al., 2022, Levan et al., 2024]. They highlighted the diversity of jet-launching conditions and demonstrate that GRB duration alone is not always a reliable indicator of the progenitor system.

Further complexity arises from the structure and geometry of GRB jets. Increasingly, observations favor *structured jets*, in which the energy and Lorentz factor smootly decrease with angle from the jet axis (like a Gaussian), rather than a uniform *top-hat* model [Mooley et al., 2018, Ghirlanda et al., 2010]. In such scenarios, the observed properties of a GRB depend strongly on the viewing angle. GRBs viewed slightly *off-axis* appear fainter and spectrally softer in gamma rays and their afterglows may emerge only once the jet decelerates and spreads into the observer's line of sight, days after the merger. These off-axis events broaden the range of detectable EM signatures from compact mergers and can reveal KN counterparts even when the prompt GRB is weak or absent. Given the limited sky-localization capability of current GW detectors, even such faint prompt signals can provide crucial temporal alerts for associating EM counterparts with GW events [Kathirgamaraju et al., 2018].

GRBs observed at *slightly off-axis* angles are then particularly important for interpreting subluminous events. For an observer at $\theta_{\rm obs} > \theta_j$, relativistic beaming strongly suppresses the prompt emission. The observed energy scales approximately as

$$E_{\rm obs} \propto \delta^3, \qquad \delta = \left[\Gamma(1 - \beta \cos\theta_{\rm obs})\right]^{-1}, \tag{3.1.4}$$

where δ is the Doppler factor and Γ the Lorentz factor. As the jet decelerates and expands sideways, the afterglow becomes visible to off-axis observers. The interpretation of subluminous GRBs as off-axis events is further constrained by relativistic compactness arguments. Matsumoto et al. [2019] generalized the compactness condition to arbitrary viewing angles and showed that, for a given observed fluence and variability timescale, the minimum Lorentz factor required to avoid $\gamma\gamma$ pair production is smallest for on-axis observers. As a consequence, the compactness condition imposes an upper limit on the viewing angle at which prompt γ-ray emission can be detected from a uniform jet. This result implies that simple top-hat jets cannot easily explain low-luminosity GRBs observed at moderate off-axis angles, strengthening the case for angular jet structure, in which the energy and Lorentz factor decrease smoothly away from the jet axis. This model reproduces the rising afterglow of GRB 170817A, that still remains the only well studied example of an off-axis sGRB. However, other candidates have been identified: GRB 150101B, for example, exhibited a low-luminosity prompt emission and an afterglow consistent with a structured jet observed at moderate viewing angles, together with a likely KN component [Troja et al., 2018]. In Chapter 4 we will present a procedure designed to identify such events from their prompt emission, in order to enhance the follow-up of potential KN-associated candidates.

Kilonovae

KNe, first theorized by Li and Paczyński [1998], are rapid thermal transients powered by the radioactive decay of heavy nuclei synthesized in the neutron-rich ejecta of BNS and NSBH mergers. The main mechanism in these environments is the rapid neutron-capture, since matter expelled during the merger presents low electron fraction (Y_e) and high neutron density sufficient to produce heavy unstable nuclei [Metzger, 2020]. As the ejecta expand

and cool, the decay products of the formed nuclei deposit energy through thermalisation, producing the emission characteristic of KNe.

Matter in a coalescence can be expelled through multiple channels [Perego et al., 2022]. In the *dynamical ejecta* scenario the ejecta is launched within a very small window, of a few milliseconds. It consists of a cold neutron-rich tidal tail, produced by strong tidal deformation and ejected mainly in the equatorial plane at $v \sim 0.1$–$0.3\,c$, with low entropy and $Y_e \sim 0.05$–0.15, and a hotter shock-driven component produced when colliding stellar cores launch shocks into the outer layers. A second major channel is the *disc-wind ejecta*, which originates in the accretion disc that forms around the merger remnant. Viscous heating, nuclear recombination, neutrino absorption and spiral-wave instabilities drive outflows from tens of milliseconds to seconds. These winds can drag ~ 10–40% of the disc mass and exhibit broad distributions in entropy and electron fraction ($Y_e \sim 0.1$–0.45), strongly depending on the lifetime of the remnant NS.

Following ejection, the matter undergoes rapid expansion and transitions into homologous flow after a few characteristic expansion times. The ejecta consist of a charge-neutral plasma of free neutrons and protons, α-particles, heavy nuclei, electrons and photons, with density dropping roughly exponentially during the first milliseconds. Initially the ejecta are opaque. Photons are therefore trapped and the emission approximates a quasi-thermal photosphere. As the ejecta expand and the density decreases, photons begin to diffuse outward and are eventually released, producing the observed KN emission. At later times, non-thermal processes become more important and the transient enters a nebular phase. The time of maximum brightness typically ranges from a few hours to several days after merger, depending on the ejecta mass, velocity and opacity.

As the ejecta expand and cool ($T \lesssim 4$–$5\,\mathrm{GK}$), conditions become suitable for r-process nucleosynthesis. Seed nuclei form during NSE freeze-out and following neutron captures drive the nuclear flow to highly neutron-rich isotopes until processes like β-decay determine the final abundances. The resulting distribution depends sensitively on the Y_e, entropy and expansion timescale. Ejecta with $Y_e \lesssim 0.2$ synthesize heavy lanthanides and actinides, while higher-Y_e outflows ($Y_e \gtrsim 0.25$) produce predominantly first-peak elements. Radioactive heating from β-decays, α-decays, and fission injects energy into the expanding plasma from seconds to weeks after the merger [Metzger et al., 2010, Metzger, 2020]. But only a fraction of this energy is thermalised. The *thermalisation efficiency* $f_{\mathrm{th}}(t)$ decreases with time as the ejecta become optically thin to γ-rays and supra-thermal particles. Charged particles thermalise efficiently during the first few days, while γ-ray thermalisation becomes ineffective within ~ 1 day. Typical values decrease from $f_{\mathrm{th}} \sim 0.6$ at one day to ~ 0.1 at ten days [Metzger, 2020]. The opacity of the ejecta, dominated by bound–bound line transitions, is extremely sensitive to composition and ionisation state. Lanthanides and actinides possess open f-shells, producing a high density of spectral lines that dramatically increase the effective opacity ($\kappa \gtrsim 10\,\mathrm{cm^2\,g^{-1}}$) compared to ejecta lacking heavy r-process elements ($\kappa \lesssim 1\,\mathrm{cm^2\,g^{-1}}$). As a result, lanthanide-poor outflows yield fast, blue KN components, while lanthanide-rich ejecta produce slower, redder emission peaking in the near-infrared [Metzger, 2020].

Analytical models assuming spherical, homologously expanding ejecta offer useful scaling relations in qualitative agreement with full radiative-transfer simulations [Perego et al., 2022]. For ejecta mass m_{ej}, mean velocity $\langle v \rangle$ and opacity κ, the peak time is approximately

$$t_{\mathrm{peak}} \approx \left(\frac{m_{\mathrm{ej}}\,\kappa}{4\pi c\,\langle v \rangle} \right)^{1/2},$$

which for $m_{\mathrm{ej}} \sim 0.01\,M_\odot$, $\kappa \sim 10\,\mathrm{cm^2\,g^{-1}}$, and $\langle v \rangle \sim 0.1c$ gives $t_{\mathrm{peak}} \sim$ a few days.

The luminosity near peak is controlled by the available radioactive heating, $L_{\rm peak} \simeq \dot{e}_{\rm nuc}(t_{\rm peak})\, f_{\rm th}(t_{\rm peak})\, m_{\rm ej}$, yielding typical near-infrared luminosities of 10^{40}–$10^{41}\,{\rm erg\,s^{-1}}$ for lanthanide-rich ejecta.

3.2 GW170817

Despite the increasing number of GW detections, only one event has so far been firmly established as a multimessenger source: the BNS coalescence of 17 August 2017. The merger GW170817 was observed at 12:41:04 UTC by the LIGO-Virgo network with a signal-to-noise ratio of 32.4 and a false-alarm rate (FAR) of less than one per 8×10^4 years (Figure 3.2) [Abbott et al., 2017]. Although Virgo's sensitivity and detector orientation limited its individual contribution to the waveform, its data were crucial in constraining the sky localization. The parameter estimation revealed component masses in the range 1.17–1.60 $M_\odot$, with a total mass of $2.74^{+0.04}_{-0.01}\,M_\odot$, consistent with neutron stars. Its luminosity distance was estimated at 40^{+8}_{-14} Mpc, and the 90% credible sky area covered approximately 28 deg^2, with a best-fit position near RA = $13^{\rm h}09^{\rm m}48^{\rm s}$ Dec = –23°22′53″ (J2000) [Abbott et al., 2017].

The pivotal point was the nearly simultaneous detection of the short GRB 170817A by the Fermi Gamma-ray Burst Monitor [Meegan et al., 2009, Goldstein et al., 2017] and *INTEGRAL* [Savchenko et al., 2017], only 1.7 seconds after the GW merger time. GRB 170817A was an intrinsically faint sGRB with $T_{90} \sim 2.48$ s and an isotropic-equivalent energy of $E_{\rm iso} \sim 10^{46}$ erg, approximately four orders of magnitude lower than typical sGRBs [Goldstein et al., 2017, Savchenko et al., 2017]. This faintness is consistent with an off-axis viewing angle of about $25 - 30°$. Multi-wavelength afterglow observations in X-ray, optical and radio enabled the reconstruction of the jet structure, revealing a narrow ultra-relativistic core surrounded by slower mildly relativistic material.

The temporal coincidence between GW and GRB detections immediately suggested a physical association, which was subsequently confirmed by an extensive worldwide follow-up campaign involving more than 70 EM observatories. The first EM observations, obtained several hours after the merger, identified a rapidly evolving optical transient, AT 2017gfo, in the galaxy NGC 4993, fully consistent with the GW localization volume [Coulter et al., 2017]. Multi-wavelength observations, spanning from the UV to the IR, were performed by all active facilities at the time, including Pan-STARRS [Kaiser et al., 2002], ESO [Smartt et al., 2017, Pian et al., 2017], DECam and the Swope Telescope. These efforts revealed a transient powered by a KN, driven by the radioactive decay of heavy nuclei synthesized via r-process nucleosynthesis in neutron-rich ejecta. This provided the first direct probe that BNS mergers are major production sites of heavy elements. AT 2017gfo remains to date the only comprehensively observed KN, with multi-band photometry and spectroscopy capturing its rapid colour evolution: an initial blue component from lighter r-process nuclei, followed by redder emission dominated by lanthanides and actinides with high opacities. The observed photometric and spectroscopic evolution matches theoretical KN models, reinforcing the link between BNS mergers and r-process nucleosynthesis. The total ejecta mass for this event was estimated to lie between 0.02 and 0.1 $M_\odot$. Spectroscopic analyses identified strontium in early spectra [Watson et al., 2019] and later evidence consistent with tellurium, directly confirming the synthesis of heavy elements.

The host galaxy, NGC 4993, was a massive lenticular system dominated by an old stellar population (≥ 1 Gyr) and showing evidence of a minor merger a few tens of millions of years ago. No underlying globular cluster was detected at the transient position, suggesting the progenitor binary originated within the field population. Host-galaxy studies thus

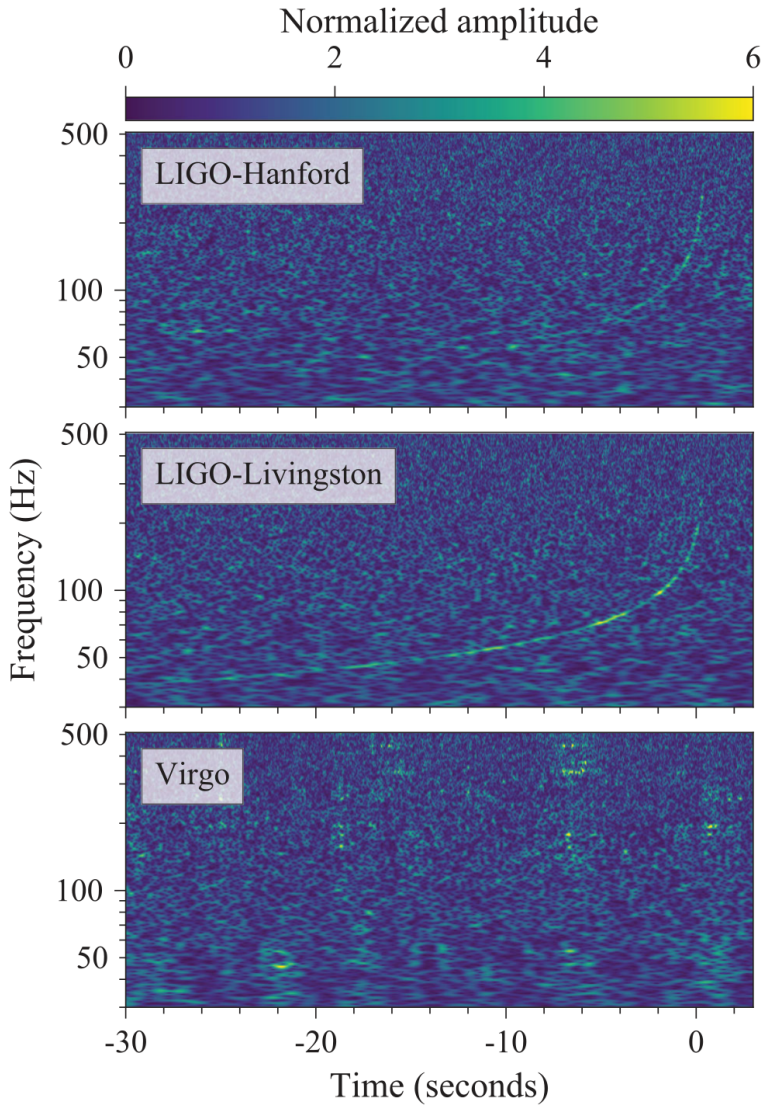


Figure 3.2: The top panel shows the GW signal observed by LIGO-Hanford, the middle panel the signal from LIGO-Livingston, and the bottom panel that from Virgo. The signal is less pronounced in the Virgo dataset due to its lower sensitivity and orientation, although its information was essential for constraining the source position. Credits: LIGO Scientific Collaboration and Virgo Collaboration.

provide constraints on BNS formation channels, natal kicks and delay-time distributions [Levan et al., 2017, Im et al., 2017, Kilpatrick et al., 2022].
The joint GW and EM observations made GW170817 the first *standard siren*, allowing an independent inference of cosmological parameters. Combining the GW-measured luminosity distance with the host galaxy redshift yielded an estimate of the Hubble constant of $H_0 = 71.9 \pm 7.1$ km s^{-1} Mpc^{-1} [245 and 247, 2017, Cantiello et al., 2018]. The delay between the GW and GRB signals allowed to contraint the speed of GWs to agree with the speed of light to within one part in 10^{15}, placing stringent limits on modified gravity theories [Langlois et al., 2018]. Furthermore, tidal deformability measurements, together with ejecta mass constraints from the KN, provided valuable information on the NS equation of state. Although no high-energy neutrinos were detected in coincidence with

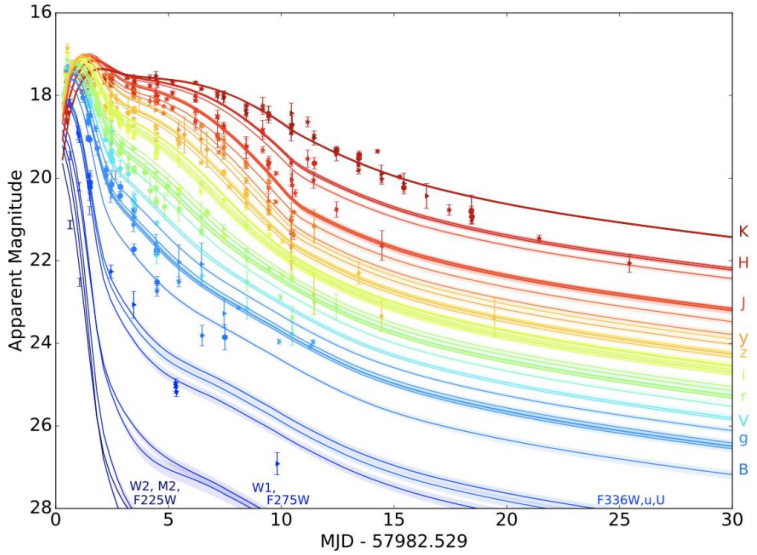


Figure 3.3: Light curves of AT2017gfo from [Villar et al., 2017].

GW170817, dedicated searches were conducted both around the merger time and during the ensuing two weeks. While current upper limits remain below the expectations of most theoretical models, a future detection of neutrinos from similar events would offer crucial insights into particle acceleration and jet physics in relativistic outflows.

3.3 Search for Electromagnetic counterpart during O4

During the O4 of the LVK Collaboration, the search for EM counterparts to compact binary mergers has been one of primary goals for both the LVK and the broader network of EM follow-up consortia. In the absence of a simultaneous clear detection of KN emission, the standard strategy consists in systematically monitoring galaxies located within the GW localization region. The major issue in the identification of a counterpart lies in the large sky map provided by the LVK Collaboration, thus a coordinate search from the follow-up teams can maximize the probability of identifying transients whose distances and early-time photometric evolution could be consistent with a merger-driven KN. The multi-wavelength follow-up relies on multiple facilities operating in high-energy and optical bands, including *Fermi*-GBM [Meegan et al., 2009], *Swift* [Burrows et al., 2005], the *Zwicky Transient Facility* (ZTF) [Bellm et al., 2018], *ATLAS* [Tonry et al., 2018], and *Pan-STARRS* [Kaiser et al., 2002]. The combined observational capability of these instruments enables rapid and deep coverage of the LVK localization regions, producing large numbers of transient candidates.
Among the candidates identified throughout O4, several events emerged as particularly significant for assessing the challenges and opportunities in optical counterpart searches. In this Section we focus on five representative cases, which together illustrate the diversity of EM follow-up scenarios encountered during the run. Special emphasis is placed on the event S250818k. Its observational dataset provides an ideal testbed for the analysis framework developed in Chapter 5, where we will present our methodology for the simulation of KN lightcurves.

- **S240422ed**, a compact binary merger event detected on 2024-04-22 at 21:35:13.417

UTC (GPS time: 1397856931.417). One of the key features of this event was its FAR of 3.13×10^{-13} Hz, a value that substantially strengthens confidence in the astrophysical origin of the trigger [LIGO/Virgo/KAGRA Collaboration, 2024]. Prompt low-latency classification reported a very high probability for a remnant (P(HasNS)> 99%) and a large probability for matter to remain outside the remnant (P(HasRemnant)> 99%), motivating rapid multi-wavelength follow-up [LIGO/Virgo/KAGRA Collaboration, 2024, EP Team at NAOC/CAS, 2024c]. A promising candidate counterpart, EP240426a, was reported by the Einstein Probe Follow-up X-ray Telescope (EP-FXT) within the LVK localization region [EP Team at NAOC/CAS, 2024b]. Swift/XRT subsequently confirmed X-ray emission consistent with the EP localization [Burrows et al., 2005]. Early near-infrared and radio searches were performed, and EP's wide-field WXT instrument provided early X-ray upper limits across the skymap [EP Team at NAOC/CAS, 2024c,a]. However, continued monitoring and archival checks revealed that the EP240426a position coincided with a previously known variable X-ray/radio source; further analysis suggested the emission is more likely associated with an active galactic nucleus or another persistent variable X-ray source than with merger ejecta [EP Team at NAOC/CAS, 2024b]. Consequently, the candidate counterpart was retracted and no convincing optical/NIR kilonova counterpart was identified despite intensive follow-up, highlighting the challenge of distinguishing true counterparts from persistent or variable X-ray sources in dense fields [EP Team at NAOC/CAS, 2024b,c].

- **S250206dm**, a compact binary merger candidate detected on 2025-02-06 at 21:25:30.439 UTC (GPS time: 1422912348.439). The online FAR was reported as 1.3×10^{-9} Hz [LIGO/Virgo/KAGRA Collaboration, 2025a], placing this trigger in a sub-threshold but follow-up-worthy regime. Preliminary classification indicated mixed probabilities among compact-binary classes, with non-negligible NSBH probability (∼55%) and BNS probability (∼37%), and a high probability for residual matter (P(HasRemnant) ∼99%), thereby justifying extensive EM searches [LIGO/Virgo/KAGRA Collaboration, 2025a]. Pan-STARRS reported a candidate transient, AT2025bbo, associated with WISEA J013717.29+454331.9 at $z \simeq 0.062$ shortly after the trigger [Pan-STARRS Collaboration / Young et al., 2025]. Follow-up spectroscopy and imaging (Gemini-North, COLIBRÍ, DDRAGO and others) showed little or no photometric evolution over the subsequent days and suggested the candidate was not a fast-evolving kilonova; the Pan-STARRS candidate AT2025bbo was eventually retracted after additional checks and spectroscopy [Pan-STARRS / Smartt et al., 2025, et al., 2025c,d]. Deep tilings with DECam and other wide-field imagers placed limits on fast blue transients in the skymap region, but no secure counterpart emerged [et al., 2025b,f]. Taken together, the data indicate no confirmed EM counterpart for S250206dm and that early optical candidates were likely unrelated or non-evolving sources rather than merger ejecta [Pan-STARRS / Smartt et al., 2025, et al., 2025c].

- **S250814bg**, a compact binary merger candidate detected on 2025-08-14 at 05:11:48 UTC (GPS time: 1427058726). The preliminary LVK notice reported a comparatively low online FAR of $\sim 1.2 \times 10^{-5}$ Hz and an initial classification with a modest NS probability ($\sim$ 35%) and remnant probability ($\sim$ 25%), which motivated rapid follow-up [LIGO/Virgo/KAGRA Collaboration, 2025b]. Both Fermi/GBM and Swift/BAT independently reported a long-duration gamma-ray burst, GRB 250814A, temporally and spatially consistent with the LVK skymap [Fermi/GBM Team, 2025, Swift/BAT Team, 2025]. This temporal/positional coincidence prompted an intensive

campaign spanning optical, X-ray and radio bands. Despite the promising association between S250814bg and GRB 250814A, no variable optical or NIR counterpart with properties expected from a nearby merger afterglow or a KN was confirmed; deep imaging and rapid follow-up yielded non-detections or sources consistent with unrelated field transients. The absence of an obvious counterpart supports scenarios in which the GRB originated from a more distant or heavily obscured explosive event whose afterglow was too faint for the follow-up facilities [LIGO/Virgo/KAGRA Collaboration, 2025b, Fermi/GBM Team, 2025, Swift/BAT Team, 2025].

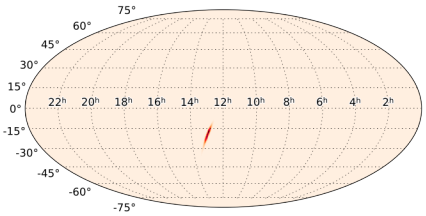
- **S250818k**, a compact binary merger candidate, was detected on 2025-08-18 at 01:20:06.030 UTC (GPS time: 1439515224.030). The prompt analysis reported a FAR of $\sim 6.8 \times 10^{-8}$ Hz and assigned a non-negligible probability to a BNS scenario ($\sim 29\%$), with the astrophysical posterior strongly suggesting the presence of a NS (P(HasNS)$> 99\%$) and significant matter remaining outside the compact remnant (P(HasRemnant)$> 99\%$) [Ligo Scientific Collaboration et al., 2025a]. Within the localization region of the event, the Zwicky Transient Facility identified an optical transient, AT2025ulz, which was initially considered a promising EM counterpart candidate. Early photometric evolution displayed rapid blue emission reminiscent of KN behavior, motivating an extensive multi-wavelength follow-up campaign involving optical facilities, near-infrared observations, Swift/XRT, radio telescopes, and the *Hubble Space Telescope*. Initial interpretations explored the possibility of a super-kilonova associated with a low-mass BNS merger [et al., 2025a,e, up Collaboration, 2025]. However, continued monitoring revealed that AT2025ulz underwent a clear rebrightening phase and developed spectroscopic features inconsistent with any KN model. A comprehensive study by the Pan-STARRS Collaboration [Collaboration, 2025], including full coverage of the sky-localization region and a detailed reconstruction of the transient's light curve, found no evidence for KN emission consistent with benchmark events such as AT 2017gfo across a large fraction of the LVK distance posterior. Instead the luminosity, rise time and spectral development matched those of a stripped-envelope Type IIb SN. Further HST observations showed that the transient remained too luminous and evolved too slowly to represent NS merger ejecta, and its colours were incompatible with KN expectations [up Collaboration, 2025]. The combined optical, infrared, and spectroscopic analyses therefore point toward an unrelated CCSN coincidentally located within the sky region of S250818k [Gillanders et al., 2025].

- **S251112cm**, compact binary-merger candidate detected on 2025-11-12 at 15:18:45.362 UTC (GPS time 1446995943.362) [Ligo Scientific Collaboration et al., 2025b] with a FAR of 5.1×10^{-9} Hz.The source classification analysis indicates a non-negligible probability of containing a sub-solar component (P(Subsolar) $\simeq 8\%$), placing S251112cm among the relatively rare candidates that may involve unusually low-mass compact objects. Given its proximity and the localization, a large multi-wavelength follow-up campaign was launched. For example, the Wide Field Survey Telescope (WFST) started observations $\sim$20.2 h after the trigger, covering 727 deg^2($\sim$64% of the 90% skymap) in g, r, i bands and continued for three nights[Liu et al., 2025]. So far, no robust EM counterpart has been confirmed for S251112cm. Gamma-ray searches by Fermi-GBM around the event time also yielded no credible GRB-like candidate [Bala et al., 2025]. Spectroscopic follow-up of transient candidates reportedly returned non-conclusive or non-transient behaviour. More detail of these events will be discussed in Chapter 5.

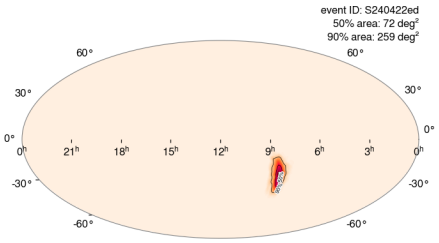
Table 3.3.1: Summary of the properties of the BNS/NSBH events presented in this Chapter, the area refers to the 90% credible region. In bold we have the only BNS event observed with a confirmed counterpart, [1] identifies the potential counterparts then retracted.

Event	Distance (Mpc)	Area (deg^2)	GRB	Optical Counterpart
GW170817	$\mathbf{40^{+8}_{-14}}$	**28**	**170817A**	**AT2017gfo**
S240422ed	188 ± 43	272	-	EP240426a[1]
S250206dm	373 ± 104	1544	-	AT2025bbo[1]
S250814bg	13504 ± 6537	7867	250814A[1]	-
S250818k	237 ± 62	786	-	AT2025ulz[1]
S241112cm	93 ± 27	1681	-	-

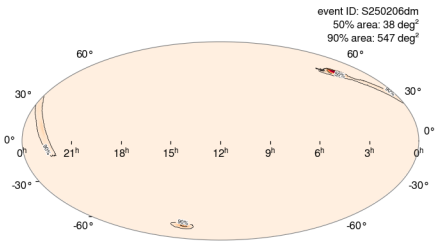
Despite the efforts carried out during O4, no confirmed KN counterpart was identified for any event. A first reason can be the distance of the GW triggers. Differently than the GW170817 event, all GW triggers lie at significantly larger luminosity distances. Moreover, the limiting magnitudes achievable by current surveys therefore introduce another problem, particularly in detecting fast blue KN components that fade on hour to day timescales. A second challenge is the large sky-localization regions. As seen in Table 3.3.1 and Figure 3.4 the GW triggers have areas of hundreds to thousands of square degrees that cannot always be fully covered during the time window when a KN is brightest. The absence of associated gamma-ray bursts for most events does not rule out the presence of a GRB or an afterglow but highlights some limitations of the current facilities. Instruments such as Fermi–GBM and Swift–BAT do not observe the entire sky at all times and a fraction of sGRBs may fall outside their instantaneous fields of view or occur during passages through regions of high background. Taken together, these factors underscore the importance of next-generation facilities with deeper limiting magnitudes, faster cadence and broader sky coverage for enhancing the detectability of EM counterparts in future observing runs.



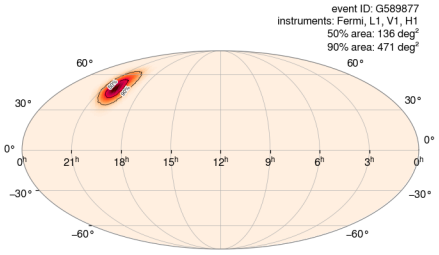
GW170817



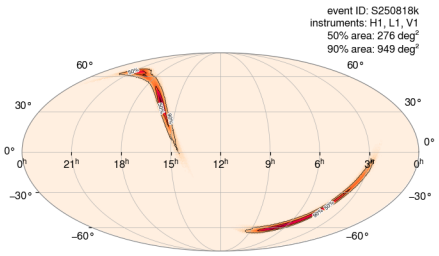
s240422ed



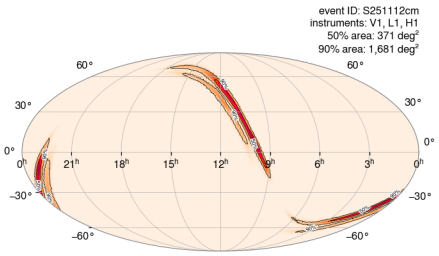
s250206dm



s250814bg



S250818k



s25112cm

Figure 3.4: Mollweide projections and distance predictions for the GW events.

Part II

Search for electromagnetic counterparts of Binary Neutron Star mergers

Chapter 4

Potential Binary Neutron Star merger events from the Fermi GBM Burst Catalog

The detection of compact binary mergers through GWs has started a new era of multi-messenger astronomy. With the second generation of GW detectors, the identification of these events has become almost routine but the majority of confirmed signals from the LVK Collaboration are coalescences of BBHs, systems believed to be essentially electromagnetically silent. On the other hand, BNS and NSBH mergers are expected not only to emit GWs, but also to produce observable EM counterparts: sGRBs and KNe. These counterparts can offer unique insights into fundamental physics, heavy-element synthesis (via the r-process) and the evolution of compact objects.
The first event GRB 170817A, associated with the GW event GW170817, definitively demonstrated this connection: a BNS merger identified through GWs, followed 1.7 s later by a sGRB, and then by a KN (AT 2017gfo) whose optical/infrared evolution signaled heavy-element synthesis [Abbott et al., 2017]. Additional promising cases such as GRB 150101B, a faint short burst in an elliptical host galaxy, with a luminous optical counterpart consistent with a kilonova and a bright X-ray afterglow, reinforce the view that sGRBs often trace compact object mergers [Troja et al., 2018]. Despite these successes, the majority of sGRBs do not yet have confirmed KN associations and many compact object mergers may go undetected in GWs.
In this Chapter we present a data-driven methodology aimed at providing an alternative channel to identify KN events, exploiting its relation with sGRBs, by isolating GRBs with characteristics similar to the known KN-associated events [1]. Specifically, we employ unsupervised clustering algorithms to classify GRBs from the Fermi GBM catalog into distinct families and to isolate events that share intrinsic properties with known KN-associated GRBs, providing a benchmark for identifying bursts that may correspond to off-axis short GRBs originating from binary neutron star mergers. Off-axis GRBs (bursts observed at larger angles from the jet axis) represent a particularly interesting class. Their prompt emission is fainter and softer, often peaking in X-rays rather than gamma-rays, and their afterglow becomes visible only after the jet slows and expands into the observer's line of

[1]The content of this chapter is adapted from Giudice, I. F., et al. (2025), "Identifying potential binary neutron star merger events from the Fermi GBM Gamma-Ray Burst Catalog," *Astronomy & Astrophysics*, 701, A83 [Giudice et al., 2025]. The results and methodology have been included here with minor modifications and additional discussion to fit the context of this dissertation.

sight. These characteristics make off-axis GRBs valuable probes for identifying KNe, as they increase the detectable population of mergers via electromagnetic emission. Moreover, given the limited localization capabilities of current GW detectors, even faint prompt signals from such GRBs may serve as a temporal link to GW events. GRB 170817A itself exhibited off-axis afterglow behavior, and GRB 150101B represents another similar case with a likely KN counterpart. While our method does not explicitly distinguish between on- and off-axis events, since the latter are usually confirmed through afterglow behavior, the clustering approach highlights GRBs that are statistically consistent with the known KN-associated population.

Our statistical, prompt-based methodology provides a rapid tool for early classification of promising GRB candidates: the algorithm is capable of determining whether a newly detected GRB falls within the cluster of interest in under two minutes, enabling timely alerts that can guide follow-up observations. Such real-time capability is crucial, as rapid identification of electromagnetic counterparts significantly increases the chances of detecting KNe and other transient signals that fade on short timescales. To enhance the astrophysical utility of this approach, we developed a dedicated pipeline for the systematic association of candidate GRBs with potential host galaxies. This pipeline integrates astrophysical and positional filters to narrow down possible host environments, particularly for relatively nearby GRBs, where galaxy catalogs can be effectively cross-matched. By prioritizing galaxies most likely to host the progenitor system, this framework increases the efficiency of targeted follow-up campaigns and improves the prospects for detecting optical counterparts such as KNe. The combined methodology, clustering-based identification of KN-like GRBs together with host galaxy association, has demonstrated effectiveness in guiding candidate selection and filtering processes. Focusing on GRBs detected by the same instrument ensures methodological consistency and reduces biases from heterogeneous datasets, ultimately improving reliability. This strategy is well-suited to the rapidly expanding multimessenger field, where the growing number of GRB detections and GW triggers demands scalable, automated tools for counterpart identification.Looking ahead, this framework could be relevant in light of forthcoming advances in GW detector sensitivity, such as those expected with the Einstein Telescope [Punturo et al., 2010], and complement the existing detectors, such as LIGO [Aasi et al., 2015], Virgo [Acernese et al., 2014] and KAGRA [Akutsu et al., 2021].

4.1 Clustering procedure

4.1.1 Pre-processing data phase

In clustering analysis is essential to pre-process data that spans a wide range of parameters in order to prevent uncertainties caused by the influence of outliers or extreme values, which can significantly impact the results of clustering analysis. The variables selected for clustering exhibit a considerable range across several orders of magnitude. In particular, the variables of fluence and E_{peak} display a high degree of variance, which has the potential to overshadow the influence of other variables in the clustering process. In order to mitigate this effect, a logarithmic transformation was applied to each feature. This transformation reduces the impact of extreme values, whilst also making the data distribution more uniform. This, in turn, facilitates the detection of patterns and improves the stability of the clustering results. After the logarithmic transformation, the data were standardized to ensure that each feature contributed equally to the clustering model. Standardization

involves rescaling each feature by using different algorithms according to the necessities of the specific case. In our methodology we relied on the *Z-score* standardization, which scale the sample to have a mean of zero and a standard deviation of one[Mohamad and Usman, 2013]. Formally, given a set of raw data, the Z-score is given by:

$$x_{ij} = Z(z_{ij}) = \frac{x_{ij} - \bar{x}_j}{\sigma_j} \tag{4.1.1}$$

where $\bar{x_j}$ and σ_j are the sample mean and standard deviation of the j feature, respectively and i indexes the individual data points within that feature. This step is particularly necessary when using distance-based clustering algorithms like K-Means, as unscaled features with high variance can disproportionately influence cluster formation. By applying z-scores, we effectively brought fluence, E_{peak} and T_{90} onto a common scale, allowing the algorithm to treat each feature with equal importance in determining cluster boundaries. Finally, we proceeded to process the sample by applying a technique for dimensionality reduction, which is essential for clustering analysis and visualizing datasets with high dimensionality. To perform this procedure we employed the Python modules `numpy` and `StandardScaler` from `sklearn.preprocessing`.

4.1.2 Dimensionality reduction

Dimensionality reduction techniques are widely employed to simplify high-dimensional datasets, reduce noise and highlight the most relevant features, making them particularly useful in clustering applications. In this study, we applied three such techniques to the processed data: t-Distributed Stochastic Neighbor Embedding (t-SNE), Principal Component Analysis (PCA) and Uniform Manifold Approximation and Projection (UMAP). While PCA, as a linear method, preserves global variance and is well-suited for linearly structured data, t-SNE and UMAP are non-linear techniques that excel in capturing local relationships and uncovering complex patterns.

High-dimensional data, such as GRB feature sets, often contain complex relationships that are difficult to analyze directly. The *curse of dimensionality* can obscure patterns, as data points tend to become equidistant in high-dimensional space, reducing the effectiveness of clustering and visualization. Dimensionality reduction mitigates these challenges by projecting the dataset into a lower-dimensional space where the underlying structures become more accessible. Applied to our GRB dataset, this approach allows the identification of groups with similar astrophysical properties, supporting their classification and enabling further investigation of correlations with phenomena such as KN associations or host galaxy characteristics. We reduced our original 3-dimensional dataset to two dimension, facilitating the interpretation of clusters and latent structures, by employing the Python modules `TSNE` from `sklearn.manifold`, `umap` and `PCA` from `sklearn.decomposition`.

t-SNE technique

The t-SNE is a non-linear method designed to enhance and resolve the limitations of the Stochastic Neighbor Embedding technique[Mohamad and Usman, 2013]. To achieve the dimensionality reduction, the initial step is to transform the high-dimensional distances between the data points into conditional probabilities that represent similarities. The resulting probability distribution will assign a higher probability to similar objects. If we consider a set of N-dimensional objects, represented by the vectors $(\bar{x}_0..., \bar{x}_i, ..., \bar{x}_N)$, the

conditional probability can be expressed as follows:

$$p_{j|i} = \frac{exp(-||x_i - x_j||^2/2\sigma_i^2)}{\sum_{k\neq i} exp(-||x_i - x_k||^2/2\sigma_i^2)} \tag{4.1.2}$$

where σ_i defines the variance of the Gaussian centerd on x_i and $p_{i|i}$ is set to 0 in order to guarantee that we are considering only pairs of datapoints. Since the aim of the t-SNE transformation is to map the dataset into a lower dimensional one, it is possible to compute again the conditional probability for the low-dimensional counterparts ($\bar{y}_0..., \bar{y}_i, ..., \bar{y}_N$), as follows:

$$q_{j|i} = \frac{exp(-||y_i - y_j||^2)}{\sum_{k\neq i} exp(-||y_i - y_k||^2)} \tag{4.1.3}$$

where $q_{i|i}$ is still set to 0. Assuming a correct transformation into the low-dimensional set we should have $p_{j|i}$ equal to $q_{j|i}$ [Mohamad and Usman, 2013]. To quantify how well the low-dimensional mapping represents the high-dimensional data structure, t-SNE minimizes the divergence between the two probability distributions, $p_{j|i}$ and $q_{j|i}$, using the Kullback-Leibler (KL) divergence. The KL divergence is given by:

$$KL(P||Q) = \sum_i \sum_j p_{j|i} log \frac{p_{j|i}}{q_{j|i}} \tag{4.1.4}$$

Here, P and Q are the joint probability distributions in the high-dimensional and low-dimensional spaces, respectively. The algorithm iteratively adjusts the positions of the low-dimensional points to minimize this divergence, ensuring that the local relationships between points in the high-dimensional space are faithfully represented in the low-dimensional embedding. A critical enhancement introduced by t-SNE is the use of a t-distribution, rather than a Gaussian, to model similarities in the low-dimensional space. The t-distribution, characterized by its heavier tails, mitigates the "crowding problem" that often arises in dimensionality reduction, where dissimilar points are artificially forced into close proximity. This adjustment ensures better preservation of the global structure by allowing distant points to remain separated while maintaining the local clustering of similar points. The perplexity parameter, a key hyperparameter in t-SNE, balances the trade-off between local and global data structure. It effectively determines the number of neighbors considered for each point in the high-dimensional space, influencing the granularity of the resulting clusters. Lower perplexity values emphasize finer structures, while higher values capture broader, more general trends in the data.

Principal Component Analysis

PCA is a widely utilised linear technique for dimensionality reduction. The method identifies new orthogonal components, known as principal components, which correspond to directions in the feature space that maximize the variance of the data [Maćkiewicz and Ratajczak, 1993]. These principal components are defined as new uncorrelated variables, which are derived from the linear combination of the initial components. The procedure begins with the computation of the covariance matrix of the dataset, which captures the correlations between features. If we consider a dataset ($X = x_0..., x_i, ..., x_N$), the covariance matrix is defined as follows:

$$\Sigma = \big(\mathrm{Cov}(x_i, x_j)\big)_{i,j=1}^{N} = \begin{bmatrix} \mathrm{Cov}(x_1, x_1) & \mathrm{Cov}(x_1, x_2) & \cdots & \mathrm{Cov}(x_1, x_N) \\ \mathrm{Cov}(x_2, x_1) & \mathrm{Cov}(x_2, x_2) & \cdots & \mathrm{Cov}(x_2, x_N) \\ \vdots & \vdots & \ddots & \vdots \\ \mathrm{Cov}(x_N, x_1) & \mathrm{Cov}(x_N, x_2) & \cdots & \mathrm{Cov}(x_N, x_N) \end{bmatrix}.$$

Since the covariance of a variable with itself is equivalent to the variance, by performing an eigenvalue decomposition of this matrix, we can identify the directions in the feature space along which the data exhibit the largest variance. In other words, the eigenvectors of Σ define a new orthogonal basis of the feature space, the *principal components*, while the corresponding eigenvalues quantify the amount of variance captured by each of these directions.
More formally, for a dataset X with zero mean, the sample covariance matrix can be expressed as

$$C = \frac{1}{n-1} X^T X, \tag{4.1.5}$$

where n is the number of observations. Solving the eigenvalue problem

$$Cw = \lambda w, \tag{4.1.6}$$

yields a set of eigenvectors w (principal directions) and eigenvalues λ (variances along those directions). Ordering the eigenvalues from largest to smallest ranks the principal components by the proportion of total variance they explain. By selecting the k eigenvectors associated with the largest eigenvalues and projecting the original data onto these directions,

$$Z = XW_k, \tag{4.1.7}$$

we obtain a k-dimensional representation that retains the dominant structure of the dataset while discarding less informative directions. This reduced representation simplifies subsequent analyses by mitigating noise and correlations between features, and often reveals patterns or groupings that are hidden in the original high-dimensional space.

Uniform Manifold Approximation and Projection

UMAP is a non-linear dimensionality reduction technique based on Riemann geometry, manifold learning and topological data analysis [McInnes et al., 2018]. Its focus is the construction of a weighted k-nearest neighbor (k-NN) graph to capture the local topological structure of the data, providing a more understandable embedding in low-dimensional space.
The first step in UMAP is to build a *fuzzy simplicial set* from the high-dimensional dataset. For each data point x_i, UMAP computes a distance-dependent probability of correlation to its neighbors x_j, defined as:

$$\mu_{ij} = \exp\left(-\frac{\max(0, d(x_i, x_j) - \rho_i)}{\sigma_i}\right), \tag{4.1.8}$$

where $d(x_i, x_j)$ is the distance between x_i and x_j, ρ_i ensures local connectivity and σ_i is a normalization factor [McInnes et al., 2018].
In the low-dimensional embedding, UMAP constructs an analogous fuzzy simplicial set using a simpler function of the Euclidean distance. The algorithm then minimizes the *cross-entropy* between the high- and low-dimensional fuzzy sets via stochastic gradient descent. The cross-entropy quantifies the divergence between the neighborhood probabilities in the original space and those in the embedding, minimizing it drives the low-dimensional representation to reproduce the high-dimensional connectivity structure as closely as possible. Formally the cross-entropy is defined as

$$\mathrm{CE}(P, Q) = -\sum_{i,j} \left[P_{ij} \log Q_{ij} + (1 - P_{ij}) \log (1 - Q_{ij})\right], \tag{4.1.9}$$

where P_{ij} is the relationship strength between points i and j in the high-dimensional space, Q_{ij} is the corresponding value in the low-dimensional space and the second term accounts for non-neighbor relationships. This optimization preserves both local neighborhoods and larger-scale topological structure. UMAP behavior is then governed by two main hyperparameters:

- the number of neighbors ($n_{\text{neighbors}}$), which controls the balance between local and global structure;
- the minimum distance (min_{dist}), which regulates how tightly points are packed in the embedding. Low min_{dist} values produce denser clusters, whereas higher values preserve broader structures.

Compared to PCA, UMAP is capable of uncovering non-linear manifolds in the data, and compared to t-SNE it provides superior preservation of global relationships and scales more efficiently with large datasets .

4.1.3 K-Means algorithm

To uncover patterns within the Fermi GBM catalog, we employed the K-Means clustering algorithm, an unsupervised machine learning technique widely used for identifying underlying structures in complex datasets. K-Means is particularly effective for segmenting data into k clusters based on shared characteristics, which in our analysis include $fluence$, t_{90} and E_{peak}. By grouping GRBs based on these parameters, K-Means facilitates the classification of GRB candidates into distinct categories, potentially reflecting different astrophysical mechanisms or populations.

The K-Means algorithm operates by minimizing the within-cluster sum of squares (WCSS), a measure of the variance within each cluster. Initially, k centroids are selected and each data point is assigned to the nearest centroid. The algorithm then iteratively updates the centroid positions by calculating the mean of all points assigned to each cluster, reassigns points to the nearest updated centroid, and repeats this process until the cluster assignments stabilize. This iterative refinement is computationally efficient and converges quickly for well-separated clusters, making it a robust choice for clustering high-dimensional datasets [Lloyd, 1982].

For our analysis, we implemented K-Means with several enhancements to improve stability and ensure robust clustering results. The initial centroids were selected using random initialization, which, while computationally straightforward, introduces variability in the clustering outcomes due to the random selection of starting points. To address this, we set the parameter $n_{\text{init}} = 1000$, instructing the algorithm to perform 1000 independent runs with different random initializations. The best solution, as determined by the lowest WCSS, was then retained. This approach significantly reduces the likelihood of convergence to a suboptimal local minimum, enhancing the reliability of the clustering results.

The maximum number of iterations for centroid updates was set to $n_{\text{iter}} = 10000$, ensuring that the algorithm had ample opportunity to refine cluster assignments even for complex datasets. Additionally, we specified a convergence tolerance of tol $= 10^{-1}$, meaning the algorithm terminated when changes in WCSS across iterations fell below this threshold. This parameter strikes a balance between computational efficiency and precision, allowing for meaningful convergence without excessive iteration.

4.2 GRB sample

The selected sample for this study is the Fermi Gamma-ray Burst Monitor (GBM) Burst Catalog ([Von Kienlin et al., 2014], [Gruber et al., 2014], [Von Kienlin et al., 2020], [Bhat et al., 2016]),the dataset encompassing all the GRBs detected by the Fermi spacecraft [Meegan et al., 2009, Connaughton et al., 2015]. The GBM consists of 14 scintillation detectors: 12 sodium iodide (NaI) detectors sensitive to the low-energy range of 8 keV to 1 MeV and two bismuth germanate (BGO) detectors covering the high-energy range from 200 keV to 40 MeV. The NaI detectors are positioned in a strategic configuration around the spacecraft, with varying orientations, in order to achieve optimal sensitivity and a broad field of view. The cosine-like angular response enables the precise localisation of GRB sources through the comparison of detection rates from different viewing angles. The two BGO detectors, situated on opposing sides of the spacecraft, guarantee comprehensive coverage of the entire sky, ensuring that all positions can be observed by at least one BGO detector. This configuration, coupled with the GBM's extensive field of view and continuous monitoring of the sky, has facilitated the collection of a substantial sample of GRB events, with the instrument detecting transient phenomena at an average rate of approximately two events per day. Since commencing operations in July 2008, the catalog has recorded over 3,000 GRB triggers, each carefully classified and documented for in-depth analysis. A landmark achievement of the GBM was its role in the detection of GRB 170817A, linked to the GW event GW170817, a breakthrough moment in MMA [Abbott et al., 2017].

The data were retrieved in January 2025 and our final dataset consisted in 3917 GRBs, including both long and short events. The analysis of the complete array of GRB events ensures the identification of underlying patterns while refining the search for sGRBs candidates linked to KNe. The parameters chosen to categorize GRBs are *fluence*, peak energy (E_{peak}) and duration (T_{90}), as they reflect the bursts energy output and temporal behavior, essential for interpreting GRB progenitors and host environments [Berger, 2014]. The T_{90}, or the time over which 90% of the GRB's gamma-ray energy is emitted, serves as a key criterion for differentiating between short and long GRBs, where the former is more strongly associated with compact object mergers [Kouveliotou et al., 1993]. *Fluence* (representing the total energy per unit area) and E_{peak}, the peak energy of the gamma-ray spectrum, offer essential information on the burst energetics and spectral shape, both of which can reveal whether the burst is observed off-axis. Although these parameters alone cannot reliably differentiate between progenitor types (e.g., BNS, NSBH, or NSWD mergers), they are sufficient for characterizing individual bursts and identifying subgroups that share similar prompt emission characteristics. Following this parameter selection our database was reduced to a subset of 3585 GRBs.

Table 4.2.1: Selected parameters of the GRBs with confirmed association to a KN.

	fluence (10^{-7} erg/cm^2)	E*peak* (keV)	T90 (s)
170817A	2.79±0.17	215±56	2.48±0.47
150101B	0.76 ±0.11	208±109	0.48±0.10

4.3 Cluster number selection

The determination of an appropriate number of clusters, denoted as n_{cluster}, is a pivotal aspect of any clustering analysis, as it directly impacts both the interpretability and the scientific reliability of the results. Since the K-Means algorithm does not intrinsically provide an optimal cluster count, a comprehensive evaluation was performed using two well-established clustering quality metrics: the Silhouette score [Rousseeuw, 1987] and the Davies–Bouldin Index (DBI)[Davies and Bouldin, 1979]. These evaluations were conducted across the three dimensionality reduction techniques for values of n_{cluster} ranging from 2 to 8. The Silhouette score quantifies the coherence and separation of clusters by measuring how similar a given data point is to its own cluster compared to others. It yields values between -1 and 1, where a higher score reflects more compact and well-separated clusters. As a result, this metric is particularly useful for identifying the configuration in which cluster boundaries are most distinct. Conversely, the Davies–Bouldin Index evaluates the average similarity between each cluster and its most similar counterpart. It is calculated as the ratio between intra-cluster dispersion and inter-cluster separation, with lower values indicating better-defined clustering structures. For this analysis, the Silhouette and DBI computations were implemented using the `silhouette_score` and `davies_bouldin_score` modules from the `sklearn.metrics` Python package. A summary of clustering performance across all techniques and cluster numbers is presented in Table 4.3.1. Notably, each dimensionality reduction method displayed varying performance, reflecting the importance of considering multiple perspectives when determining n_{cluster}. UMAP and t-SNE generally exhibited higher Silhouette scores, while PCA yielded comparatively lower values, although still within a reasonable range for interpretative analysis. While lower values of n_{cluster} (such as 2 or 3) may yield better metric scores, they risk oversimplifying the structure of the data, particularly in a dataset focused on GRBs with potentially diverse merger-related origins. On the other hand, higher values (up to 8) allow for the exploration of finer substructures that might correspond to variations in astrophysical properties such as host galaxy environments or spatial offsets. Ultimately, configurations with n_{cluster} values of 4 and 5 emerged as strong candidates, achieving favorable Silhouette and DBI scores across all three dimensionality reduction methods. The final decision to adopt $n_{\text{cluster}} = 5$ was guided by further empirical assessment. At this value, the resulting clusters were more distinct and internally consistent, facilitating clearer interpretation and improved categorization of individual GRBs. Furthermore, this choice did not compromise the integrity of the analysis: the key reference events, GRB 170817A and GRB 150101B, consistently co-located within the same cluster for both $n_{\text{cluster}} = 4$ and 5. This ensures that the clustering preserves essential scientific information, while also enhancing the resolution of potential subgroups within the population.

This choice is also consistent with a number of earlier investigations that reported a five-cluster structure in GRB populations, despite differences in instruments, parameters and clustering strategies. For example, [Acuner and Ryde, 2018] analyzed the Fermi GBM catalog using spectral features (including E_{peak}, fluence and T_{90}) and Gaussian Mixture Models, identifying five statistically significant groups that were linked to distinct emission mechanisms. Similar conclusions were reached by [Misra et al., 2023] and [Misra et al., 2024], who employed PCA and t-SNE on Swift/BAT and Fermi GBM data, respectively, and showed that two of the resulting clusters aligned with GRBs known to be associated with kilonovae. Likewise, [Chattopadhyay and Maitra, 2017] examined the BATSE dataset with both K-Means and Gaussian Mixture Models, again recovering five clusters and attributing

Table 4.3.1: Comparison of clustering scores across PCA, t-SNE and UMAP.

Method	DBI	Silhouette	n_{cluster}
t-SNE	1.00	0.39	2
t-SNE	0.84	0.42	3
t-SNE	0.79	0.42	4
t-SNE	0.79	0.42	5
t-SNE	0.83	0.40	6
t-SNE	0.83	0.41	7
t-SNE	0.83	0.40	8
PCA	0.83	0.39	2
PCA	0.92	0.37	3
PCA	0.72	0.37	4
PCA	0.74	0.36	5
PCA	0.75	0.36	6
PCA	0.82	0.33	7
PCA	0.83	0.33	8
UMAP	0.88	0.44	2
UMAP	0.82	0.44	3
UMAP	0.83	0.42	4
UMAP	0.72	0.45	5
UMAP	0.76	0.43	6
UMAP	0.78	0.42	7
UMAP	0.80	0.42	8

the separation primarily to burst energetics and duration. Collectively, these independent studies provide converging evidence that a five-cluster framework is not dataset-specific but rather a recurring and physically meaningful description of GRB diversity.

To further evaluate the robustness of our selected clustering configuration, we conducted a comparative analysis using an alternative unsupervised method: DBSCAN. Unlike K-Means, DBSCAN does not require specifying the number of clusters a priori and instead identifies clusters based on density. This makes it an effective method to cross-validate whether the structure captured by K-Means is intrinsic to the data. We applied DBSCAN using the `DBSCAN` class from `sklearn.cluster` to the same three dimensionality reduction outputs. The resulting cluster assignments were compared to those from K-Means using two standard agreement metrics: Adjusted Rand Index (ARI) and Normalized Mutual Information (NMI). Both ARI and NMI assess the similarity between different clustering results: ARI accounts for chance agreement while NMI measures the mutual dependence between clusterings. Higher values in both metrics indicate stronger agreement. Table 4.3.2 shows that for $n_{cluster} = 5$, the ARI and NMI scores were consistently higher, particularly for UMAP and t-SNE, compared to $n_{cluster} = 4$. This observation further supports our decision to use five clusters, as it suggests that this configuration not only produces well-separated clusters but also exhibits consistency across fundamentally different clustering algorithms. In summary, the selection of $n_{cluster} = 5$ is supported by both internal clustering quality metrics (Silhouette score and DBI) and external validation against an alternative algorithm (DBSCAN) using ARI and NMI. This multi-faceted validation framework ensures that our clustering configuration is not only optimal in terms of structure and separation but also robust across different methodological approaches.

Table 4.3.2: Comparison of clustering performance scores between DBSCAN and K-Means for $n_{cluster} = 4$ and 5, across dimensionality reduction techniques PCA, t-SNE and UMAP.

Method	ARI	NMI	$n_{cluster}$
t-SNE	0.06	0.43	4
t-SNE	0.09	0.48	5
PCA	0.002	0.008	4
PCA	0.0008	0.006	5
UMAP	0.05	0.39	4
UMAP	0.06	0.44	5

4.4 Clustering results and merger-associated GRB Sample

To investigate GRBs potentially associated with KNe, we applied the machine learning-based clustering approach described above to the Fermi GBM dataset. We first employed the three dimensionality reduction techniques combined with K-Means clustering (see Figure 4.1) and a first interesting result is that GRB 150101B and GRB 170817A consistently appear within the same cluster across all dimensionality reduction methods, reinforcing the reliability of our approach. From the previous discussion on the metric scores, we found that the UMAP + K-Means combination performed best in identifying five distinct GRB subpopulations. Therefore, the results discussed below refer specifically to this combination. Each cluster was characterized by consistent values of T90, fluence and E*peak*, providing a statistical separation of the dataset based on the physical properties of the bursts. The full distributions of cluster parameters are provided in Appendix B.1. Among the five clusters, Cluster 2 emerged as the most promising candidate subpopulation for merger-associated GRBs, as it contains both reference events and displays intrinsic properties consistent with compact binary merger origins. The cluster properties and ranges are summarized in Table 4.4.2, while Table 4.4.1 reports the centroids of all clusters, mapped back to the original three-dimensional space for easier physical interpretation. Notably, the centroid of Cluster 2 aligns with the typical characteristics of short GRBs, whereas the other clusters largely represent long GRBs. The centroid E*peak* value is relatively high, reflecting a mixture of on-axis and off-axis events. For example, GRB 170817A, 150101B and 160821B display lower E*peak* values characteristic of off-axis sGRBs, while highly energetic bursts such as GRB 090510 contribute to the average, demonstrating that off-axis events are represented within this population.

Table 4.4.1: Centroid properties of the five clusters in original three-dimensional space. n denotes the number of elements in each cluster.

	Fluence (10^{-6} erg/cm^2)	E*peak* (keV)	T90 (s)	n
Cluster 1	19.75	186.60	51.72	914
Cluster 2	0.40	596.53	0.79	657
Cluster 3	1.19	86.78	8.34	695
Cluster 4	3.87	380.57	24.83	621
Cluster 5	3.92	65.29	36.00	698

To further analyze Cluster 2, we compared its consistency with the sGRB catalog from [Fong et al., 2022], restricting the analysis to Fermi-detected events. Most sGRBs in this catalog

Table 4.4.2: Cluster 2 parameter ranges and centroid values, including potential off-axis sGRBs.

	Fluence (10^{-6} erg/cm^2)	E*peak* (MeV)	T90 (s)
lower limit	0.005	0.007	0.008
upper limit	11.1 $\times 10^{-5}$	1.17 $\times 10^{14}$	90.11
centroid	0.40	596.53	0.79

fall within Cluster 2, reinforcing its identification as a merger-associated subpopulation. A few sGRBs, such as GRB 211211A, are found in other clusters, highlighting the diversity of KN-associated GRBs (Figure 4.2). Two GRBs outside Cluster 2, 170728B and 151229A, have longer observed durations in Fermi GBM than typical sGRBs, although Swift/BAT measurements classify them as short, reflecting instrumental differences. This also suggests that T_{90} is likely the primary driver distinguishing merger-like GRBs from collapsars, supported by the exclusion of GRB 200826A, which, despite its short duration (0.5 s), shows collapsar-like properties such as soft energetics, compliance with the Amati relation, and an optical/NIR bump associated with a SN. Following the identification of Cluster 2, we applied an additional filtering step to select GRBs with error radius ≤ 0.1 degrees. This refinement enhances localization accuracy, which is critical for associating bursts with host galaxies and potential optical counterparts. By applying this filter post-clustering, we avoid biases arising from instrumental variations in redshift or afterglow detection. This procedure reduced Cluster 2 from 657 to 75 GRBs, allowing the identification of a "gold" sample of nine events with both X-ray afterglows and reliable redshift measurements, including the reference bursts GRB 150101B and 170817A (Table 4.4.3):

- GRB 080905A, observed in a region with low star formation and far from the galactic center of its host, showed no associated SN but enabled the detection of a faint afterglow within its host galaxy at redshift $z = 0.122$ [Nicuesa Guelbenzu et al., 2021]. The environmental conditions make a massive star progenitor unlikely, consistent with typical sGRB environments [Rowlinson et al., 2010]. Moreover, its optical counterpart resembled a standard afterglow model, although the steep early X-ray decay and absence of X-ray detections beyond 1,000 seconds suggest a limited late-time afterglow, potentially allowing for faint kilonova contributions.

- GRB 090510A was an energetic event, also detected by Fermi-LAT [Ackermann et al., 2010]. The Nordic Optical Telescope observation [Olofsson, 2009] facilitated its immediate association with the host galaxy, s a late-type galaxy at $z = 0.903$ [Rau et al., 2009]. The burst exhibited key properties, including duration, environment and spectral hardnes, consistent with a compact-object merger origin [Ghirlanda et al., 2010, Ruffini et al., 2016]. Then Swift XRT observations (0.3–10 keV) also revealed non-thermal X-ray emission, a weak precursor and GeV-range emission, features aligning with expected kilonova-powered burst signatures.

- GRB 160821B showed one of the best-sampled afterglows, supported by a complete multi-wavelength dataset including X-ray, optical and radio observations [Lamb et al., 2019]. The KN component, identified via excess red and near-infrared emission in the days following the burst, matches models of neutron star mergers ejecting neutron-rich material. The burst's environment and characteristics support a compact binary merger origin, consistent with other sGRBs associated with kilonova emissions [Troja

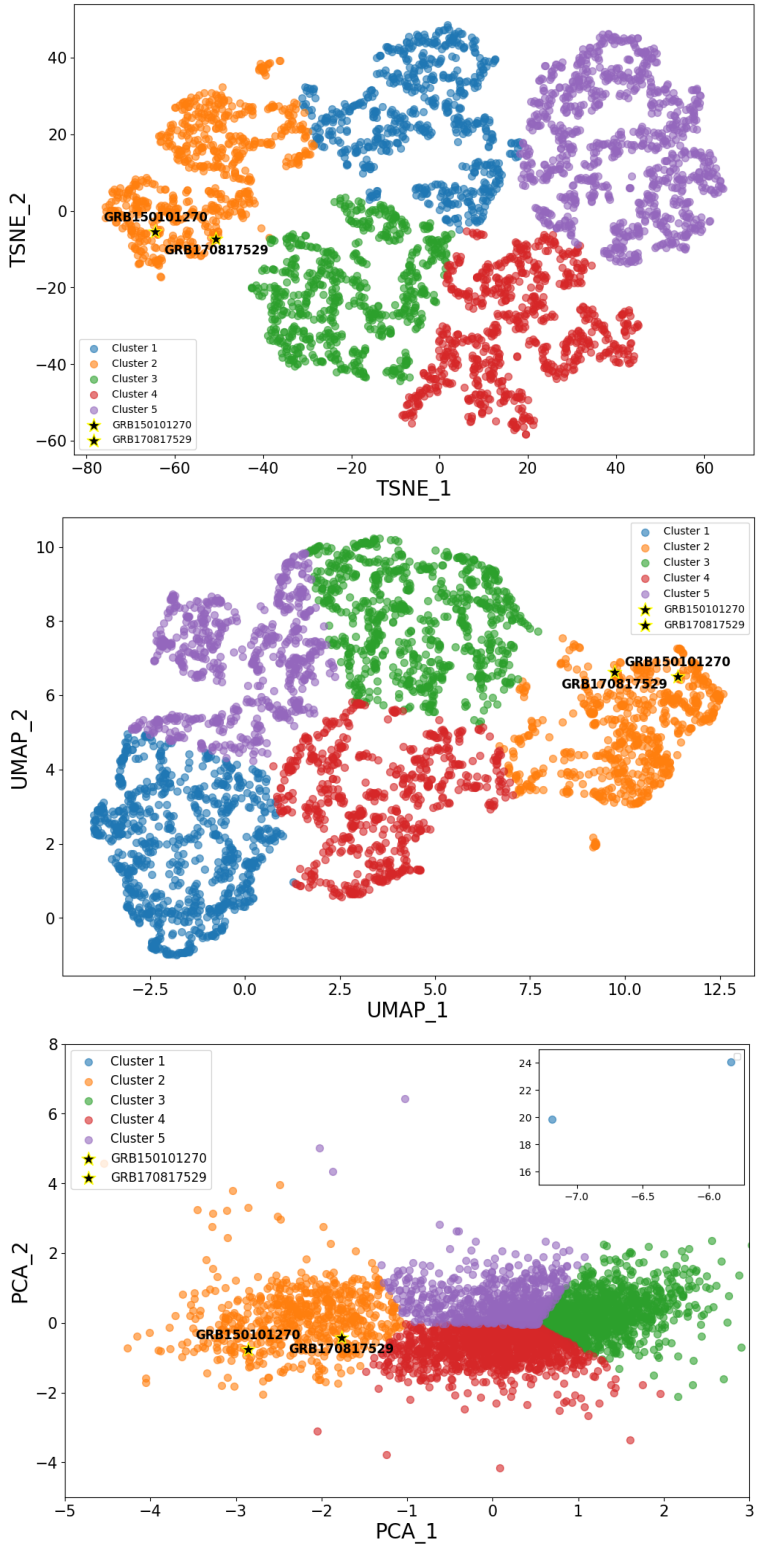


Figure 4.1: Clustering results for $n = 5$ using t-SNE (top), UMAP (middle) and PCA (bottom). Black stars highlight GRB 150101B and GRB 170817A.

et al., 2019].

- GRB 210323A was a short-hard burst featuring a long-lasting X-ray plateau of

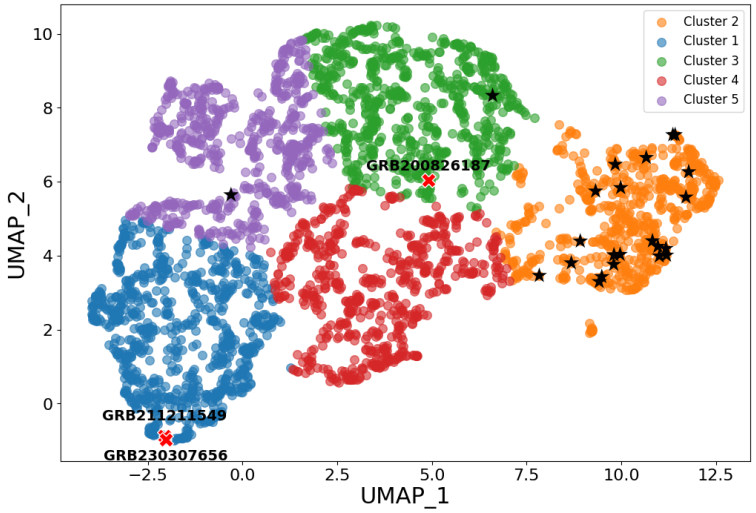


Figure 4.2: Comparison of clustering results with sGRBs from [Fong et al., 2022], marked as black stars. GRB 200826A (collapsar) is highlighted in red, as well as long-duration KNe-associated GRBs GRB 211211A and GRB 230307A.

approximately 10^4 s, followed by rapid decay. Although no optical counterpart was detected, [Shan et al., 2024] proposed that a supra-massive magnetar, formed after the merger of two neutron stars, could have powered the event. The extended plateau emission, followed by a sharp decline, is consistent with models of energy injection from a supra-massive neutron star that eventually collapses into a black hole.

- GRB 090927, 131004A and 191031D, all lacked supernova associations, although progenitor classification remains uncertain.

Table 4.4.3: Properties of the gold sample GRBs, including reference and promising merger candidates. Note: [a] Fermi GBM; [b] Swift/BAT; [c] photometric redshift from [O'Connor et al., 2022]; [d] photometric redshift from [Nugent et al., 2024]; [e] distances computed using `Planck18` cosmology.

	t90[a] (s)	fluence[a] (10^{-7} erg/cm^2)	E*peak*[a] (keV)	t90[b] (s)	fluence[b] (10^{-7} erg/cm^2)	E*peak*[b] (ph/cm^2/s)	redshift	distance[e] (Mpc)
080905A	0.96±0.35	8.50±0.46	317.17±52.54	1	1.4±0.2	1.3±0.2	0.122	524.86
090510	0.96±0.14	33.7±0.41	4248.14±440.05	0.3	3.4±0.4	9.7±1.1	0.903	3147.53
090927	0.512±0.231	3.03±0.18	195.22±69.05	2.2	2.0±0.3	2.0±0.3	1.37	4224.11
131004A	1.15±0.59	5.10±0.19	118.12±24.42	1.54	2.8±0.2	3.4±0.2	0.71	26608.86
150101B	0.48±0.10	0.76±0.11	208.18±109.55	0.02	0.23±0.06	-	0.134	574.32
170817A	2.48±0.47	2.79±0.17	214.70±56.59	-	-	-	0.009	39.79
160821B	1.09±0.98	1.95±0.2	38.17±27.48	0.48	1.0±0.1	1.7±0.2	0.161	685.88
191031D	0.25±0.02	39.68±0.15	681.54±32.55	0.29	4.1±0.4	4.3±0.4	0.5[c]	1946.42
210323A	0.96±0.78	10.92±0.30	1440.78±339.89	1.12	2.4±0.3	2.9±0.3	0.733[d]	2676.40

To assess the reliability of our selection approach, we compared our findings with the sample of KN candidates compiled by Troja et al. (2023) [Troja, 2023] in their review of Swift-detected GRBs (Figure 4.4.4).
Launched in 2004, Swift is a multi-wavelength observatory equipped with the Burst Alert Telescope (BAT) [Barthelmy et al., 2005], which operates in the 15–150 keV range and primarily targets GRBs at lower energies. In contrast, Fermi-GBM spans a wider energy range, from 8 keV to 40 MeV, making it more responsive to high-energy gamma-ray emissions.

Table 4.4.4: Group 1 GRBs from [Troja, 2023].

GRB	Redshift	Type	Presence in Cluster 2
051221A	0.5464	Afterglow dominated	No
070724A	0.4571	Dust obscured	No
080905A	0.1218	Possible KN	Yes
130603B	0.3565	Candidate KN	No
140903A	0.3510	Afterglow dominated	No
150101B	0.1341	Candidate KN	Yes
160821B	0.1613	Candidate KN	Yes
170428A	0.4540	Afterglow dominated	No
200522A	0.5541	Afterglow dominated	No

Swift's additional instruments, the X-Ray Telescope (XRT) [Burrows et al., 2005] and the Ultraviolet/Optical Telescope (UVOT) [Roming et al., 2005], allow for accurate afterglow localization and multi-wavelength follow-up. This combination of capabilities makes Swift an essential tool for detecting GRBs and their associated counterparts. We observed that all three GRBs identified by [Troja, 2023] as prime KN candidates (Group 1) that were also observed by Fermi appear in our cluster. These events are distinguished by well-established host galaxy associations, reliable redshift measurements and optical/near-infrared (nIR) excesses consistent with KN emission above the non-thermal afterglow. Of the nine GRBs in Group 1, those missing from our analysis were either not detected by Fermi or occurred before its operational period. Identifying the same candidates with Fermi, an instrument with different energy coverage and detection properties, reinforces the robustness of our clustering method.

While our study primarily focuses on short GRBs, two long-duration KN-associated GRBs, GRB 211211A [Rastinejad et al., 2022, Troja et al., 2022] and GRB 230307A [Levan et al., 2024, Dichiara et al., 2023], associated with KN events and detected by Fermi, were assigned to Cluster 1 (key parameters in Table 4.4.5). Their durations exceed 2 s, indicating potential on-axis emission or distinct physical mechanisms. Their clustering together suggests a possible similarity in origin, highlighting the complexity of KN-associated GRBs and the limitations of a simple short-long classification. Investigating these events may reveal additional subpopulations of merger-driven GRBs and improve our understanding of their progenitors. In conclusion, our integrated clustering and filtering approach robustly

Table 4.4.5: Cluster 1 key parameters, including long-duration KNe-associated GRBs.

	Fluence (10^{-6} erg/cm^2)	E*peak* (keV)	T90 (s)
lower limit	3.59	38.10	2.69
upper limit	3147.5	1936.72	478.24
centroid	19.75	186.60	51.72

identifies GRBs with properties consistent with compact binary mergers, confirming the validity of the five-cluster framework and highlighting a reproducible methodology for constructing merger-associated GRB samples. Comparison with Swift-detected KN

candidates further and in the future with Einstein Probe [Yuan et al., 2022] and SVOM [Atteia et al., 2022] events will demonstrate the complementarity of multi-instrument observations.

4.5 Host galaxy association procedure

Following the detection of a GRB, it is crucial to identify potential host galaxies promptly in order to initiate an efficient follow-up process and, ideally, to detect counterparts. In the case of off-axis sGRBs, such as those that have been shown to be consistently associated with a KN, it is expected that these events occur on smaller cosmological distances, due to the lowest intensity of their flux. However, given the substantial error map of the Fermi detector, it may be challenging to promptly impose constraints on the host galaxy, thereby limiting the potential for follow-up observations. To facilitate this process, we developed a pipeline to systematically associate candidate GRBs with likely host galaxies, assuming the GRB occurs within a relatively nearby volume of the Universe, as was the case for GRB 170817A.
We utilized the NED Local Volume Sample (LVS) Extragalactic Database [Cook et al., 2023], which was subjected to a thorough filtering process to select viable candidates. The NED-LVS is a specific subset of the NED-GWF Catalog, initially created for GW follow-up studies. One significant advantage of the NED-LVS Catalog is its comprehensive nature. Compared to other catalogs like HECATE [Kovlakas et al., 2021] and GLADE+ [Dálya et al., 2018], which are complete over smaller volumes, the NED-LVS achieves a notable level of completeness within a volume of 80 Mpc. The catalog comprises approximately 1.9 million galaxies located within a distance of 1000 Mpc, alongside their associated physical properties, including star formation rate (SFR) and stellar mass ($M_\odot$) [Cook et al., 2023].

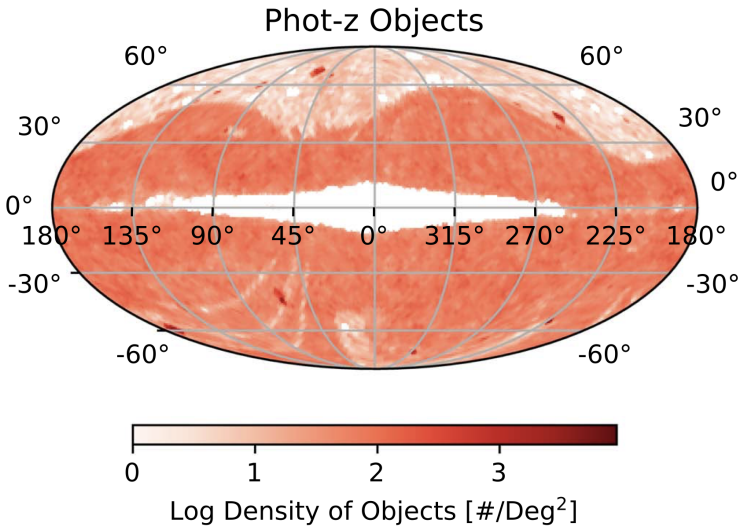


Figure 4.3: All-sky density plot of NED objects with spectroscopic redshifts [Cook et al., 2023].

The initial filtering process selects galaxies within a 1 square degree region centered on the Fermi GRB position, narrowing the volume to a smaller area than the error box, thereby decreasing the likelihood of associating the GRB with a foreground or background galaxy that is coincidentally located within the larger error region but is not physically related to the GRB. A further constraint is applied based on the physical offset between the GRB

and candidate host galaxy. Population synthesis models indicate that the median projected offset is typically between 5 and 7 kpc. Approximately 10 to 25% of events are expected to occur at offsets greater than 20 kpc, with up to 10% extending beyond 100 kpc [Fong and Berger, 2013, Fong et al., 2022, Nugent et al., 2024]. Observational data on sGRBs, whether exhibiting extended emission or not, suggests that the physical offset can range from a few kpc to tens of kpc [Fong et al., 2009]. By analyzing the physical offsets of the sGRBs cataloged by Nugent et al. (2024) [Nugent et al., 2024] (Fig. 4.4), we established a fiducial boundary at a distance of 40 kpc.

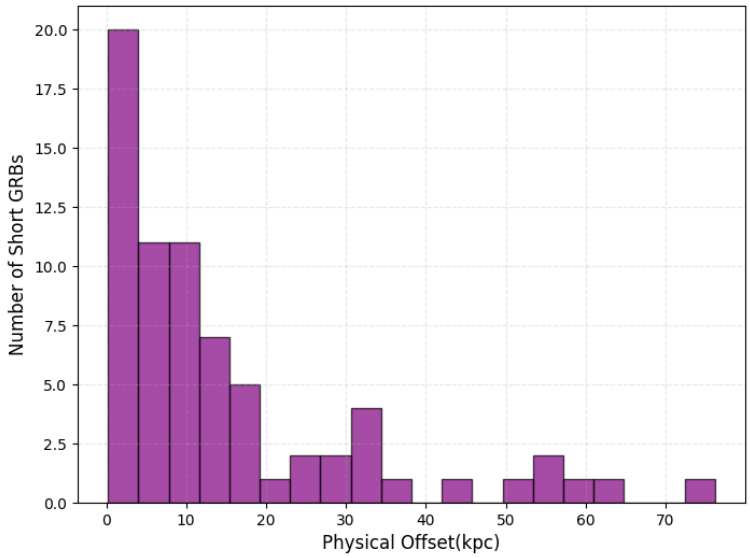


Figure 4.4: Number of sSGRB in function of the physical offsets(kpc).Data from Nugent et al. catalog [Nugent et al., 2024].

An additional diagnostic flag is assigned based on the specific star formation rate (sSFR) of the candidate galaxies, which quantifies the rate of star formation relative to the stellar mass of a galaxy. It is defined as follows:

$$sSFR = \frac{SFR}{M_*} \tag{4.5.1}$$

where M_* is the stellar mass. Typically, lower sSFR values indicate that the galaxies are forming relatively few stars, or may even be quiescent. Evidence suggests that sGRBs are often found in regions where most star formation has already occurred [Fong et al., 2009]. To establish a constraint on the sSFR, we analyzed the host galaxies of the short GRBs cataloged by[Nugent et al., 2024] (Fig. 4.5 illustrates the range of sSFR, which falls between 10^{-12} and 10^{-8}).
Finally we tested the host association procedure on GRB 170817A, the only event in the "gold" sample close enough to fall within the NED LVS limits. The pipeline successfully identified its known host, NGC 4993, thereby demonstrating its reliability for nearby events. In order to provide further validation of the pipeline, a retroactive search was also performed for 66 Fermi GRBs from Cluster 2 for which no measured redshifts were available. Candidate host galaxies were identified using the NED LVS database, followed by a search for potential optical counterparts in the TNS catalog [2], limited to detections within three months of the GRB. For GRBs with known afterglows, searches were conducted within 10

[2]https://www.wis-tns.org

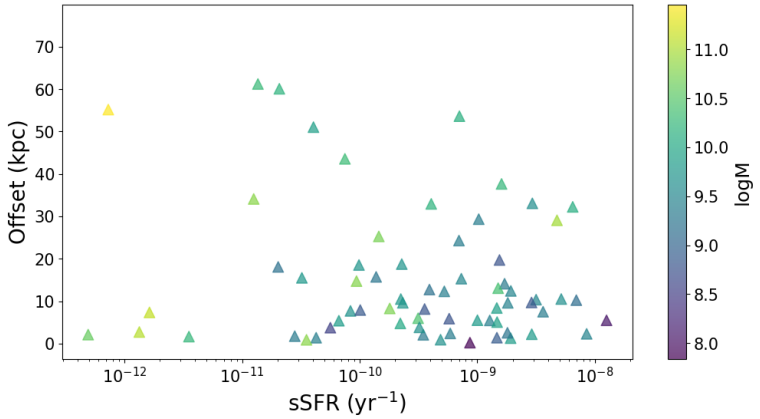


Figure 4.5: Correlation between offset and sSFR for the sGRBs in the Nugent et al. catalog. [Nugent et al., 2024]

arcseconds of the X-ray position, while for others, the search was centred on NED-selected candidate hosts. This search identified one potential counterpart (AT 2022kpe) for GRB 220412713, located 36 kpc from WISEA J212432.06-000919.7; however, the transient's discovery one month after the GRB suggests it is likely unrelated.
This methodology establishes a systematic framework for associating sGRBs with likely host galaxies, thereby improving the efficiency of follow-up observations. Although the pipeline is currently optimized for nearby events, it is suited for future wide-field facilities such as the Vera C. Rubin Observatory's LSST [Ivezić et al., 2019, Bianco et al., 2021] or Euclid [Mellier et al., 2024], whose extensive coverage can complement this approach by crossmatching numerous candidate galaxies within Fermi GRB error regions.

4.6 Conclusions

The work presented in this Chapter demonstrates the potential of data-driven approaches to identify promising EM counterparts of compact binary mergers even in the absence of a confirmed GW trigger. Building on the connection between sGRBs and BNS mergers, our methodology provides a systematic framework for the identification of GRBs with properties consistent with KN-associated events. By applying unsupervised clustering algorithms to the Fermi GBM catalog, we successfully identified a subpopulation of GRBs that share intrinsic characteristics with the known KN-associated GRBs. The robustness of the resulting clusters, validated across different dimensionality reduction techniques and comparison with similar works, highlights the capability of machine learning to distinguish astrophysically consistent subpopulations. The integrated pipeline for host galaxy association proved particularly effective in recovering known associations and constraining the search for plausible hosts in new candidates. This approach not only aims to improve the localization and characterization of GRB events but also to enhance the efficiency of follow-up observations by prioritizing galaxies most likely to host merger progenitors, expecially in preparation for new wide-field facilities like the Vera C. Rubin Observatory's LSST and Euclid.
The framework presented in this Chapter is also adaptable for real-time analysis. The ability to classify a newly detected GRB within minutes of detection enables timely alerts to the broader multimessenger community, a key advantage in the pursuit of rapidly fading KN counterparts. As next-generation facilities such as Einstein Probe and SVOM will increase

the number of detections, and as GW detector networks expand their sensitivity, the synergy between prompt gamma-ray classification and host galaxy association will become increasingly powerful. In addition, while the present study focuses on BNS mergers, the methodology can be extended to explore other GRB progenitor classes, such as collapsars or magnetar-driven explosions. By identifying distinct parameter-space regions associated with different physical origins, this approach could provide new insights into the diversity of GRB populations and their underlying progenitor mechanisms.

Chapter 5

Modeling kilonova and sGRB afterglow emission

In the previous Chapter, we introduced a methodology designed to search for BNS mergers and their KN counterparts through analysis of the high-energy emission from GRBs, with particular attention to off-axis events [Giudice et al., 2025]. This approach is based on the connection established by the observation of GRB 170817A, detected 1.7 seconds after the corresponding GW signal [Goldstein et al., 2017, Savchenko et al., 2017]. The prompt emission based pipeline presented earlier can act as a powerful tool for the early identification of potentially interesting events that may be missed in GW searches, thereby providing a, if not the main, channel to uncover KNe.
In addition, we developed a rapid galaxy-association tool capable of linking GRB events to their most probable host galaxies. This can potentially enhance the follow-up efficiency by guiding observational facilities toward the most promising targets. Such an approach may be particularly relevant for future wide-field facilities like LSST [Bianco et al., 2021, Ivezić et al., 2019]: thanks to its large sky coverage, this facility will be able to scan Fermi GRB error regions and promptly inspect candidate hosts, thereby strengthening the search for KN signatures. Since KNe are fast-evolving transients with a narrow observational window, the presence of a GRB, especially an off-axis one, implies an additional optical component that can significantly influence the overall light curve and potentially enhance detectability. Building on this framework, the work presented in this Chapter aims to simulate how a KN associated with an sGRB would appear under different physical and observational conditions. By varying parameters such as the viewing angle, the burst energetics and the CSM density and by adopting an updated realistic LSST cadence, we aim at generate template light curves and mock observations for a wide set of afterglow scenarios. This enables us to assess the detectability of these events and to explore the interplay between GRB afterglows and their underlying KN emission [1].

The Chapter is organized as follows. Section 5.1 discusses the role of the LSST survey, which we take as a reference for generating realistic mock observations. Section 5.2 then outlines the framework adopted to simulate both the KN a and sGRB afterglow light curves. In Section 5.3 we present the results of our simulations and in Section 5.4 we apply our simulated light curves to a real case. Finally, Section 5.5 summarizes our main findings and conclusions.

[1]The material presented in this chapter is part of an ongoing research project that is currently under preparation and will be finalized within the forthcoming months.

5.1 The Vera Rubin Observatory and the Legacy Survey of Space and Time

The Vera Rubin Observatory is the new facility that will observe the Southern Hemisphere sky from the El Peñón peak of Cerro Pachón, Chile, for the next 10 years. The observatory



Figure 5.1: The Vera Rubin Observatory.

is equipped with the 3.2 gigapixel LSST Camera mounted on the 8.4 meter Simonyi Survey Telescope and represents a major advance in wide-field deep time-domain optical astronomy. The design of the observatory combines a large aperture with a very wide field of view ($\sim$9.6 deg^2), enabling rapid coverage of vast areas of sky with high sensitivity [Bianco et al., 2021]. During its operation the facility will conduct the Legacy Survey of Space and Time (LSST), in which it will take repeatedly image up to 18,000 deg^2 of the southern sky over a 10 year period, in six photometric bands (u, g, r, i, z, y). This configuration provides an unprecedented combination of depth, cadence and sky coverage, ideal for detecting transient and variable phenomena (Figure 5.2).

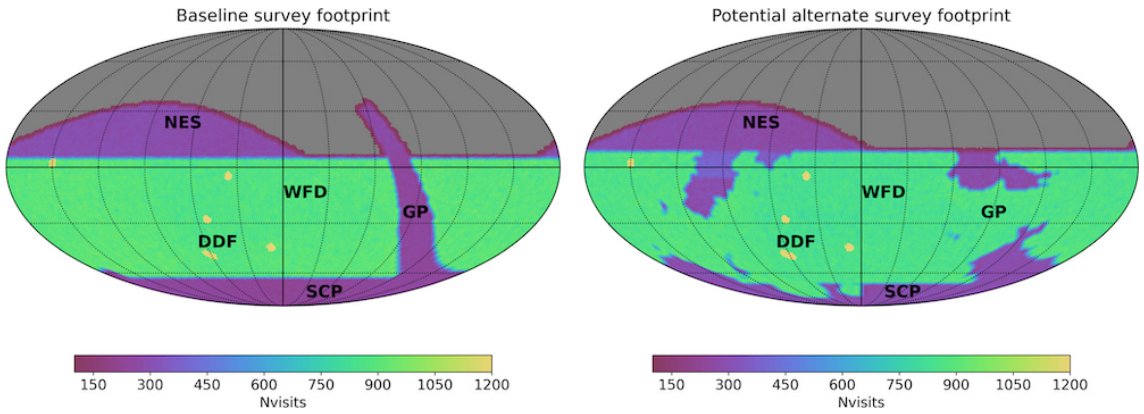


Figure 5.2: LSST footprint showing the number of visits as a function of position on the sky [Bianco et al., 2021].

The relevance of Rubin for GW follow-up has already been proved. In fact, during the observations of the sub-solar mass merger candidate S251112cm, the Rubin Observatory performed its first Target-of-Opportunity (ToO) observations since the beginning of its operations in late October 2025 [MacBride et al., 2025]. The LSST Camera scanned a

substantial fraction of the localization region (covering 39.2% of the 90% credible region in g-band and 33.5% in i-band), reaching a median depth of ~ 24.8 mag (g-band) and ~ 23.7 mag (i-band) in single 30s exposures.
The abilty to cover hundreds of square degrees in a small time window hence supports the choice of LSST as reference survey for mock observations of this work. Its wide field, depth and cadence make this survey ideal for capturing fast and faint transients such as KNe and GRB afterglows. While the baseline LSST survey is dominated by the Wide-Fast-Deep strategy, a subset of fields will be observed with a significantly higher cadence through the Deep Drilling Field program. Transients occurring in these regions will benefit from denser temporal sampling, especially at early times, enabling a more detailed reconstruction of rapidly evolving light curves. In addition, the LSST observing strategy places strong emphasis on the g-, r- and i-bands, which are expected to provide the most constraining information for the optical detection and characterization of KNe. By adopting a realistic LSST cadence as a baseline, our simulations of KN and sGRB afterglow detectability can be more robust.

5.2 Simulation framework

For the KN emission, we used a dataset obtained with `POSSIS` [Bulla, 2019, 2023], a time-dependent three-dimensional Monte Carlo radiative-transfer code developed to compute spectra and light curves for transients. The key strength of POSSIS lies in its ability to handle arbitrary 3D geometries and direction-dependent emission. This is particularly relevant for KNe originating from BNS mergers: numerical-relativity simulations predict that the ejecta are highly asymmetric, consisting of multiple components with different compositions, opacities and velocity distributions. POSSIS can accurately model how such asymmetries and viewing angles can affect the emission. The Monte Carlo framework follows the propagation, absorption, scattering and re-emission of photon packets through the ejecta as a function of time. The code incorporates wavelength-dependent opacities, including the high lanthanide opacities that strongly shape KN light curves. Thermalization efficiencies, ionization states and energy deposition from radioactive decay are also included, enabling a realistic reconstruction of the evolving emission.
In this work we adopt the common two-component KN framework, consisting of a lanthanide-rich dynamical ejecta component produced during the tidal and shock-driven phases of the merger and a lanthanide-poor post-merger wind originating from the accretion disk. The model assumes a dynamical ejecta component with mass $M_{\rm ej,dyn} = 0.005\,M_\odot$, expansion velocity $v_{\rm ej,dyn} = 0.20\,c$ and electron fraction $\bar{Y}_{e,\rm dyn} = 0.20$, and a wind component with $M_{\rm ej,wind} = 0.050\,M_\odot$, $v_{\rm ej,wind} = 0.05\,c$ and $\bar{Y}_{e,\rm wind} = 0.30$. To fully capture the anisotropic nature of the KN emission, we generate synthetic light curves for 12 viewing angles uniformly distributed between 0° and 90° (Figure 5.3). We adopted the following convention: 90° corresponds to an off-axis configuration, roughly perpendicular to the ejecta, while 0° corresponds to the on-axis case, where the line of sight is aligned with the jet direction.These angle dependent outputs allow us to combine the KN models with our simulated sGRB afterglows and to quantify how the line of sight influences the observed lightcurve behaviour. This is crucial for assessing detectability, especially in the case of off-axis GRBs where the viewing geometry plays a dominant role in shaping the observed light curve.
To model the GRB afterglow emission, we employed the `afterglowpy` Python module [Ryan et al., 2025], a numerical library designed to compute broadband light curves from relativistic jets interacting with the circumburst medium. `afterglowpy` solves for the jet dynamics, synchrotron emission and relativistic beaming as a function of time, modeling

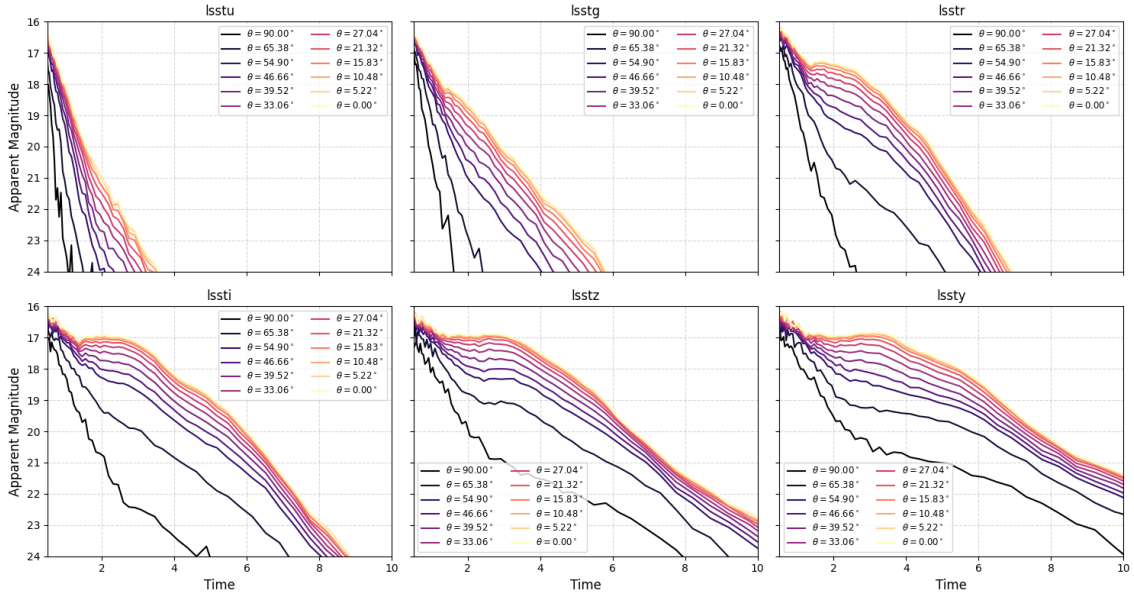


Figure 5.3: KN simulated light curves for the optical filters of LSST at different viewing angles using `POSSIS` .

on parameters such as the isotropic-equivalent kinetic energy, circumburst density, jet opening angle, microphysical shock parameters (ϵ_e, ϵ_B) and the electron power-law index p. For our analysis we adopted a Gaussian jet structure, implemented by setting `jetType = afterglowpy.jet.Gaussian`. The jet angular structure is described by a core width $\theta_{\rm core} = 5^\circ$ and a characteristic wing scale $\theta_{\rm wing} = 20^\circ$. We assume standard microphysical parameters for modeling sGRBs, such as electron power-law index $p = 2$ and shock energy partition fractions $\epsilon_e = 0.1$ and $\epsilon_B = 0.01$. The source is placed at a luminosity distance of $d_L = 40\,\mathrm{Mpc}$. Light curves are computed over the time interval 0.5–30 days with 100 logarithmically spaced steps.

To explore the dependence of the afterglow emission on the external environment, we tested for three different ambient densities, $n_0 = 1$, 0.1, and $0.01\,\mathrm{cm}^{-3}$. The parameter n_0 represents the density of particles in the circumburst medium and controls both the strength of the shock interaction and the deceleration rate of the jet: higher densities lead to brighter and more rapidly evolving afterglows, while low-density environments produce fainter, slower-evolving light curves. In addition, we explored two characteristic isotropic energy scales by adopting $E_0 = 10^{50}\,\mathrm{erg}$ and $E_0 = 10^{52}\,\mathrm{erg}$. These values lie in the typical range of sGRB energetics and allow us to test how the relative contribution of the afterglow compares to the KN emission across different physical regimes. For each combination of (E_0, n_0) we compute the afterglow emission at the same 12 viewing angles used for the KN simulations.

5.3 Results

Based on the data obtained from the softwares described above, we proceeded by combining the angle-dependent GRB afterglow densities to the corresponding `POSSIS` KN light curve at each epoch. These combined models are crucial to determine under which conditions the afterglow influences the KN signature and how this affects detectability within the LSST cadence.

To ensure that the modeled GRB and GRB+KN light curves can be directly compared with realistic LSST observations, we compute the afterglow emission through the official LSST filter responses. These filter response functions were obtained from the public LSST baseline throughput repository[2] and incorporated into our pipeline by registering them as custom `sncosmo` bandpasses. This step guarantees an accurate mapping between the model spectral energy distribution and the expected LSST photometry, avoiding biases associated with idealized or simplified filter profiles. For each LSST band (u, g, r, i, z, y) we generated light curves in apparent magnitude for all components (KN, GRB afterglow and their sum) across the same 12 viewing angles used throughout our simulations.

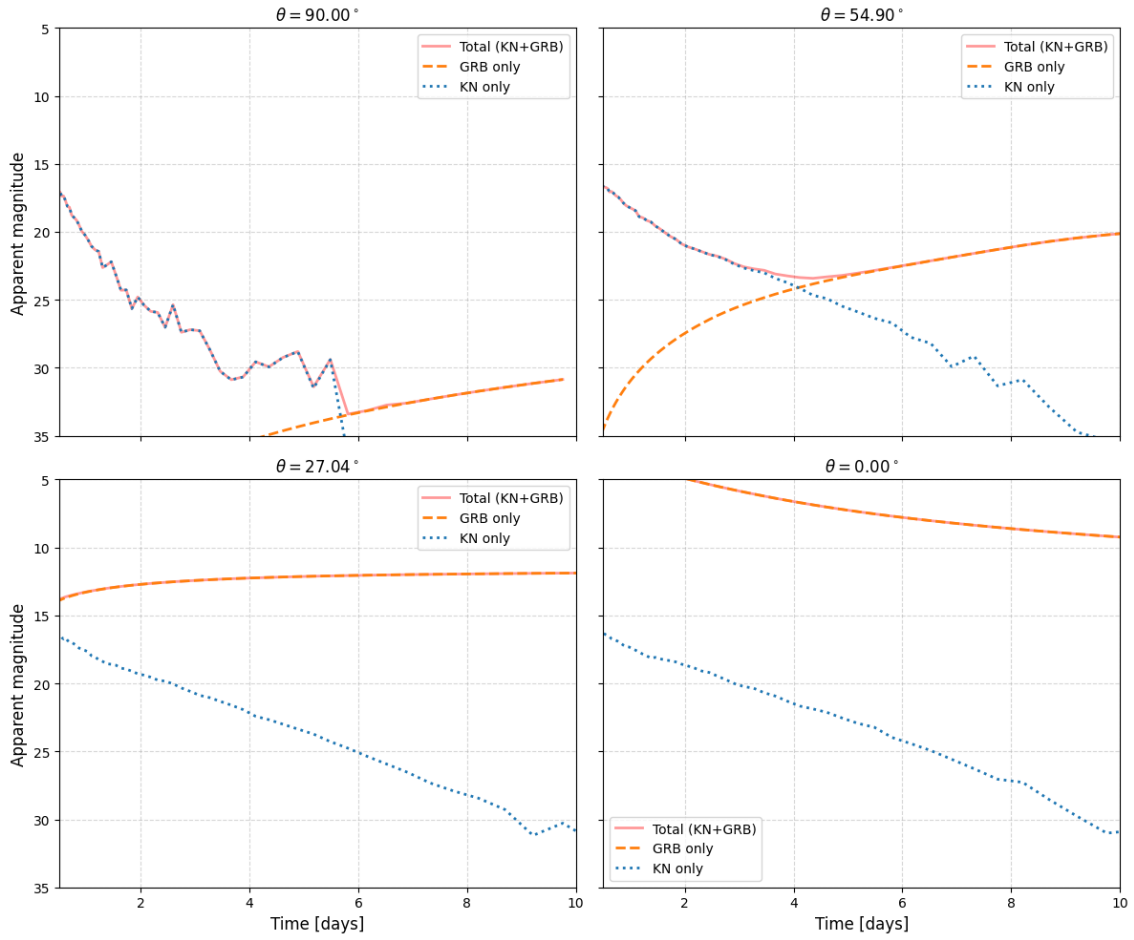


Figure 5.4: Simulated g-band light curves for four different viewing angles. Blue dotted lines represent the KN emission, orange dashed lines correspond to the GRB afterglow and solid red lines indicate the combined emission.

In the following we will discuss the adopted *best case*, corresponding to a choice of $E_{iso} = 10^{52}$ erg and n_0=0.1 cm^{-3}. The full curve sample for the corresponding lower energy case ($E_{iso} = 10^{50}$, n_0=0.1) are in Appendix C. To explore the impact of viewing geometry, light curves were simulated for four different observer angles ($\theta = 90°, 54.90°, 27.04°, 0°$). For each angle, the apparent magnitude was calculated separately for the KN, the GRB afterglow and their combined emission, in the LSST g-band (Figure 5.4), i-band (Figure 5.5) and r-band (Figure 5.6). In all scenarios the KN exhibits the expected rapid decline within the first 3-5 days, typical of these fast-evolving transients. On the other hand, the GRB

[2] `https://github.com/lsst/throughputs/tree/main/baseline`

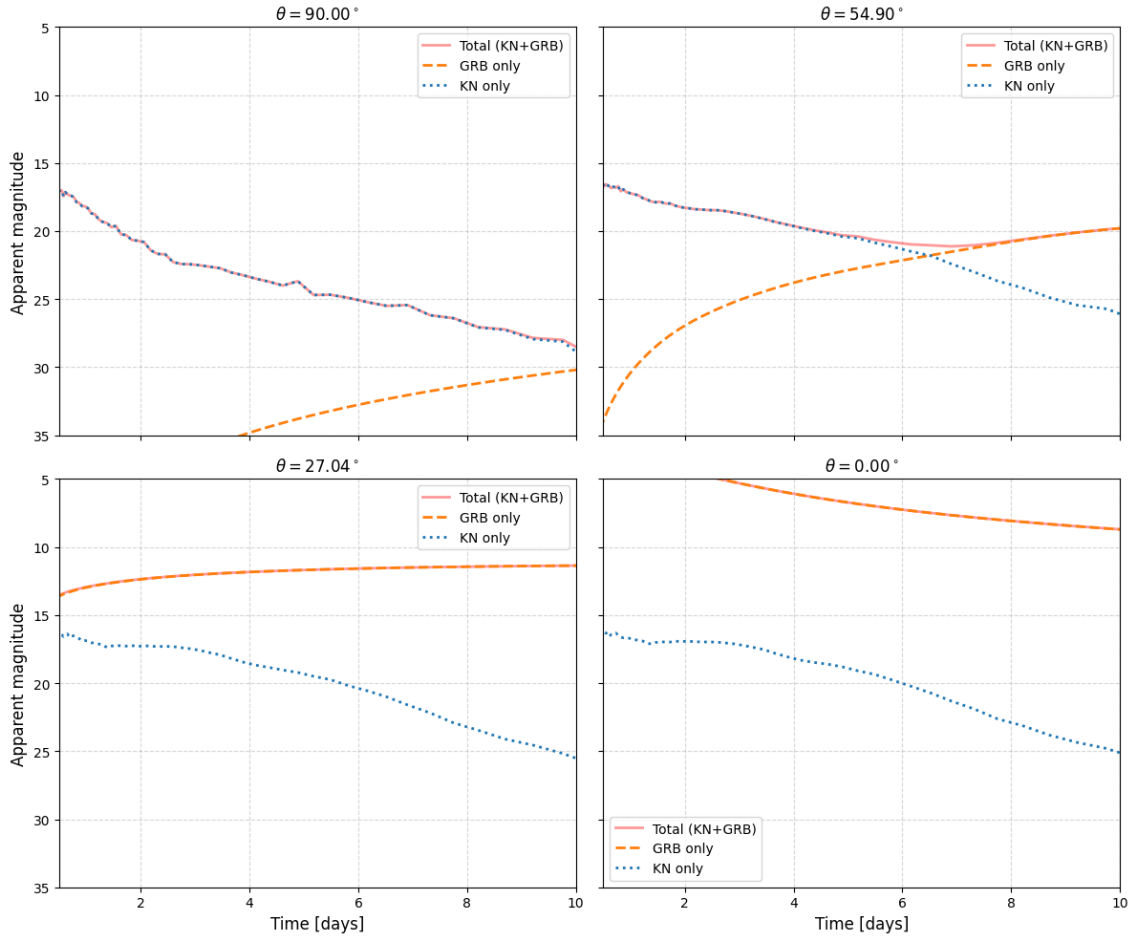


Figure 5.5: Simulated i-band light curves for four different viewing angles. Blue dotted lines represent the KN emission, orange dashed lines correspond to the GRB afterglow and solid red lines indicate the combined emission.

afterglow evolves more gradually and can remain detectable for longer timescales, leading to complex combined light curves. The influence of the viewing angle is clearly visible in all the bands. In the case of extreme off-axis ($\theta = 90°$), the afterglow is strongly suppressed at early times, allowing the KN to dominate initially. In the $\theta = 54.9°$ configuration, both components contribute significantly, with the afterglow rising and overtaking the KN after $\sim$4–6 days, depending on the filter. As the angle dethe crease to the on-axis configuration ($\theta = 0°$), the afterglow becomes increasingly dominant and can exceed the KN brightness by several magnitudes at all epochs.This behavior has important observational implications. For on-axis and near-on-axis events, the afterglow can completely mask the KN, producing a light curve that is effectively indistinguishable from a standard afterglow. In such cases, the KN may be entirely invisible in without additional multi-wavelength or spectroscopic information. Conversely, in strongly off-axis orientations, the early afterglow is faint while the KN is detectable, but its rapid fading can cause the transient to mimic a fast-declining SN or an unclassified optical flash. Such KN-dominated off-axis events therefore carry a real risk of misidentification, unless follow-up observations or color evolution are available. These results illustrate the necessity of accurate joint modeling of KN and afterglow components for interpreting observations and highlight the strong dependence of detectability on viewing geometry. Finally, we note that the plots shown in Figures 5.4, 5.5 and 5.6 present

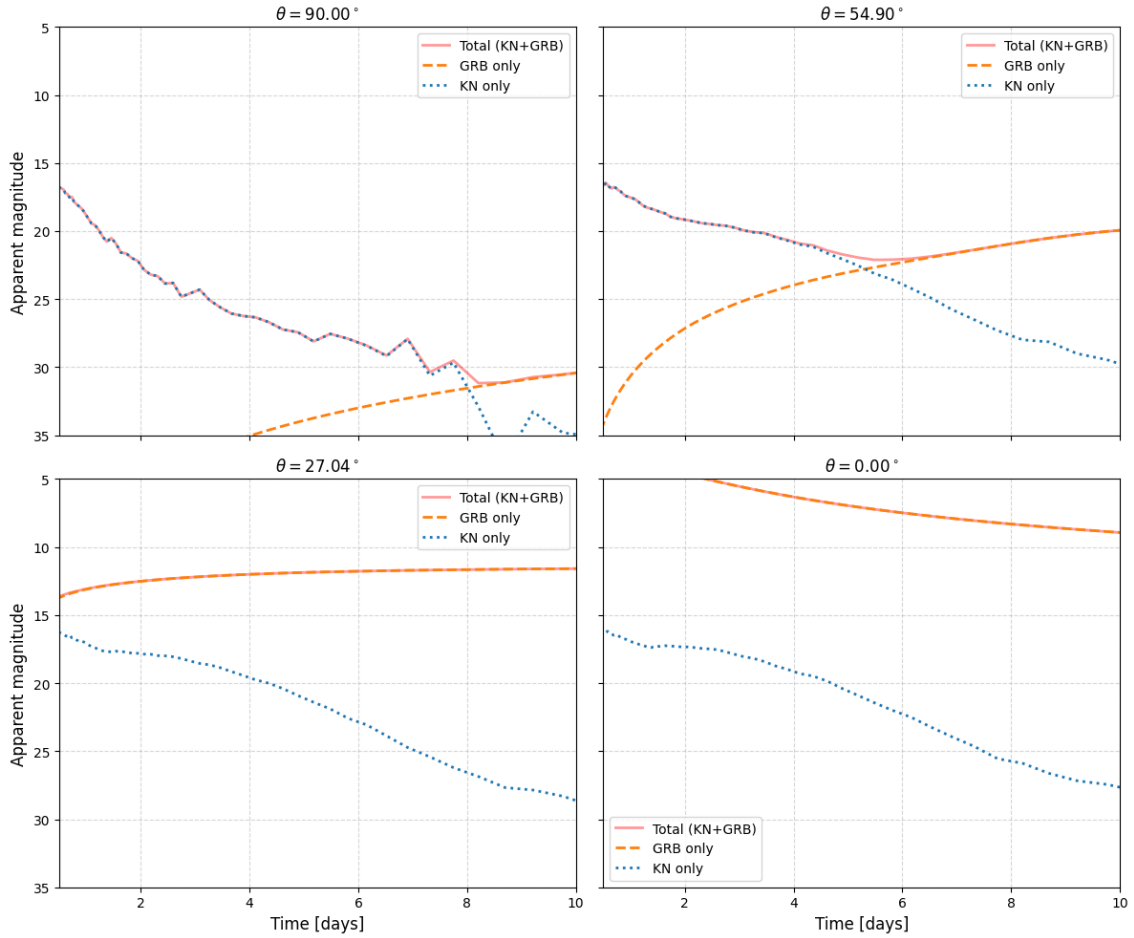


Figure 5.6: Simulated r-band light curves for four different viewing angles. Blue dotted lines represent the KN emission, orange dashed lines correspond to the GRB afterglow and solid red lines indicate the combined emission.

a range of apparent magnitudes wider than those expected to be routinely observed by LSST. This choice is intentional and aims to facilitate a clear visualization of the relative contribution of the KN and GRB afterglow components across different viewing angles and bands.

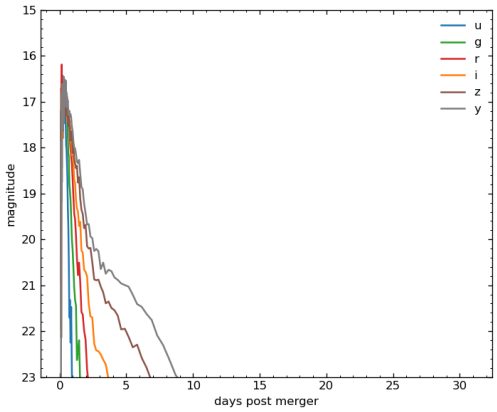
Then we investigated how these transients would be observed by LSST in a realistic survey scenario, by adopting the same four viewing angles and generating LSST-band light curves for each configuration. These model light curves were then sampled using a realistic LSST cadence, reproducing the expected observational gaps, filter sequence and single-visit depth of the survey. This procedure allowed us to construct mock LSST observations that incorporate both instrumental and scheduling constraints.

To obtain a realistic LSST observing pattern, we extracted the survey cadence at the sky position of GW170817 (RA = 197.45°, Dec = −23.38°). This location lies within the LSST footprint and therefore can be representative example of the visit sequence, limiting magnitudes,and filter distribution expected for a typical field. The choice of these coordinates is not physically connected to our simulated events, the same procedure can be applied to any position within the LSST footprint. Howevere, this position does not fall within the Deep Drilling Field and, as a result, the simulated observations follow the Wide-Fast-Deep survey cadence rather than a high-cadence deep-field strategy. This choice

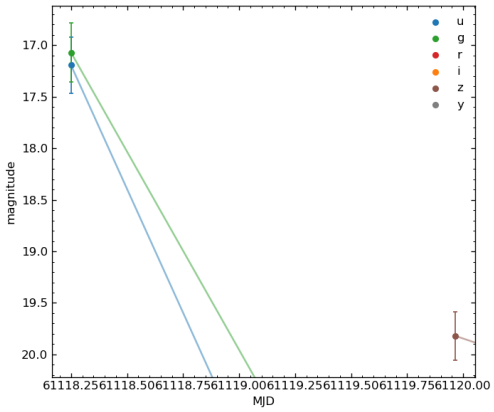
provides a representative example of standard LSST observations. For a transient located in the Deep Drilling Field the higher cadence would yield a more sampled light curve, particularly at early times, improving the reconstruction of the rapid KN evolution.
Then to model a best sampled scenario, we assumed that the transient explosion occurs at the time of the first LSST visit in the chosen field. This ensures that the simulated LSST sampling includes the very beginning of the event and allows us to probe an upper bound on LSST's ability to capture the rapid early evolution of KNe.
The analysis was performed for two densities, $n_0 = 0.1$ cm^{-3} (our best-case scenario) and a lower-density case $n_0 = 0.01$ cm^{-3}. The resulting mock observations illustrate how the visibility of the KN and afterglow components vary with viewing geometry, bandpass and local density, providing a direct estimate of LSST's ability to detect and correctly classify such events. In Figures 5.7 and 5.8, we present the simulated LSST detections for both density regimes across the four viewing angles. These mock LSST observations reveal that for the smaller viewing angles ($\theta = 27.04°$ and $0°$), several early-time points fall above the LSST saturation limit. This is a direct consequence of the adopted distance of 40 Mpc and isotropic energy. Although this saturation would not occur for more distant mergers, the result suggests how the detection of a nearby event can benefit of different observational strategies (GRB detection or spectroscopy).
As an additional validation of our methodology, we repeated the same modeling procedure to simulate an event analogous to GW170817, the only BNS merger for which a KN has been unambiguously observed to date. In this case, the GRB afterglow component was modeled using the physical parameters inferred from the analysis presented in [Hajela et al., 2019], while adopting the same KN modeling framework used throughout this work.For an off-axis configuration corresponding to a viewing angle of $\theta \simeq 27°$, the resulting combined light curves reproduce the main features observed in GW170817. In particular, the KN emission remains dominant during the first $\sim$7–8 days, after which the afterglow gradually overtakes the KN component. This temporal behavior is fully consistent with the observational results and interpretations reported in [Hajela et al., 2019].
The ability of our pipeline to recover the observed evolution of GW170817 in the off-axis configuration provides an important validation of the adopted joint KN+afterglow modeling approach. The corresponding light curves are presented in Appendix D.

5.4 Case study: 2025ulz

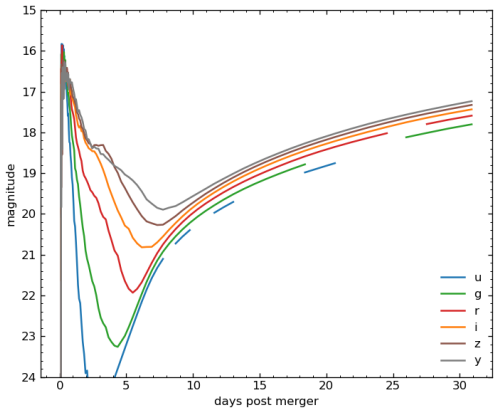
The simulated KN+sGRB framework presented in this Chapter can be applied to real events in order to assess whether their photometric behaviour is compatible with emission from a BNS merger. Among the candidate counterparts identified during O4, one of the most discussed case was the optical transient AT2025ulz, discovered within the localization region of the GW event S250818k. As discussed in Section 3.3, early-time photometry initially suggested a possible KN-like evolution, prompting intensive follow-up efforts across multiple wavelengths. However, as the transient evolved, its luminosity and spectroscopic development ultimately pointed toward a core-collapse origin [Gillanders et al., 2025].
While these conclusions were reached through detailed observational analyses, the event provides an instructive test case for the modelling strategy presented here. In particular, AT2025ulz offers the possibility to evaluate whether a physically realistic KN+afterglow light curve, generated under a broad range of viewing angles, circum-burst densities and jet properties, could reproduce the temporal behaviour observed in the optical bands.
Hence, we compare the r-band photometry from Pan-STARRS of AT2025ulz with our simulated light curves. Since KN emission is expected to dominate the optical flux



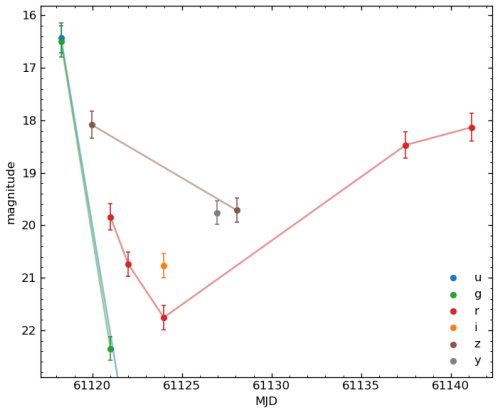
(a) $\theta = 90°$ light curve



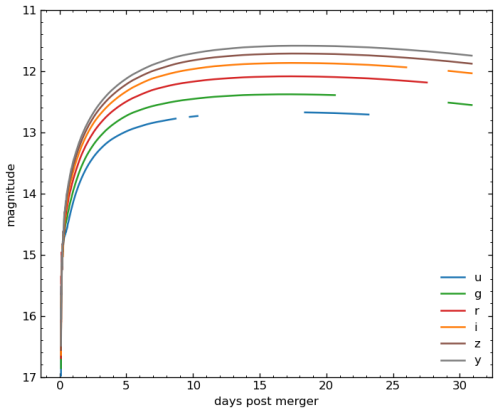
(b) $\theta = 90°$ mock observation



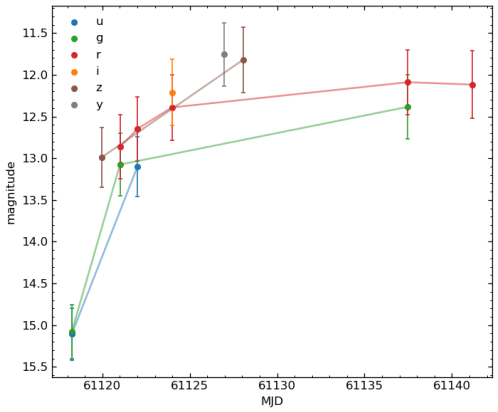
(c) $\theta = 54.90°$ light curve



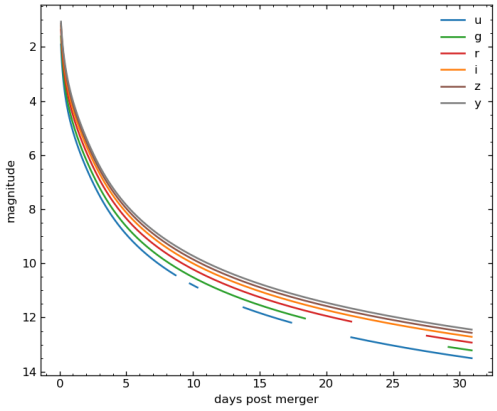
(d) $\theta = 54.90°$ mock observation



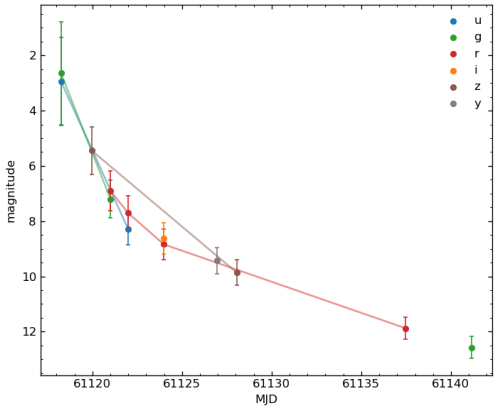
(e) $\theta = 27.04°$ light curve



(f) $\theta = 27.04°$ mock observation

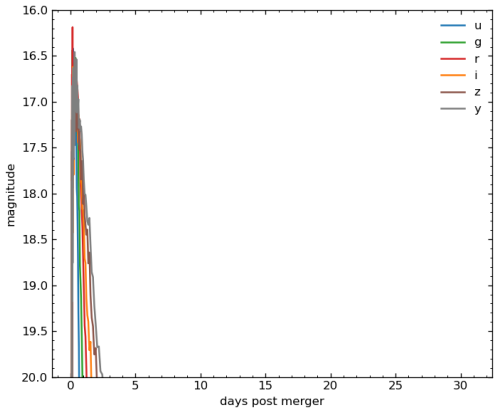


(g) $\theta = 0°$ light curve

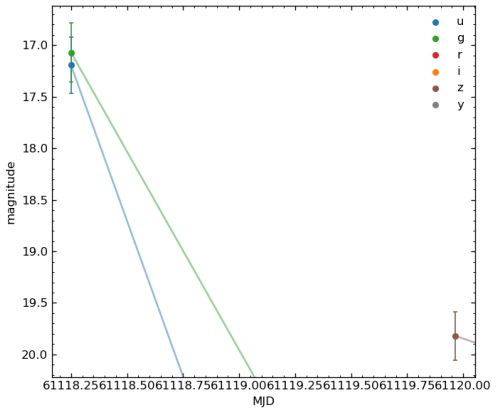


(h) $\theta = 0°$ mock observation

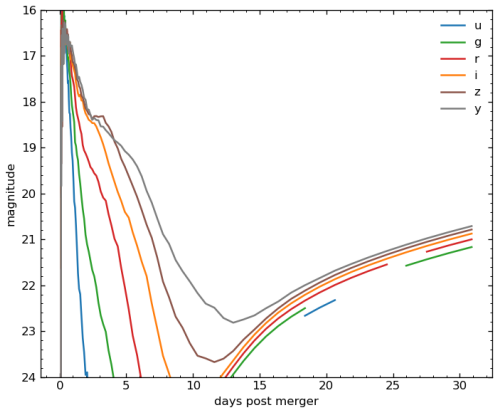
Figure 5.7: Case $n_0 = 0.1$: Light curves (left) and LSST mock observations (right) for different viewing angles.



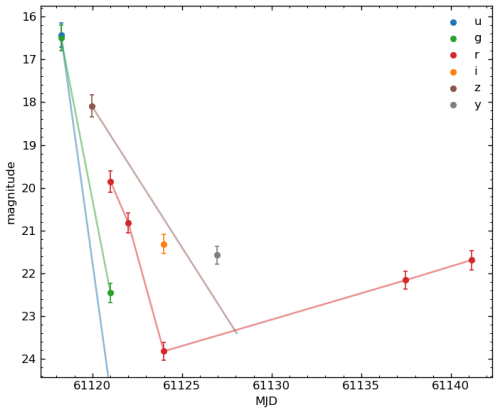
(a) $\theta = 90°$ light curve



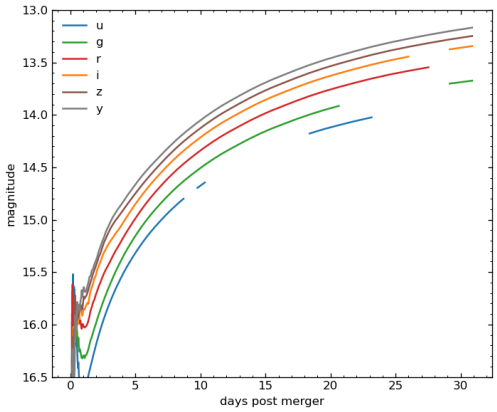
(b) $\theta = 90°$ mock observation



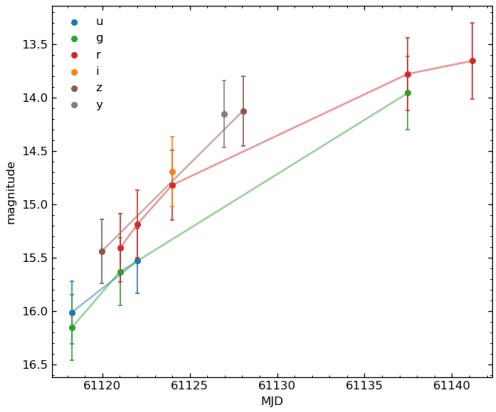
(c) $\theta = 54.90°$ light curve



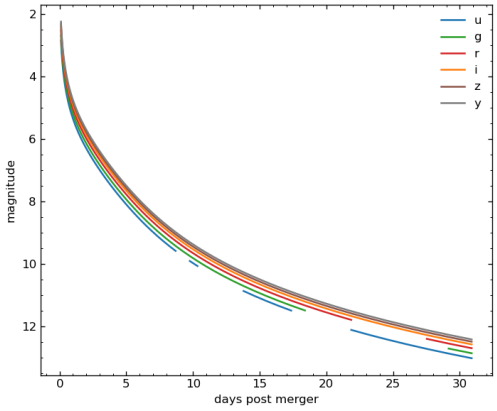
(d) $\theta = 54.90°$ mock observation



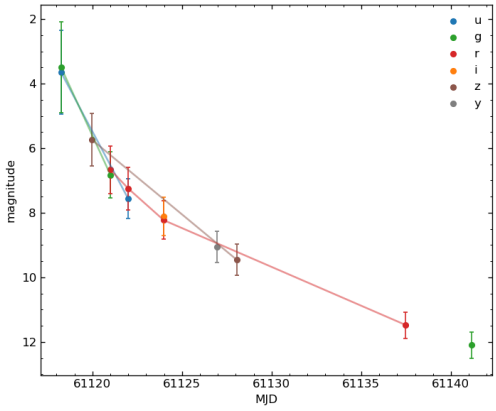
(e) $\theta = 27.04°$— light curve



(f) $\theta = 27.04°$ mock observation



(g) $\theta = 0°$ light curve



(h) $\theta = 0°$ mock observation

Figure 5.8: Case $n_0 = 0.01$: Light curves (left) and LSST mock observations (right) for different viewing angles.

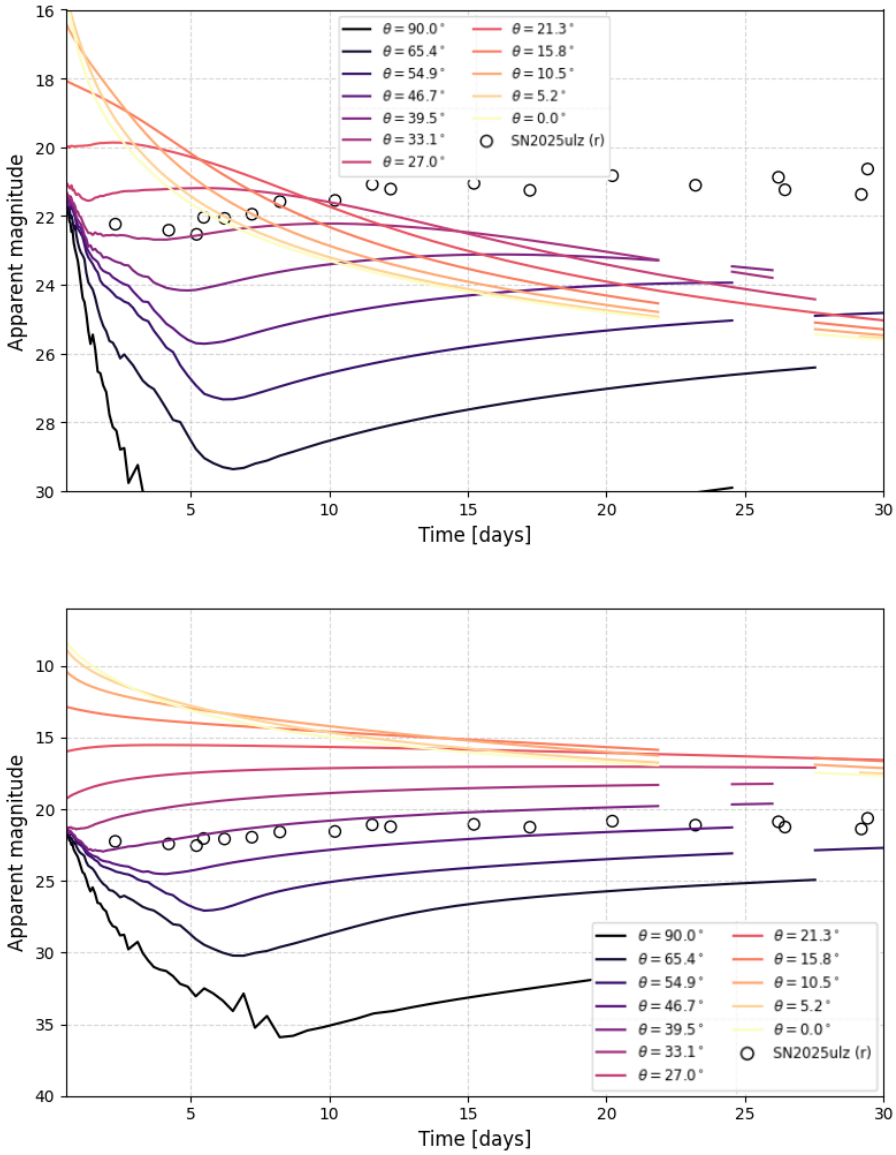


Figure 5.9: Comparison between the r-band light curve of AT2025ulz (black points) and the KN+afterglow models in the LSST r-filter for two isotropic-equivalent energies: $E_{\rm iso} = 10^{50}$ erg (top) and $E_{\rm iso} = 10^{52}$ erg (bottom), each shown for multiple viewing angles.

on timescales of hours to days, especially for moderately off-axis configurations, our KN+afterglow templates may provide a reference for the characteristic rise, peak luminosity and post-peak decline expected from a BNS merger viewed at different geometries. Any deviation from this behaviour can therefore be interpreted as evidence against a KN origin. The comparison shown in Figure 5.9 demonstrates that the observed evolution of AT2025ulz is incompatible with most simulated KN+afterglow scenarios, in full agreement with the conclusions drawn from the multi-wavelength follow-up and provides an independent, model-driven confirmation that AT2025ulz is not associated with the GW event S250818k. However, further analysis of Figure 5.9 revealed an important result. While the lower-energy scenario ($E_{\rm iso} = 10^{50}$ erg) fails to reproduce the observed behaviour of AT2025ulz at all viewing angles, the higher-energy case ($E_{\rm iso} = 10^{52}$ erg) produces at least one configuration whose early-time luminosity and decline rate agree with the observed behavior of 2025ulz.

Although this agreement was not confirmed by spectroscopy of the event, the comparison shows that, under certain energetic and geometric conditions, a KN+afterglow composite model can approach the photometric behaviour of AT2025ulz. This example highlights the importance of combining multi-band photometry with spectroscopic and multimessenger information to correctly interpret ambiguous transients.
Such degeneracies underscore the importance of constructing comprehensive, physically motivated template libraries that span the full range of plausible KN and GRB afterglow combinations. These templates can provide a powerful diagnostic tool for interpreting ambiguous events: by enabling direct light curve matching across different energies, densities and viewing angles, they may help identify when a transient is truly compatible with a BNS merger or when apparent similarities are coincidental. In the broader context of multi-messenger astronomy, this approach will be essential for rapidly evaluating candidate counterparts in future observing runs, independent of the specific facility (LSST or others).

5.5 Conclusions

In this Chapter we developed a modelling framework for KNe and sGRB afterglows in order to explore how their combined emission depends on the geometry, the energetics of the relativistic jet and the properties of the circumburst medium.

Our results clearly show that the detectability of KN emission strongly depend on viewing geometry. In on-axis or near-on-axis configurations, the afterglow dominates, often exceeding the KN luminosity by several magnitudes. Conversely, in off-axis configurations the afterglow weakens substantially, allowing the KN to emerge during the first few days.
The case study of AT2025ulz provided a concrete application of this framework. Although the observed evolution of the transient is incompatible with any physically plausible KN+afterglow model, the partial overlap with one high-energy configuration highlights a non-negligible degeneracy: different combinations of energetics and viewing angles can mimic, at least for a limited temporal window, the behaviour of non-merger transients. This reinforces the importance of building extensive libraries of joint KN+afterglow templates that span the full parameter space. Such libraries will be essential for interpreting ambiguous events in future observing runs, enabling rapid compatibility tests with BNS merger models directly from photometric data.
With the advent of next generation GW detector, the ability to identify and classify their EM counterparts efficiently will be crucial. In this context our framework provides a foundation for that goal that can be extended to incorporate alternative ejecta morphologies, structured jets or future survey cadences in preparation for upcoming observing campaigns.

Part III

Perspectives for Detection of Gravitational Waves from Core-Collapse Supernovae

Chapter 6

Prediction for the Einstein Telescope within the Milky Way

The 3rd generation GW detector ET hold promises for significantly enhancing detection sensitivity, extending the detection horizon and enabling the observation of weaker and low-frequency GW signals such as those produced by CCSNe (as discussed in Chapter 1). Understanding ET's capabilities for CCSN detection is essential for optimizing coordinated MM observing strategies. In this context, ET, together with next-generation neutrino observatories, will provide key triggers for rapid follow-up campaigns across the optical, radio and X-ray bands. Future neutrino detectors such as *Hyper-Kamiokande* [Di Lodovico et al., 2017], *DUNE* [Falcone et al., 2022] and *JUNO* [collaboration et al., 2022] will greatly increase sensitivity to SN neutrinos, enabling precise measurements of their fluxes, energy spectra and flavor composition. When combined with GW data, these observations will provide a direct probe of the physics behind the collapse of massive stars.
In this Chapter, we present a study aimed at evaluating the detection capabilities of the ET for CCSN events occurring within the Milky Way (MW) [1]. The methodology employed in this work is based on the `GWFISH` simulation framework, originally employed by the ET community to assess the detector's sensitivity to binary coalescence signals. For the purposes of this study, `GWFISH` has been adapted to incorporate simulated CCSN waveforms and a realistic spatial distribution of CCSN progenitors within the MW. The progenitor population was generated using TRIdimensional modeL of thE GALaxy (`TRILEGAL`) [Girardi et al., 2005], a well-established tool for modeling stellar populations. This chapter is structured as follows: Section 6.1 introduces the progenitor simulation employed in this work. Then Section 6.2 discuss the rate estimate within the MW from the literature and from the simulation. In Section 6.4 and 6.3 we present the framework employed to test the detection capabilities of ET and in Section 6.5 we discuss our results. Finally Section 6.6 outlines the key conclusions of this work.

6.1 CCSN progenitor simulation in the Milky Way

In our work we employed an all-sky distribution of massive stars simulated using the `TRILEGAL` code [Girardi et al., 2005], a C-based population synthesis code designed to generate stellar populations of our Galaxy through a Monte Carlo in which stars are simulated according to probability distributions based on a broad set of Galactic and

[1] The material presented in this chapter is part of an ongoing research project that is currently under preparation and will be finalized within the forthcoming months.

stellar parameters. The first ingredients in TRILEGAL are the evolutionary tracks and stellar spectral libraries used to simulate the photometry, from which theoretical isochrones and bolometric corrections can be respectively extrapolated. In our simulations, we assumed a Kroupa IMF [Kroupa, 2002] and evolutionary tracks based on PARSEC v1.2S [Bressan et al., 2012] and COLIBRI PR16 [Marigo et al., 2013, Rosenfield et al., 2016]. These tracks were then converted into isochrones to determine the Hertzsprung–Russell diagram positions of stars for given ages, metallicities and masses. TRILEGAL also requires a comprehensive model of the Galaxy's structure that incorporates: i) the thin disk, ii) the thick disk, iii) the bulge, and iv) the halo. The Galactic structure parameters used in our TRILEGAL simulations follow the prescriptions of [Pieres et al., 2020] and [Mazzi et al., 2021], which define the physical properties of these four components. The code combines realistic assumptions for the star formation history (SFH), initial mass function (IMF), age-metallicity relations and stellar evolution to produce a spatially resolved stellar population.
The stars for a given magnitude m_λ, where λ is the passband, and towards an element of Galactic coordinates (l, b), are generated according to

$$N(m_\lambda, l, b) = dm_\lambda \int_0^\infty dr\, r^2 \rho(\bar{r}) \phi(M_\lambda, \bar{r}) d\Omega, \tag{6.1.1}$$

where r is the line-of-sight distance, $\rho(\bar{r})$ is the stellar density, M_λ the absolute magnitude, and $\phi(M_\lambda, \bar{r})$ the intrinsic distribution of stellar absolute magnitudes. For each simulated star, the SFR, IMF and metallicity are employed to extrapolate its age and mass.

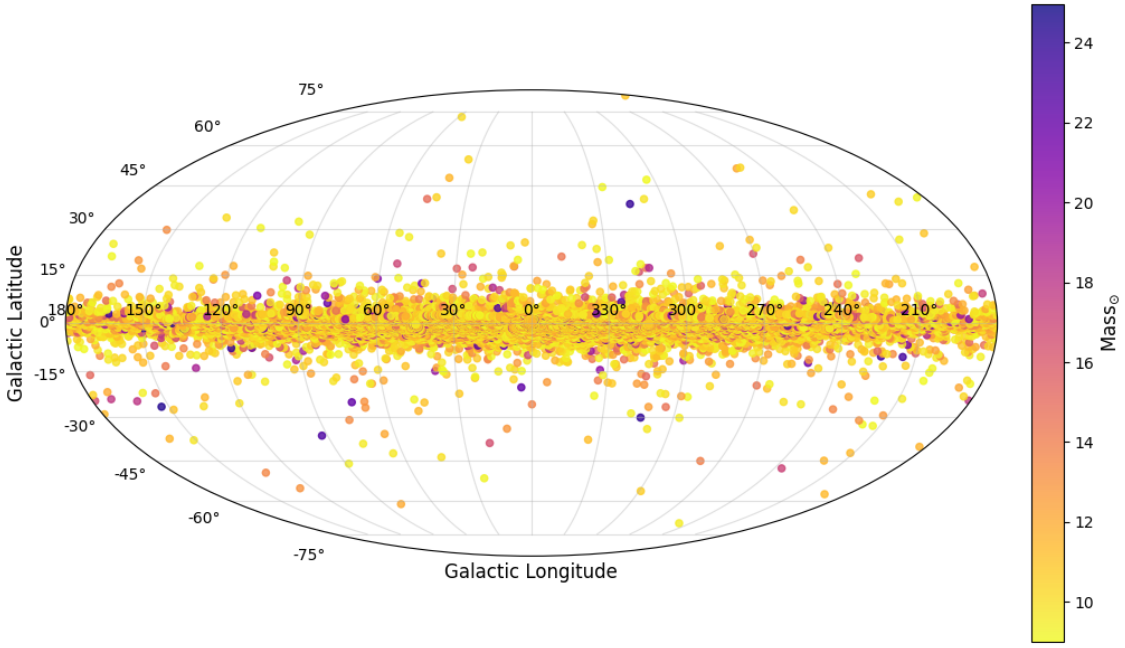


Figure 6.1: Spatial distribution of the progenitor simulation.

In our analysis, we selected stars with initial masses between 9 and 25 $M_\odot$ as CCSN progenitor, to match our CCSN waveform sample. The simulated catalog provides the total number, the age and spatial distribution of these massive stars (Figures 6.1 and 6.2). The age distribution enables the identification of a subsample of potential *near-explosion* candidates as progenitor of CCSN, from which number we can estimate the Galactic CCSN

rate (CCSNR). Then, the spatial distribution of this subsample allows to model ET detection capabilities for this potential GW sources.
To ensure completeness in the TRILEGAL simulated sample, we imposed a bolometric absolute magnitude cut of $M_{bol} < 30$ mag. This threshold ensures inclusion of progenitor stars that might be undetectable in optical surveys yet remain relevant for the GW source population.

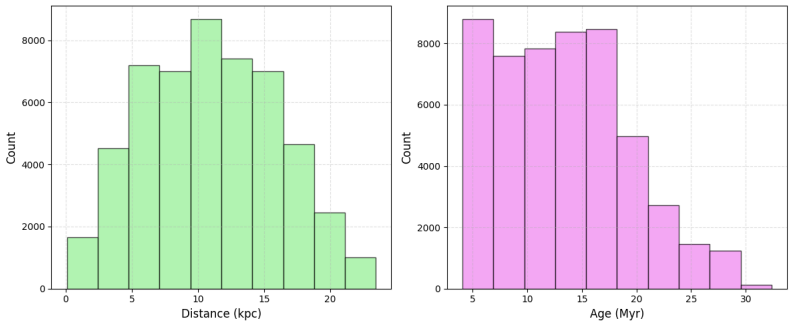


Figure 6.2: Age and distance distribution of the simulated progenitor stars.

6.2 CCSN rate

Any strategy for the detection of CCSN GWs, such as the study of detection horizon and SNR of ET, can benefit from the estimate of how many events we can expect within a certain volume. No Galactic SN has been optically observed since 1604, primarily due to dust extinction in the Galactic plane. Nevertheless, studies of SN remnants suggest that recent core collapse events may have occurred, with G1.9+0.3 being the youngest known remnant, dated to approximately 110–180 years ago [Reynolds, 2018, Luken et al., 2020]. Historical records provide direct evidence for only two CCSNE: SN 1054, likely a Type IIn-P SN [Smith, 2013], and SN 1181, whose classification remains uncertain [Kothes, 2013]. In the absence of direct observation, the estimates of the CCSNR within our Galaxy rely on indirect proxies, such as models of Galactic stellar population and dust, historical records, NS measurements, simulations and so on. Hence, in this Section we discuss the current CCSNR estimates from the literature and introduce our estimate extrapolated from the massive star progenitor simulation from TRILEGAL.

Rate measurements from literature

The first qualitative estimate of the Galactic CCSNR relies on the historical records. Historical documentation reports five SNe in the MW over the past millennium: SN1006 (Type Ia), SN1054 (CCSN), SN1181 (CCSN), SN1572 (Type Ia), and SN1604 (Type Ia). In their work, [Tammann et al., 1994] derived the CCSNe by combining the observed historical SNe with rate measured in other galaxies. By assuming that about 85% of SN events are CCSNe, they found a Galactic rate of $2.1(100\text{yr})^{-1}$.
A similar methodology was applied by [Adams et al., 2013]. They used updated Galactic stellar population models and modern dust maps, performing Monte Carlo simulations to reproduce the spatial and dust distributions for SNe. Assuming a Salpeter IMF and progenitor masses between 8-100 $M_{\odot}$, they derived a cumulative apparent magnitude distribution that, combined with the historical SNe, suggested a CCSNR of $3.2^{+7.3}_{-2.6}(100\text{yr})^{-1}$.

Following this, the most recent measurement based on this approach was performed by [Murphey et al., 2021]. Modeling the visibility of naked-eye of SNe events and combining this with the distributions from [Adams et al., 2013], they found that almost 33% of CCSNe would be visible within our Galaxy at magnitude limit $m_{V,lim}$=-2 mag. Then, inferring their magnitude distribution with the historical SNe, the rate estimates ielded a value of $1.4^{+1.6}_{-0.9}(100\text{yr})^{-1}$.

Another strategy to extrapolate the rate is to estimate its value in samples of galaxies of different Hubble types and then normalizing it to B- or K-band galaxy luminosity. Independent measurements, based on different assumptions on the MW morphology and extragalactic SN surveys, yield consistent results. From rate measurements in over 10,000 galaxies and assuming the MW is an Sb±0.5 system with luminosity 2.0 ±0.6[10] [van den Bergh and McClure, 1994], [Cappellaro et al., 1993] derived a Galactic CCSNR of 1.7 ±1.0 (100 yr)$^{-1}$. Similarly, [van den Bergh and McClure, 1994] analyzing 800 galaxies from the Shapley-Ames catalogue and assuming the MW resembles an Sbc system, obtained a total SN rate of 3.0 ± 1.0 (100 yr)$^{-1}$, corresponding to a CCSNR of 2.4–2.7 ±0.9 (100 yr)$^{-1}$, when 80–90% of all SNe are assumed to be core-collapse events. Consistent results were found by [Li et al., 2011], who used LOSS survey data and adopted similar Galactic parameters, finding a value of 2.30 ± 0.48 (100 yr)$^{-1}$.

Additional constraints have been derived from the local birthrate of massive stars. Based on a census of about 420 O3–B2 dwarfs within a volume of 1.5 kpc from the Sun to a limiting magnitude M_V=-8 mag, [Reed, 2005] estimated a massive star birthrate by adopting a two-component "disk + hole" model for the stellar density distribution, along with models for extinction and main-sequence star lifetime. From the birthrate, of about 7.86 $\times 10^6 \text{yr}^{-1}$ kpc^{-3} in the plane, assuming a mass-cutoff for progenitors at 10 $M_\odot$, the CCSNR was of 1–2 (100 yr)$^{-1}$. Similarly to [Reed, 2005], [Quintana et al., 2025] conducted a census of OB stars within 1 kpc of the Sun. By adopting the same plane density function, ρ_{plane}, introduced by [Reed, 2005], they extrapolated the CCSNR from their measured OB star density. The resulting CCSNR is 0.5 ± 0.1 (100 yr)$^{-1}$, roughly half the value reported by [Reed, 2005]. This discrepancy arises from several factors. First [Quintana et al., 2025] used a smaller sample, moreover [Reed, 2005] included O3–B2 stars and adopted non-rotating stellar evolutionary models, therby shortening the stellar lifetimes.

Estimates based on the birthrate of NS tend to be higher. A synthesis of NS population studies, including magnetars, radio pulsars, RRATs, XDINSs, and X-ray binaries [Keane and Kramer, 2008], yields an average rate of 7.2 (100yr)$^{-1}$, using the NE2001 Galactic electron density model. This value exceeds most other CCSNR determinations, suggesting the presence of a "neutron star birthrate problem." Conversely, analyses of Galactic SN remnants provide much lower values. Approximately 300 remnants have been observed within the MW, however only a small sample has been characterized. Modeling a subsample of 43 well-characterized remnants with known distances and temperatures [Leahy et al., 2020] gives a rate of 1/260 yr, or 1/160 yr when including an extended sample. After correcting for incompleteness in X-ray detections, the inferred CCSNR becomes ∼0.43 (100 yr)$^{-1}$, likely an underestimate due to observational biases.

Further constraints come from radioactive isotopes. By mapping the Galactic gamma-ray emission from the decay of ^{26}Al, [Diehl et al., 2006] found that this is primarily concentrated along the plane, suggesting that CCSNe are major contributors to this isotope. Using a Scalo IMF ($\phi(m) \sim m^{-2.7}$) and a progenitor mass range of 10–120 $M_\odot$, the inferred CCSNR is (1.9 ± 1.1) (100 yr)$^{-1}$.

Finally, [Rozwadowska et al., 2021] obtained a more precise estimate by combining the measurements from the literature over the past twenty years with direct information on

Table 6.2.1: Galactic CCSNR stimates grouped by methodology.

Method	**Reference**	**CCSNR** $100yr^{-1}$
Historical Supernovae	Tammann et al. [1994]	2.1
	Adams et al. [2013]	$3.2^{+7.3}_{-2.6}$
	Murphey et al. [2021]	$1.4^{+1.6}_{-0.9}$
Extragalactic SN Surveys	Cappellaro et al. [1993]	1.7 ± 1.0
	van den Bergh and McClure [1994]	$2.4–2.7 \pm 0.9$
	Li et al. [2011]	2.30 ± 0.48
Massive Star Birthrate	Reed [2005]	1–2
	Quintana et al. [2025]	0.5 ± 0.1
Neutron Star Birthrate	Keane and Kramer [2008]	7.2
Supernova Remnants	Leahy et al. [2020]	~ 0.43
Radioactive Isotopes	Diehl et al. [2006]	1.9 ± 1.1
Combined Bayesian Estimates	Rozwadowska et al. [2021]	1.63 ± 0.46

the CCSNR from historical SNe in the Local Group. The first attempt to estimate the CCSNR is based on the values from: i) counts of massive stars, ii) the NS birthrate, iii) CCSNR measurement from a large galaxy sample, iv) Galactic enrichment of ^{26}Al. The CCSNR obtained by multiplying the likelihood functions of these different estimates is 1.79 $\pm$0.55 $(100\text{yr})^{-1}$. The second estimate considers: i) the Galactic CCSNR from historical records adopting the fraction of visible CCSNe by [Murphey et al., 2021], ii) the CCSNR fromneutrino observations of the MW, iii) CCSNR in M31 galaxy, iv) CCSNR in other galaxies within the Local Group. This combination yield a range of [0.66 - 2.04] $(100\text{yr})^{-1}$. Then by incorporating both results, the authors performed a global fit, obtaining a CCSNR of $1.63 \pm 0.46(100\text{yr})^{-1}$.
In Table 6.2.1 we summarized all the Galactic CCSNR estimates in the literature.

Rate measurements from the progenitor simulation

An alternative approach to derive the expected CCSNR within the MW is simulate a progenitor population. To estimate the rate value, we employed the `TRILEGAL` catalog of massive stars introduced in Section 6.1. We divided our data sample into mass bins to account for the mass-dependent variation in stellar lifetimes, and identified those within the final 3 Myr of their evolutionary lifespan, defined here as *near-explosion* candidates.

Table 6.2.2: Properties of each mass bin of the simulation.

Mass Bin $M_\odot$	Age Range Myr	Cut Age Myr	% Near Expl
9–11	0.10 – 32.89	29.89	0.68%
11–13	0.10 – 23.01	20.01	1.64%
13–15	0.10 – 17.66	14.66	6.90%
15–17	0.10 – 14.35	11.35	10.35%
17–21	0.10 – 12.25	9.25	10.32%
21–5	0.10 – 9.27	6.27	23.48%

Figure 6.3 shows the age distribution for each mass bin, while Figure 6.4 displays the spatial distribution of the full simulated sample and the corresponding near-explosion

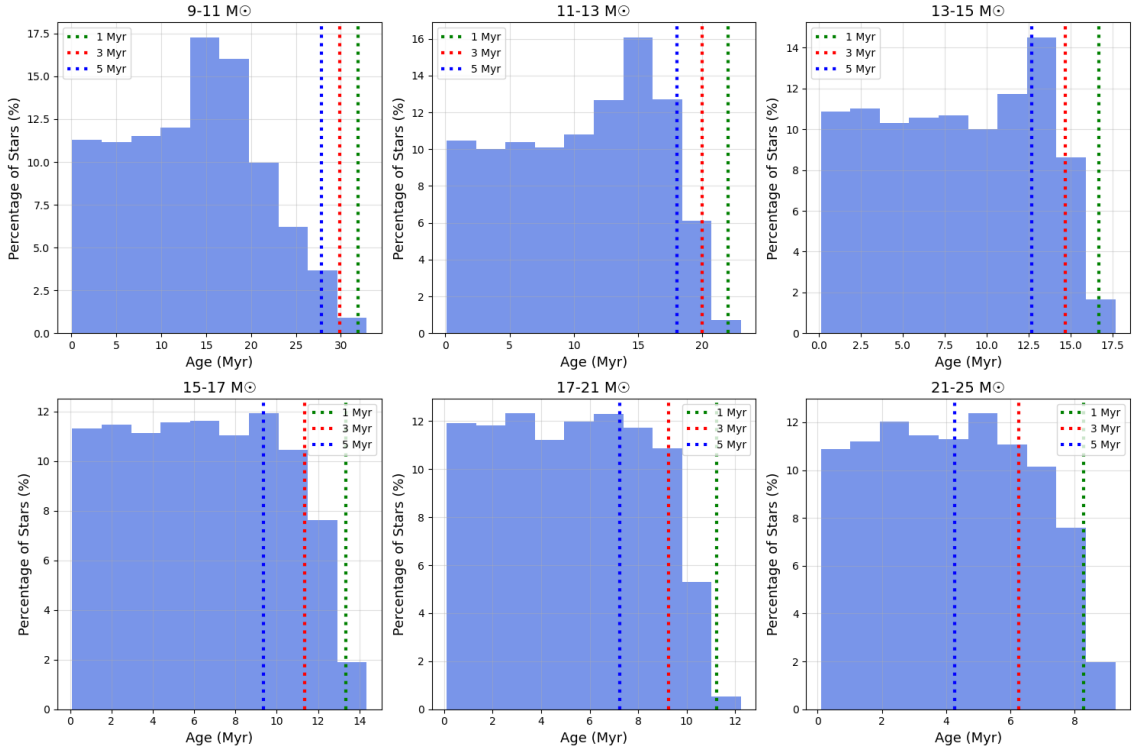


Figure 6.3: Age distribution of the mass bins. In blue is shown the age cut at the last 5 Myr of the total distribution. In red and green are shown the cuts at 3 Myr and 1 Myr respectively.

subsample. The progenitors are mostly localized within the thick and thin disk, consistently with the usual environments of CCSNe. This selection across all the complete mass range reduced the number of progenitors to a sub-sample of potentially *near-explosion* candidates (see Table 6.2.2). By normalizing their number over the 3Myr range, this preliminar analysis produced an intrinsic CCSNR of 0.17 ± 0.003 (100^{-1}yr) where the uncertainty is the Poissonian error. However, this value is significantly lower than the indirect CCSNR estimates discussed in the previous section. Although our result is marginally consistent with the lower estimate of [Quintana et al., 2025], several sources of uncertainties likely contribute to the discrepancy.
For example, the choice of a 3 Myr window for defining near-explosion candidates is intrinsically arbitrary and can influence the inferred rate. To assess this, we repeated the analysis adopting alternative cuts of 5 Myr and 1 Myr on the total lifespan for each bin. These yield CCSNR values of 0.3 ± 0.02 and 0.03 ± 0.001 per century, respectively.
Neverthless, for the following horizon and SNR analysis we will consider the 3 Myr cut, as it provides a statistically significant sample.

6.3 CCSN Waveforms

To capture the broad phenomenology of GWs from CCSNe, we employed two complementary waveform catalogs derived using `Fornax`, a state-of-the-art radiation-hydrodynamics simulation framework. `Fornax` includes detailed microphysics, neutrino transport, and general relativistic effects to model CCSN dynamics.
The two waveform sets are from Radice et al. (2019) [Radice et al., 2019] and Vartanyan et

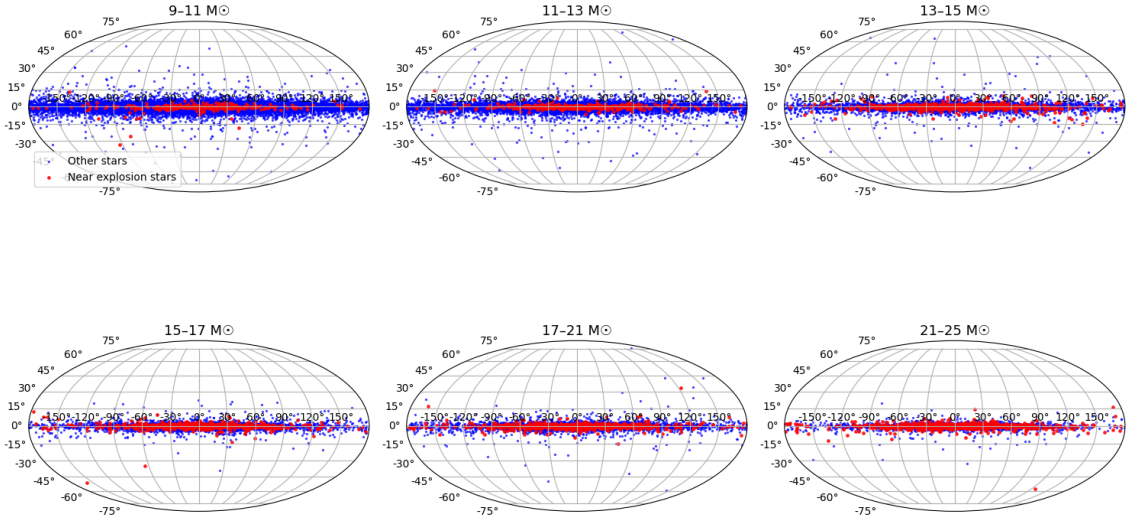
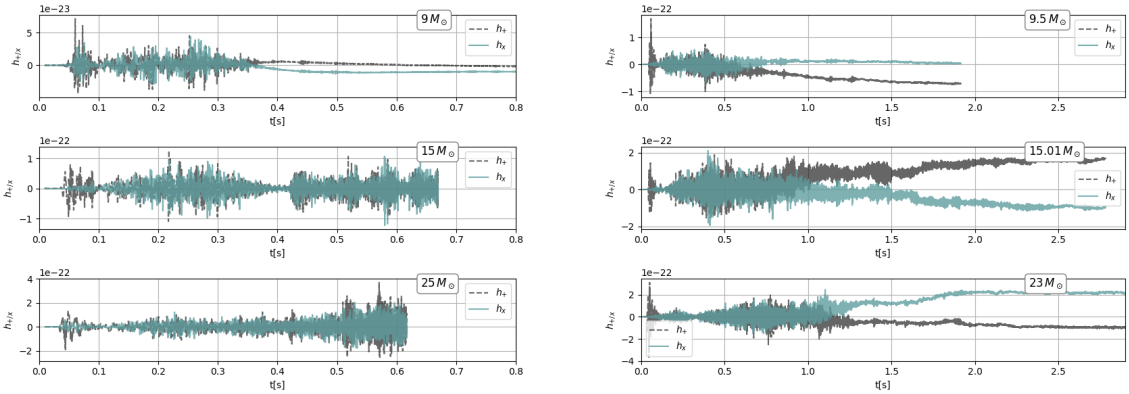


Figure 6.4: Spatial distribution of the TRILEGAL simulated sample for each mass bin employed in the rate analysis. The *near-explosions* subsample is shown in red.



(a) Waveforms simulated from [Radice et al., 2019].

(b) Waveforms simulated from [Vartanyan et al., 2023].

Figure 6.5: Representative GWs used in this work. For each simulation set, we present three progenitors sampling the low- and high-mass ends and an intermediate mass of our selected range.

al. (2023) [Vartanyan et al., 2023], and are summarized in Table 6.3.1. Together, they span a progenitor mass range of 9–25 $M_\odot$ and provide complementary insights into different stages of GW emission.

The simulations from [Radice et al., 2019] (Figure 6.5a) focus on the early to intermediate post-bounce evolution, spanning from 500 ms to just over one second. These simulations emphasize how the initial phases of GW emission are dominated by the g- and f- mode in the periphery of the PNS. The SASI feature is only observed in the more massive 25$M_\odot$ progenitor within this set. For consistency with our rate estimates and to remain within a comparable mass range, we exclude their 60$M_\odot$ model from our analysis.

In contrast, the second set from [Vartanyan et al., 2023] extends the coverage into the late-time evolution, following the CCSN event beyond the prompt emission phase through to explosion or black hole formation. This longer timescale approach (up to several seconds post-bounce) captures continued PNS oscillations and late-time dynamical features that

Table 6.3.1: Details of the CCSN waveform sample.

M_{star} ($M_\odot$)	Index	Duration (s)	Software	Reference
9	9BW	1.03		
9	9TH	1.33		
9	9a	1.76		
9	9b	2.00		
9.25	9.25	2.78		
9.5	9.5	1.90	FORNAX	[Vartanyan et al., 2023]
11	11	4.44		
12.25	12.25	2.05		
14	14	1.02		
15.01	15.01	2.77		
23	23	6.18		
9	s9	1.04		
10	s10	0.76		
11	s11	0.56		
12	s12	0.54		
13	s13	0.50	FORNAX	[Radice et al., 2019]
14	s14	0.73		
15	s15	0.66		
19	s19	0.86		
25	s25	0.61		

shape the gravitational waveform during the full duration of the event (Figure 6.5b).These simulations indicate that the majority of GW energy is carried by the f- and g-mode oscillations of the PNS, whose characteristic frequency increases steadily as the PNS contracts over time. These modes are predominantly excited by accretion plumes striking the surface of the PNS, which not only stimulate coherent oscillations but also contribute to a broadband high-frequency component, correlated with the episodic nature of violent accretion.

Together, these waveform catalogs cover a broad range of progenitor masses (9–25 $M_\odot$) and CCSN evolutionary stages, enabling a comprehensive analysis of GW emission across both prompt and late-time phases of CCSNe.

6.4 GWFISH

To asses the CCSN detectability from the ET we employed `GWFish` framework [Dupletsa et al., 2023][2], a Fisher matrix-based simulation software developed for evaluating parameter estimation and detection capabilities of GW detectors. `GWFish` offers the flexibility to define detector networks, noise power spectral densities (PSDs) and waveform models. The code has been primarily used for well-modeled sources such as compact binary coalescences, where the Fisher matrix approach provides reliable uncertainty estimates under Gaussian noise assumptions.

[2]https://github.com/janosch314/GWFish

The stochastic nature of CCSNe introduces new challenges, due to turbulent hydrodynamics, neutrino-driven convection and multi-dimensional instabilities. This make them poorly suited to Fisher matrix analyses, nevertheless `GWFish` includes a dedicated horizon estimation module that can still provide meaningful results for stochastic waveforms. In this context, the *horizon* is the maximum luminosity distance at which a GW signal can be detected with a given signal-to-noise ratio (SNR) threshold, while the SNR is defined as

$$\mathrm{SNR}^2 = 4 \int \mathrm{d}f \frac{|\tilde{h}(f)|^2}{S_n(f)} \tag{6.4.1}$$

where $S_n(f)$ is the one-sided noise PSD of the detector and $\tilde{h}(f)$ is the frequency domain signal projected onto the detector. Usually the SNR quantifies how well the observed data d matches a given GW model h an under ideal Gaussian noise and excluding glitches, it follows a χ^2 distribution. However, the detector noise is non-Gaussian and affected by glitches. Since future noise realizations cannot be predicted, horizon estimates typically adopt an SNR threshold in the range 8–12. This range has a limited effect on the final horizon distance, and we use a confident value of 10 as threshold throughout this work. `GWFish` incorporates cosmological effects into horizon computations by accounting for the redshift dependence of the waveform. At cosmological distances, the gravitational waveform amplitude scales as $1/d_L$ instead of the Newtonian $1/r$, where d_L is the luminosity distance. As a result, determining the detection horizon requires solving the following equation numerically:

$$SNR^* = SNR(z, d_L) \tag{6.4.2}$$

where SNR^* is the detection threshold. `GWFish` addresses this by using a root-finding algorithm to compute the luminosity distance at which the target SNR is achieved, given a specific cosmological model.

For CCSNe, whose GW signals are typically concentrated in the kilo-Hertz regime, accurate modeling of the *detector transfer function* is essential. The commonly used long-wavelength approximation, which assumes a unity transfer function at all frequencies, breaks down at characteristic frequencies $f_c = c/(2\pi L)$, where L is the detector arm length. As shown in [Dhani et al., 2025], the ET transfer function deviates significantly from unity at kHz frequencies, leading to reduced sensitivity in this regime. `GWFish` explicitly incorporates these high-frequency corrections, which are crucial for reliable horizon estimates for CCSNe.

To enable horizon estimation for CCSNe, we extended `GWFish` to interface with our hydrodynamical time-domain waveform catalogue and with the simulated spatial distribution of CCSN progenitors (see Sections 6.1 and 6.3). For each near-explosion candidate in our simulated population, we assign a CCSN waveform by selecting the one corresponding to the *closest progenitor mass* in the catalogue. This approach allows us to make the best possible use of a limited set of available waveforms. Although this matching can sometimes overestimate or underestimate the signal energy for certain progenitor masses, it provides a reasonable first-order approximation of the expected SNR distribution.

For each source in the simulation `GWFISH` requires its right ascension (RA), declination (Dec), distance and progenitor mass. In addition to these parameters, we randomize the *event detection time*, since neither the timing nor the phase of a real CCSN signal relative to the detector can be predicted. `GWFish` computes the detector response by projecting each strain signal onto the ET (or network) antenna pattern given the source's sky position and the chosen event time. Because the Earth's rotation and orbital motion continuously alter the detector's orientation relative to each source, we evaluate SNRs over multiple geocentric times to capture realistic temporal variations.

The resulting SNR map provides a statistical description of detectability across the simulated population. Since this approach does not employ matched filtering, our SNR estimates should be considered *lower bounds*. Importantly, our methodology acknowledges the intrinsic uncertainties in CCSN waveform modeling. Given the current state of CCSN modeling, our matching strategy represents the most robust approximation achievable. While no previous study has yet performed a direct simulation-based estimate of the joint detection probability of GW and EM counterparts for CCSNe, our framework establishes the necessary foundation for such analysis. This could be extended to evaluate, for instance, the likelihood of optical detection given a GW trigger under realistic survey coverage and pointing constraints.

6.5 Results

To assess detectability within the MW, we employed `GWFISH` to derive an SNR distribution and detection horizons by injecting the simulated sources at sky positions sampled from the massive star distribution discussed in Section 6.1 and the two set of waveforms described in Section 6.3. We examined four detector/network configurations, comparing in particular the ET designs, the 10 km triangular (Δ) configuration and the 15 km dual-L (2L) layout, operating both independently and in combination with the 40km CE.

Table 6.5.1: Detection horizon at SNR = 10 for CCSN waveforms of different progenitor masses for both the 2L and triangular configurations. We indicate the median d_L value together with the 90% confidence level.

Mass	ET		ET+CE40	
$M_\odot$	*kpc*	*kpc*	*kpc*	*kpc*
	2L	Triangle	2L	Triangle
9	$19.1^{+12.4}_{-8.0}$	$16.2^{+10.2}_{-7.1}$	$28.4^{+7.2}_{-10.3}$	$26.5^{+5.0}_{-10.2}$
9.25	$31.0^{+19.6}_{-12.0}$	$26.8^{+16.8}_{-10.6}$	$46.6^{+10.5}_{-16.7}$	$43.6^{+8.0}_{-15.9}$
9.50	$42.6^{+28.0}_{-20.5}$	$36.0^{+23.0}_{-17.7}$	$62.0^{+19.9}_{-23.2}$	$57.2^{+19.3}_{-22.5}$
10	$60.4^{+38.6}_{-23.3}$	$53.5^{+33.8}_{-20.9}$	$91.4^{+20.6}_{-32.6}$	$86.4^{+16.3}_{-31.4}$
11	$85.1^{+55.7}_{-38.1}$	$73.0^{+46.2}_{-33.1}$	$125.7^{+36.4}_{-46.2}$	$118.1^{+32.3}_{-45.4}$
12.25	$46.9^{+30.1}_{-19.6}$	$41.8^{+26.3}_{-18.1}$	$68.8^{+17.8}_{-24.9}$	$65.7^{+12.9}_{-24.5}$
13	$55.7^{+36.0}_{-23.6}$	$47.1^{+29.9}_{-20.1}$	$83.0^{+21.5}_{-30.0}$	$77.5^{+16.4}_{-29.5}$
14	$64.5^{+42.9}_{-34.2}$	$54.0^{+35.0}_{-29.4}$	$93.1^{+36.3}_{-35.1}$	$84.5^{+36.2}_{-33.5}$
15.01	$105.8^{+67.5}_{-43.2}$	$92.9^{+58.6}_{-38.1}$	$158.8^{+38.8}_{-57.3}$	$150.4^{+29.0}_{-55.4}$
19	$115.0^{+73.2}_{-45.5}$	$102.6^{+64.7}_{-41.3}$	$172.5^{+40.5}_{-61.8}$	$164.7^{+30.0}_{-60.3}$
23	$98.9^{+64.6}_{-46.7}$	$85.2^{+54.5}_{-41.3}$	$145.5^{+44.2}_{-54.9}$	$136.0^{+41.3}_{-53.5}$
25	$94.5^{+61.6}_{-41.9}$	$83.5^{+52.8}_{-37.9}$	$139.6^{+38.4}_{-51.0}$	$132.3^{+31.0}_{-51.3}$

In Table 6.5.1 we present the detection horizons at SNR = 10 for all waveform models and network configurations. Although the horizon generally increases with progenitor mass, the trend is not strictly monotonic due to model-dependent variations in waveform morphology and explosion dynamics. One first result is that the inclusion of CE40 significantly improves the horizon, by roughly 45–50%, extending the detection range well beyond the MW and enabling realistic prospects for multimessenger observations of extragalactic CCSNe. In Figure 6.6 we compared the performance of the two ET configurations in both scenarios for one of the best cases, the 25 $M_\odot$. The 2L 15 km layout yields a modest enhancement

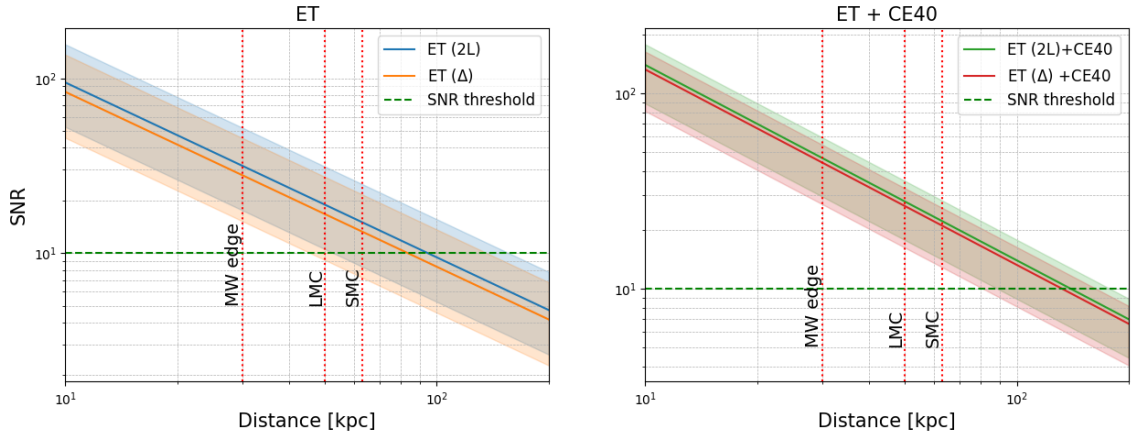


Figure 6.6: Horizon as a function of the SNR for the 25 $M_{\odot}$ waveform from [Radice et al., 2019]. In the left plot we compare the performances of the two ET designs, in the right panel the comparison is between the ET designs combined with CE.

(15–20%) relative to the triangular configuration when ET operates alone, and a smaller but still noticeable improvement (5–10%) in a network with CE40. While CE tends to mitigate the differences between ET designs in network mode, the performance gain remains relevant for standalone ET observations, particularly for lower-mass progenitors close to the detectability threshold. To explore in more detail the detectability of a Galactic CCSN, we constructed a two-dimensional SNR probability map over Galactic coordinates using kernel density estimation applied to our source injections (Figure 6.7). This map highlights regions where SNR values exceed the detection threshold (SNR=10), indicating where high-confidence detections are most likely to occurr.

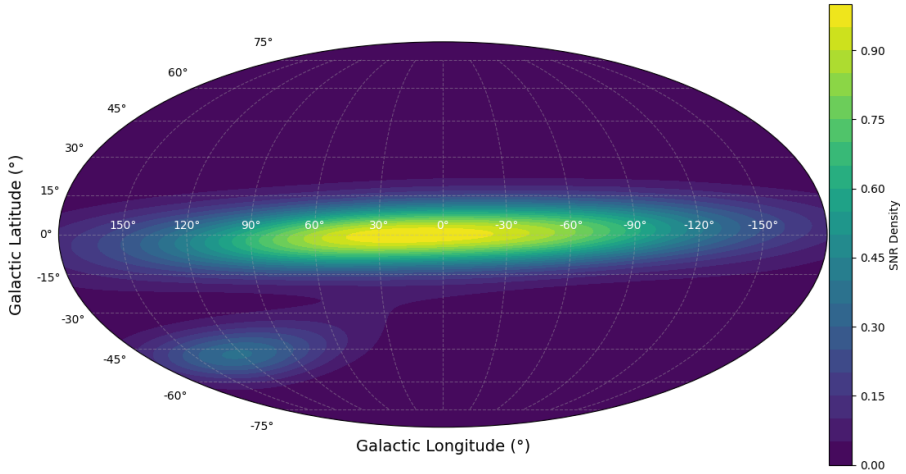


Figure 6.7: Probability map of the SNR exceeding the detection threshold.

We then compared the SNR density distribution with the spatial locations of the *near-explosion* candidate stars introduced in Section 6.1 (Figure 6.8). The comparison shows that most progenitors lie in regions in which ET achieves SNR > 10, suggesting that the next Galactic CCSN would be detectable via GWs also for CCSNe missed by optical searches, obscured by dust.
The spatial distribution in Figure 6.8 also reveals a decline in SNR with increasing distance

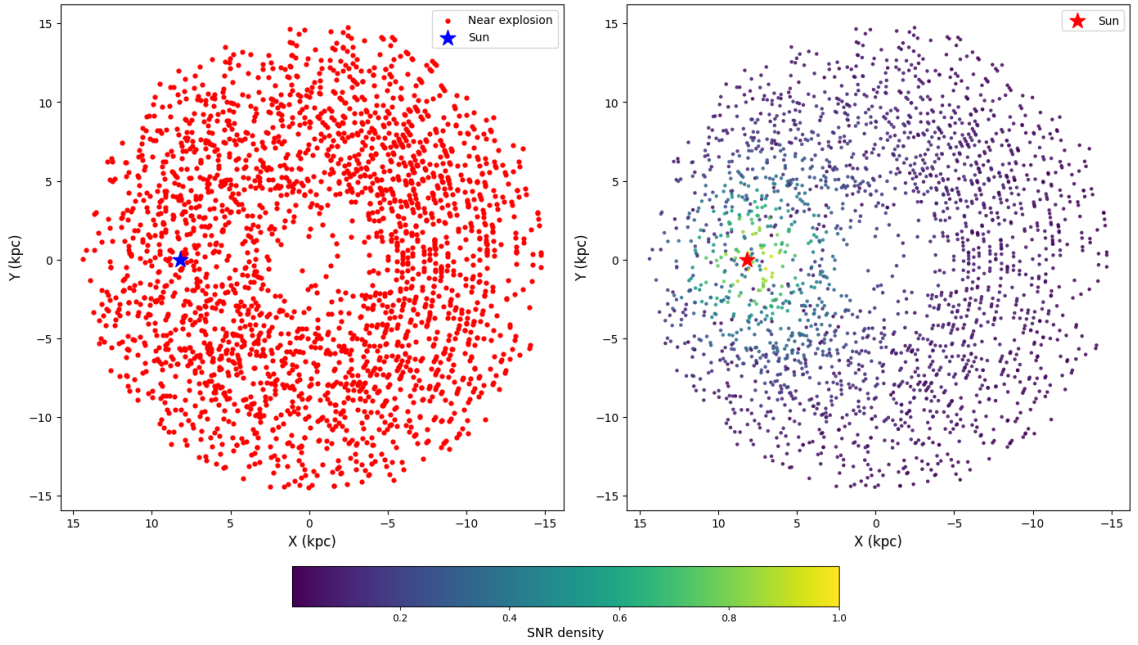


Figure 6.8: Comparison between the progenitor distribution and the SNR density distribution. The left panel shows how the progenitors (in red) are well distributed across the Galactic disk. The face-on SNR map (right) shows that ET yields an SNR above the detection threshold in the same regions.

d_L, consistent with the expected $1/d_L$ scaling of the strain amplitude, and clearly visible in Figure 6.6. Finally, to assess the detectability of Galactic CCSNe in the absence of EM counterpart, we analyzed the impact of interstellar dust extinction on CCSNe detections. To model dust absorption across the MW, we employed the all-sky Galactic extinction map released by the *Planck* Collaboration [Abergel et al., 2014]. The extinction A_V was derived from the dust optical depth at 353 GHz (τ_{353}) following their calibration

$$A_V = R_V \times 1.49 \times 10^4 \, \tau_{353}, \tag{6.5.1}$$

and adopting $R_V = 3.1$. Extinction in the B-band was then obtained using the Cardelli relation [Cardelli et al., 1989]

$$A_B = 1.323 \, A_V. \tag{6.5.2}$$

Because our progenitor population model does not explicitly assign the intrinsic luminosity of the subsequent CCSN, we associated to each near-explosion star an intrinsic CCSN peak magnitude from a Gaussian distribution centered at $M_B = -17$ mag with $\sigma = 0.9$, averagin the values for different CCSN types from [Richardson et al., 2002]. The apparent magnitude was then computed as

$$m_B = M_B + \mu + A_B, \tag{6.5.3}$$

where μ is the distance modulus, generated by the `TRILEGAL` simulation, and A_B is the line-of-sight dust extinction extracted from the Planck map at the angular coordinates of each progenitor.
Figure 6.9 shows the distribution of progenitors that would remain undetectable in optical surveys with a fiducial limiting magnitude of $m_{\mathrm{B,lim}} = 22 mag$.
Under these assumptions, approximately $\sim 50\%$ of all potential CCSNe in the Galaxy would be too heavily obscured to be detected, particularly toward the inner disk where

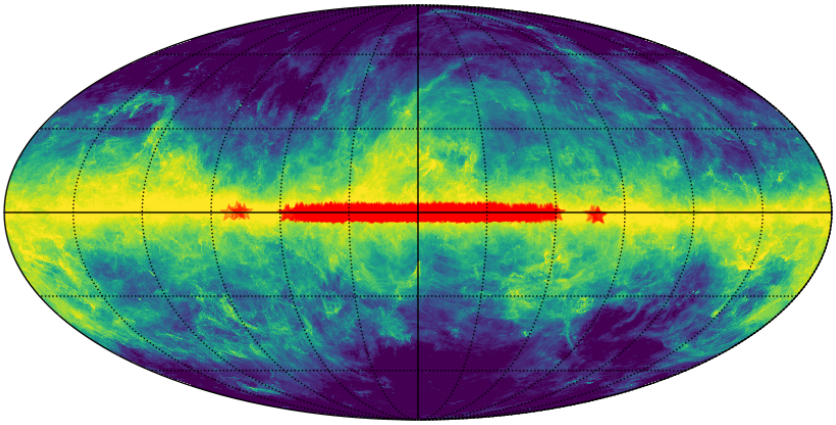


Figure 6.9: Sky distribution of near-explosion progenitors projected onto the *Planck* τ_{353} map. The red stars represent the sources whose expected CCSN peak magnitude falls below the limit $m_{\mathrm{B,lim}} = 22$ mag once dust extinction is included.

dust density peaks. This result, more evident in Figure 6.10, highlights the essential role of GW observations as an extinction independent probe of core-collapse events, especially in the regions of the MW where dust absorption is most severe.

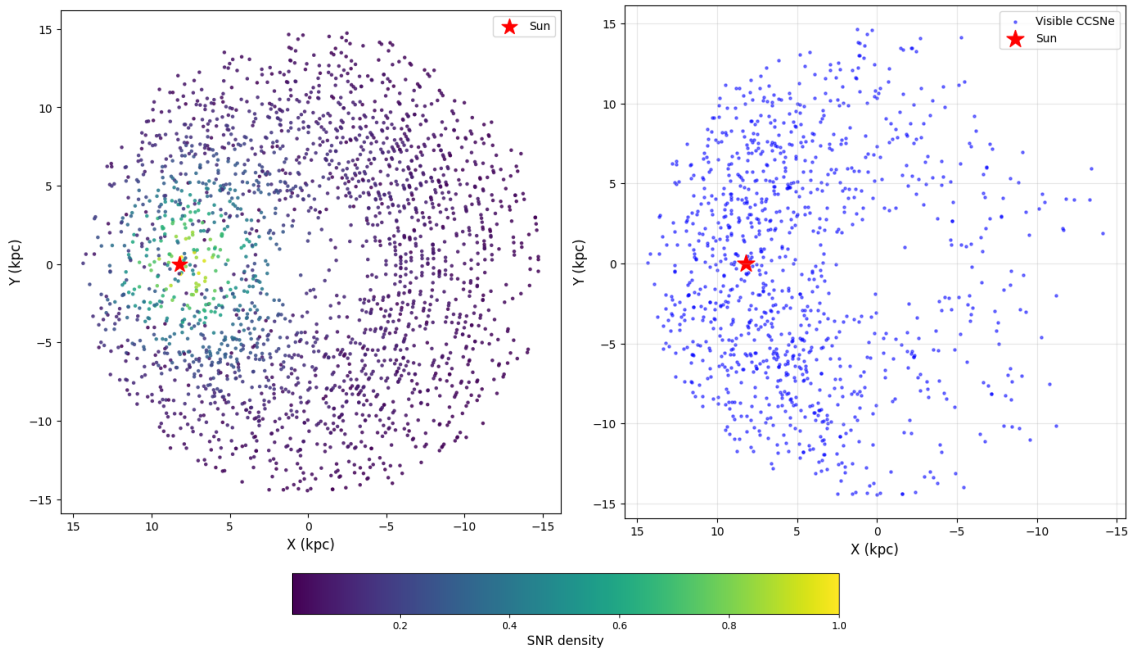


Figure 6.10: Comparison between the SNR density and the spatial distribution of the CCSNe visible from optical searches.

To quantify the impact of the uncertainty in the intrinsic luminosity of CCSNe, we repeated the analysis using two other absolute magnitudes, $M_B = -19$ mag, and -15 mag, corresponding respectively to the bright and faint ends of the CCSN population. This yields a visibility fraction of

$$f_{\mathrm{vis}} = 45\% \pm 3 \tag{6.5.4}$$

where the upper and lower errors correspond to the fractions computed for $M_B = -19$

mag and $M_B = -15$ mag.

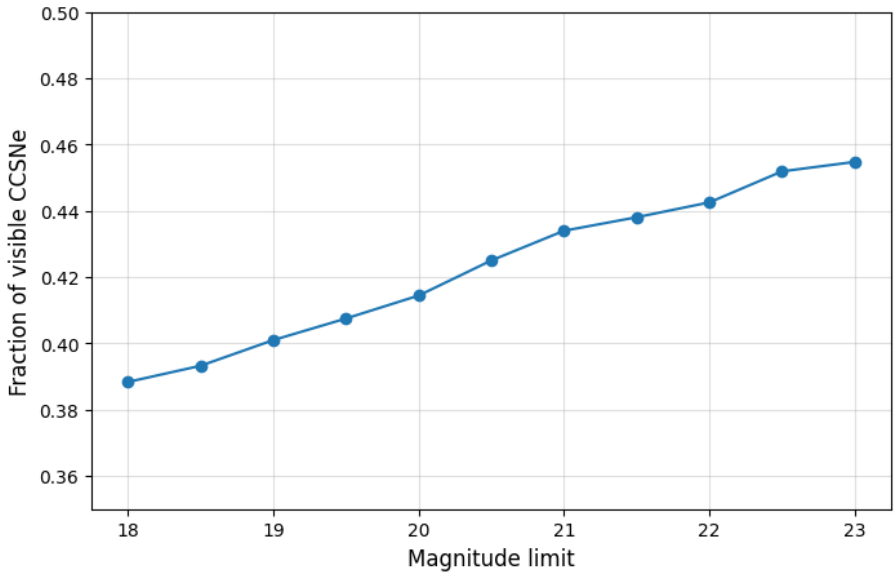


Figure 6.11: Fraction of CCSN progenitors expected to be detectable as a function of the survey limiting magnitude.

Finally, Figure 6.11 illustrates how the visibility fraction varies as a function of the survey limiting magnitude. As expected, surveys with magnitude limit lower than $m_{\rm lim} \approx 20$ mag recover only a minor fraction of Galactic CCSNe, while going beyond $m_{\rm lim} = 22$mag yields marginal improvements due to extinction dominated lines of sight.

6.6 Conclusions

In this Chapter, we analyzed the detectability of Galactic CCSNe with the ET. By combining a simulated progenitor population with state-of-the-art 3D CCSN waveform catalogs, we find that ET, in both triangular and 2L configurations, is expected to detect GWs from the next Galactic CCSN with high confidence (Figure 6.8). Many CCSN progenitors appeared to be concentrated toward the Galactic center, where interstellar dust can severely obscure EM signals. GWs then provide an unobstructed view of these events, enabling detections independent of optical detectability (Figure 6.10).
The detection horizons derived from our analysis are based on a limited set of publicly available 3D simulations [Vartanyan et al., 2023, Radice et al., 2019]. Although these models span a broad range of progenitor masses, they do not provide a comprehensive sampling of the full diversity of CCSN waveforms. Current waveform modelling is still under development, and significant differences between models can strongly impact SNR predictions. Therefore, our results should be viewed as indicative of ET's performance under plausible scenarios.
Our study highlights the unique role of 3rd GW detectors in multimessenger campaigns: ET's ability to detect CCSNe independent of optical extinction, combined with the early-warning capabilities of future neutrino networks, will establish a framework for rapid and coordinated EM follow-up.

Chapter 7

Core-Collapse Supernova rate within the Local Universe

In the previous Chapter we presented our estimate of the detection horizon giving the current CCSN waveform simulations and ET designs. However, since the ET design is still under development, one of the long-term goals is to push its observational capabilities beyond the MW alone, enabling the detection of events occurring throughout the nearby extragalactic volume. In this perspective, obtaining a precise estimate of the CCSNR in the local Universe becomes essential for assessing the scientific potential of ET and for informing future observational and data-analysis strategies.
In this Chapter, we present our work on estimating the CCSNR within the local Universe, combining both direct and indirect measurements. This study is part of the Bluebook on the Scientific Prospects for the Einstein Telescope [Abac et al., 2025], which provides a comprehensive overview of the scientific cases for ET, contributed by various divisions of the Observational Science Board of the Einstein Telescope Collaboration. Specifically, the estimation of the CCSNR is discussed in Chapter 7 of the Bluebook, prepared by Division 7, Stellar Collapse and Spinning Neutron Stars.

The Chapter is organized as follows. In Section 7.1, the CCSNR is defined. In Section 7.2, the direct and indirect measurements used to obtain the rate estimate are outlined. In the following Section 7.3 a comparative analysis of the results obtained from the various approaches is presented.

7.1 Rate of CCSNe

The CCSNR is defined as the number of SNe exploding into a sample of galaxies normalized by the galaxies luminosity ($SN(100yr)^{-1}(10^{10}L_{B,\odot})^{-1}$), the mass, or the volume (SN yr^{-1}Mpc $^{-3}$). It can be expressed as the convolution of the SFH and a distribution of delay times $f_{\rm SN}(\tau)$, which describes the probability of early and late explosions after an instantaneous burst of star formation [Blanc and Greggio, 2008]

$$\mathrm{CCSNR}(t) = \int k(t-\tau)\,\psi(t)\,f_{\rm SN}(\tau)\,A_{\rm SN}(t-\tau)\,d\tau, \tag{7.1.1}$$

where k is the number of stars of generation τ per unit stellar mass, $A_{\rm SN}$ is the fraction of stars in the generation $(t-\tau)$ that can explode as SNe, $\psi(t)$ is the SFH.Since the lifetime of CCSN progenitors is short ($\tau < 0.5$ Gyr), the rate can be approximated as

$$\mathrm{CCSNR}(t) = A_{\rm CC}\,\psi(t), \tag{7.1.2}$$

where the factor $A_{\rm CC}$ is determined by the chosen stellar mass range and IMF ϕ (e.g., Salpeter)

$$A_{\rm CC}(\tau) = P_{\rm CC}(\tau)\,\frac{\int_{m_l^{CC}}^{m_u^{CC}}\phi(m,\tau)\,dm}{\int_{m_l}^{m_u} m\,\phi(m,\tau)\,dm}. \tag{7.1.3}$$

where $m_l - m_u$ is the mass range for the IMF and $m_l^{CC} - m_u^{CC}$ is the suitable mass range for CCSN. If we assume that

- all the suitable stars become CCSNe ($P_{\rm CC} = 1$);
- the delay time between progenitor formation and explosion is negligible;
- the IMF and the SFH are constant during $(t - \tau)$

then the equation simplifies to

$$CCSNR(t) = K_{\rm CC}\,\psi(t), \tag{7.1.4}$$

where the scaling factor $K_{\rm CC}$ represents the number of stars per unit mass that can produce a CCSN, once the IMF is chosen, and is defined as

$$K_{\rm CC} = \frac{\int_{m_l^{CC}}^{m_u^{CC}}\phi(m,\tau)\,dm}{\int_{m_l}^{m_u} m\,\phi(m,\tau)\,dm} \tag{7.1.5}$$

This relation provides a powerful diagnostic tool for studying both the progenitors of CCSNe and the star formation activity of galaxies. First by measuring both the CCSNR and the SFR in a given volume or galaxy sample, one can constrain the stellar mass range capable of producing CCSNe under a chosen IMF. On the other hand, since the final evolutionary stages of massive stars are extremely rapid, the CCSNR is tightly correlated with the SFR of the underlying stellar population and can be used as tracer of star formation. So assuming a progenitor mass range, the observed CCSNR can be used to infer the SFR of the analyzed region. From an observational point, the CCSNR is derived by counting the number of CCSNe in a galaxy sample or within a given survey search volume. A key ingredient in this measurement is the *control time* (C_t), defined as the period during which a SN remains detectable, i.e., when it is brighter than the limiting magnitude of the survey. The limiting magnitude depends on the instrument's characteristics but other factors, such as the light curve, dust extinction along the line of sight and the local environment, also influence detectability.
For a given galaxy j, the total control time for n observations is given by [Leaman et al., 2011]:

$$tC_j = \sum_{i=1}^{n} \Delta t_i c_i, \tag{7.1.6}$$

where

$$\Delta t_i = \begin{cases} C_{i,j}, & \text{if } t_i - t_{i-1} \geq C_{i,j}, \\ t_i - t_{i-1}, & \text{otherwise}, \end{cases} \tag{7.1.7}$$

and the index i refers to all observational epochs for a given SN in galaxy j.
To normalize the control time, it is convenient to weight it by the galaxy luminosity

$$t_j = tC_j\,L_j. \tag{7.1.8}$$

Then, for a sample of N_G galaxies, the rate becomes

$$\mathrm{CCSNR} = \frac{N_{\mathrm{SN}}}{\sum_{j=1}^{N_G} t_j}, \tag{7.1.9}$$

where N_{SN} is the number of detected CCSNe. Along with the control time, another crucial parameter is the survey coverage. While nearby CCSNe can be detected almost completely, incompleteness increases at higher redshift due to magnitude limits, dust extinction, k-corrections and crowding in host galaxies. To account for these effects, the *volumetric* CCSNR is used, defined as

$$\mathrm{CCSNR}(z) = \frac{1+z}{V(z)} \frac{N_{\mathrm{CCSN}}(z)}{CT_{\mathrm{CCSN}}(z)}, \tag{7.1.10}$$

where $N_{\mathrm{CCSN}}(z)$ is the number of CCSNe detected in a given redshift range, $CT_{\mathrm{CCSN}}(z)$ is the corresponding control time, and $V(z)$ is the comoving volume between z_1 and z_2, given by

$$V(z) = \frac{4\pi}{3} \frac{\Theta}{41253} \left[\frac{c}{H_0} \int_{z_1}^{z_2} \frac{dz'}{\sqrt{\Omega_M (1+z')^3 + \Omega_\Lambda}} \right]^3 \mathrm{Mpc}^3, \tag{7.1.11}$$

where Θ is the survey area in deg^2.

7.2 Current measurements

To estimate the number of CCSNe that the ET may detect, it is first necessary to determine their occurrence rate in the Local Universe. This rate can be inferred using several complementary approaches: directly, by counting CCSNe in a well-defined galaxy sample and applying an appropriate control time; indirectly, by combining measurements of the SFR with assumptions about the progenitor mass range; or by scaling rates derived from other surveys to the volumes of interest. In this study, we adopt all three strategies to obtain a comprehensive estimate of the CCSN rate. In practice, obtaining reliable measurements relies on the extensive monitoring of galaxies provided by modern transient surveys, which systematically discover and characterize CCSNe across the local Universe. Several dedicated programs have monitored the local Universe with regular cadences, improving both the frequency and depth of CCSN detections. Among the most prominent surveys are the Lick Observatory Supernova Search (LOSS)[Li et al., 2011], the Rapid Response System-PanSTARRS [Kaiser et al., 2002], and the All-Sky Automated Survey for SuperNovae (ASAS-SN). These programs leverage advancements in detector technology and automation to systematically search for transient phenomena across vast portions of the sky, enabling real-time discoveries and follow-up observations.
In particular, two modern surveys have set new benchmarks in the systematic detection of CCSNe. Since 2017, the Zwicky Transient Facility (ZTF) [Bellm et al., 2018] at the Palomar Observatory has been scanning the entire Northern sky every two days. ZTF achieves a median single-visit depth of 20.4 magnitudes (5-sigma) in the r-band, making it one of the most efficient wide-field transient detection systems. Operating alongside ZTF is the Asteroid Terrestrial-Impact Last Alert System (ATLAS)[Tonry et al., 2018], which consists of a global network of four telescopes: two in Hawaii, one in Chile and one in South Africa. ATLAS automatically surveys the entire sky multiple times each night, achieving a median depth of 19.5 magnitudes. This global coverage and rapid cadence make ATLAS particularly well-suited for detecting fast-evolving transients, including CCSNe. The contributions of

these surveys have not only increased the discovery rate of CCSNe but also enabled their detection at earlier stages, which is critical for studying progenitor properties and early explosion mechanisms. Furthermore, their large-scale systematic approaches allow for the identification of statistical trends in CCSN populations, contributing to our understanding of the star-formation history, galaxy evolution and the role of massive stars in shaping the Universe. Their impact on the number of discoveries is quantitatively evident in Figure 7.1, which highlights the substantial increase in detection rates following the advent of ZTF and ATLAS.

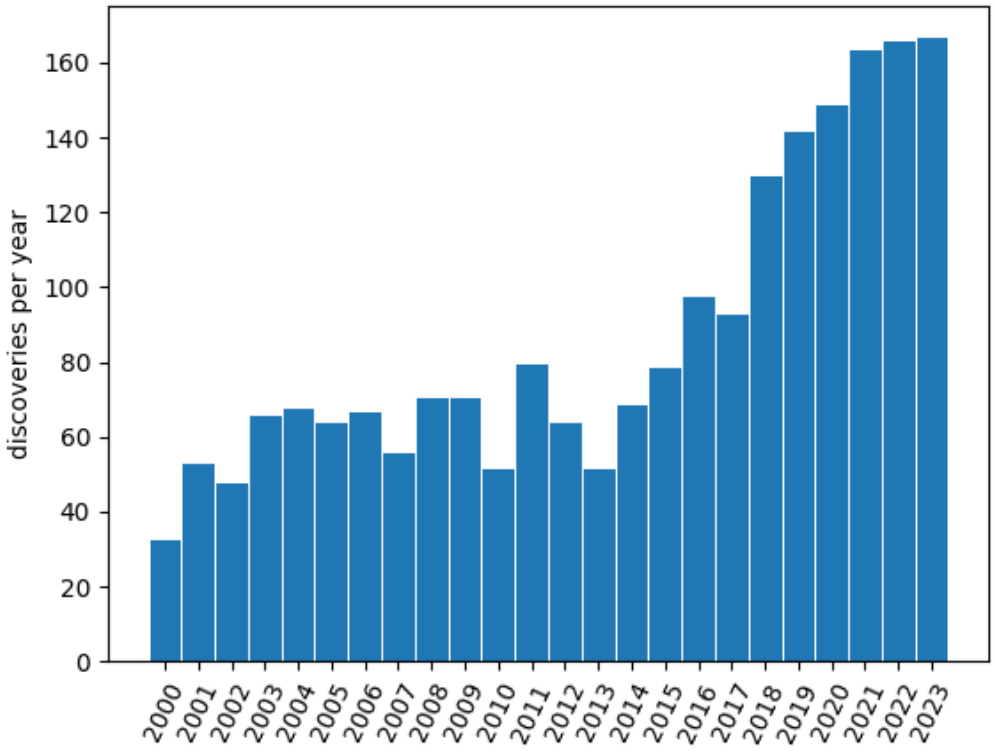


Figure 7.1: Detections of CCSNe between 2000 and 2023 within 100 Mpc.

7.2.1 Direct measurements

In order to derive the CCSNR from observational data, a catalogue was compiled of all CCSNe that occurred within different volumes (10 Mpc, 50 Mpc and 100 Mpc). The Supernova Catalogue of Asiago[1], which represents one of the most comprehensive archives up to 2017, and the Bright Supernova[2] and Transient Name Server[3] were employed in this study. For each event, data were collected regarding magnitude, redshift and host galaxy. In the case of the 10 Mpc volume, data were collected on events that occurred between 2000 and 2023 in order to increase the statistical sample size. Additionally, information was gathered on observed star formation rates, both in the H_α and UV bands. The complete CCSN sample within 10 Mpc is illustrated in Appendix A. For the 50 and 100 Mpc volumes,

[1] http://graspa.oapd.inaf.it/
[2] https://www.rochesterastronomy.org/
[3] https://www.wis-tns.org

our analysis was limited to the time interval between 2018 and 2023, in order to take account of the ZTF and ATLAS surveys.

The number of CCSNe discovered from 2000 to 2023 within 10 Mpc is 27, which led to a rate of $1.1^{+1.1}_{-0.6}$ events per year[4]. The number of CCSNe discovered from 2018 to 2023 within 50 and 100 Mpc are respectively 229 and 916, which give a rate of 38±3 and 153±5 events per year.

It is important to stress that the number of observed CCSNe represents a lower limit on the intrinsic number of CCSNe exploded in each volume for different reasons. The first and most relevant source of bias is the incompleteness of SN detection at larger distances. If the surveys were complete within the distance limits considered, we would expect the number of discoveries to scale with volume. However, we do not observe the rate scaling with volume, indicating that surveys become progressively less complete at greater distances. This incompleteness can be attributed in part to the faintness of some CCSNe, which fall below the detection limits of current surveys. To estimate the fraction of faint CCSNe missed by these surveys, we assumed an average limiting apparent magnitude of 20 mag for SNe, corresponding to absolute magnitudes of approximately -10 mag, -13 mag, and -15 mag at distances of 10 Mpc, 50 Mpc, and 100 Mpc, respectively. The cumulative luminosity function of CCSNe, as measured by LOSS[Li et al., 2011], indicates that about 20% of CCSNe are fainter than -15 mag, and approximately 5% are fainter than -13 mag. Based on this, we expect that local SN searches are nearly complete within 50 Mpc but miss about 20% of CCSNe occurring within 100 Mpc due to their faintness. Another source of incompleteness arise from SN candidates lacking spectroscopic classification. To evaluate the potential impact of these unclassified objects, we retrieved from TNS the number of unclassified SNe associated with galaxies within a distance of 20 Mpc. Among these, we identified 14 events, which we examined individually. In most cases, there was insufficient evidence to confirm that these candidates were indeed SNe. This supports the assumption that the incompleteness due to unclassified transients remains negligible out to at least 50 Mpc, given that nearby events are better monitored and more easily confirmed. However, from our sample, we estimated that approximately 35% of transients lack spectroscopic classification within a volume of 100 Mpc, implying that this effect becomes more significant at larger distances. Finally, another source depends on the fact that the surveys included in our analysis do not cover the entire sky. For the surveys considered, we estimated an average sky coverage of approximately 65%, corresponding to a correction factor of nearly 1.5. By accounting for the fraction of faint CCSNe missed by current surveys, the incompleteness due to unclassified transients, and the partial sky coverage, we infer that approximately 40% of CCSNe that explode within 100 Mpc remain undetected.

7.2.2 Indirect measurements

As anticipated in the beginning of this section, in order to derive indirect predictions regarding the number of CCSNe events that can be observed per year we can proceed

- by exploiting the CCSNR measured in other volumes;
- or, by inferring the volumetric rate derived from SFR measurements.

[4]To derive the Poissonian errors we referred to the confidential limits from Gehrels (1986)[Gehrels, 1986].

Lick Observatory Supernova Search volumetric rate

A value of the CCSNR within the Local Universe can be extrapolated from the volumetric CCSN rate by LOSS [Li et al., 2011]. LOSS was one of the most complete SN survey up to a redshift of $z \sim 0.5$, detecting SN events in galaxies different for Hubble type and colour. The volumetric rates for each kind of SN have been normalized for the galaxy luminosity functions of the two Hubble types:

$$j_{earlytype} = (2.25 \pm 0.36) \times 10^8 L_{\odot} Mpc^{-3} \tag{7.2.1}$$

$$j_{latetype} = (2.96 \pm 0.42) \times 10^8 L_{\odot} Mpc^{-3} \tag{7.2.2}$$

Since we are interested in CCSNe, we considered the Ib/c rate ($0.258^{+0.044}_{-0.058} \times 10^{-4}$ $\mathrm{Mpc^{-3}yr^{-1}}$) and the II rate ($0.447^{+0.068}_{-0.068} \times 10^{-4}$ $\mathrm{Mpc^{-3}yr^{-1}}$)[Li et al., 2011]. Their sum gave us the total CCSN volumetric rate of $0.7^{+0.11}_{-0.13} \times 10^{-4}$ $\mathrm{Mpc^{-3}yr^{-1}}$ at redshift $z \sim 0$. The total CCSN volumetric rate multiplied for the volumes within 10 Mpc, 50 Mpc and 100 Mpc gives a rate of 0.3±0.05, 37 ±6, 295±46 events per year respectively.

Rate from SFR measurements

The CCSNR can be also estimated by measuring the SFR and adopting: i) Salpeter IMF, defined as $\phi(m) = m^{\gamma}$ with $\gamma = -2.35$, constant across redshift and spanning a stellar mass range of $0.1 - 100$ $\mathrm{M_{\odot}}$; ii) a mass range of $9 - 25$ $\mathrm{M_{\odot}}$ for the CCSN progenitors. Using Equation 7.1.5, we derived the scaling factor $K_{CC_1} = 4.8 \times 10^{-3} \mathrm{M_{\odot}^{-1}}$. To estimate the CCSNR, we employed two distinct estimate for the extrapolation of the SFR within our volumes

- Direct SFR measurements from a galaxy sample;
- Parametric models of the Star Formation Density (SFD).

Additionally, we adopted a standard Λ-*Cold Dark Matter cosmology*, referred to as 737 cosmology, with $\mathrm{H_0} = 70$ km $\mathrm{s^{-1}Mpc^{-1}}$, $\Omega_M = 0.3$ and $\Omega_{\Lambda} = 0.7$.

SFR from measurements in a galaxy sample

We derived the SFR within specific volumes using different methodologies for the 10 Mpc and for the 50 and 100 Mpc volumes.

Within 10 Mpc, we calculated the total SFR by combining measurements of Hα, UV, and IR luminosities from the catalogues created by [Kennicutt Jr et al., 2008] and [Lee et al., 2010], respectively. These catalogues were constructed based on the findings of the 11Mpc H_{α} and Ultraviolet Galaxy Survey (11HUGS) [Funes et al., 2007] and Spitzer Space Telescope [Werner et al., 2004] observations. While the SFR_{UV} is directly accessible in the Lee's work, for the $SFR_{H_{\alpha}}$ evaluation we used the integrated H_{α} luminosity from the Kennicutt's catalogue and then the following conversion factor[Kennicutt Jr, 1998]

$$SFR(M_{\odot} yr^{-1}) = 7.9 \times 10^{-42} L(H_{\alpha})(ergs^{-1}) \tag{7.2.3}$$

Then to taking into account extinction we multiplied the previous relation for a scaling factor $10^{A(H_{\alpha})}$. The correction $A(H_{\alpha})$, for the galaxies in which Balmer lines have been measured, is included in the Lee's catalogue. When this value is not accessible, or when the Balmer lines measure has not been achieved, then the correction is evaluated as follows

$$A(H_{\alpha}) = \begin{cases} 0.10 \rightarrow M_B > -14.5 \\ 1.971 + 0.323 M_B + 0.0134 M_B^2 \rightarrow M_B \leq -14.5 \end{cases} \tag{7.2.4}$$

where M_B is the galaxy bolometric magnitude.

The rate measurements were obtained following the methodology described in [Botticella et al., 2012]. Depending on the luminosity tracer used, the CCSNR varies: adopting the SFR derived solely from Hα luminosity measurements yields a rate of 0.4 CCSN events per year, whereas using the SFR based on combined UV and IR luminosities increases the estimate to 0.6 events per year.
For the larger volumes, we adopted the SFD value from [Bothwell et al., 2011], which was derived using IR and UV measurements from a large sample of over 1000 galaxies. These galaxies were selected from the Imperial IRAS Faint Source Catalogue redshift database [Wang et al., 2014] and the GALEX All-Sky Imaging Survey [Bianchi et al., 2014]. The analysis accounted for both obscured and unobscured star formation, yielding an SFD value of 0.025 ± 0.0016 M$\odot$yr^{-1}Mpc^{-3} at $z \sim 0$, assuming a Salpeter IMF. To match our cosmological model, we applied a scaling factor of 0.72, resulting in an adjusted SFD value of 0.018 ± 0.015 M$\odot$yr^{-1}Mpc^{-3}. Using this value, we derived the following CCSN rates: 0.4±0.02 events per year within 10 Mpc, 45±3 events per year within 50 Mpc, and 362±23 events per year within 100 Mpc. Notably, the derived CCSN rate within 10 Mpc is consistent with the values estimated using Kennicutt's and Lee's measurements of the SFR in nearby galaxies.

SF Density models
For our analysis, we exploited two estimates from different evolutionary models of the cosmic SFD. The first approach relies on the model developed by [Madau and Dickinson, 2014], which is widely used for understanding the history of star formation in the universe. They analyzed data from a variety of galaxy surveys that measured the SFRs using rest-frame UV and MIR or FIR observations. These surveys, which include data from significant missions such as Spitzer and Herschel, provided crucial insights into star formation in both nearby and distant galaxies. Additionally, their model incorporates older measurements of local luminosity densities from the IRAS and GALEX missions. The combination of these data allowed the authors to develop a fitting function in a parametric form that captures the evolution of the SFD across different epochs:

$$\psi(z) = 0.015 \frac{(1+z)^{2.7}}{1 + [(1+z)/2.9]^{5.6}} M_{\odot} yr^{-1} Mpc^{-3} \tag{7.2.5}$$

By computing the SFR for the different redshifts of each volume of interest we obtained the following rates: 0.3 events per year within 10 Mpc, 42 events per year within 50 Mpc, and 365 events per year within 100 Mpc.
The second analytic function modeling the cosmic SFD is based on the work of [Hopkins and Beacom, 2006]. This approach builds upon a comprehensive collection of observational data, including FIR measurements from the Spitzer Space Telescope, UV observations from the Sloan Digital Sky Survey (SDSS) [Kent, 1994], GALEX, the COMBO-17 survey [Wolf et al., 2003], and the Hubble Ultra Deep Field (HUDF)[Beckwith et al., 2006] . Additionally, Hα-derived star formation rates at low redshift were also incorporated into the analysis. Hopkins & Beacom used these datasets to derive a parametric model of the cosmic SFD, fitting the data with the functional form of SFD equation proposed by [Cole et al., 2001]:

$$\psi(z) = \frac{(a+bz)h}{1 + (z/c)^d} M_{\odot} yr^{-1} Mpc^{-3} \tag{7.2.6}$$

In this equation the parameters a, b, c and d are fitted from the data and depend on the

chosen IMF. For the case of a Salpeter IMF A, the parameters are set to a=0.017, b=0.13, c= 3.3, and d=5.3. Furthermore, a scaling factor of 0.77 is applied when transitioning from the given results to a Salpeter IMF. This approach gave us the following rates: 0.3 events per year within 10 Mpc, 39 events per year within 50 Mpc, and 319 events per year within 100 Mpc.

7.3 Discussion

All the CCSNR measurements are summarized in Table 7.3.1 and their comparisons for each volume are illustrated in Figure 7.2. Notably, we observe that the measured CCSNR within 10 Mpc exceeds the estimaes from SFR by a factor of approximately 2–3. A similar result was reported in [Botticella et al., 2012], where the observed CCSN rate was also found to surpass them by a factor of about 2. This discrepancy is widely attributed to the local over-density of galaxies within 10 Mpc, which leads to a higher SFR and consequently a higher CCSNR compared to the cosmic average. This over-density has been well-documented in the literature. For example, the study by [Karachentsev et al., 2004] provided a comprehensive catalog of neighboring galaxies within 10 Mpc, showing that the number density of galaxies in this volume is significantly higher than in other regions of the local universe.
The indirect CCSN rates derived from SFR measurements and SFD models show a good agreement with the observed rate within 50 Mpc. However, they appear to overestimate the observed rate within 100 Mpc by a factor of approximately 2. This discrepancy could be attributed to several factors, like the events lacking spectroscopical classification and the incompleteness of the surveys, already discussed in Section 7.2.
Overall the results presented in this Chapter provide a comprehensive view of the current

Table 7.3.1: Estimates of the CCSNR per year within 10 Mpc, 50 Mpc and 100 Mpc. Indirect estimates are derived from the volumetric rate measured by LOSS and from different estimates of the total SFR in the same volumes. The observed rates are based on discovery reports.

	10 Mpc		**50 Mpc**		**100 Mpc**	
	SFR ($M_\odot$ yr^{-1})	CCSNR (yr^{-1})	SFR ($M_\odot$ yr^{-1})	CCSNR (yr^{-1})	SFR ($M_\odot$ yr^{-1})	CCSNR (yr^{-1})
Li et al. [2011]		0.29±0.05		37±6		295±47
Kennicutt Jr et al. [2008]	87±4	0.40±0.02				
Lee et al. [2010]	123±8	0.6±0.04				
Bothwell et al. [2011]	75±5	0.4±0.02	9420±602	45±3	75360±4814	362±23
Hopkins and Beacom [2006]	65	0.3	8836	42	76121	365
Madau and Dickinson [2014]	63	0.3	8059	39	66568	319
Observations		$1.1^{+1.7}_{-0.6}$		38±3		153±5

CCSNR in the Local Universe. The consistency between the different approaches strengthens the reliability of our rate estimates and offers a solid foundation for predicting the number of CCSN GW events expected to be detected by the ET.

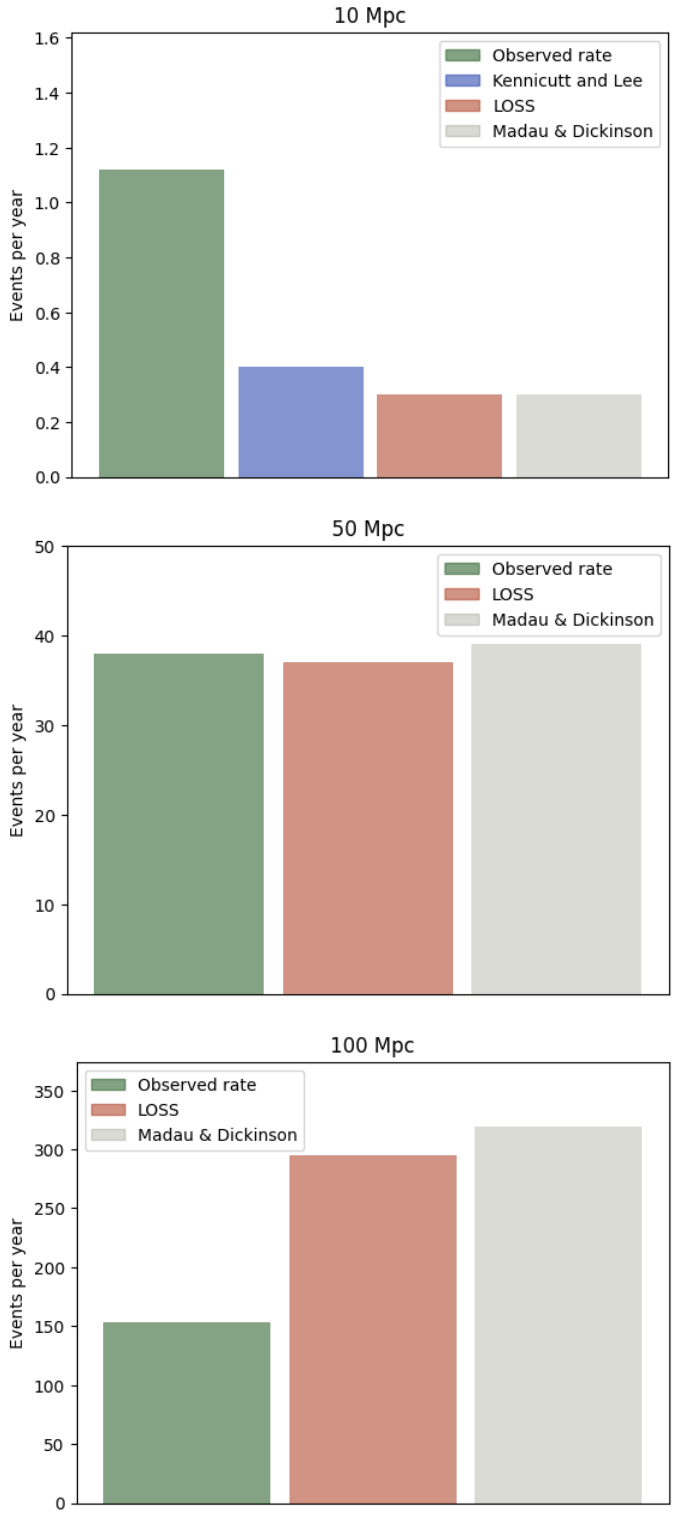


Figure 7.2: Comparison between direct and indirect rate for each volume.

Chapter 8

Conclusions

This PhD project outlines how emerging methodologies can enhance strategies for studying the transient Universe through joint GW and EM observations. Hence we focused on two classes of astrophysical sources that are crucial to MMA due to their potential to produce both GWs and EM signals: BNS mergers and CCSNe. With the current generation of GW interferometers, direct detections are limited to compact binary mergers, and the joint GW-EM observation of GW170817 marked a milestone demonstrating the extraordinary scientific return of coordinated observations across different messengers. However, despite the increased sensitivity of the GW detector network, no other EM counterparts to BNS GW signals have been observed during O4 due to both observational constraints and intrinsic astrophysical challenges (e.g. KNe evolve rapidly and are often faint compared to their associated GRB afterglows).

This motivates the need to explore alternative strategies for identifying EM signatures of BNS mergers, even in the absence of a GW trigger. Within this context, the first part of this thesis investigates methodologies to enhance the discovery and interpretation of EM counterparts to BNS mergers, with a particular focus on KNe. By applying data-driven and unsupervised clustering techniques to the *Fermi* GBM GRB sample, it was shown that the prompt emission itself can generate a structured parameter space in which known KN-associated bursts are a recognizable subsample. The discovery of a subpopulation sharing temporal and spectral properties with the known KN-associated GRBs demonstrates that machine learning can isolate physically consistent families of events, thereby offering a channel to identifying promising KN candidates even in the absence of a GW detection. This was paired with the development of a galaxy-association framework capable of narrowing the search space for candidate host galaxies using only GRB localization information and existing extragalactic catalogs. By combining these two approaches, we presented a strategy for operational MMA that can increase the probability of identifying the EM signature of a BNS merger in wide-field survey data. These methods anticipate the challenges posed by the Vera C. Rubin Observatory's LSST, whose unprecedented cadence and depth will discover tens of transient candidates.

To complement this statistical approach, we also developed a modelling strategy aimed at clarifying when and how KN emission can be disentangled from the associated GRB

afterglow. The detectability of a KN depends sensitively on viewing geometry, jet structure and circumstellar environment. By constructing light curves under realistic LSST observing conditions, we showed how off-axis GRB configurations are particularly favorable for KN discovery. In these cases, the afterglow is substantially suppressed at early times, allowing the KN to dominate the optical emission for several days. The application of this framework to an ambiguous transient, AT2025ulz, revealed that even events inconsistent with merger physics can exhibit partial similarities to certain KN–afterglow combinations, illustrating how observational degeneracies can challenge the classification. This result highlights the importance of developing extensive template libraries covering a broad range of physical conditions, which will be essential for photometric classification pipelines as surveys begin to uncover large numbers of rapidly evolving transients.

With the advent of 3rd generation GW interferometers, the multimessenger landscape will expand beyond BNS mergers, opening to the detection of GW signals from CCSNe. Hence the PhD project also investigated the role that 3rd generation GW observatories will play in advancing the understanding of the collapse of massive stars. The ET, with its great improvement in sensitivity over current ground-based detectors, will provide an unprecedented opportunity to directly observe the collapsing core. By combining progenitor distributions derived from Galactic population synthesis models with state-of-the-art 3d numerical simulations of SN explosions, we showed that the next Galactic CCSN event is expected to be detected by ET with high confidence, regardless of the exact source location or the diversity of waveform morphologies. This result is particularly significant because many CCSNe occur in regions heavily obscured by dust, where EM observations are partially or completely prevented. Hence, GWs offer a unique probe of these otherwise inaccessible events. While the current analysis is constrained by the limited availability of 3d CCSN waveform simulations, it establishes a flexible framework that can be readily extended as new and more realistic waveforms become available. Such developments will significantly enhance detection forecasts and further consolidate ET as a key instrument for multimessenger observations of stellar explosions.

To assess the prospects for extending the detection of GW signals from CCSNe to extragalactic distances, we performed a detailed analysis of the CCSN rate in the local Universe. By comparing directly observed CCSN counts with indirect estimates derived from SFH, the analysis revealed a complex picture shaped by both astrophysical effects and observational biases. Within the very nearby volume (within $\sim$10 Mpc), the observed CCSN rate exceeds indirect estimates by a factor of two, a discrepancy that can be attributed to the well-known local overdensity of galaxies. At intermediate distances (within $\sim$50 Mpc), the agreement between direct observations and indirect estimates improves significantly, indicating that the two approaches provide a consistent description of the CCSN population on these scales. However, when extending the analysis to larger volumes (within $\sim$100 Mpc), the observed CCSN rate falls below expectations. This is most likely driven by observational constraints, including survey magnitude limit and incompleteness, the faintness of distant SNe and the lack of spectroscopic classification for a fraction of detected events. These results provide an essential reference for evaluating a realistic number of CCSN GW detections that can be expected in the nearby Universe and for informing future multimessenger observing strategies beyond the Milky Way.

The frameworks developed in this dissertation are quickly extendable and can be seen as a starting point for further improvements. On the EM side, KN detection strategies

can benefit from advances in survey cadence, depth and sky coverage, as well as from the increasing improvement of machine learning classification techniques. Moreover, the integration of physically modeled template libraries with data-driven photometric classifiers will be essential to cope with the large volume of rapidly evolving transients expected from next-generation optical surveys such as LSST. On the GW side, studies of CCSNe will progress alongside advances in numerical modeling and the growing availability of 3d waveform simulations. The combination of improved waveform realism, expanded progenitor populations and enhanced detector sensitivity will enhance accurate detection forecasts and parameter inference. Moreover, the synergy between 3rd generation GW observatories, neutrino detectors and EM facilities will play a crucial role in unraveling the complex physics behind the collapse of these transients.
In this broader context, the work presented in this thesis contributes a set of complementary tools and perspectives aimed at bridging current and future observational capabilities. By addressing both the challenges of the present GW detection era and the opportunities offered by next generation observatories, this dissertation provides a coherent framework for enhancing the identification, analysis and interpretation of transient phenomena in future multimessenger studies.

Appendix A

Core-Collapse Supernova Sample within 10 Mpc

Table A.0.1: CCSNe within 10 Mpc exploded between 2000 and 2023. For each event we report: the type, the magnitude at the discovery epoch and the redshift, the host galaxy, its redshift and the corresponding distance (in Mpc), the time interval T (in days) between the discovery epoch and its maximum light, the host B band absolute magnitude and the SFR measurements ($M_{\odot}yr^{-1}$).

SN	**type**	mag_{disc}	$\mathbf{z}_{SN}$	**host**	$\mathbf{z}_{host}$	**d**	**T**	**Host** $\mathbf{M}_B$	$\mathbf{SFR}_{H\alpha}$
$\mathbf{SFR}_{UV}$									
2001ig	Ib/c	12.4	0.003	NGC 7424	-	10.5	-	-	-
-									
2002ap	Ic	14.5	-	NGC 628	0.002	9.8	5	-19.58	1.3
2									
2002bu	IIn	15.5	0.002	NGC 4242	0.0018	9.2	8	-18.18	0.1
0.17									
2002hh	IIP	16.5	-	NGC 6946	0.00013	7	6	-20.79	5.7
9.1									
2003gd	IIP	13.2	-	NGC 628	0.0022	9.8	5	-19.58	1.3
-									
2004am	IIP	17.0	-	NGC 3034	0.00068	3.5	7	-18.84	1.9
5.6									
2004dj	IIP	11.2	-	NGC 2403	0.0004	3.6	6	-18.78	0.8
1.0									
2004et	IIP	12.8	-	NGC 6946	0.0002	7	6	-20.79	5.7
9.1									
2005af	IIP	12.8	-	NGC 4945	0.0018	3.7	6	-19.26	0.9
-									
2005at	Ic	14.3	-	NGC 6744	0.0028	10.5	4	-20.94	3.3
12									
2005cs	IIP	16.3	-	NGC 5194	0.0015	7.8	4	-20.63	4.5
7.6									
2007gr	Ic	13.8	-	NGC 1058	0.0017	10.2	5	-18.24	0.3
0.5									
2008ax	IIb	16.1	-	NGC 4490	0.0019	8	7	-19.37	1.9

2.5									
2008bk	IIP	12.6	-	NGC 7793	0.0008	3.9	7	-18.41	0.5
0.7									
2011dh	IIb	14.0	0.0017	NGC 5194	0.0015	7.8	4	-20.63	4.5
7.6									
2011ja	II	14.0	0.002	NGC 4945	0.0019	3.7	6	-19.26	0.9
-									
2012fh	Ib/c	15.1	-	NGC 3344	0.0019	9.8	4	-18.75	0.3
0.8									
2013am	II	15.6	-	NGC 3623	-	10	1	-19.57	0.9
0.5									
2013ej	IIP	13.5	0.002	NGC 628	0.0022	9.8	5	-19.58	1.3
2									
2014bc	IIP	14.8	-	NGC 4258	0.0015	9.2	4	-20.44	3.1
-									
2014bi	IIP	18.2	0.0023	NGC 4096	0.0019	9.2	5	-18.15	0.3
0.6									
2016adj	IIb	14.3	-	NGC 5128	0.0018	3.7	2	-20.47	1.3
0.7									
2017bzb	II	13.0	0.003	NGC 7424	-	10.5	-	-	-
-									
2017eaw	IIP	12.2	0.00013	NGC 6946	0.00016	7	6	-20.79	5.9
9									
2023dbc	Ic	19.5	0.002	NGC 3556	-	10	-	-	-
-									
2023ixf	IIL	14.9	0.0008	NGC 5457	0.0008	5.6	6	-20.84	4.5
6.7									
2023mut	IIb	15.2	0.0022	UGC 3174	0.0022	9.3	10	-14.88	$8 \cdot 10^{-3}$
0.03									

Appendix B

GRB Clustered Sample

Table B.0.1: This Table includes all the GRB selected by the Cluster 2 with an error radius lower than 0.1. It comprises the following data for each GRB: t_{90}, fluence, energy peak and redshift, with respective errors.

name	$\mathbf{t_{90}}$	***fluence***	$\mathbf{E}_{peak}$	**redshift**
GRB170817529	2.05±0.47	$2.79\pm0.17 \times 10^{-07}$	214.7±56.59	-
GRB130626452	1.73±0.77	$2.34\pm0.39 \times 10^{-07}$	347.31±210.41	-
GRB090518080	2.05±0.41	$9.91\pm0.27\times10^{-07}$	206.12±173.48	-
GRB100216422	0.19±0.14	$3.87\pm0.15\times10^{-07}$	228.57±151.43	-
GRB140808038	4.47±0.36	$3.21\pm0.033\times10^{-06}$	117.45±6.46	-
GRB160714097	0.32±0.36	$1.12\pm0.15 \times 10^{-07}$	61.71±52.12	-
GRB141205337	1.28±0.57	$1.06 \pm0.11\times10^{-0}$	499.94±175.83	-
GRB170325331	0.58±0.33	$2.57\pm0.12\times10^{-07}$	434.19±134.51	-
GRB081101491	0.13±0.09	$1.680.04\times10^{-07}$	236.56±55.41	-
GRB160726065	0.77±0.35	$1.01\pm0.016\times10^{-06}$	271.37±72.59	-
GRB151228129	0.26±2.27	$4.63\pm0.36\times10^{-07}$	873.73±186.62	-
GRB110420946	0.13±0.52	$2.44\pm0.27\times10^{-07}$	353.52±87.07	-
GRB141102536	2.62±0.33	$1.42\pm0.04\times10^{-06}$	598.63±92.24	-
GRB081226509	0.19±0.14	$3.45\pm0.27\times10^{-07}$	359.81±77.08	-
GRB160424492	6.59±0.92	$2.73\pm0.024\times10^{-06}$	209.2±26.29	-
GRB170208758	7.17±1.06	$2.63\pm0.067\times10^{-06}$	176.72±34.47	-
GRB090531775	0.77±0.23	$3.18\pm0.18\times10^{-07}$	1659.39±399.39	-
GRB120830297	0.89±0.23	$3.069\pm0.027\times10^{-06}$	1088.52±105.29	-
GRB120817168	0.16±0.11	$1.79\pm0.013\times10^{-06}$	1348.83±217.61	-
GRB160612842	0.289±0.23	$9.099\pm0.15\times10^{-07}$	1263.31±394.01	-
GRB091010113	5.95±0.14	$9.96\pm0.058\times10^{-06}$	150.34±6.89	-
GRB180715755	0.70±0.29	$1.045\pm0.022\times10^{-06}$	900.31±147.51	-
GRB140402007	0.32±0.63	$2.84\pm0.29\times10^{-07}$	1093.35±232.98	-
GRB130216927	6.59±0.35	$5.92\pm0.06\times10^{-06}$	138.14±11.18	-
GRB100915243	7.94±3.37	$4.75\pm0.28\times10^{-07}$	93.48±20.04	-
GRB150110923	2.56±0.83	$5.80\pm0.29\times10^{-07}$	54.10±22.04	-
GRB141205337	1.28±0.57	$1.065\pm0.11\times10^{-06}$	499.94±175.83	-
GRB081024245	0.831.28	$1.98\pm0.17\times10^{-07}$	996.36±297.96	-
GRB110201399	8.19±0.87	$3.15\pm0.16\times10^{-06}$	$421.5574 - 04$	-

GRB120403857	4.29±1.93	$2.39\pm0.21\times10^{-07}$	192.80±54.88	-
GRB090927422	0.51±0.23	$3.026\pm0.18\times10^{-07}$	195.22±69.05	1.37
GRB081226044	0.83±1.032	$4.30\pm0.23\times10^{-07}$	584.04±284.04	-
GRB161001045	2.24±0.23	$1.76\pm0.015\times10^{-06}$	373.61±59.60	-
GRB130515056	0.26±0.091	$1.08\pm0.016\times10^{-06}$	452.86±74.4	-
GRB150301045	0.42±0.29	$1.80\pm0.12\times10^{-07}$	149.42±77.76	-
GRB160411062	0.67±0.44	$2.25\pm0.19\times10^{-07}$	161.5341.38	-
GRB100625773	0.240.28	$5.63\pm0.25\times10^{-07}$	482.13±61.93	-
GRB170127634	1.73±1.35	$3.06\pm0.13\times10^{-07}$	481.68±131.52	-
GRB151229285	3.46±1.03	$1.11\pm0.016\times10^{-06}$	104.02±14.15	-
GRB080905499	0.96±0.35	$8.51\pm0.46\times10^{-07}$	317.18±52.54	0.12
GRB170803729	3.58±0.32	$1.88\pm0.024\times10^{-06}$	164.11±12.59	-
GRB140320092	2.30±1.53	$1.02\pm0.097\times10^{-07}$	831.59±3338.76	-
GRB150101641	0.08±0.93	$2.38\pm0.15\times10^{-07}$	28.676.73	-
GRB150101270	0.480.96	$7.61\pm1.07\times10^{-08}$	208.18±109.55	0.93
GRB090720276	4.48±1.08	$2.91\pm0.037\times10^{-06}$	106.58±9.38	-
GRB120907017	5.76±1.78	$8.09\pm0.41\times10^{-07}$	128.25±20.26	0.97
GRB131004904	1.15±0.59	$5.10\pm0.19\times10^{-07}$	118.12±24.42	0.71
GRB100117879	0.26±0.83	$4.23\pm0.69\times10^{-07}$	327.2252.92	-
GRB130502743	3.332.06	$6.27\pm0.35\times10^{-07}$	84.6±21.44	-
GRB100206563	0.18±0.07	$7.57\pm0.11\times10^{-07}$	454-31±63.63	-
GRB130912358	0.51±0.14	$7.01\pm0.18\times10^{-07}$	407.68±163.61	-
GRB111117510	0.43±0.08	$5.64\pm0.13\times10^{-07}$	503.85±111.18	-
GRB130609129	5.38±1.49	$1.06\pm0.082\times10^{-06}$	51.67±10.02	-
GRB100816026	2.05±0.23	$3.65\pm0.053\times10^{-06}$	133.13±7.08	0.81
GRB121211574	5.63±1.71	$6.41\pm0.39\times10^{-07}$	101.23±13.86	1.023
GRB180204109	1.15±0.91	$1.75\pm0.013\times10^{-06}$	814.81±164.93	-
GRB131128629	1.98±0.54	$5.69\pm0.41\times10^{-07}$	59.62±5.29	-
GRB140209313	1.41±0.26	$8.97\pm0.053\times10^{-06}$	143.9±7.49	-
GRB150110923	2.56±0.83	$5.81\pm0.29\times10^{-07}$	54.09±22.04	-
GRB141005217	3.39±0.26	$2.50\pm0.03\times10^{-06}$	122.65±10.96	-
GRB171007498	3.46±0.35	$3.032\pm0.18\times10^{-07}$	757.53±1605.87	-
GRB101224227	1.73±1.68	$1.91\pm0.27\times10^{-07}$	253.47±217.98	-
GRB100212588	4.86±1.31	$4.45\pm0.15\times10^{-07}$	59.03±16.13	-
GRB140713780	5.38±1.38	$8.31\pm0.39\times10^{-07}$	36.84±13.29	-
GRB160821937	1.09±0.98	$1.95\pm0.2\times10^{-07}$	38.17±27.48	0.16
GRB110112934	2.3±2.54	$4.05\pm0.27\times10^{-07}$	561.54±147.76	-
GRB090621922	0.38±1.03	$4.76\pm0.19\times10^{-07}$	486.21±120.54	-
GRB160408268	1.056±0.61	$6.98\pm0.28\times10^{-07}$	841.97±170.46	-
GRB091102607	6.66±3.44	$1.88\pm0.11\times10^{-06}$	610.36±251.25	-
GRB160411062	0.67±0.44	$2.25\pm0.19\times10^{-07}$	161.53±41.38	-
GRB090510016	0.96±0.14	$3.37\pm0.041\times10^{-06}$	4248.14±440.05	0.903
GRB180402406	0.45±0.33	$1.31\pm0.028\times10^{-06}$	1328.87±161.03	-
GRB130803419	7.62±1.15	$2.82\pm0.036\times10^{-06}$	114.58±19.67	-
GRB131031482	7.42±0.6	$4.38\pm0.05\times10^{-06}$	93.46±9.63	-
GRB170318644	4.1±2.32	$5.08\pm0.52\times10^{-07}$	891.68±395.28	-
GRB130912358	0.51±0.14	$7.01\pm0.18\times10^{-07}$	407.68±163.61	-
GRB130612141	7.42±6.19	$6.80\pm0.63\times10^{-07}$	28.94±8.23	2.006
GRB090423330	7.17±2.42	$8.16\pm0.72\times10^{-07}$	66.27±10.84	8.01

GRB180418281	2.56±0.2	$5.89\pm0.097\times10^{-07}$	1051.09±951.48	-
GRB141220252	7.62±0.92	$5.34\pm0.035\times10^{-06}$	179.07±10.07	1.319
GRB150530488	7.17±0.57	$3.48\pm0.04\times10^{-06}$	134.28±42.48	-
GRB130716442	0.77±0.39	$6.40\pm0.09\times10^{-07}$	883.46±1120.96	-
GRB180618030	3.71±0.58	$1.23\pm0.014\times10^{-06}$	2292.46±874.31	-
GRB160815490	7.1±1.14	$2.11\pm0.04\times10^{-06}$	67.86±4.44	-
GRB090813174	7.55±0.36	$3.33\pm0.041\times10^{-06}$	80.46±17.28	-

B.1 Parameter distributions

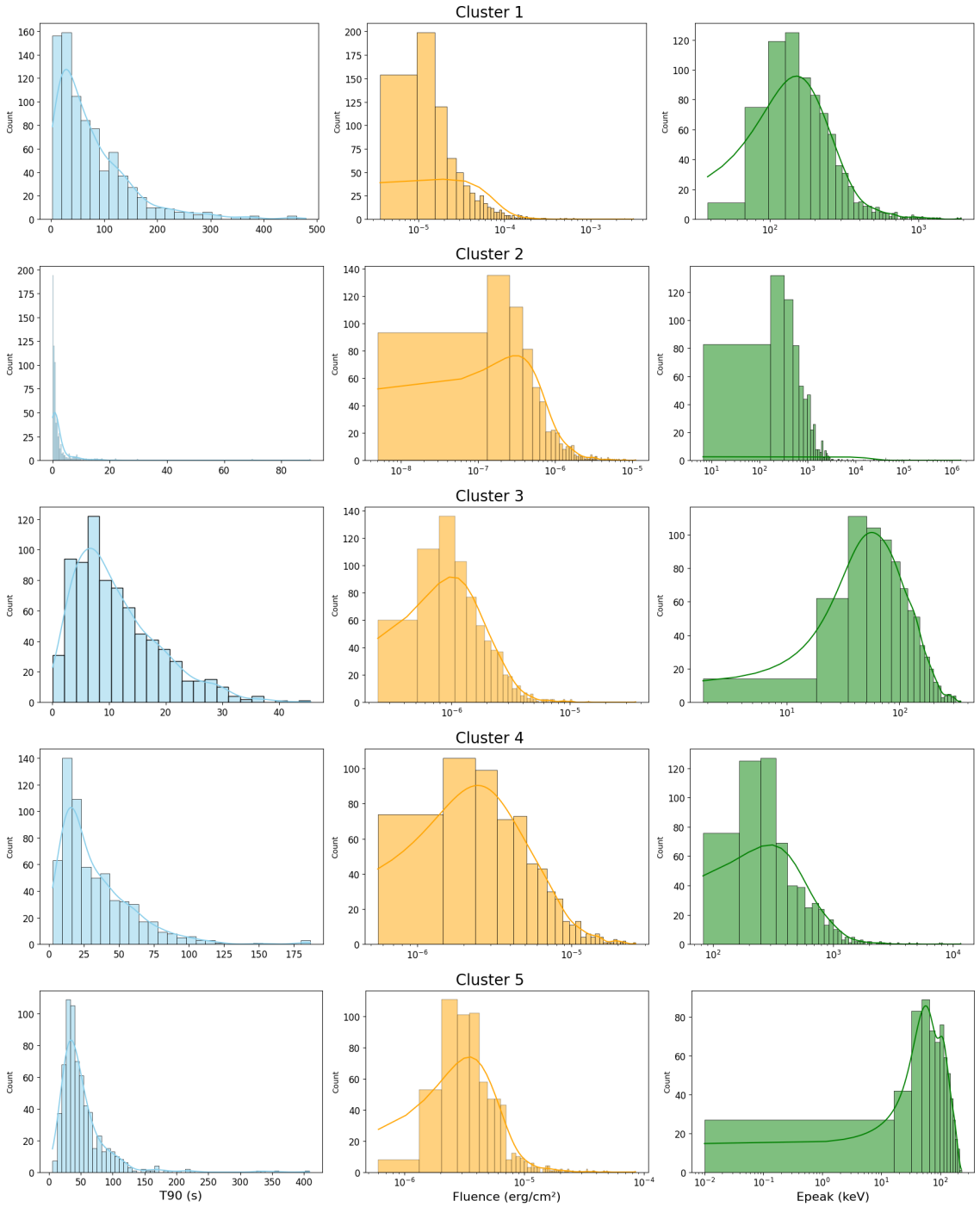


Figure B.1: Distributions of T_{90}, fluence, and E_{peak} for each cluster obtained using UMAP.

Appendix C

Kilonova and afterglow emission modeled for E_{iso}=10^{50}

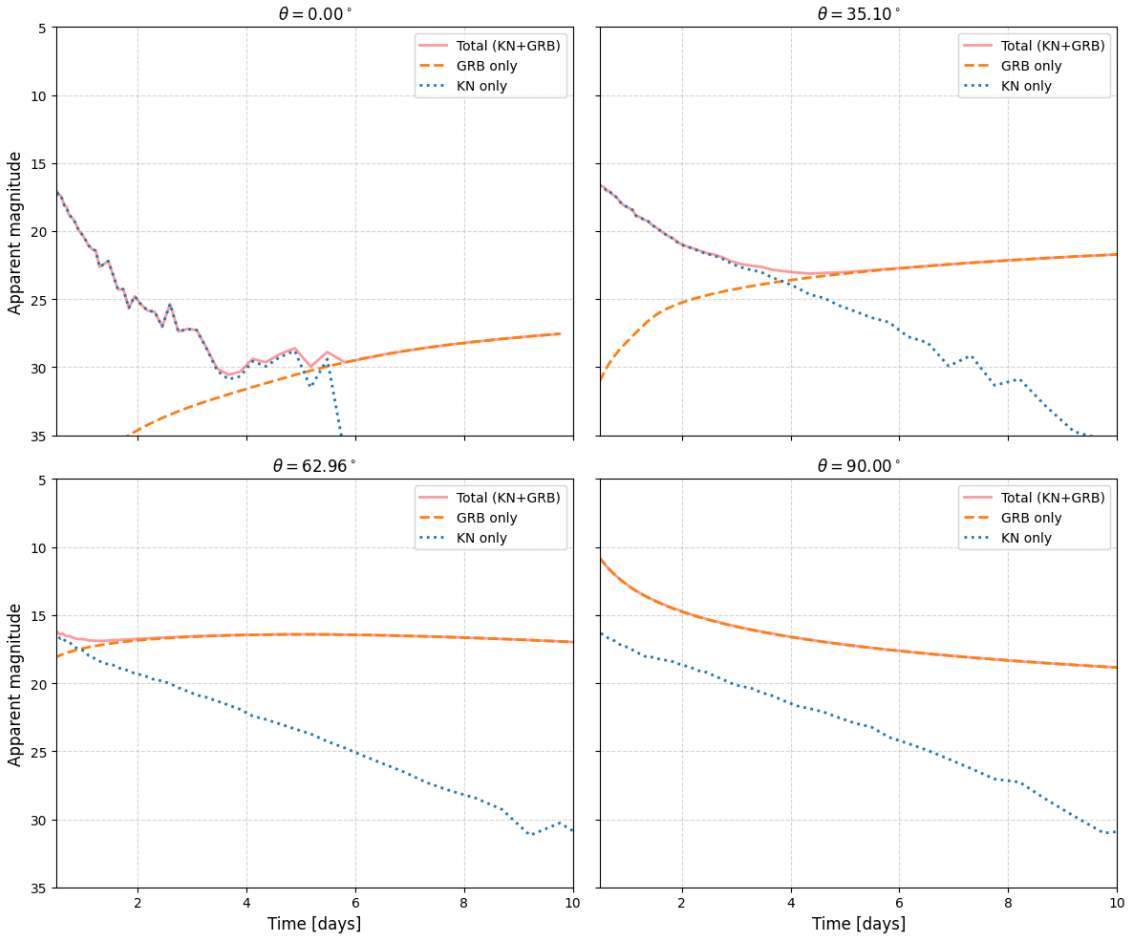


Figure C.1: Simulated g-band light curves for four different viewing angles. Blue dotted lines represent the KN emission, orange dashed lines correspond to the GRB afterglow, and solid red lines indicate the combined emission.

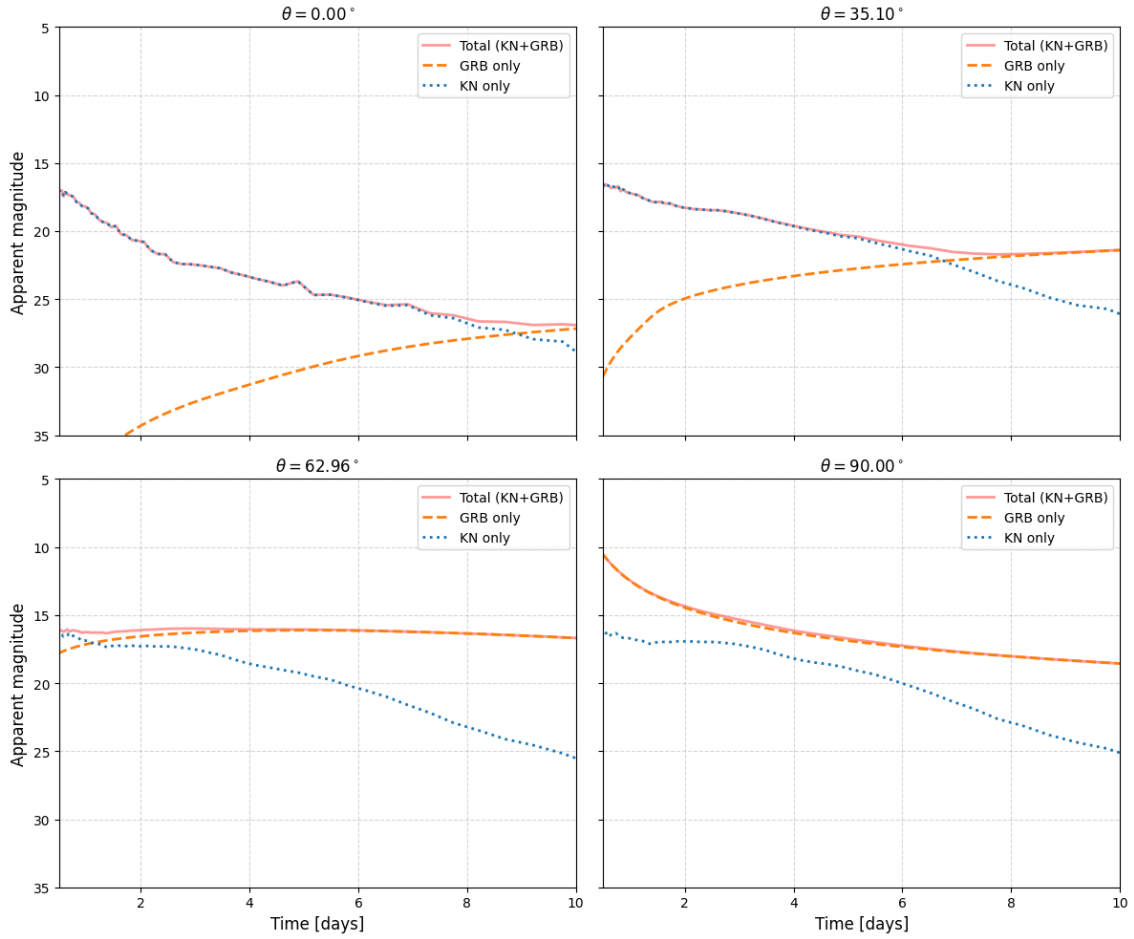


Figure C.2: Simulated i-band light curves for four different viewing angles. Blue dotted lines represent the KN emission, orange dashed lines correspond to the GRB afterglow, and solid red lines indicate the combined emission.

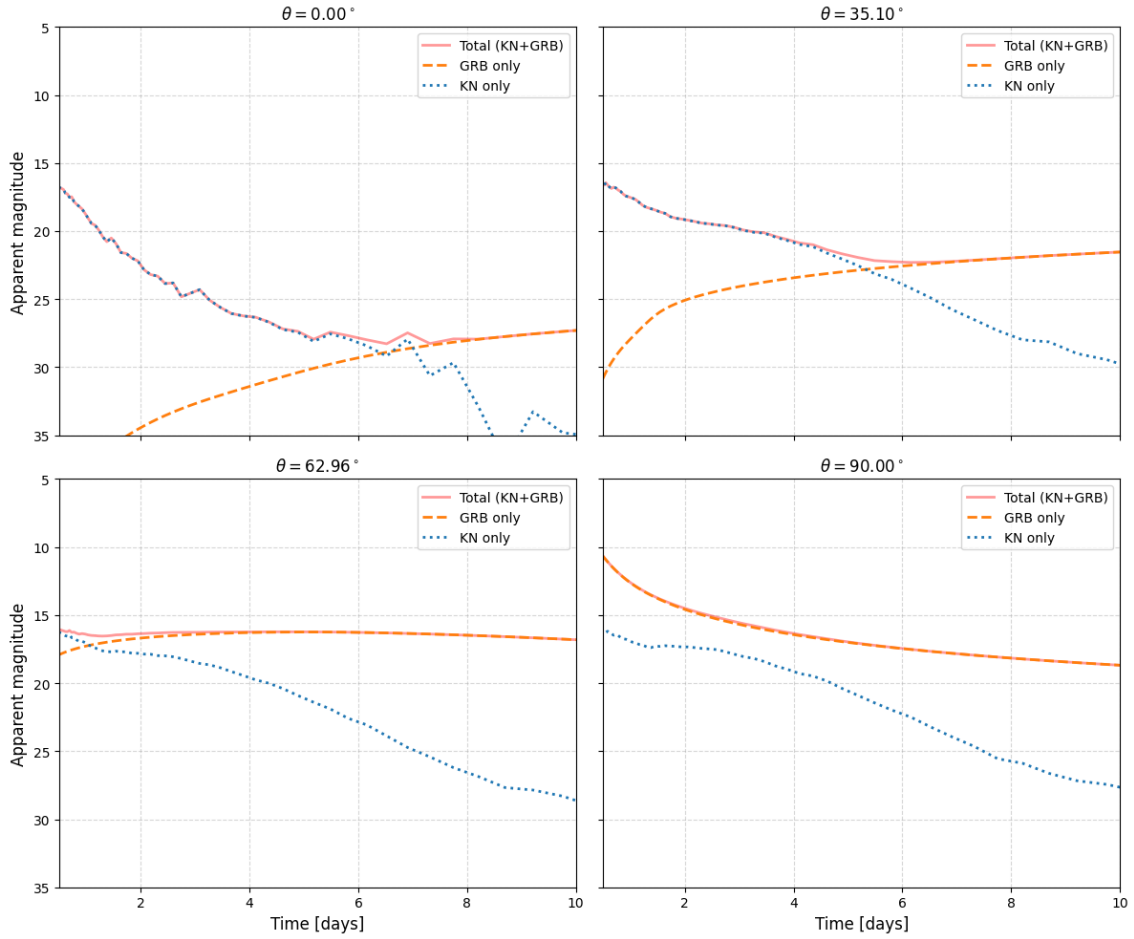
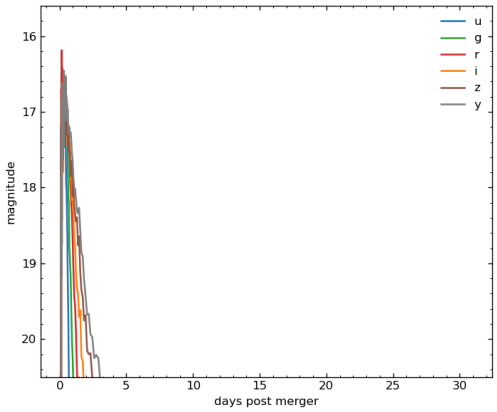
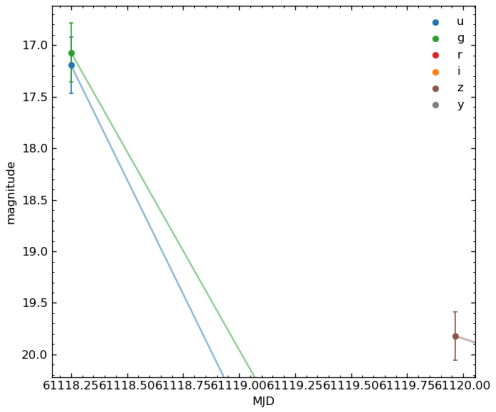


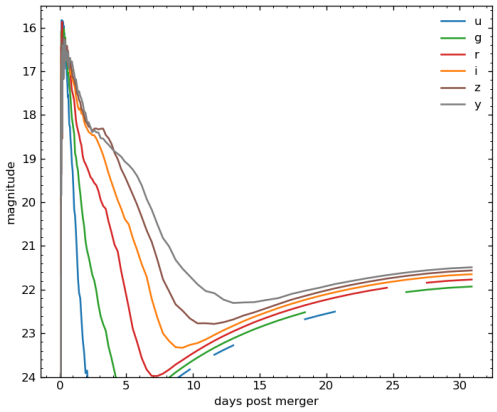
Figure C.3: Simulated r-band light curves for four different viewing angles. Blue dotted lines represent the KN emission, orange dashed lines correspond to the GRB afterglow, and solid red lines indicate the combined emission.



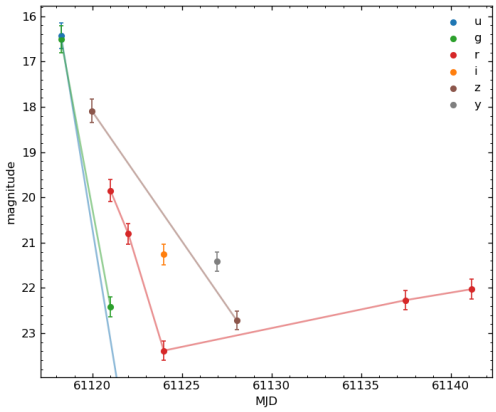
(a) $\theta = 90°$ light curve



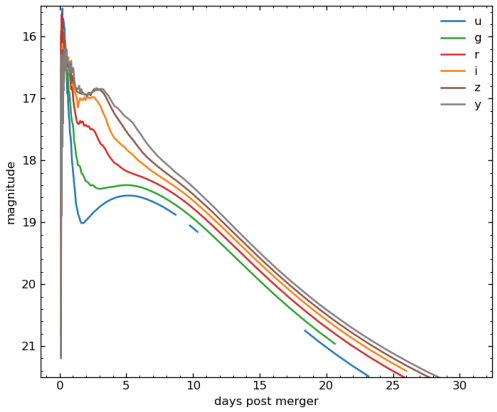
(b) $\theta = 90°$ mock observation



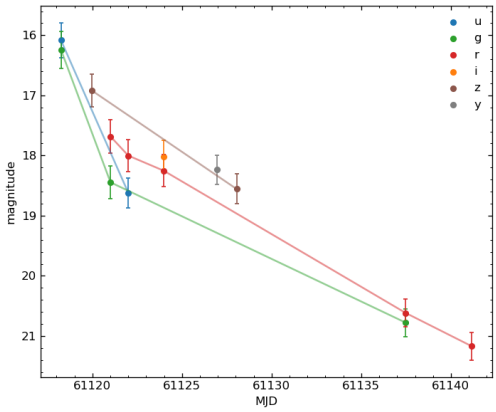
(c) $\theta = 54.90°$ light curve



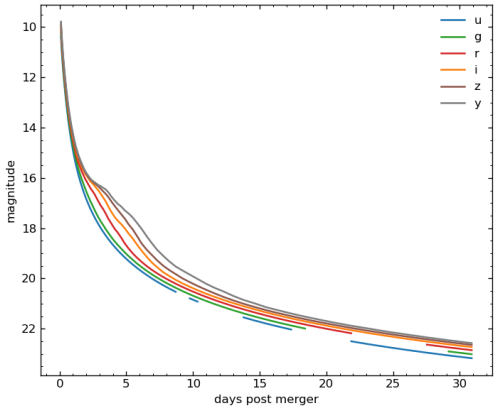
(d) $\theta = 54.90°$ mock observation



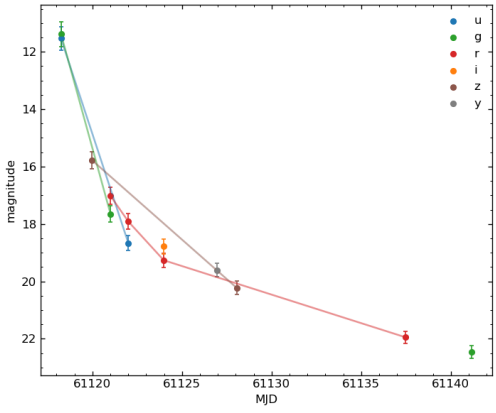
(e) $\theta = 27.04°$ light curve



(f) $\theta = 27.04°$ mock observation

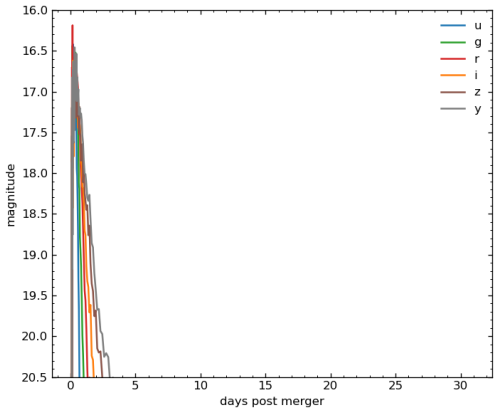


(g) $\theta = 0°$ light curve

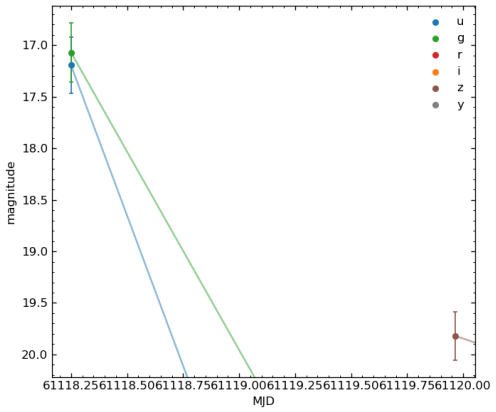


(h) $\theta = 0°$ mock observation

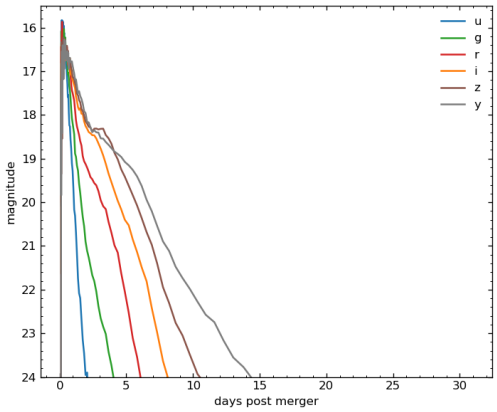
Figure C.4: Case $n_0 = 0.1$: Light curves (left) and LSST mock observations (right) for different viewing angles.



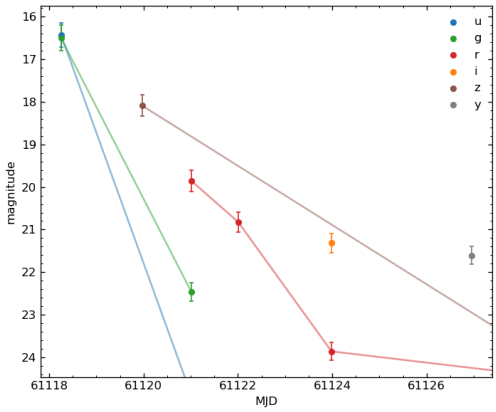
(a) $\theta = 90°$ light curve



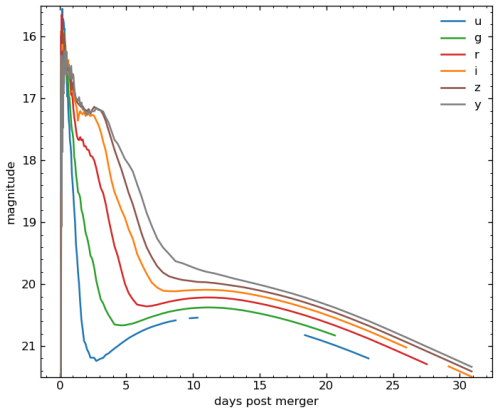
(b) $\theta = 90°$ mock observation



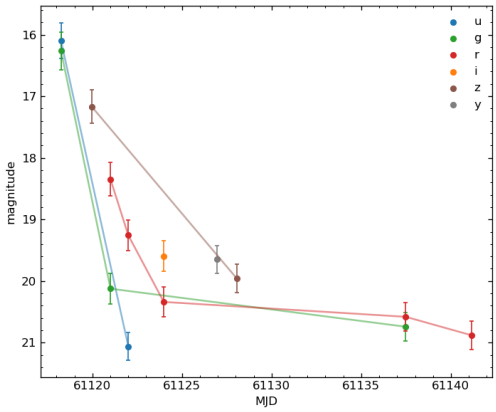
(c) $\theta = 54.90°$ light curve



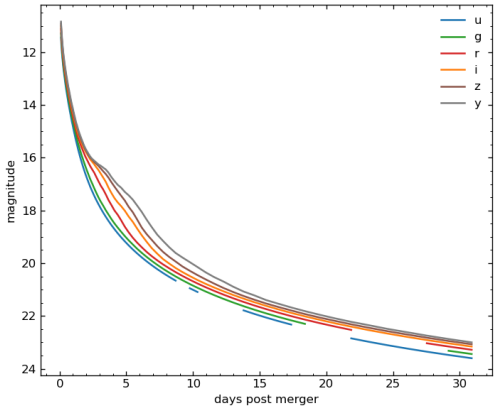
(d) $\theta = 54.90°$ mock observation



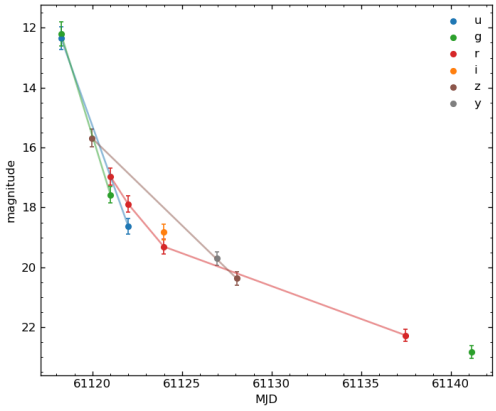
(e) $\theta = 27.04°$ light curve



(f) $\theta = 27.04°$ mock observation



(g) $\theta = 0°$ — light curve



(h) $\theta = 0°$ — mock obs

Figure C.5: Case $n_0 = 0.01$: Light curves (left) and LSST mock observations (right) for different viewing angles.

Appendix D

Kilonova and afterglow emission modeled for an event GW170817-like

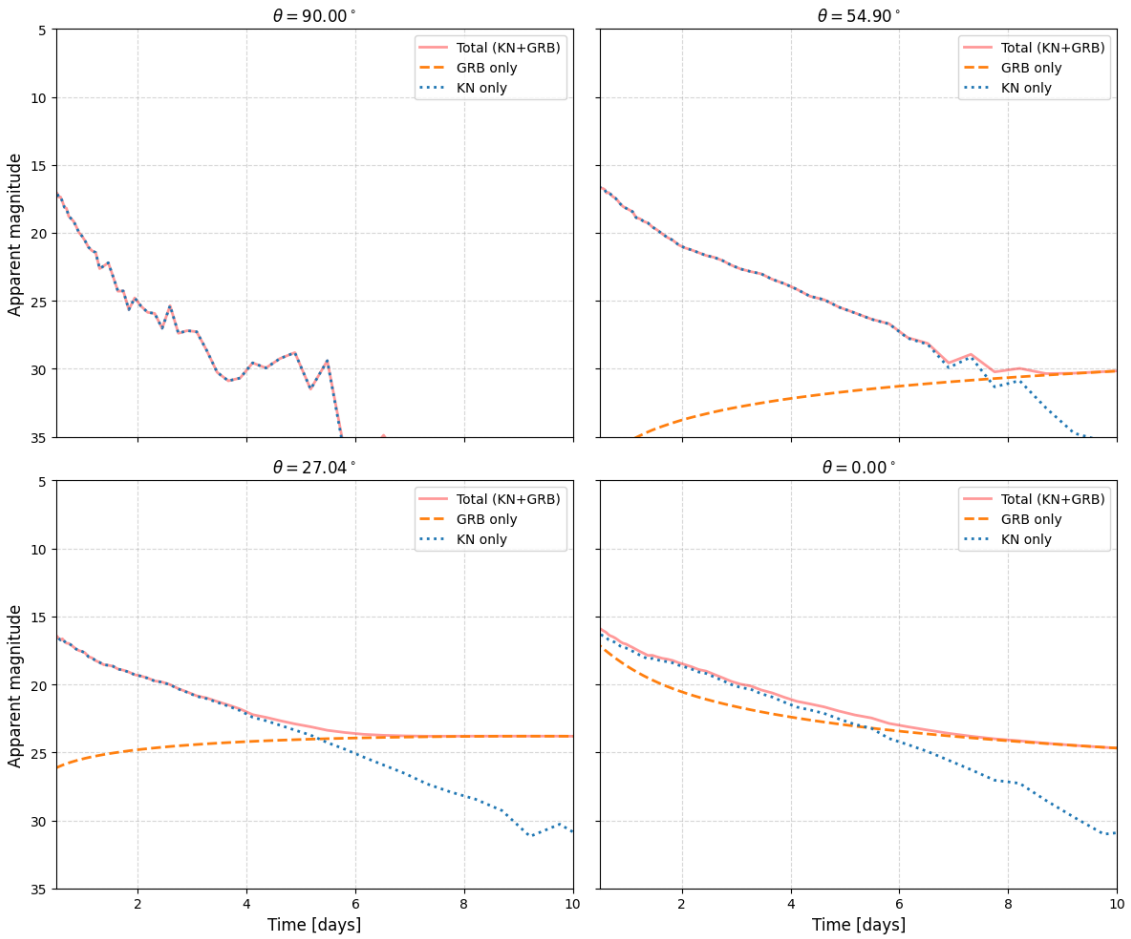


Figure D.1: Simulated g-band light curves for four different viewing angles. Blue dotted lines represent the KN emission, orange dashed lines correspond to the GRB afterglow, and solid red lines indicate the combined emission.

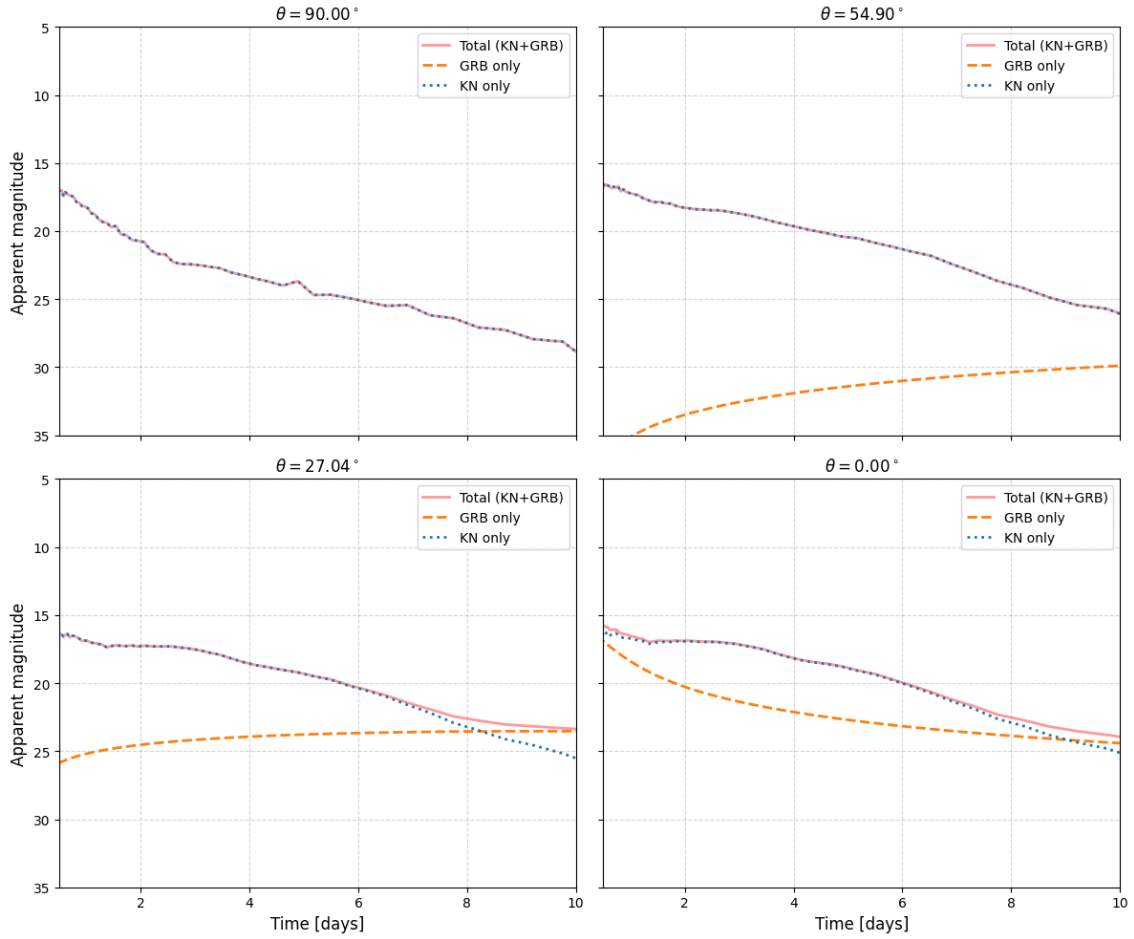


Figure D.2: Simulated i-band light curves for four different viewing angles. Blue dotted lines represent the KN emission, orange dashed lines correspond to the GRB afterglow, and solid red lines indicate the combined emission.

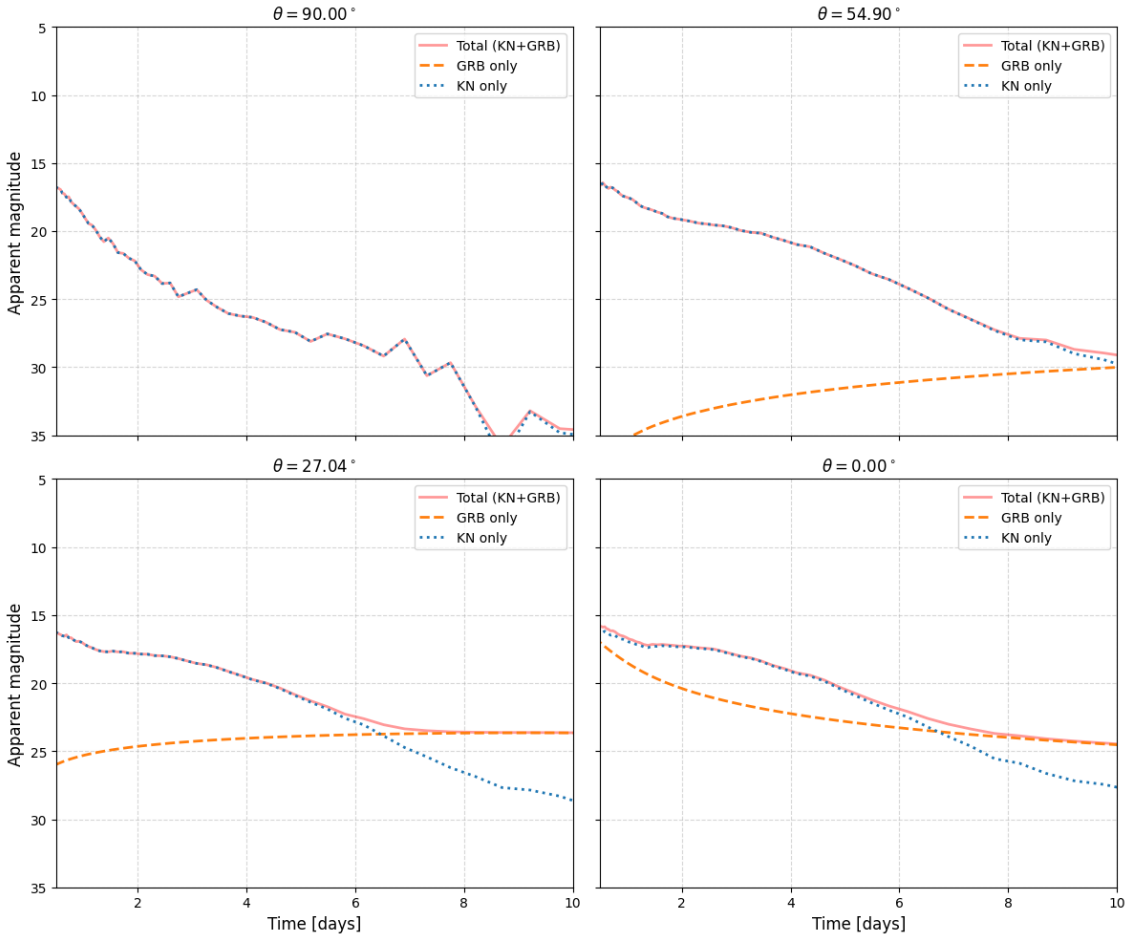
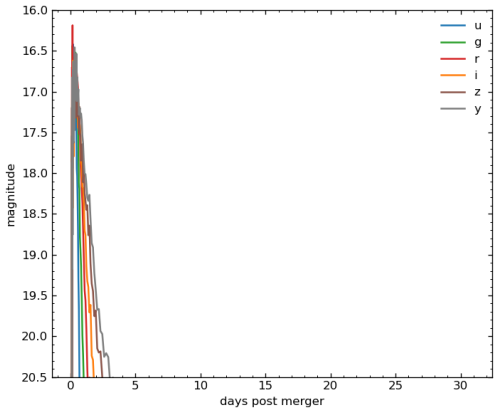
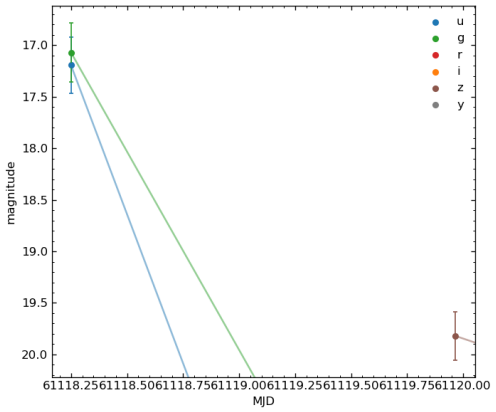


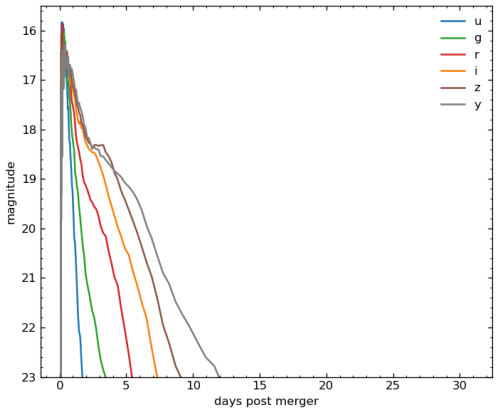
Figure D.3: Simulated r-band light curves for four different viewing angles. Blue dotted lines represent the KN emission, orange dashed lines correspond to the GRB afterglow, and solid red lines indicate the combined emission.



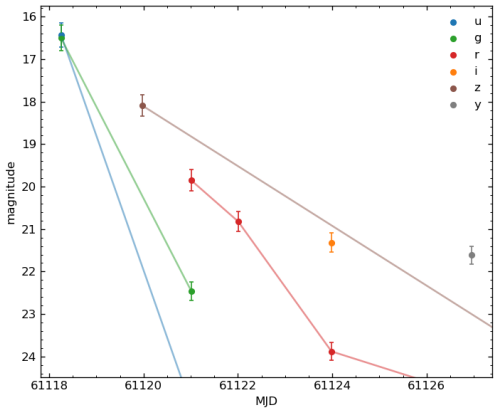
(a) $\theta = 90°$ light curve



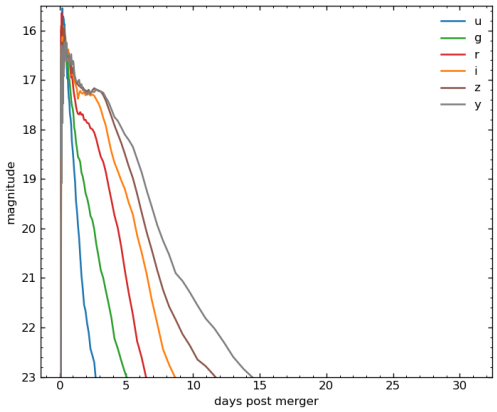
(b) $\theta = 90°$ mock observation



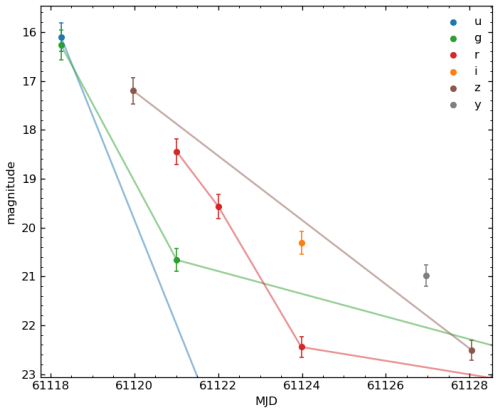
(c) $\theta = 54.90°$ light curve



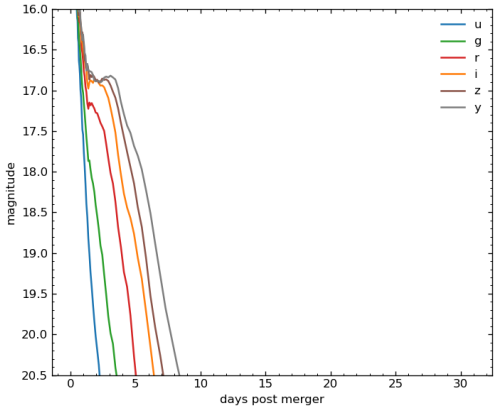
(d) $\theta = 54.90°$ mock observation



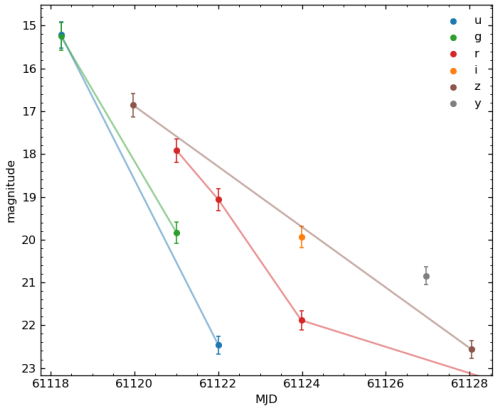
(e) $\theta = 27.04°$ light curve



(f) $\theta = 27.04°$ mock observation



(g) $\theta = 0°$ — light curve



(h) $\theta = 0°$ — mock obs

Figure D.4: Light curves (left) and LSST mock observations (right) for different viewing angles for a GW170817-like event.

Bibliography

Ligo em follow-up user guide. `https://emfollow.docs.ligo.org/userguide/capabilities.html`, 2026. Accessed: 2026-02-03.

DLT40 Collaboration Haislip JB 241 Kouprianov VV 241 Reichart DE 241 Tartaglia L. 242 243 Sand DJ 242 Valenti S. 243 Yang S. 243 244 245 and Las Cumbres Observatory Collaboration Arcavi Iair 246 247 Hosseinzadeh Griffin 246 247 Howell D. Andrew 246 247 McCully Curtis 246 247 Poznanski Dovi 248 Vasylyev Sergiy 246 247. A gravitational-wave standard siren measurement of the hubble constant. *Nature*, 551(7678):85–88, 2017.

Junaid Aasi, B. P. Abbott, Richard Abbott, Thomas Abbott, M. R. Abernathy, Kendall Ackley, Carl Adams, Thomas Adams, Paolo Addesso, R. X. Adhikari, et al. Advanced ligo. *Classical and Quantum Gravity*, 32(7):074001, 2015.

Adrian Abac, Raul Abramo, Simone Albanesi, Angelica Albertini, Alessandro Agapito, Michalis Agathos, Conrado Albertus, Nils Andersson, Tomás Andrade, Igor Andreoni, et al. The science of the einstein telescope. *arXiv preprint arXiv:2503.12263*, 2025.

Benjamin P. Abbott, R. Abbott, T. D. Abbott, M. R. Abernathy, Fausto Acernese, K. Ackley, C. Adams, T. Adams, Paolo Addesso, R. X. Adhikari, et al. Gw150914: The advanced ligo detectors in the era of first discoveries. *Physical Review Letters*, 116(13): 131103, 2016a.

Benjamin P. Abbott, Richard Abbott, Thomas D. Abbott, Matthew R. Abernathy, Fausto Acernese, Kendall Ackley, Carl Adams, Thomas Adams, Paolo Addesso, Rana X. Adhikari, et al. Observation of gravitational waves from a binary black hole merger. *Physical Review Letters*, 116(6):061102, 2016b.

Benjamin P. Abbott, Rich Abbott, T. D. Abbott, Fausto Acernese, Kendall Ackley, Carl Adams, Thomas Adams, Paolo Addesso, Rana X. Adhikari, Vaishali B. Adya, et al. Gw170817: Observation of gravitational waves from a binary neutron star inspiral. *Physical Review Letters*, 119(16):161101, 2017.

R. Abbott, T. D. Abbott, S. Abraham, F. Acernese, K. Ackley, C. Adams, R. X. Adhikari, V. B. Adya, C. Affeldt, M. Agathos, K. Agatsuma, Aggarwal, and others. GW190521: A Binary Black Hole Merger with a Total Mass of 150 M$\odot$. *Physical Review Letters*, 125 (10):101102, September 2020. doi: 10.1103/PhysRevLett.125.101102.

R. Abbott, T. D. Abbott, S. Abraham, F. Acernese, K. Ackley, A. Adams, C. Adams, R. X. Adhikari, V. B. Adya, C. Affeldt, M. Agathos, K. Agatsuma, N. Aggarwal, O. D. Aguiar, L. Aiello, A. Ain, P. Ajith, Allen, The LIGO Scientific Collaboration, and the Virgo Collaboration. Population properties of compact objects from the second ligo–virgo gravitational-wave transient catalog. *The Astrophysical Journal Letters*, 913(1):L7, may

2021. doi: 10.3847/2041-8213/abe949. URL https://doi.org/10.3847/2041-8213/abe949.

R. Abbott, T. D. Abbott, F. Acernese, K. Ackley, C. Adams, N. Adhikari, R. X. Adhikari, V. B. Adya, C. Affeldt, D. Agarwal, M. Agathos, K. Agatsuma, N. Aggarwal, O. D. Aguiar, L. Aiello, Ain, and others. GWTC-3: Compact Binary Coalescences Observed by LIGO and Virgo during the Second Part of the Third Observing Run. *Physical Review X*, 13(4):041039, October 2023. doi: 10.1103/PhysRevX.13.041039.

R. Abbott, T. D. Abbott, F. Acernese, K. Ackley, C. Adams, N. Adhikari, R. X. Adhikari, V. B. Adya, C. Affeldt, D. Agarwal, M. Agathos, Agatsuma, and others. GWTC-2.1: Deep extended catalog of compact binary coalescences observed by LIGO and Virgo during the first half of the third observing run. , 109(2):022001, January 2024. doi: 10.1103/PhysRevD.109.022001.

Ernazar Abdikamalov, Giulia Pagliaroli, and David Radice. Gravitational waves from core-collapse supernovae. In *Handbook of Gravitational Wave Astronomy*, pages 909–945. Springer, 2022.

Ade Abergel, Peter AR Ade, N Aghanim, MIR Alves, G Aniano, C Armitage-Caplan, M Arnaud, M Ashdown, F Atrio-Barandela, J Aumont, et al. Planck 2013 results. xi. all-sky model of thermal dust emission. *Astronomy & Astrophysics*, 571:A11, 2014.

Fausto Acernese, M. Agathos, K. Agatsuma, Damiano Aisa, N. Allemandou, A. Allocca, J. Amarni, Pia Astone, G. Balestri, G. Ballardin, et al. Advanced virgo: a second-generation interferometric gravitational wave detector. *Classical and Quantum Gravity*, 32(2):024001, 2014.

Markus Ackermann, K. Asano, W. B. Atwood, Magnus Axelsson, Luca Baldini, Jean Ballet, Guido Barbiellini, M. G. Baring, Denis Bastieri, K. Bechtol, et al. Fermi observations of grb 090510: A short–hard gamma-ray burst with an additional, hard power-law component from 10 kev to gev energies. *The Astrophysical Journal*, 716(2):1178, 2010.

Zeynep Acuner and Felix Ryde. Clustering of gamma-ray burst types in the fermi gbm catalogue: indications of photosphere and synchrotron emissions during the prompt phase. *Monthly Notices of the Royal Astronomical Society*, 475(2):1708–1724, 2018.

Scott M Adams, CS Kochanek, John F Beacom, Mark R Vagins, and KZ Stanek. Observing the next galactic supernova. *The Astrophysical Journal*, 778(2):164, 2013.

S. Akiyama and J. C. Wheeler. Non-axisymmetric instabilities in core-collapse supernovae. In *New Horizons in Astronomy: Frank N. Bash Symposium*, volume 352, page 221, 2006.

T. Akutsu, M. Ando, K. Arai, Y. Arai, S. Araki, A. Araya, N. Aritomi, H. Asada, Y. Aso, S. Bae, et al. Overview of kagra: Kagra science. *Progress of Theoretical and Experimental Physics*, 2021(5), 2021.

E. N. Alekseev, L. N. Alekseeva, I. V. Krivosheina, and V. I. Volchenko. Detection of the Neutrino Signal from Supernova 1987A Using the INR Baksan Underground Scintillation Telescope. In I. J. Danziger, editor, *European Southern Observatory Conference and Workshop Proceedings*, volume 26 of *European Southern Observatory Conference and Workshop Proceedings*, page 237, January 1987.

Pau Amaro-Seoane, Heather Audley, Stanislav Babak, John Baker, Enrico Barausse, Peter Bender, Emanuele Berti, Pierre Binetruy, Michael Born, Daniele Bortoluzzi, et al. Laser interferometer space antenna. *arXiv preprint arXiv:1702.00786*, 2017.

J.-L. Atteia, B. Cordier, and J. Wei. The svom mission. *International Journal of Modern Physics D*, 31(05):2230008, 2022.

Luca Baiotti. Binary neutron stars. In *Handbook of Gravitational Wave Astronomy*, pages 495–525. Springer, 2022.

S. Bala, Jameson, A., and Fermi-GBM Team. LIGO/Virgo/KAGRA S251112cm: Upper limits from Fermi-GBM Observations. *GRB Coordinates Network*, 42655:1, November 2025.

Scott D. Barthelmy, Louis M. Barbier, Jay R. Cummings, Ed E. Fenimore, Neil Gehrels, Derek Hullinger, Hans A. Krimm, Craig B. Markwardt, David M. Palmer, Ann Parsons, et al. The burst alert telescope (bat) on the swift midex mission. *Space Science Reviews*, 120:143–164, 2005.

Steven V. W. Beckwith, Massimo Stiavelli, Anton M. Koekemoer, John A. R. Caldwell, Henry C. Ferguson, Richard Hook, Ray A. Lucas, Louis E. Bergeron, Michael Corbin, Shardha Jogee, et al. The hubble ultra deep field. *The Astronomical Journal*, 132(5): 1729, 2006.

Eric C. Bellm, Shrinivas R. Kulkarni, Matthew J. Graham, Richard Dekany, Roger M. Smith, Reed Riddle, Frank J. Masci, George Helou, Thomas A. Prince, Scott M. Adams, et al. The zwicky transient facility: system overview, performance, and first results. *Publications of the Astronomical Society of the Pacific*, 131(995):018002, 2018.

Edo Berger. Short-duration gamma-ray bursts. *Annual Review of Astronomy and Astrophysics*, 52(1):43–105, 2014.

P. Narayana Bhat, Charles A. Meegan, Andreas Von Kienlin, William S. Paciesas, Michael S. Briggs, J. Michael Burgess, Eric Burns, Vandiver Chaplin, William H. Cleveland, Andrew C. Collazzi, et al. The third fermi gbm gamma-ray burst catalog: The first six years. *The Astrophysical Journal Supplement Series*, 223(2):28, 2016.

Luciana Bianchi, Alberto Conti, and Bernie Shiao. The ultraviolet sky: An overview from the galex surveys. *Advances in Space Research*, 53(6):900–912, 2014.

Federica B Bianco, Željko Ivezić, R Lynne Jones, Melissa L Graham, Phil Marshall, Abhijit Saha, Michael A Strauss, Peter Yoachim, Tiago Ribeiro, Timo Anguita, et al. Optimization of the observing cadence for the rubin observatory legacy survey of space and time: a pioneering process of community-focused experimental design. *The Astrophysical Journal Supplement Series*, 258(1):1, 2021.

Nigel T. Bishop. Introduction to Gravitational Wave Astronomy. In Cosimo Bambi, Stavros Katsanevas, and Konstantinos D. Kokkotas, editors, *Handbook of Gravitational Wave Astronomy*, page 1. 2021. doi: 10.1007/978-981-15-4702-7_1-1.

Guillaume Blanc and Laura Greggio. Supernova progenitors and iron density evolution from sn rate evolution measurements. *New Astronomy*, 13(8):606–618, 2008.

John M Blondin, Anthony Mezzacappa, and Christine DeMarino. Stability of standing accretion shocks, with an eye toward core-collapse supernovae. *The Astrophysical Journal*, 584(2):971, 2003.

Joshua S Bloom, Dale A Frail, and Re'em Sari. The prompt energy release of gamma-ray burstsusing a cosmologicalk-correction. *The Astronomical Journal*, 121(6):2879, 2001.

M. S. Bothwell, R. C. Kennicutt, B. D. Johnson, Y. Wu, J. C. Lee, D. Dale, C. Engelbracht, D. Calzetti, and E. Skillman. The star formation rate distribution function of the local universe. *Monthly Notices of the Royal Astronomical Society*, 415(2):1815–1826, 2011.

M. T. Botticella, S. J. Smartt, E. Cappellaro, M. Sereno, J. C. Lee, et al. A comparison between sfr diagnostics and cc sn rate within 11 mpc. *Memorie della Società Astronomica Italiana Supplement*, 19:158, 2012.

Marica Branchesi, Michele Maggiore, David Alonso, Charles Badger, Biswajit Banerjee, Freija Beirnaert, Enis Belgacem, Swetha Bhagwat, Guillaume Boileau, Sohrab Borhanian, et al. Science with the einstein telescope: a comparison of different designs. *Journal of Cosmology and Astroparticle Physics*, 2023(07):068, 2023.

Alessandro Bressan, Paola Marigo, Léo Girardi, Bernardo Salasnich, Claudia Dal Cero, Stefano Rubele, and Ambra Nanni. Parsec: stellar tracks and isochrones with the padova and trieste stellar evolution code. *Monthly Notices of the Royal Astronomical Society*, 427(1):127–145, 2012.

Mattia Bulla. Possis: predicting spectra, light curves, and polarization for multidimensional models of supernovae and kilonovae. *Monthly Notices of the Royal Astronomical Society*, 489(4):5037–5045, 2019.

Mattia Bulla. The critical role of nuclear heating rates, thermalization efficiencies, and opacities for kilonova modelling and parameter inference. *Monthly Notices of the Royal Astronomical Society*, 520(2):2558–2570, 2023.

David N. Burrows, J. E. Hill, J. A. Nousek, J. A. Kennea, A. Wells, J. P. Osborne, A. F. Abbey, A. Beardmore, K. Mukerjee, A. D. T. Short, et al. The swift x-ray telescope. *Space Science Reviews*, 120:165–195, 2005.

Michele Cantiello, JB Jensen, JP Blakeslee, E Berger, AJ Levan, NR Tanvir, Gabriella Raimondo, Enzo Brocato, KD Alexander, PK Blanchard, et al. A precise distance to the host galaxy of the binary neutron star merger gw170817 using surface brightness fluctuations. *The Astrophysical Journal Letters*, 854(2):L31, 2018.

E Cappellaro, M Turatto, D Yu Tsvetkov, OS Bartunov, IN Makarova, et al. The rate of supernovae. ii. the selection effects and the frequencies per unit blue luminosity. *arXiv preprint astro-ph/9302017*, 1993.

Jason A Cardelli, Geoffrey C Clayton, and John S Mathis. The relationship between infrared, optical, and ultraviolet extinction. *Astrophysical Journal, Part 1 (ISSN 0004-637X), vol. 345, Oct. 1, 1989, p. 245-256.*, 345:245–256, 1989.

Souradeep Chattopadhyay and Ranjan Maitra. Gaussian-mixture-model-based cluster analysis finds five kinds of gamma-ray bursts in the batse catalogue. *Monthly Notices of the Royal Astronomical Society*, 469(3):3374–3389, 2017.

Shaun Cole, Peder Norberg, Carlton M. Baugh, Carlos S. Frenk, Joss Bland-Hawthorn, Terry Bridges, Russell Cannon, Matthew Colless, Chris Collins, Warrick Couch, et al. The 2df galaxy redshift survey: Near-infrared galaxy luminosity functions. *Monthly Notices of the Royal Astronomical Society*, 326(1):255–273, 2001.

IceCube Collaboration, MAGIC, AGILE, ASAS-SN, HAWC, HESS, INTEGRAL, Kanata, Kiso, Kapteyn, et al. Multimessenger observations of a flaring blazar coincident with high-energy neutrino icecube-170922a. *Science*, 361(6398):eaat1378, 2018.

JUNO collaboration et al. Juno physics and detector. *Progress in Particle and Nuclear Physics*, 123:103927, 2022.

Pan-STARRS Collaboration. Pan-starrs follow-up of the gravitational-wave event s250818k and the lightcurve of sn 2025ulz. *arXiv e-prints*, 2025.

V. Connaughton, M. S. Briggs, A. Goldstein, C. A. Meegan, W. S. Paciesas, R. D. Preece, C. A. Wilson-Hodge, M. H. Gibby, J. Greiner, D. Gruber, et al. Localization of gamma-ray bursts using the fermi gamma-ray burst monitor. *The Astrophysical Journal Supplement Series*, 216(2):32, 2015.

D. O. Cook, J. M. Mazzarella, G. Helou, A. Alcala, T. X. Chen, R. Ebert, C. Frayer, J. Kim, T. Lo, B. F. Madore, et al. Completeness of the nasa/ipac extragalactic database (ned) local volume sample. *The Astrophysical Journal Supplement Series*, 268(1):14, 2023.

DA Coulter, RJ Foley, CD Kilpatrick, MR Drout, AL Piro, BJ Shappee, MR Siebert, JD Simon, N Ulloa, D Kasen, et al. Swope supernova survey 2017a (sss17a), the optical counterpart to a gravitational wave source. *Science*, 358(6370):1556–1558, 2017.

Gergely Dálya, Gábor Galgóczi, László Dobos, Zsolt Frei, Ik Siong Heng, Ronaldas Macas, Christopher Messenger, Péter Raffai, and Rafael S. de Souza. Glade: A galaxy catalogue for multimessenger searches in the advanced gravitational-wave detector era. *Monthly Notices of the Royal Astronomical Society*, 479(2):2374–2381, 2018.

Karsten Danzmann, LISA Study Team, et al. Lisa: laser interferometer space antenna for gravitational wave measurements. *Classical and Quantum Gravity*, 13(11A):A247, 1996.

David L. Davies and Donald W. Bouldin. A cluster separation measure. *IEEE Transactions on Pattern Analysis and Machine Intelligence*, (2):224–227, 1979.

Arnab Dhani, Alessandro Camilletti, Alessio Ludovico De Santis, Andrea Cozzumbo, David Radice, Domenico Logoteta, Albino Perego, Jan Harms, and Marica Branchesi. Direct Measurement of the Accretion Disk Formed in Prompt Collapse Mergers with Future Gravitational-Wave Observatories. *arXiv e-prints*, art. arXiv:2507.14071, July 2025. doi: 10.48550/arXiv.2507.14071.

Francesca Di Lodovico, Hyper-Kamiokande Collaboration, et al. The hyper-kamiokande experiment. In *Journal of physics: conference series*, volume 888, page 012020. IOP Publishing, 2017.

S. Dichiara, D. Tsang, E. Troja, D. Neill, J. P. Norris, and Y.-H. Yang. A luminous precursor in the extremely bright grb 230307a. *The Astrophysical Journal Letters*, 954 (1):L29, 2023.

Roland Diehl, Hubert Halloin, Karsten Kretschmer, Giselher G Lichti, Volker Schönfelder, Andrew W Strong, Andreas Von Kienlin, Wei Wang, Pierre Jean, Jürgen Knödlseder, et al. Radioactive 26al from massive stars in the galaxy. *Nature*, 439(7072):45–47, 2006.

T. Dietrich, T. Hinderer, and A. Samajdar. Interpreting binary neutron star mergers: describing the binary neutron star dynamics, modelling gravitational waveforms, and analyzing detections. *General Relativity and Gravitation*, 53(3):27, 2021.

Georg Drenkhahn. Acceleration of grb outflows by poynting flux dissipation. *Astronomy & Astrophysics*, 387(2):714–724, 2002.

Ulyana Dupletsa, Jan Harms, Biswajit Banerjee, Marica Branchesi, Boris Goncharov, Andrea Maselli, Ana Carolina Silva Oliveira, Samuele Ronchini, and Jacopo Tissino. gwfish: A simulation software to evaluate parameter-estimation capabilities of gravitational-wave detector networks. *Astronomy and Computing*, 42:100671, 2023.

David Eichler, Mario Livio, Tsvi Piran, and David N Schramm. Nucleosynthesis, neutrino bursts and γ-rays from coalescing neutron stars. *Nature*, 340(6229):126–128, 1989.

Albert Einstein. Näherungsweise integration der feldgleichungen der gravitation. *Sitzungsberichte der Königlich Preußischen Akademie der Wissenschaften*, pages 688–696, 1916.

Albert Einstein. Über gravitationswellen. *Sitzungsber. Preuss. Akad. Wiss.*, 1:154, 1918.

Einstein Telescope Collaboration. Milestone 04.02: Common methodology to estimate impact of et design choices on science. `https://apps.et-gw.eu/tds/call_file=ET-0138A-2`, 2025. Accessed: 03-02-2026.

EP Team at NAOC/CAS. LIGO/Virgo/KAGRA S240422ed: X-ray Upper Limits from EP-WXT. `https://gcn.nasa.gov/circulars/36282`, 2024a. GCN Circular 36282.

EP Team at NAOC/CAS. LIGO/Virgo/KAGRA S240422ed: EP-FXT detection of a candidate counterpart EP240426a. `https://gcn.nasa.gov/circulars/36313`, 2024b. GCN Circular 36313.

EP Team at NAOC/CAS. LIGO/Virgo/KAGRA S240422ed: Early X-ray Upper Limits from EP-WXT. `https://gcn.nasa.gov/circulars/36277`, 2024c. GCN Circular 36277.

Richard I Epstein. The eruption of supernova shock waves. *Astrophysical Journal, Part 2-Letters to the Editor, vol. 244, Mar. 1, 1981, p. L89-L91.*, 244:L89–L91, 1981.

Andreoni et al. Ztf25abjmnps (at2025ulz) and s250818k: A candidate superkilonova from a sub-threshold sub-solar mass gravitational wave trigger. *arXiv e-prints*, 2025a.

Cabrera et al. LIGO/Virgo/KAGRA S250206dm: DECam GW-MMADS observations. `https://gcn.nasa.gov/circulars/39318`, 2025b. GCN Circular 39318.

Huber et al. LIGO/Virgo/KAGRA S250206dm: Gemini-North spectroscopic observation of AT2025bbo and its host. `https://gcn.nasa.gov/circulars/39272`, 2025c. GCN Circular 39272.

Kankare et al. LIGO/Virgo/KAGRA S250206dm: Retraction / update on AT2025bbo. `https://gcn.nasa.gov/circulars/39273`, 2025d. GCN Circular 39273.

Smith et al. At2025ulz and s250818k: Investigating early-time observations of a sub-solar mass gravitational-wave binary neutron star merger candidate. *arXiv e-prints*, 2025e.

Steeghs et al. LIGO/Virgo/KAGRA S250206dm: GOTO observations. `https://gcn.nasa.gov/circulars/39215`, 2025f. GCN Circular 39215.

Matthew Evans, Rana X Adhikari, Chaitanya Afle, Stefan W. Ballmer, Sylvia Biscoveanu, Ssohrab Borhanian, Duncan A. Brown, Yanbei Chen, Robert Eisenstein, Alexandra Gruson, Anuradha Gupta, Evan D. Hall, Rachael Huxford, Brittany Kamai, Rahul Kashyap, Jeff S. Kissel, Kevin Kuns, Philippe Landry, Amber Lenon, Geoffrey Lovelace, Lee McCuller, Ken K. Y. Ng, Alexander H. Nitz, Jocelyn Read, B. S. Sathyaprakash, David H. Shoemaker, Bram J. J. Slagmolen, Joshua R. Smith, Varun Srivastava, Ling Sun, Salvatore Vitale, and Rainer Weiss. A Horizon Study for Cosmic Explorer: Science, Observatories, and Community. *arXiv e-prints*, art. arXiv:2109.09882, September 2021. doi: 10.48550/arXiv.2109.09882.

Andrea Falcone, DUNE Collaboration, et al. Deep underground neutrino experiment: Dune. *Nuclear Instruments and Methods in Physics Research Section A: Accelerators, Spectrometers, Detectors and Associated Equipment*, 1041:167217, 2022.

Sydney W Falk. Shock steepening and prompt thermal emission in supernovae. *Astrophysical Journal, Part 2-Letters to the Editor, vol. 225, Nov. 1, 1978, p. L133-L136. Research supported by the RR McCormick Foundation and Arthur Holly Compton Fund*, 225: L133–L136, 1978.

Fermi/GBM Team. Grb 250814a: Fermi gbm final real-time localization. `https://gcn.nasa.gov/circulars/41357`, 2025. GCN Circular 41357.

Thierry Foglizzo, Rémi Kazeroni, Jérôme Guilet, Frédéric Masset, Matthias González, Brendan K Krueger, Jérôme Novak, Micaela Oertel, Jérôme Margueron, Julien Faure, et al. The explosion mechanism of core-collapse supernovae: progress in supernova theory and experiments. *Publications of the Astronomical Society of Australia*, 32:e009, 2015.

Wen-fai Fong and Edo Berger. The locations of short gamma-ray bursts as evidence for compact object binary progenitors. *The Astrophysical Journal*, 776(1):18, 2013.

Wen-fai Fong, E. Berger, and D. B. Fox. Hubble space telescope observations of short gamma-ray burst host galaxies: morphologies, offsets, and local environments. *The Astrophysical Journal*, 708(1):9, 2009.

Wen-fai Fong, Anya E. Nugent, Yuxin Dong, Edo Berger, Kerry Paterson, Ryan Chornock, Andrew Levan, Peter Blanchard, Kate D. Alexander, Jennifer Andrews, et al. Short grb host galaxies. i. photometric and spectroscopic catalogs, host associations, and galactocentric offsets. *The Astrophysical Journal*, 940(1):56, 2022.

D. A. Frail, S. R. Kulkarni, R. Sari, S. G. Djorgovski, J. S. Bloom, T. J. Galama, D. E. Reichart, E. Berger, F. A. Harrison, P. A. Price, S. A. Yost, A. Diercks, R. W. Goodrich, and F. Chaffee. Beaming in Gamma-Ray Bursts: Evidence for a Standard Energy Reservoir. , 562(1):L55–L58, November 2001. doi: 10.1086/338119.

G. S. J. Funes, Robert C. Kennicutt Jr, C. Janice Lee, Shoko Sakai, Christy Tremonti, and Liese van Zee. The 11mpc hα and ultraviolet galaxy survey. In *Island Universes: Structure and Evolution of Disk Galaxies*, pages 441–444. Springer, 2007.

Neil Gehrels. Confidence limits for small numbers of events in astrophysical data. *Astrophysical Journal*, 303:336–346, 1986.

G. Ghirlanda, G. Ghisellini, and L. Nava. The onset of the gev afterglow of grb 090510. *Astronomy and Astrophysics*, 510:L7, 2010.

JH Gillanders, ME Huber, M Nicholl, SJ Smartt, KW Smith, KC Chambers, DR Young, JW Tweddle, S Srivastav, MD Fulton, et al. Pan-starrs follow-up of the gravitational-wave event s250818k and the lightcurve of sn 2025ulz. *arXiv preprint arXiv:2510.01142*, 2025.

L Girardi, MAT Groenewegen, E Hatziminaoglou, and L Da Costa. Star counts in the galaxy-simulating from very deep to very shallow photometric surveys with the trilegal code. *Astronomy & Astrophysics*, 436(3):895–915, 2005.

I. F. Giudice, L. Izzo, R. Martone, M. T. Botticella, E. Cappellaro, R. De Rosa, and M. Della Valle. Identifying potential binary neutron star merger events from the fermi gbm gamma-ray burst catalog. *Astronomy & Astrophysics*, 701:A83, 2025.

Adam Goldstein, Péter Veres, E Burns, MS Briggs, R Hamburg, D Kocevski, CA Wilson-Hodge, RD Preece, S Poolakkil, OJ Roberts, et al. An ordinary short gamma-ray burst with extraordinary implications: Fermi-gbm detection of grb 170817a. *The Astrophysical Journal Letters*, 848(2):L14, 2017.

David Gruber, Adam Goldstein, Victoria Weller von Ahlefeld, P. Narayana Bhat, Elisabetta Bissaldi, Michael S. Briggs, Dave Byrne, William H. Cleveland, Valerie Connaughton, Roland Diehl, et al. The fermi gbm gamma-ray burst spectral catalog: Four years of data. *The Astrophysical Journal Supplement Series*, 211(1):12, 2014.

Todd Haines, CB Bratton, D Casper, A Ciocio, R Claus, M Crouch, ST Dye, S Errede, W Gajewski, M Goldhaber, et al. Neutrinos from sn1987a in the imb detector. *Nuclear Instruments and Methods in Physics Research Section A: Accelerators, Spectrometers, Detectors and Associated Equipment*, 264(1):28–31, 1988.

A Hajela, R Margutti, KD Alexander, A Kathirgamaraju, A Baldeschi, C Guidorzi, D Giannios, W Fong, Y Wu, A MacFadyen, et al. Two years of nonthermal emission from the binary neutron star merger gw170817: rapid fading of the jet afterglow and first constraints on the kilonova fastest ejecta. *The Astrophysical Journal Letters*, 886 (1):L17, 2019.

Brynmor Haskell and Kai Schwenzer. Isolated neutron stars. In *Handbook of Gravitational Wave Astronomy*, pages 527–554. Springer, 2022.

Kazuto Hirata, Takaaki Kajita, Masatoshi Koshiba, M Nakahata, Yt Oyama, N Sato, A Suzuki, M Takita, Y Totsuka, T Kifune, et al. Observation of a neutrino burst from the supernova sn1987a. *Physical Review Letters*, 58(14):1490, 1987.

Andrew M. Hopkins and John F. Beacom. On the normalization of the cosmic star formation history. *The Astrophysical Journal*, 651(1):142, 2006.

Russell A Hulse and Joseph H Taylor. Discovery of a pulsar in a binary system. *Astrophysical Journal, vol. 195, Jan. 15, 1975, pt. 2, p. L51-L53.*, 195:L51–L53, 1975.

Myungshin Im, Yongmin Yoon, Seong-Kook J Lee, Hyung Mok Lee, Joonho Kim, Chung-Uk Lee, Seung-Lee Kim, Eleonora Troja, Changsu Choi, Gu Lim, et al. Distance and properties of ngc 4993 as the host galaxy of the gravitational-wave source gw170817. *The Astrophysical Journal Letters*, 849(1):L16, 2017.

Željko Ivezić, Steven M. Kahn, J. Anthony Tyson, Bob Abel, Emily Acosta, Robyn Allsman, David Alonso, Yusra AlSayyad, Scott F. Anderson, John Andrew, et al. Lsst: From science drivers to reference design and anticipated data products. *The Astrophysical Journal*, 873(2):111, 2019.

Hans-Thomas Janka. Neutrino-driven explosions. In *Handbook of Supernovae*, pages 1–56. Springer, 2017.

Nicholas Kaiser, Herve Aussel, Barry E. Burke, Hans Boesgaard, Ken Chambers, Mark Richard Chun, James N. Heasley, Klaus-Werner Hodapp, Bobby Hunt, Robert Jedicke, et al. Pan-starrs: a large synoptic survey telescope array. In *Survey and Other Telescope Technologies and Discoveries*, volume 4836, pages 154–164. SPIE, 2002.

Igor D. Karachentsev, Valentina E. Karachentseva, Walter K. Huchtmeier, and Dmitry I. Makarov. A catalog of neighboring galaxies. *The Astronomical Journal*, 127(4):2031, 2004.

Adithan Kathirgamaraju, Rodolfo Barniol Duran, and Dimitrios Giannios. Off-axis short grbs from structured jets as counterparts to gw events. *Monthly Notices of the Royal Astronomical Society: Letters*, 473(1):L121–L125, 2018.

Evan Francis Keane and M Kramer. On the birthrates of galactic neutron stars. *Monthly Notices of the Royal Astronomical Society*, 391(4):2009–2016, 2008.

Robert C. Kennicutt Jr. Star formation in galaxies along the hubble sequence. *Annual Review of Astronomy and Astrophysics*, 36(1):189–231, 1998.

Robert C. Kennicutt Jr, Janice C. Lee, José G. Funes, Shoko Sakai, Sanae Akiyama, et al. An hα imaging survey of galaxies in the local 11 mpc volume. *The Astrophysical Journal Supplement Series*, 178(2):247, 2008.

Stephen M. Kent. Sloan digital sky survey. *Astrophysics and Space Science*, 217(1):27–30, 1994.

Charles D Kilpatrick, Wen-fai Fong, Peter K Blanchard, Joel Leja, Anya E Nugent, Antonella Palmese, Kerry Paterson, Tjitske Starkenburg, Kate D Alexander, Edo Berger, et al. Hubble space telescope observations of gw170817: complete light curves and the properties of the galaxy merger of ngc 4993. *The Astrophysical Journal*, 926(1):49, 2022.

Shiho Kobayashi and Peter Mészáros. Gravitational radiation from gamma-ray burst progenitors. *The Astrophysical Journal*, 589(2):861, 2003.

Kei Kotake and Takami Kuroda. Gravitational waves from core-collapse supernovae. In *Handbook of Supernovae*. 2017.

Kei Kotake, Tomoya Takiwaki, Yudai Suwa, Wakana Iwakami Nakano, Shio Kawagoe, Youhei Masada, and Shin-ichiro Fujimoto. Multimessengers from core-collapse supernovae: Multidimensionality as a key to bridge theory and observation. *Advances in Astronomy*, 2012(1):428757, 2012.

Roland Kothes. Distance and age of the pulsar wind nebula 3c 58. *Astronomy & Astrophysics*, 560:A18, 2013.

Chryssa Kouveliotou, Charles A. Meegan, Gerald J. Fishman, Narayana P. Bhat, Michael S. Briggs, Thomas M. Koshut, William S. Paciesas, and Geoffrey N. Pendleton. Identification of two classes of gamma-ray bursts. *The Astrophysical Journal Letters*, 413:L101–L104, 1993.

Konstantinos Kovlakas, Andreas Zezas, Jeff J. Andrews, Antara Basu-Zych, Tassos Fragos, Ann Hornschemeier, Konstantinos Kouroumpatzakis, Bret Lehmer, and Andrew Ptak. The heraklion extragalactic catalogue (hecate): A value-added galaxy catalogue for multimessenger astrophysics. *Monthly Notices of the Royal Astronomical Society*, 506(2): 1896–1915, 2021.

Pavel Kroupa. The initial mass function of stars: evidence for uniformity in variable systems. *Science*, 295(5552):82–91, 2002.

Takami Kuroda, Tomoya Takiwaki, and Kei Kotake. Gravitational wave signatures from low-mode spiral instabilities in rapidly rotating supernova cores. *Physical Review D*, 89 (4):044011, 2014.

Gavin P. Lamb, N. R. Tanvir, A. J. Levan, A. de Ugarte Postigo, Kyohei Kawaguchi, A. Corsi, P. A. Evans, Benjamin Gompertz, D. B. Malesani, K. L. Page, et al. Short grb 160821b: A reverse shock, a refreshed shock, and a well-sampled kilonova. *The Astrophysical Journal*, 883(1):48, 2019.

David Langlois, Ryo Saito, Daisuke Yamauchi, and Karim Noui. Scalar-tensor theories and modified gravity in the wake of gw170817. *Physical Review D*, 97(6):061501, 2018.

DA Leahy, S Ranasinghe, and M Gelowitz. Evolutionary models for 43 galactic supernova remnants with distances and x-ray spectra. *The Astrophysical Journal Supplement Series*, 248(1):16, 2020.

Jesse Leaman, Weidong Li, Ryan Chornock, and Alexei V Filippenko. Nearby supernova rates from the lick observatory supernova search–i. the methods and data base. *Monthly Notices of the Royal Astronomical Society*, 412(3):1419–1440, 2011.

Janice C. Lee, Armando Gil de Paz, Christy Tremonti, Robert Kennicutt, et al. Uv/h-α turmoil. *arXiv preprint arXiv:1011.2181*, 2010.

Andrew J Levan, JD Lyman, NR Tanvir, J Hjorth, Ilya Mandel, Elizabeth R Stanway, D Steeghs, AS Fruchter, E Troja, SL Schrøder, et al. The environment of the binary neutron star merger gw170817. *The Astrophysical Journal Letters*, 848(2):L28, 2017.

Andrew J Levan, Benjamin P Gompertz, Om Sharan Salafia, Mattia Bulla, Eric Burns, Kenta Hotokezaka, Luca Izzo, Gavin P Lamb, Daniele B Malesani, Samantha R Oates, et al. Heavy-element production in a compact object merger observed by jwst. *Nature*, 626(8000):737–741, 2024.

Li-Xin Li and Bohdan Paczyński. Transient events from neutron star mergers. *The Astrophysical Journal*, 507(1):L59, 1998.

Weidong Li, Ryan Chornock, Jesse Leaman, Alexei V. Filippenko, Dovi Poznanski, Xiaofeng Wang, Mohan Ganeshalingam, and Filippo Mannucci. Nearby supernova rates from the

lick observatory supernova search–iii. the rate–size relation, and the rates as a function of galaxy hubble type and colour. *Monthly Notices of the Royal Astronomical Society*, 412(3):1473–1507, 2011.

Ligo Scientific Collaboration, VIRGO Collaboration, and Kagra Collaboration. LIGO/Virgo/KAGRA S250818k: Properties of the low-significance GW compact binary merger candidate potentially associated with AT 2025ulz. *GRB Coordinates Network*, 41437:1, August 2025a.

Ligo Scientific Collaboration, VIRGO Collaboration, and Kagra Collaboration. LIGO/Virgo/KAGRA S251112cm: Identification of a GW compact binary merger candidate. *GRB Coordinates Network*, 42650:1, November 2025b.

LIGO/Virgo/KAGRA Collaboration. LIGO/Virgo/KAGRA s240422ed: Lvk notice (low-latency). `https://gcn.nasa.gov/circulars/36236`, 2024. GCN Circular 36236.

LIGO/Virgo/KAGRA Collaboration. LIGO/Virgo/KAGRA s250206dm: Lvk notice (low-latency). `https://gcn.nasa.gov/circulars/39175`, 2025a. GCN Circular 39175.

LIGO/Virgo/KAGRA Collaboration. LIGO/Virgo/KAGRA s250814bg: Lvk notice (low-latency). `https://gcn.nasa.gov/circulars/41364`, 2025b. GCN Circular 41364.

Z. Y. Liu, W. Zhao, J.-A. Jiang, Z. L. Xu, D. Z. Meng, M. X. Cai, T. G. Wang, X. Kong, Z. G. Dai, L. L. Fan, Z. P. Jin, Y. Z. Fan, and WFST Collaboration. LIGO/Virgo/KAGRA S251112cm: WFST follow-up observations and preliminary results. *GRB Coordinates Network*, 42722:1, November 2025.

Stuart Lloyd. Least squares quantization in pcm. *IEEE Transactions on Information Theory*, 28(2):129–137, 1982.

Kieran J Luken, Miroslav D Filipović, Nigel I Maxted, Roland Kothes, Ray P Norris, James R Allison, Rebecca Blackwell, Catherine Braiding, Robert Brose, Michael Burton, et al. Radio observations of supernova remnant g1. 9+ 0.3. *Monthly Notices of the Royal Astronomical Society*, 492(2):2606–2621, 2020.

Sean MacBride, Erin Howard, Ian Sullivan, Peter Yoachim, Eric Bellm, Shreya Anand, Federica Bianco, Tiago Ribeiro, Lynne Jones, Alysha Shugart, Narayan Khadka, Kshitija Kelkar, Danica Zilkova, Kevin Fanning, Paulina Venegas, Kate Napier, Erik Dennihy, Anastasia Alexov, Bob Blum, Yousuke Utsumi, Robert Lupton, Keith Bechtol, and NSF-DOE Vera C Rubin Observatory. LIGO/Virgo/KAGRA S251112cm: Observations with the NSF-DOE Vera C. Rubin Observatory. *GRB Coordinates Network*, 42707:1, November 2025.

Andrzej Maćkiewicz and Waldemar Ratajczak. Principal components analysis (pca). *Computers & Geosciences*, 19(3):303–342, 1993.

Piero Madau and Mark Dickinson. Cosmic star-formation history. *Annual Review of Astronomy and Astrophysics*, 52:415–486, 2014.

Michele Maggiore, Chris Van Den Broeck, Nicola Bartolo, Enis Belgacem, Daniele Bertacca, Marie Anne Bizouard, Marica Branchesi, Sebastien Clesse, Stefano Foffa, Juan García-Bellido, et al. Science case for the einstein telescope. *Journal of Cosmology and Astroparticle Physics*, 2020(03):050, 2020.

Paola Marigo, Alessandro Bressan, Ambra Nanni, Léo Girardi, and Maria Letizia Pumo. Evolution of thermally pulsing asymptotic giant branch stars–i. the colibri code. *Monthly Notices of the Royal Astronomical Society*, 434(1):488–526, 2013.

Tatsuya Matsumoto, Ehud Nakar, and Tsvi Piran. Generalized compactness limit from an arbitrary viewing angle. *Monthly Notices of the Royal Astronomical Society*, 486(2): 1563–1573, 2019.

Alessandro Mazzi, Léo Girardi, Simone Zaggia, Giada Pastorelli, Stefano Rubele, Alessandro Bressan, Maria-Rosa L Cioni, Gisella Clementini, Felice Cusano, João Pedro Rocha, et al. The vmc survey–xliii. the spatially resolved star formation history across the large magellanic cloud. *Monthly Notices of the Royal Astronomical Society*, 508(1):245–266, 2021.

Leland McInnes, John Healy, Nathaniel Saul, and Lukas Großberger. Umap: Uniform manifold approximation and projection. *Journal of Open Source Software*, 3(29):861, 2018.

Charles Meegan, Giselher Lichti, P. N. Bhat, Elisabetta Bissaldi, Michael S. Briggs, Valerie Connaughton, Roland Diehl, Gerald Fishman, Jochen Greiner, Andrew S. Hoover, et al. The fermi gamma-ray burst monitor. *The Astrophysical Journal*, 702(1):791, 2009.

Y. Mellier, Abdurroúf Abdurroúf, J. A. Acevedo Barroso, A. Achúcarro, J. Adamek, R. Adam, G. E. Addison, N. Aghanim, M. Aguena, V. Ajani, et al. Euclid. i. overview of the euclid mission. *Astronomy & Astrophysics*, 2024.

P Mészáros and MJ Rees. Optical and long-wavelength afterglow from gamma-ray bursts. *The Astrophysical Journal*, 476(1):232, 1997.

B. D. Metzger, G. Martínez-Pinedo, S. Darbha, E. Quataert, A. Arcones, D. Kasen, R. Thomas, P. Nugent, I. V. Panov, and N. T. Zinner. Electromagnetic counterparts of compact object mergers powered by the radioactive decay of r-process nuclei. , 406(4): 2650–2662, August 2010. doi: 10.1111/j.1365-2966.2010.16864.x.

Brian D Metzger. Kilonovae. *Living Reviews in Relativity*, 23(1):1, 2020.

K. Misra, K. G. Arun, et al. Evidence for two distinct populations of kilonova-associated gamma-ray bursts. *The Astrophysical Journal Letters*, 949(2):L22, 2023.

K. Misra, K. G. Arun, et al. Diversity in fermi/gbm gamma-ray bursts: New insights from machine learning. *The Astrophysical Journal*, 974(1):55, 2024.

Ismail Bin Mohamad and Dauda Usman. Research article: standardization and its effects on k-means clustering algorithm. *Research Journal of Applied Sciences, Engineering and Technology*, 6(17):3299–3303, 2013.

KP Mooley, DA Frail, D Dobie, E Lenc, A Corsi, K De, AJ Nayana, S Makhathini, I Heywood, T Murphy, et al. A strong jet signature in the late-time light curve of gw170817. *The Astrophysical Journal Letters*, 868(1):L11, 2018.

C Tanner Murphey, Jacob W Hogan, Brian D Fields, and Gautham Narayan. Witnessing history: sky distribution, detectability, and rates of naked-eye milky way supernovae. *Monthly Notices of the Royal Astronomical Society*, 507(1):927–943, 2021.

Jeremiah W. Murphy, Christian D. Ott, and Adam Burrows. A model for gravitational wave emission from neutrino-driven core-collapse supernovae. *The Astrophysical Journal*, 707(2):1173, 2009.

A. M. Nicuesa Guelbenzu, S. Klose, Patricia Schady, K. Belczynski, D. H. Hartmann, Leslie Kipp Hunt, and M. J. Michałowski. Vlt/muse and atca observations of the host galaxy of the short grb 080905a at z = 0.122. *The Astrophysical Journal*, 923(1):38, 2021.

Anya E. Nugent, Wen-fai Fong, Cristian Castrejon, Joel Leja, Michael Zevin, and Alexander P. Ji. A population of short-duration gamma-ray bursts with dwarf host galaxies. *The Astrophysical Journal*, 962(1):5, 2024.

Göran Olofsson. Grb 090510: Not afterglow confirmation. *GRB Coordinates Network, Circular Service*, (9338):1, 2009.

B O'Connor, E Troja, S Dichiara, P Beniamini, SB Cenko, C Kouveliotou, J Becerra González, J Durbak, P Gatkine, A Kutyrev, et al. A deep survey of short grb host galaxies over z 0–2: implications for offsets, redshifts, and environments. *Monthly Notices of the Royal Astronomical Society*, 515(4):4890–4928, 2022.

Pan-STARRS / Smartt et al. LIGO/Virgo/KAGRA S250206dm: further Pan-STARRS observations and one candidate AT2025bbo. `https://gcn.nasa.gov/circulars/39244`, 2025. GCN Circular 39244.

Pan-STARRS Collaboration / Young et al. LIGO/Virgo/KAGRA S250206dm: Pan-STARRS candidate AT2025bbo (ZTF/PS ID ZTF25...) . `https://gcn.nasa.gov/circulars/39210`, 2025. GCN Circular 39210.

Ajith Parameswaran, Pau Amaro Seoane, Manuel Arca Sedda, Riccardo Arcodia, Francesca Badaracco, Biswajit Banerjee, Enis Belgacem, Giovanni Benetti, Stefano Benetti, Alexey Bobrick, et al. The lunar gravitational-wave antenna: mission studies and science case. *Journal of Cosmology and Astroparticle Physics*, 108:1–25, 2025.

Ferdinando Patat, A. W. Alsabti, and Paul Murdin. *Handbook of Supernovae*. Springer, 2017.

Albino Perego, F-K Thielemann, and Gabriele Cescutti. r-process nucleosynthesis from compact binary mergers. In *Handbook of Gravitational Wave Astronomy*, pages 555–610. Springer, 2022.

Philip Carl Peters. Gravitational radiation and the motion of two point masses. *Physical Review*, 136(4B):B1224, 1964.

Elena Pian, Paolo D'Avanzo, Stefano Benetti, M Branchesi, Enzo Brocato, Sergio Campana, Enrico Cappellaro, Stefano Covino, V d'Elia, JPU Fynbo, et al. Spectroscopic identification of r-process nucleosynthesis in a double neutron-star merger. *Nature*, 551 (7678):67–70, 2017.

Adriano Pieres, L Girardi, E Balbinot, B Santiago, LN Da Costa, A Carnero Rosell, AB Pace, K Bechtol, MAT Groenewegen, A Drlica-Wagner, et al. Modelling the milky way–i. method and first results fitting the thick disc and halo with des-y3 data. *Monthly Notices of the Royal Astronomical Society*, 497(2):1547–1562, 2020.

M. Punturo, M. Abernathy, Fausto Acernese, B. Allen, Nils Andersson, K. Arun, Fabrizio Barone, B. Barr, M. Barsuglia, M. Beker, et al. The einstein telescope: a third-generation gravitational wave observatory. *Classical and Quantum Gravity*, 27(19):194002, 2010.

Alexis L Quintana, Nicholas J Wright, and Juan Martínez García. A census of ob stars within 1 kpc and the star formation and core collapse supernova rates of the milky way. *Monthly Notices of the Royal Astronomical Society*, 538(3):1367–1383, 2025.

David Radice, Viktoriya Morozova, Adam Burrows, David Vartanyan, and Hiroki Nagakura. Characterizing the gravitational wave signal from core-collapse supernovae. *The Astrophysical Journal Letters*, 876(1):L9, 2019.

Markus Rampp, Ewald Müller, and Maximilian Ruffert. Simulations of non-axisymmetric rotational core collapse. *arXiv preprint astro-ph/9711122*, 1997.

Jillian C. Rastinejad, Benjamin P. Gompertz, Andrew J. Levan, Wen-fai Fong, Matt Nicholl, Gavin P. Lamb, Daniele B. Malesani, Anya E. Nugent, Samantha R. Oates, Nial R. Tanvir, et al. A kilonova following a long-duration gamma-ray burst at 350 mpc. *Nature*, 612(7939):223–227, 2022.

A Rau, S McBreen, and T Kruehler. Grb090510: Vlt/fors2 spectroscopic redshift. *GRB Coordinates Network*, 9353:1, 2009.

B Cameron Reed. New estimates of the solar-neighborhood massive star birthrate and the galactic supernova rate. *The Astronomical Journal*, 130(4):1652, 2005.

Martin J Rees and Péter Mészáros. Unsteady outflow models for cosmological gamma-ray bursts. *arXiv preprint astro-ph/9404038*, 1994.

MJ Rees and P Mészáros. Relativistic fireballs: energy conversion and time-scales. *Monthly Notices of the Royal Astronomical Society*, 258(1):41P–43P, 1992.

Stephen Reynolds. Evolution of the youngest galactic supernova remnant g1. 9+ 0.3. *Chandra Proposal*, page 5389, 2018.

Dean Richardson, David Branch, Darrin Casebeer, Jennifer Millard, RC Thomas, and E Baron. A comparative study of the absolute magnitude distributions of supernovae. *The Astronomical Journal*, 123(2):745, 2002.

Peter W. A. Roming, Thomas E. Kennedy, Keith O. Mason, John A. Nousek, Lindy Ahr, Richard E. Bingham, Patrick S. Broos, Mary J. Carter, Barry K. Hancock, Howard E. Huckle, et al. The swift ultra-violet/optical telescope. *Space Science Reviews*, 120:95–142, 2005.

Philip Rosenfield, Paola Marigo, Léo Girardi, Julianne J Dalcanton, Alessandro Bressan, Benjamin F Williams, and Andrew Dolphin. Evolution of thermally pulsing asymptotic giant branch stars. v. constraining the mass loss and lifetimes of intermediate-mass, low-metallicity agb stars. *The Astrophysical Journal*, 822(2):73, 2016.

Stephan Rosswog, Enrico Ramirez-Ruiz, and Melvyn B Davies. High-resolution calculations of merging neutron stars–iii. gamma-ray bursts. *Monthly Notices of the Royal Astronomical Society*, 345(4):1077–1090, 2003.

Peter J. Rousseeuw. Silhouettes: A graphical aid to the interpretation and validation of cluster analysis. *Journal of Computational and Applied Mathematics*, 20:53–65, 1987.

Antonia Rowlinson, Klaas Wiersema, Andrew J. Levan, Nial R. Tanvir, P. T. O'Brien, Evert Rol, Jens Hjorth, C. C. Thöne, Antonio de Ugarte Postigo, Johan Peter Uldall Fynbo, et al. Discovery of the afterglow and host galaxy of the low-redshift short grb 080905a. *Monthly Notices of the Royal Astronomical Society*, 408(1):383–391, 2010.

Karolina Rozwadowska, Francesco Vissani, and Enrico Cappellaro. On the rate of core collapse supernovae in the milky way. *New Astronomy*, 83:101498, 2021.

R. Ruffini, M. Muccino, Y. Aimuratov, C. L. Bianco, C. Cherubini, M. Enderli, M. Kovacevic, R. Moradi, A. V. Penacchioni, G. B. Pisani, et al. Grb 090510: A genuine short grb from a binary neutron star coalescing into a kerr–newman black hole. *The Astrophysical Journal*, 831(2):178, 2016.

Geoffrey Ryan, Hendrik van Eerten, Luigi Piro, Eleonora Troja, Brendan O'Connor, and Roberto Ricci. afterglowpy: Compute and fit grb afterglows. *Astrophysics Source Code Library*, pages ascl–2505, 2025.

Om Sharan Salafia. Detection probability of light compact binary mergers in future observing runs of the current ground-based gravitational wave detector network. , 702: A54, October 2025. doi: 10.1051/0004-6361/202555997.

Re'em Sari, Tsvi Piran, and Jules P Halpern. Jets in gamma-ray bursts. *The Astrophysical Journal*, 519(1):L17, 1999.

Volodymyr Savchenko, C Ferrigno, E Kuulkers, ANGELA Bazzano, E Bozzo, S Brandt, J Chenevez, TJ-L Courvoisier, R Diehl, A Domingo, et al. Integral detection of the first prompt gamma-ray signal coincident with the gravitational-wave event gw170817. *The Astrophysical Journal Letters*, 848(2):L15, 2017.

Karl Schwarzschild. Über das gravitationsfeld eines massenpunktes nach der einsteinschen theorie. *Sitzungsberichte der königlich preussischen Akademie der Wissenschaften*, pages 189–196, 1916.

Yingze Shan, Xiao-Xuan Liu, Xing Yang, Haoyu Yuan, and Houjun Lu. Grb 210323a: Signature of long-lasting lifetime of supra-massive magnetar as the central engine from the merger of binary neutron star. *Research in Astronomy and Astrophysics*, 2024.

SJea Smartt, T-W Chen, A Jerkstrand, M Coughlin, E Kankare, SA Sim, M Fraser, C Inserra, K Maguire, KC Chambers, et al. A kilonova as the electromagnetic counterpart to a gravitational-wave source. *Nature*, 551(7678):75–79, 2017.

Nathan Smith. The crab nebula and the class of type iin-p supernovae caused by sub-energetic electron-capture explosions. *Monthly Notices of the Royal Astronomical Society*, 434(1):102–113, 2013.

Swift/BAT Team. Grb 250814a: Swift/bat detection. `https://gcn.nasa.gov/circulars/41358`, 2025. GCN Circular 41358.

GA Tammann, W Loeffler, and A Schroeder. The galactic supernova rate. *The Astrophysical Journal Supplement Series, vol. 92, no. 2, p. 487-493*, 92:487–493, 1994.

J. L. Tonry, L. Denneau, H. Flewelling, A. N. Heinze, C. A. Onken, Stephen J. Smartt, B. Stalder, H. J. Weiland, and Christian Wolf. The atlas all-sky stellar reference catalog. *The Astrophysical Journal*, 867(2):105, 2018.

E. Troja, Alberto J. Castro-Tirado, J. Becerra González, Y. Hu, G. S. Ryan, S. B. Cenko, R. Ricci, G. Novara, R. Sánchez-Rámirez, J. A. Acosta-Pulido, et al. The afterglow and kilonova of the short grb 160821b. *Monthly Notices of the Royal Astronomical Society*, 489(2):2104–2116, 2019.

Eleanora Troja, Geoffrey Ryan, Luigi Piro, Hendrik Van Eerten, S. B. Cenko, Y. Yoon, S.-K. Lee, M. Im, T. Sakamoto, P. Gatkine, et al. A luminous blue kilonova and an off-axis jet from a compact binary merger at z = 0.1341. *Nature Communications*, 9(1): 4089, 2018.

Eleonora Troja. Eighteen years of kilonova discoveries with swift. *Universe*, 9(6):245, 2023.

Eleonora Troja, C. L. Fryer, B. O'Connor, G. Ryan, S. Dichiara, A. Kumar, N. Ito, R. Gupta, R. T. Wollaeger, J. P. Norris, et al. A nearby long gamma-ray burst from a merger of compact objects. *Nature*, 612(7939):228–231, 2022.

HST Follow up Collaboration. At2025ulz and s250818k: Zooming in with the hubble space telescope. *arXiv e-prints*, 2025.

Sidney van den Bergh and Robert D McClure. Rediscussion of extragalactic supernova rates derived from evans's 1980-1988 observations. *Astrophysical Journal, Part 1 (ISSN 0004-637X), vol. 425, no. 1, p. 205-209*, 425:205–209, 1994.

David Vartanyan, Adam Burrows, Tianshu Wang, Matthew S. B. Coleman, and Christopher J. White. Gravitational-wave signature of core-collapse supernovae. *Physical Review D*, 107(10):103015, 2023.

V Ashley Villar, James Guillochon, Edo Berger, Brian D Metzger, Philip S Cowperthwaite, Matt Nicholl, Kate D Alexander, Peter K Blanchard, Ryan Chornock, Tarraneh Eftekhari, et al. The combined ultraviolet, optical, and near-infrared light curves of the kilonova associated with the binary neutron star merger gw170817: unified data set, analytic models, and physical implications. *The Astrophysical Journal Letters*, 851(1):L21, 2017.

A. Von Kienlin, C. A. Meegan, W. S. Paciesas, P. N. Bhat, E. Bissaldi, M. S. Briggs, E. Burns, W. H. Cleveland, M. H. Gibby, M. M. Giles, et al. The fourth fermi-gbm gamma-ray burst catalog: A decade of data. *The Astrophysical Journal*, 893(1):46, 2020.

Andreas Von Kienlin, Charles A. Meegan, William S. Paciesas, P. N. Bhat, Elisabetta Bissaldi, Michael S. Briggs, J. Michael Burgess, David Byrne, Vandiver Chaplin, William Cleveland, et al. The second fermi gbm gamma-ray burst catalog: The first four years. *The Astrophysical Journal Supplement Series*, 211(1):13, 2014.

Lifan Wang and J. Craig Wheeler. Spectropolarimetry of supernovae. *Annual Review of Astronomy and Astrophysics*, 46(1):433–474, 2008.

Lingyu Wang, Michael Rowan-Robinson, Peder Norberg, Sebastien Heinis, and Jiaxin Han. The revised iras-fsc redshift catalogue (rifscz). *Monthly Notices of the Royal Astronomical Society*, 442(3):2739–2750, 2014.

Darach Watson, Camilla J Hansen, Jonatan Selsing, Andreas Koch, Daniele B Malesani, Anja C Andersen, Johan PU Fynbo, Almudena Arcones, Andreas Bauswein, Stefano Covino, et al. Identification of strontium in the merger of two neutron stars. *Nature*, 574(7779):497–500, 2019.

Eli Waxman and Boaz Katz. Shock breakout theory. In *Handbook of supernovae*, pages 967–1015. Springer, 2017.

Michael W. Werner, Thomas L. Roellig, F. J. Low, George H. Rieke, M. Rieke, W. F. Hoffmann, E. Young, J. R. Houck, B. Brandl, G. G. Fazio, et al. The spitzer space telescope mission. *The Astrophysical Journal Supplement Series*, 154(1):1, 2004.

Christian Wolf, Klaus Meisenheimer, Hans-Walter Rix, Andreas Borch, Simon Dye, and Martin Kleinheinrich. The combo-17 survey: Evolution of the galaxy luminosity function from 25,000 galaxies with z. *Astronomy & Astrophysics*, 401(1):73–98, 2003.

SE Woosley and Alexander Heger. The progenitor stars of gamma-ray bursts. *The Astrophysical Journal*, 637(2):914, 2006.

Weimin Yuan, Chen Zhang, Yong Chen, and Zhixing Ling. The einstein probe mission. In *Handbook of X-ray and Gamma-ray Astrophysics*, pages 1–30. Springer, 2022.